

A COMPUTATIONAL FRAMEWORK FOR DIABETIC RETINOPATHY SEVERITY GRADING CATEGORIZATION USING OPHTHALMIC IMAGE PROCESSING

*Thesis submitted in fulfillment of the requirements for the
Degree of*

DOCTOR OF PHILOSOPHY

By

CHARU BHARDWAJ



Department of Electronics and Communication Engineering

JAYPEE UNIVERSITY OF INFORMATION TECHNOLOGY
WAKNAGHAT, SOLAN-173234, HIMACHAL PRADESH, INDIA

November, 2020

@ Copyright JAYPEE UNIVERSITY OF INFORMATION TECHNOLOGY, WAKNAGHAT
November, 2020
ALL RIGHT RESERVED

TABLE OF CONTENTS

CONTENTS

DECLARATION BY THE SCHOLAR	i
SUPERVISOR’S CERTIFICATE	ii
ACKNOWLEDGEMENT	iii-iv
LIST OF ABBREVIATIONS AND ACRONYMS	v-viii
LIST OF FIGURES	ix-xiii
LIST OF TABLES	xiv-xvi
ABSTRACT	xvii-xix

CHAPTER 1

INTRODUCTION	2-36
1.1 Anatomy of Eye	2
1.2 Modalities of Ophthalmic Images	3
1.2.1 Retinal Fundus Imaging	4
1.2.2 Optical Coherence Tomography	5
1.3 Diabetic Retinopathy	6
1.3.1 Optical Disc and Blood Vessels of Retinal Images	7
1.3.2 Lesions in Diabetic Retinopathy	8
1.3.3 Diabetic Retinopathy Grading	10
1.4 Statistical Analysis for Extracted Features	11
1.5 Classification Techniques	13
1.5.1 Machine Learning Classifiers	13
1.5.1.1 Support Vector Machine Classifier	13
1.5.1.2 k-Nearest Neighbour Classifier	14
1.5.1.3 Artificial Neural Network Classifier	15
1.5.2 Deep Neural Networks	17
1.5.2.1 Convolutional Neural Networks	18
1.5.2.2 Pre-trained CNN Classifiers	20
1.6 Dataset Details	24
1.6.1 DRIVE Dataset	25

1.6.2	STARE Dataset	26
1.6.3	DIARETDB1 Dataset.....	26
1.6.4	MESSIDOR Dataset.....	26
1.6.5	IDRiD Dataset	26
1.7	Computer-Aided Diagnosis System	27
1.8	Performance Indices	28
1.9	Software Platform.....	31
1.10	Motivation	32
1.11	Research Gaps	32
1.12	Objectives of Research Work	34
1.13	Outline of the Thesis.....	35

CHAPTER 2

LITERATURE REVIEW.....38-59

2.1	OD Localization and Blood Vessel Extraction.....	39
2.2	Lesion Discrimination	45
2.2.1	Red Lesion Detection	45
2.2.2	Yellow Lesion Detection.....	47
2.3	Diabetic Retinopathy Grading	50
2.4	Deep Learning Classification	52
2.4.1	Machine Learning based Classification	53
2.4.2	Deep Neural Network based Classification	54

CHAPTER 3

RETINAL BLOOD VASCULATURE SEGMENTATION FRAMEWORK.....61-99

3.1	Introduction	61
3.1.1	Retinal Landmark Segmentation.....	62
3.2	OD Localization and Blood Vasculature Segmentation.....	66
3.2.1	Fundus Image Pre-processing	67
3.2.2	Optical Disc Localization.....	70
3.2.2.1	Mathematical Morphology based OD Localization	70
3.2.2.2	Circular Hough Transform based OD Localization	71
3.2.3	Blood Vasculature Segmentation	73

3.2.3.1	Modified Kirsch’s Edge Detection	73
3.2.3.2	Fuzzy Inference based Blood Vessel Segmentation.....	75
3.3	Proposed Hybrid Blood Vessel Segmentation.....	76
3.3.1	Feature Attribute Selection for Blood Vessel Segmentations	78
3.4	Results of OD Localization and Blood Vasculature Segmentation.....	79
3.4.1	Results of Image Pre-processing	80
3.4.2	Results of OD Localization	83
3.4.2.1	Results of Morphology based OD Localization	83
3.4.2.2	Results for Circular Hough Transform based OD Localization	84
3.4.2.3	Performance Analysis of OD Localization.....	86
3.4.3	Results of Blood Vasculature Segmentation	87
3.4.3.1	Performance Analysis of Segmented Blood Vessels.....	88
3.5	Results of Proposed HBV-MR Approach	89
3.5.1	Statistical Analysis of HBV-MR.....	90
3.5.2	Performance Analysis of HBV-MR	96
3.6	Comparitive Analysis of Proposed HBV-MR	97
3.7	Conclusion.....	98

CHAPTER 4

A HYBRID LESION DETECTION TECHNIQUE FOR DR ABNORMALITY		
DISCRIMINATION.....	101-129	
4.1	Introduction	101
4.1.1	Diabetic Retinopathy Abnormalities	102
4.2	Proposed Methodology.....	103
4.2.1	Diabetic Retinopathy Discrimination.....	105
4.2.1.1	Fundus Image Discrimination	105
4.2.1.2	DR Lesion Discrimination.....	107
4.2.2	Proposed Hybrid Lesion Detection Technique	108
4.3	Results of Diabetic Retinopathy Discrimination	112
4.3.1	Statistical Analysis and Discrimination of Fundus Images.....	113
4.3.1.1	Statistical Analysis of Derived Feature set.....	114
4.3.1.2	Fundus Image Discrimination	117
4.3.2	Results of Proposed HLD Technique.....	118
4.3.2.1	Statistical analysis for Feature selection.....	120

4.3.2.2	Discrimination of DR pathologies	125
4.4	Discussion.....	126
4.4.1	Comparative analysis with the existing techniques.....	126
4.5	Conclusion.....	128

CHAPTER 5

DIABETIC RETINOPATHY CATEGORIZATION AND ITS SEVERITY GRADING

.....**131-162**

5.1	Introduction	131
5.2	DR Severity Grading	132
5.3	Proposed Methodology.....	134
5.3.1	Retinal Contextual Landmark Segmentation	138
5.3.2	Retinal Lesion Discrimination	139
5.3.3	Reduced Image Feature Vector Selection	139
5.4	Results and Discussion	143
5.4.1	Statistical analysis	144
5.4.2	Results for DR Severity Grade Classification.....	146
5.4.2.1	Classification-Case 1	146
5.4.2.2	Classification-Case 2	149
5.4.2.3	Classification-Case 3	152
5.5	Validation and Comparative Analysis of HSG system	156
5.5.1	Performance validation of the proposed system employing IDRiD dataset	156
5.5.2	Comparative Analysis with other state-of-the-art methods.....	160
5.6	Conclusion.....	161

CHAPTER 6

ENSEMBLED TRANSFER LEARNING MODEL FOR DR SEVERITY GRADING

.....**164-214**

6.1	Introduction	164
6.1.1	Deep Neural Networks	165
6.1.2	Transfer Learning.....	166
6.2	Gradient Based Deep Learning Methods.....	169
6.2.1	Conventional CNN models	170
6.2.2	Ensembled Deep Learning DR Detection Model for Binary Classification	183

6.2.3	Results of EDLDR CNN model	188
6.3	Proposed Methodology for Deep Learning based DR Grading	192
6.3.1	Transfer-Learning based Automated DR Severity Grading Detection System	192
6.3.1.1	Image Feature based Transfer Learning Model.....	194
6.3.1.2	Prominent Feature based Transfer Learning Model.....	196
6.3.2	Quadrant Ensembled Inception V-3 Framework	198
6.4	Results and Discussion	204
6.4.1	Results of Transfer Learning based Automated DR Detection System.....	204
6.4.1.1	Comparative Analysis of different transfer learning approaches	206
6.4.1.2	Comparative Analysis with existing state-of-the-art techniques.....	207
6.4.2	Results of the proposed QEIV-3 model	208
6.4.2.1	Comparison of Inception V-3 and proposed QEIV-3 model.....	211
6.4.2.2	Comparison of different Pre-trained models for MESSIDOR dataset	212
6.4.2.3	Comparison of proposed QEIV-3 model with other automated DR screening methods..	213
6.5	Conclusion	214

CHAPTER 7

CONCLUSION AND FUTURE SCOPE216-219

7.1	Conclusion and Contribution.....	216
7.2	Future scope.....	219

LIST OF PUBLICATIONS.....221-222

REFERENCES.....224-242

APPENDICES244-250

DECLARATION BY THE SCHOLAR

I hereby declare that the work reported in the Ph.D. thesis entitled **“A Computational Framework for Diabetic Retinopathy Severity Grading Categorization using Ophthalmic Image Processing”** submitted at **Jaypee University of Information Technology, Wagnaghat, India**, is an authentic record of my work carried out under the supervision of **Dr. Shruti Jain and Dr. Meenakshi Sood**. I have not submitted this work elsewhere for any other degree or diploma. I am fully responsible for the contents of my Ph.D. thesis.



Charu Bhardwaj

Department of Electronics and Communication Engineering

Jaypee University of Information Technology,

Wagnaghat, Solan-173234, Himachal Pradesh, India

Date: 19-11-2020



JAYPEE UNIVERSITY OF INFORMATION TECHNOLOGY

(Established by H.P. State Legislative vide Act No. 14 of 2002)
P.O. Wagnaghat, Teh. Kandaghat, Distt. Solan - 173234 (H.P.) INDIA

Website: www.juit.ac.in
Phone No. (91) 01792-257999
Fax: +91-01792-245362

SUPERVISOR'S CERTIFICATE

This is to certify that the work reported in the Ph.D. thesis entitled “**A Computational Framework for Diabetic Retinopathy Severity Grading Categorization using Ophthalmic Image Processing**”, submitted by **Charu Bhardwaj** at **Jaypee University of Information Technology, Wagnaghat, India**, is a bonafide record of her original work carried out under our supervision. This work has not been submitted elsewhere for any other degree or diploma.

Dr. Shruti Jain

Associate Professor

Department of ECE

Jaypee University of Information

Technology, Wagnaghat, H.P, India

Dr. Meenakshi Sood

Associate Professor

Department of CDC

National Institute of Technical Teachers

Training & Research, Chandigarh, India

ACKNOWLEDGEMENT

My first and foremost thanks to Almighty God for providing me the strength and bestowing his endless blessings upon me throughout this endeavor. All this could never be possible without his persistence and wisdom. The successful completion of this research work has been possible by the contribution of number of people in different aspects. I would like to extend my sincere gratitude to all of them who stood by me during the entire course of my Ph.D. work.

*I would like to extend foremost gratitude and special appreciations to my Ph.D. supervisors **Dr. Shruti Jain** and **Dr. Meenakshi Sood** for their tremendous encouragement, unconditional support and guidance through their enlightening views on several issues related to my research topic. **Dr. Shruti Jain**, Associate Professor, Jaypee University of Information Technology, has always fortified me by her careful guidance and positive feedback during this entire study. Her optimistic attitude, smart work and great spirit kept me encouraged to work energetically with liveliness and innovative ideas. **Dr. Meenakshi Sood**, Associate Professor, NITTTR, has always inspired me with her intelligence, perseverance and constructive criticism that has kept me going in the positive path of success throughout the entire course of my Ph.D. I would like to thank her for the undying support, endurance and motivation during tough times. They both have always supported and guided me to the right path, inspiring me for the successful completion of my research work. It's my privilege to work under their supervision as their advices on both research as well as on my career has been priceless. I have been blessed with their continuous moral support, invaluable inputs and suggestions when I needed the most.*

*I gratefully acknowledge Jaypee University of Information Technology for offering me the platform for this research and providing the necessary facilities and support. I owe my gratitude to the Vice-chancellor **Prof. (Dr.) Vinod Kumar** for his optimism and humble nature that has always been an inspiration for me. A special thanks to the Director & Academic Head **Prof. (Dr.) Samir Dev Gupta** for imparting quality education with ethics and values as its bedrock.*

*My heartfelt appreciation to **Prof. (Dr.) M.J. Nigam** Ex. Head of Department of Electronics and Communication and **Dr. Rajiv Kumar**, Head of Department of Electronics and Communication, for their co-operation, support and constant encouragement. I wish to convey my sincere thanks to all the faculty members of Department of Electronics and Communication Engineering, for their help and guidance at the various stages of this study. It is my pleasure to acknowledge the timely help of the members of technical staff of the department, special thanks to **Mr. Pramod Kumar** and **Mr. Mohan Lal** for always providing the technical support whenever needed. I am also thankful to **Prof. (Dr.) P.B. Barman** and **Dr. Harsh Sohal** for their guidance and valuable suggestions throughout my research work.*

*I cannot forget the serenity of my parents throughout my research work. It is only because of their support, love and blessings that I could overcome all frustrations and failures. I would like to thank **my parents, both sisters Garima Bhardwaj and Hemadri Bhardwaj, all other family members and relatives** for their unconditional moral support, extraordinary belief and care throughout my Ph.D. They always stood by me and provided all the resources to help me achieve my goals and realize my dreams.*

*Besides, I am also very thankful to my colleagues and friends **Vishakha Thakur, Urvashi, Amit Sharma, Pankaj Sharma, Ashutosh Sharma, Anchal Sharma, Kirti Tripathi, Kanishka Katoch** and others for helping me in numerous ways and creating a healthy atmosphere for work. Their optimism, support and encouraging opinions kept me focused and positive in the pathway of my research work. I cherish the years spent in the Department of Electronics and Communication Engineering, JUIT, Wagnaghat.*

I am indebted to all those people who have made this Ph.D. work possible and because of whom this research experience and wonderful journey shall remain everlasting and memorable forever.

All may not be mentioned, but no one is forgotten.

Thanks to all of you!

Charu

LIST OF ABBREVIATIONS AND ACRONYMS

Acc	Accuracy
ANN	Artificial Neural Network
ANOVA	Analysis of Variance
AUC	Area under the Curve
CAD	Computer-Aided Diagnosis
CBD	Compact Binary Descriptor
CCD	Charge Coupled Device
CLAHE	Contrast Limited Adaptive Histogram Equalization
CNN	Convolutional Neural Network
CWs	Cotton Wools
DIARETDB1	DIAbetic RETinopathy DataBase-calibration level 1
DCNN	Deep Convolutional Neural Network
DLDR	Deep Learning Diabetic Retinopathy
DNN	Deep Neural Network
DR	Diabetic Retinopathy
DRIVE	Digital Retinal Images for Vessel Extraction
EDLDR	Ensembled Deep Learning DR
EXs	Exudates
FN	False Negative
FOV	Field of View
FP	False Positive
GA	Genetic Algorithm

GLCM	Gray-Level Co-occurrence Matrix
GMM	Gaussian Mixer Model
GPU	Graphics Processing Unit
GSO	Glow-worm Swarm Optimization
GUI	Graphical User Interface
GT	Ground Truth
HBV-MR	Hybrid Blood Vessel Extraction Approach using Morphological Reconstruction
HEMs	Haemorrhages
HLD	Hybrid Lesion Detection
HRF	High Resolution Fundus image database
HSG	Hierarchal Severity Grading
HIS	Hue saturation intensity
HSV	Hue, Saturation and Value
IDF	International Diabetic Federation
IDRiD	Indian Diabetic Retinopathy Image Dataset
IFTL	Image Feature based Transfer Learning
IFV	Image Feature Vector
IQR	Inter-quartile Range
IRMA	Intraretinal Microvascular Abnormality
kNN	k-Nearest Neighbour
LoG	Laplacian of Gaussian
MAD	Mean Absolute Difference
MAs	Microaneurysms
MATLAB	Matrix Laboratory

MESSIDOR	Method of Evaluating Segmentation and Indexing Techniques in the Field of Retinal Ophthalmology
ML-BEC	Machine Learning Bagging Ensemble Classification
MLP	Multilayer Perceptron
MLPNN	Multilayer Perceptron Neural Network
MRF	Markov Random Field
NN	Neural Network
NPDR	Non-Proliferative Diabetic Retinopathy
OCT	Optical Coherence Tomography
OD	Optical Disc
PCA	Principle Component Analysis
PDR	Proliferative Diabetic Retinopathy
PFTL	Prominent Feature based Transfer Learning
PFV	Prominent feature vector
PNN	Probabilistic Neural Network
PPV	Positive Prediction Value
PSNR	Peak Signal to Noise Ratio
PSO	Particle Swarm Optimization
QEIV-3	Quadrant Ensembled Inception-V3 model
RAM	Regression Activation Map
RBF	Radial Basis Function
RELU	Rectified Linear Unit
ResNet	Residual Neural Network
RFFI	Random Forest Feature Importance
RIFV	Reduced Image Feature Vector

RMSE	Root Mean Square Error
ROC	Receiver Operating Characteristics
SD	Standard Deviation
SD-OCT	Spectral-Domain Optical Coherence Tomography
SN	Sensitivity or Recall rate
SP	Specificity
SPSS	Statistical Package for Social Sciences
SSIM	Structural Similarity Index
STARE	Structured Analysis of Retina dataset
SURF	Speeded-Up Robust Features
SVD	Singular value decomposition
SVM	Support Vector Machine
TN	True Negative
TP	True Positive
VggNet	Visual Geometry Group Network
VVPPA	Vessel Vector-based Phase Portrait Analysis
WHO	World Health Organization

LIST OF FIGURES

Figure No.	Title	Page No.
1.1	Cross-sectional view of human eye anatomy	2
1.2	Back view of human eye using ophthalmoscope	4
1.3	OCT image of right and left eye	5
1.4	Global prevalence of diabetic retinopathy population	6
1.5	Difference between (a) normal retina and (b) diabetic retinopathy affected retina	7
1.6	Retinal physiological portions (a) optical disc (b) blood vessels	8
1.7	Different categories of DR lesions	9
1.8	Sample fundus images indicating different DR severity levels	10
1.9	Hyperplane representation of SVM classifier	13
1.10	MLPNN Architecture	16
1.11	A basic CNN architecture	18
1.12	Different pre-trained CNN model architectures	22
1.13	Fundus images taken from different datasets: (a) DRIVE (b) STARE (c) DIARETDB1 (d) MESSIDOR (e) IDRiD	25
2.1	Sequential overview of literature review	39
2.2	The computational framework for DR severity grading	59
3.1	(a) Manually marked OD center (b) OD boundary localization	62
3.2	(a) Colored retinal fundus image (b) Manually labelled blood vessels	63
3.3	Flowchart of OD localization and blood vasculature segmentation	66
3.4	Block diagram of image pre-processing steps	67
3.5	Flowchart of Circular Hough Transform based OD localization	72

3.6	Flowchart of proposed HBV-MR approach	76
3.7	Retinal fundus image from DRIVE dataset after applying image pre-processing steps	80
3.8	Retinal fundus image from STARE dataset after applying image pre-processing steps	81
3.9	Denoised image and contrast limited adaptive histogram equalized image with their respective histograms	81
3.10	(a), (d) Original fundus image from DRIVE and STARE dataset (b), (e) Segmented optical disc (c), (f) Fundus image after OD removal using mathematical morphology based OD localization	84
3.11	Original fundus images (a), (d) from DRIVE dataset (g), (j) from STARE dataset; (b), (e), (h), (k) Segmented optical disc; (c), (f), (i), (l) Fundus image database after OD removal using Circular Hough Transform based OD localization approach	85
3.12	(a), (e), (i), (m) Original fundus images; (b), (f), (j), (n) Ground truth blood vessels labeled by experts; Extracted blood vessel output using (c), (g), (k), (o) Modified Kirsch's Edge Detection and (d), (h), (l), (p) Fuzzy Inference based Blood Vessel Segmentation respectively	87
3.13	(a), (d), (g), (j) Original fundus images; (b), (e), (h), (k) Ground truth blood vessels labeled by experts; (c), (f), (i), (l) Extracted blood vessels using the proposed HBV-MR respectively	89
3.14	Box plots of shape features for proposed HBV-MR	91
3.15	Box plots of intensity features for proposed HBV-MR	92
3.16	Box plots comparison of fractal features for Ground Truth (GT) blood vessels and Extracted (Ex) vessels using the proposed approach	93
4.1	Lesions present in DR affected fundus image	102
4.2	Block Diagram of proposed methodology for DR abnormality discrimination	104
4.3	Adopted methodology for fundus image discrimination	106
4.4	DR lesion discrimination methodology	107
4.5	Flowchart for Proposed Hybrid Lesion Detection	109

4.6	Image Pre-processing stages for DIARETDB1 dataset image: (From left to right) (a) Original fundus image, (b) Variation attenuated fundus image, (c) Green channeled fundus image, (d) Contrast-enhanced fundus image, (e) Segmented OD portion, (f) Extracted blood Vessels.	112
4.7	Image Pre-processing stages for STARE dataset image: (From left to right) (a) Original fundus image, (b) Variation attenuated image, (c) Green channeled fundus image, (d) Contrast-enhanced fundus image, (e) Segmented OD portion, (f) Extracted blood vessels	113
4.8	Box plots of some of the Extracted Feature Set: (a) and (b) Shape features, (c) and (d) Intensity features, (e) and (f) GLCM features	114
4.9	Performance metrics for fundus image discrimination	117
4.10	Experimental results of Red Lesion Detection: (a), (c), (e), (g) Original fundus image; (b), (d), (f), (h) Detected red lesion candidates from DIARETDB1 and STARE datasets respectively	118
4.11	Experimental results of Yellow Lesion Detection: (a), (c), (e), (g) Original fundus image; (b), (d), (f), (h) Detected yellow lesion candidates from DIARETDB1 and STARE dataset respectively	119
4.12	MLPNN classification performance for DR lesion detection	125
4.13	Percentage accuracy improvement of fundus image discrimination approach over the other approaches for classification of non-diseased and diseased fundus images	127
5.1	Differentiation of normal and DR affected retina	132
5.2	Block Diagram of the proposed HSG grading system	135
5.3	Flowchart of the proposed HSG system	137
5.4	Representation of retinal contextual landmark segmentation	138
5.5	Identified anomalies from the foreground portion (MA- Microaneurysms, HEM- Haemorrhage)	139
5.6	Box plots of some extracted GLCM textural features	144
5.7	ROC curves for classification- case 1 (a) SVM classifier using IFV, (b) SVM classifier using RIFV	148

5.8	ROC curves for classification- case 1 (a) kNN classifier using IFV, (b) kNN classifier using RIFV	148
5.9	ROC curves for classification- case 1 (a) ANN classifier using IFV, (b) ANN classifier using RIFV	149
5.10	ROC curves for classification-case 2 (a) SVM classifier using IFV, (b) SVM classifier using RIFV, (c) kNN classifier using IFV, (d) kNN classifier using RIFV, (e) ANN classifier using IFV, (f) ANN classifier using RIFV	151
5.11	ROC curves for classification-case 3 (a) SVM classifier using IFV, (b) SVM classifier using RIFV, (c) kNN classifier using IFV, (d) kNN classifier using RIFV, (e) ANN classifier using IFV, (f) ANN classifier using RIFV	155
5.12	Percentage improvement in classification performance of RIFV over IFV	156
5.13	ROC curves for HSG classification-case 3 utilizing IDRiD dataset (a) SVM classifier using IFV, (b) SVM classifier using RIFV, (c) kNN classifier using IFV, (d) kNN classifier using RIFV, (e) ANN classifier using IFV, (f) ANN classifier using RIFV	158
5.14	Validation of the proposed HSG system in terms of accuracy and computational time with MESSIDOR and IDRiD datasets	159
6.1	A basic CNN architecture as feature extractor and classifier	165
6.2	Network architecture of different pre-trained CNN models	167
6.3	Flowchart of proposed DLDR classification model	183
6.4	Layer wise description of the proposed DLDR models	184
6.5	Results of the proposed EDLDR CNN model (a) Accuracy (b) Cross Entropy Loss	190
6.6	Comparison of different Pre-trained models with the proposed EDLDR model	191
6.7	Transfer learning based automated DR detection system	193
6.8	Flowchart of proposed IFTL approach	194
6.9	Flowchart of proposed PFTL model	196
6.10	Fundus image cropping strategy	198

6.11	Structure of proposed Quadrant Ensembled Inception V-3 CNN model	199
6.12	Proposed QEIV-3 framework for DR severity grading	200
6.13	Comparative analysis of accuracies for Conventional, IFTL and PFTL approaches	206
6.14	Performance comparison of Inception V-3 and proposed QEIV-3 models	211
6.15	Comparison of different Pre-trained models for MESSIDOR dataset	212

LIST OF TABLES

Table No.	Title	Page No.
1.1	Layer wise description of LeNet architecture	21
1.2	Dataset description and their usage	24
2.1	Comparison of different optical disc localization and retinal blood vessel segmentation techniques	44
2.2	Comparison of different red and yellow lesion detection methods	49
2.3	Comparison of different DR grading approaches	52
2.4	Comparison of deep convolutional neural network based DR classification approaches	57
3.1	Quality assessment of images taken from DRIVE dataset	82
3.2	Quality assessment of images taken from STARE dataset	83
3.3	Performance evaluation of OD localization approach	86
3.4	Performance parameters for Blood vessel Segmentation techniques	88
3.5	p -value for normality check of fractal feature set	94
3.6	SPSS Pearson correlation analysis of fractal features observed for Extracted (Ex) vessels and Ground Truth (GT)	95
3.7	SPSS Spearman's correlation analysis of fractal features observed for Extracted (Ex) vessels and Ground Truth (GT)	95
3.8	Levene's test and t-test results for the fractal feature set	96
3.9	Performance parameter analysis of Proposed HBV-MR approach for benchmark datasets	97
3.10	Comparison of proposed HBV-MR with the existing approaches	98
4.1	Statistical analysis of extracted feature set using t -test and ANOVA	116
4.2	SPSS Pearson Correlation analysis of Shape features	121

4.3	SPSS Pearson Correlation analysis of Intensity features	122
4.4	SPSS Pearson Correlation analysis of GLCM features	123
4.5	Statistical analysis of extracted feature set using t-test and ANOVA	124
4.6	Accuracy improvement of lesion detection approach with the existing state of the art approaches	128
5.1	Illustration of International clinical DR severity scale	133
5.2	DR severity grades and their description	133
5.3	NPDR grades distribution for MESSIDOR and IDRiD datasets	136
5.4	GLCM textual features	140
5.5	Annotations for different classification cases	143
5.6	Levene's test and <i>t</i> -test for IFV set comprising GLCM features	145
5.7	Performance indices of HSG system for classification-Case 1	147
5.8	Performance indices of HSG system for classification-Case 2	150
5.9	Performance indices of HSG system for classification-Case 3	153
5.10	Performance indices of HSG system for classification-Case 3 utilizing IDRiD dataset	157
5.11	Comparison of different DR severity grading methods with the proposed HSG system	160
6.1	Layer wise description of network parameters in AlexNet architecture	173
6.2	Time-elapsed, accuracy and cross-entropy loss performance for AlexNet	174
6.3	Layer wise description of network parameters in GoogleNet Architecture	175
6.4	Time-elapsed, accuracy and cross-entropy loss performance for GoogleNet	176
6.5	Layer wise description of network parameters in ResNet architecture	177

6.6	Time-elapsed, accuracy and cross-entropy loss performance for ResNet	178
6.7	Layer wise description of network parameters in VggNet16 Architecture	179
6.8	Time-elapsed, accuracy and cross-entropy loss VggNet16	180
6.9	Layer wise description of network parameters in Inception V-3 architecture	181
6.10	Time-elapsed, accuracy and cross-entropy loss for Inception V-3 model	182
6.11	Layer-wise specifications of network parameters for the proposed DLDR models	187
6.12	Performance Metrics of the proposed DLDR models for MESSIDOR dataset	189
6.13	Evaluation parameters for the proposed IFTL and PFTL approaches	205
6.14	Comparative analysis of proposed PFTL with existing CNN models	207
6.15	Results of proposed QEIV-3 model without OD localization and contrast enhancement	209
6.16	Results proposed QEIV-3 model with OD localization and contrast enhancement	210
6.17	Comparative analysis of proposed QEIV-3 model with existing CNN models	213

ABSTRACT

Diabetic Retinopathy (DR) is a retinal vascular disease characterized by prolonged diabetic complication leading to severe blindness. The eye related impediment arises due to progressive deterioration of retinal blood vessels and can be distinguished by the appearance of different types of clinical lesions. Regular screening and diagnosis can reduce the chances of vision loss up to a large extent. Early stage prognosis of DR requires regular eye examination and ophthalmologists rely on retinal fundus segmentations for the treatment of DR abnormalities. Automated detection, segmentation and classification approaches have become an eminent research area for effective DR diagnosis and treatment of severe eye diseases preventing visual impairment. Accurate segmentation of retinal vasculatures distinguishing between the anatomy and pathology of retinal fundus images is significant for precise prediction of the disease. Detection and analysis of different DR lesion as well as disease severity grades help the ophthalmic experts in analyzing the variations in the fundus images and taking necessary action before disease progression. Diagnostic relevance of DR prediction and grading to aid the ophthalmologists in regular screening has led to the expansion of automated DR severity systems.

In this thesis, DR diagnosis is addressed by proposing a retinal anatomical structure segmentation approach to reduce fallacious lesion segmentation. Physiology identification and detection are accomplished by developing an effective lesion discrimination approach to provide a robust DR lesion detection solution and optimal categorization capability. A robust framework is proposed for DR categorization that offers a generalized approach for DR severity grading. A computation transfer learning framework has been proposed in this thesis, to provide a Deep Learning based mass screening solution for DR classification problem. All the proposed approaches were tested on designated benchmark datasets defined in the literature for DR diagnostic tasks.

Accurate instinctive segmentation of retinal landmarks, Optical Disc (OD) and blood vasculatures results in effective DR diagnosis. An accurate differentiation of these anatomical structures from other retinal features is a research issue due to the presence of various discrepancies in the raw fundus images.

In this work, a Circular Hough based OD localization approach and Hybrid Blood Vessel Segmentation Approach using Morphological Reconstruction (HBV-MR) have been proposed to combat this issue. Inconsistencies due to the presence of background noise, varying inadequate illumination, varying contrast between the background and blood vasculatures have been addressed by the utilization of the proposed approach. Remarkable improvement of Circular Hough based OD localization approach demonstrates its viability and localization efficiency. Visual, statistical, and performance analysis of HBV-MR approach signifies its relevance in reducing the fallacious detection of pathological symptoms having similar features as OD or blood vessels.

This research work also deals with the identification of DR anomalies after efficient segmentation of background anatomies, to aid the DR diagnosis process. The poor ability of discrimination between the actual affected area from background noise and other anatomical structures arises the need for reliable DR lesion detection solution. The anomalies can be perplexed with noise and retinal tissue pigmentations due to lesion size variability. The novelty of this proposed approach lies in the statistical analysis performed on the comprehensive feature set for optimal feature selection as well as improved candidate classification scheme using multi-layer perceptron networks. This approach integrates the ophthalmic image processing with optimally selected feature sets, providing successful discrimination ability between healthy and DR symptomatic fundus images.

Pathology discrimination is followed by the recognition of retinal feature patterns yielding the DR severity grading based on the identified lesions. This aid the ophthalmologists in understanding the likelihood of vision loss for prognosis and patient referral. A hierarchal severity grading (HSG) system has been proposed in this work for disease detection and DR severity classification employing different machine learning techniques. The retinal fundus image feature attributes are reduced to an optimal feature set utilizing the extensive statistical analysis. A noteworthy performance improvement of 32.25% is realized from the state-of-the-art comparison and the system is generalized through its performance validation for a latest dataset.

The last part of this research aims at automated DR lesion severity grading incorporating transfer learning approach accompanying robust accountable analysis. An Ensembled Deep Learning based DR (EDLDR) model is proposed for the binary classification and to address DR severity grading, two deep learning based models;

Prominent Feature based Transfer Learning (PFTL) model and Quadrant Ensembled Inception V-3 (QEIV-3) model, are proposed. EDLDR model provides 1.13% accuracy improvement comparative to the VggNet16 deep learning model, thereby, determining effective diagnostic proficiency. The PFTL DR severity grading approach provides maximum improvement of 21.49% when compared with the state-of-the-art techniques using the benchmark dataset establishing its capability for faster and efficient DR diagnosis. The proposed QEIV-3 model incorporates a quadrant based Convolutional Neural Network model to enhance the grading efficiency and the state-of-the-art comparison justifies its viability validating its generalization capabilities and robustness. Deep learning removes the requirement of feature engineering proving its suitability for DR classification by providing a mass screening DR severity grading solution.

This research work is targeted to the development of a computation framework for providing better prognosis for DR diagnostic system. This is generic application-oriented work and helpful in accurate DR classification for effective diagnosis and timely treatment of severe retinal diseases.

CHAPTER 1

INTRODUCTION

CHAPTER 1

INTRODUCTION

1.1 ANATOMY OF EYE

An eye is a vital part of the human visual system which acts as a receptor organ to capture the image of outside world. The incident light falling on the scene is allowed to pass through the cornea onto the retina focused by the lens. The incoming incident light falls on the retina which thereby encodes and transmits the visual information to the brain via optic nerves [1]. The cross-sectional perspective of the human eye is illustrated in Figure 1.1.

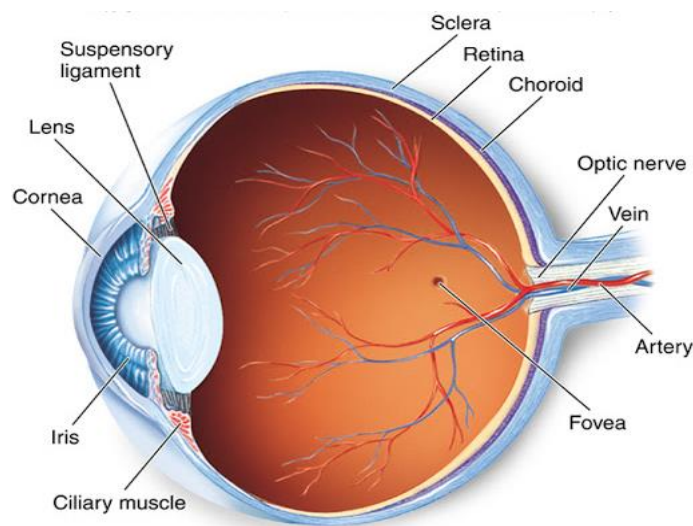


Figure 1.1: Cross-sectional view of human eye anatomy [2]

Eye-care is very critical as some of the eye diseases create serious complications resulting in blindness if left untreated for a longer duration. The common symptoms involved with eye-related disorders are blurred vision, spots or dark string floating in-front of the eye, impaired colored vision, fluctuating vision, empty areas in front of the vision, etc. However, many of the eye diseases like glaucoma, macular degeneration, diabetic retinopathy, etc. have no visible symptoms unless the final stage reaches. A regular eye examination is critical for early diagnosis and treatment of such eye complications. Out of several eye-related ailments, some of the eye disorders are detailed further [3].

Cataract is a disorder in the lens of the eye which causes opaque cloudy area in front of the lens. *Chalazion* is an eye condition that arises due to the formation of lumps caused due to the blockage and swelling of oil glands in the eyelid. *Color Vision Deficiency* leads to the inability in clear distinction between certain color shades and complete inability to see colors at all in the worst case. A thin transparent tissue layer lining on the inner eyelid surface covering the white surface of the eye is called *Conjunctiva*. Any inflammation or infection caused in this portion is referred to as *Conjunctivitis*. *Dry Eye disorder* is caused due to insufficient formation of eye tears for the lubrication and nourishment of the eye. *Floater*s are the particle that floats in the fluid filling the inside of the eye, sometimes leading to the floating spots or objects in the field of the vision. This condition is referred to as floaters. *Glaucoma* is a condition that occurs due to progressive damage to the optic nerves of the eye causing the loss of nerve tissue which may result in vision loss. *Macular Degeneration* affects the macula of the eye, the main light-sensitive part of retina, which may further result in central vision loss. *Retinal Detachment* is characterized by the retinal separation from the underlying tissue. *Retinitis Pigmentosa* is considered as a poor night vision and progressive loss of side vision due to various inherited retinal disorders. *Retinoblastoma* is a very rare type of eye cancer that occurs in the retina of young children. *Diabetic Retinopathy* is a progressive condition occurring due to the persistent diabetic conditions causing damage to the retina (light-sensitive line coating at the back of the eye).

The advancement in the medical imaging field has led to the development of a domain for medical image analysis which is discussed in the next section of this chapter. Medical image analysis attains the fine details from different imageries for effectual data processing which cannot be done effectively using traditional visual assessment techniques.

1.2 MODALITIES OF OPHTHALMIC IMAGES

Current medical research and diagnosis relies on medical image processing for efficient detection and treatment. There are diverse imaging modalities like Computed Tomography Scans, fundus imaging, X-ray, ultrasound and Magnetic Resonance Imaging which aids the clinicians in diagnostic procedures.

Medical image analysis has developed as a fascinating research area attracting intensive physicians' interest in the development of significant computer-based medical analysis [4]. Automated medical image analysis methods have opened the barriers for digital image processing and machine learning field. They mainly focus on the designing of various algorithms for the extraction of relevant medical image information for clear visualization and interpretation of critical pathological symptoms. Studies have revealed that the chances of acute blindness can be reduced by prioritizing ophthalmic image analysis strategies. The eye examination is considered beneficial in mitigating various health concerns including diabetes, hypertension, strokes, occlusion and many more [5]. Thus, eye modalities involved in ophthalmic image processing are discussed in the following subsection of this chapter.

There are two ophthalmic image modalities: Retinal fundus images and Optical Coherence Tomography images.

1.2.1 Retinal Fundus Imaging

Retinal fundus images capture the interior portion of human retina, that is light sensitive. These fundus images typically include Optical Disc, Macula, and Blood Vessels. Although, retinal pathologies if exists, are also visible in retinal fundus images. Fundus photographs are captured by the ophthalmologist using an ophthalmoscope, which is a specialized fundus camera equipped with low power microscopes to capture the image of interior of the eye [6]. Figure 1.2 provides the view of the back of the eye using an ophthalmoscope.

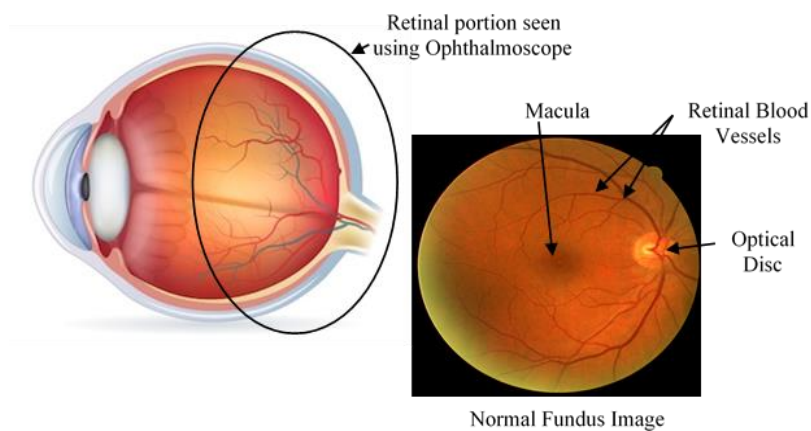


Figure 1.2: Back view of human eye using ophthalmoscope

Ophthalmoscope acts as a digital microscopic camera that provides a close-up view of the interior of eyeball [7]. The light entering through the eye is reflected back into the camera which captures and digitizes the image of the retina at the moment of light reflection from the eye. These fundus images are further subjected to medical image analysis for efficient screening and patient prioritization based on the disease severity level.

1.2.2 Optical Coherence Tomography

The second ophthalmic image modality is Optical Coherence Tomography (OCT) which deals with the third dimension of the retina. This retinal imaging modality captures the micrometer-resolution of the depth of retinal tissue. Lateral scans are captured in an OCT image that determines the depth of sub-layers of the retina. Individual lateral scans when combined, forms a three-dimensional view of the retina which is useful in the location and treatment of macular pathologies [8]. An OCT image of the retina is depicted in Figure 1.3.

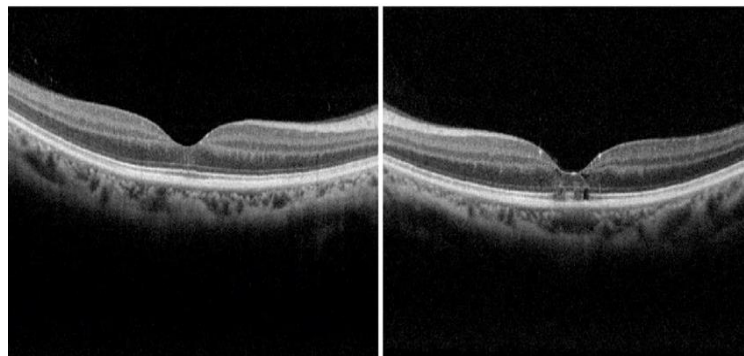


Figure 1.3: OCT image of right and left eye

OCT image segmentation is widely used for management and follow-ups of retinal surgeries. OCT analysis can be beneficial for identifying disease progression over time. This type of imaging modality is helpful for clinical studies to observe the impact of pathology localization and treatment for laser surgeries [9]. To deal with the large-scale DR diagnosis for mass screening, fundus images are preferred over OCT scans. The main problem concerned in this thesis is Diabetic Retinopathy abnormality whose detailed overview is provided in the upcoming section.

1.3 DIABETIC RETINOPATHY

According to the survey conducted by International Diabetic Federation (IDF) ninth edition [10], approximately 463 million adults around the age of 20-79 years are suffering from diabetes and this number will rise to 700 million by the year 2045 [10, 11]. There were 10 million more adults with diabetes in 2017 than in 2007 and most of them were undiagnosed due to the lack of early-stage detection facilities. The global prevalence statistics for Diabetic Retinopathy population provided by Vision Atlas [12] is depicted in Figure 1.4.

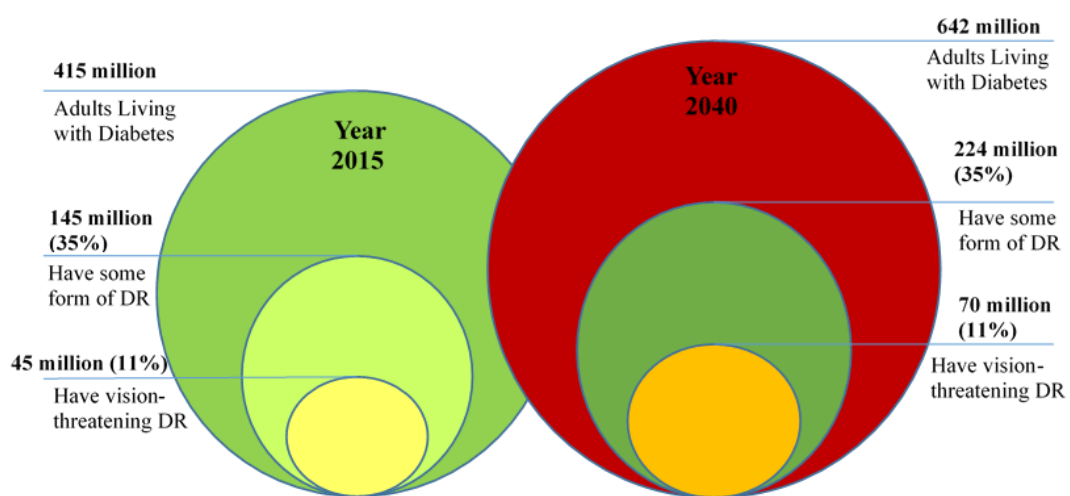


Figure 1.4: Global prevalence of diabetic retinopathy population [12]

Figure 1.4 reveals that the diabetic population was 415 million in the year 2015, out of this 35% of patients have some form of DR and 11% develop vision-threatening DR. This diabetic population is expected to rise to 642 million with 224 million diabetic patients developing some form of DR and 70 million population having vision-threatening DR if precautionary measures are not taken. The need for automated detection facilitating ophthalmic services is revealed, especially in rural areas and developing countries like India.

Most of the people with diabetes develop the risk of vision loss from eye diseases. Diabetes accounts for the majority of eye diseases and DR is the most severe complication resulting from prolonged diabetic conditions. DR is a condition arising from high glucose level that causes damage to the small blood vessels inside the retina.

There are some risk factors associated which influences the growth of severity in diabetic retinopathy. Blood sugar level, fluctuation in the blood pressure, long duration of diabetes, blood cholesterol levels and pregnancy are some of the crucial risk factors affecting diabetic retinopathy and its progression [13]. Figure 1.5 depicts the difference between normal retina and the retina having DR symptoms.

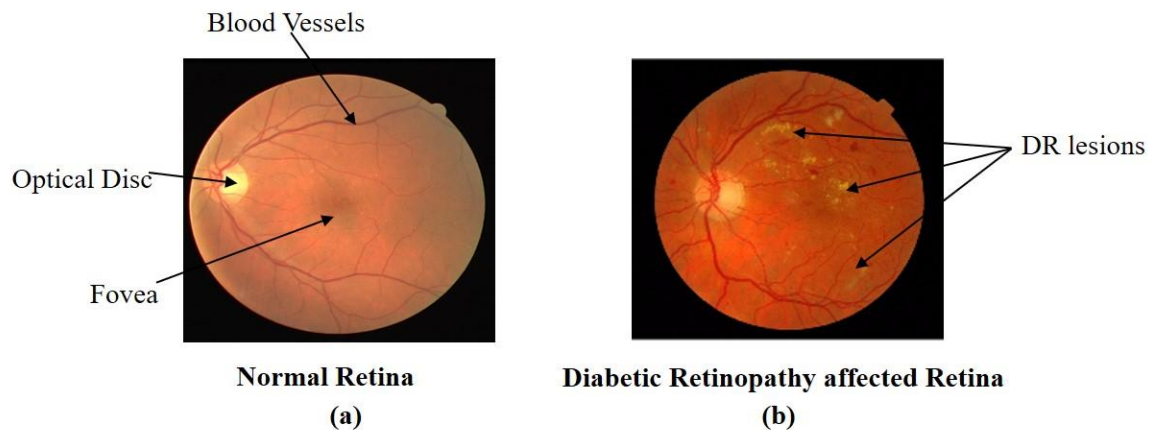


Figure 1.5: Difference between (a) normal retina and (b) diabetic retinopathy affected retina

The main anatomical portions of a normal retina include optical disc and blood vessels which are discussed in the next section followed by the discussion of various DR lesions and DR severity grading.

1.3.1 Optical Disc and Blood Vessels of Retinal Images

Retinal physiological portions include optical disc, veins, and arteries situated in the retina. Optical disc (OD) is oval-shaped brightest appearing part in retinal fundus image as shown in Figure 1.6 (a). The optical disc can also be referred as optic nerve head that is a tiny blind spot in the eye due to the absence of rods and cones in this portion. Blood vessels shown in Figure 1.6 (b) are another important retinal component that supplies blood and nutrition to the retina and OD is the entry point of these blood vasculatures.

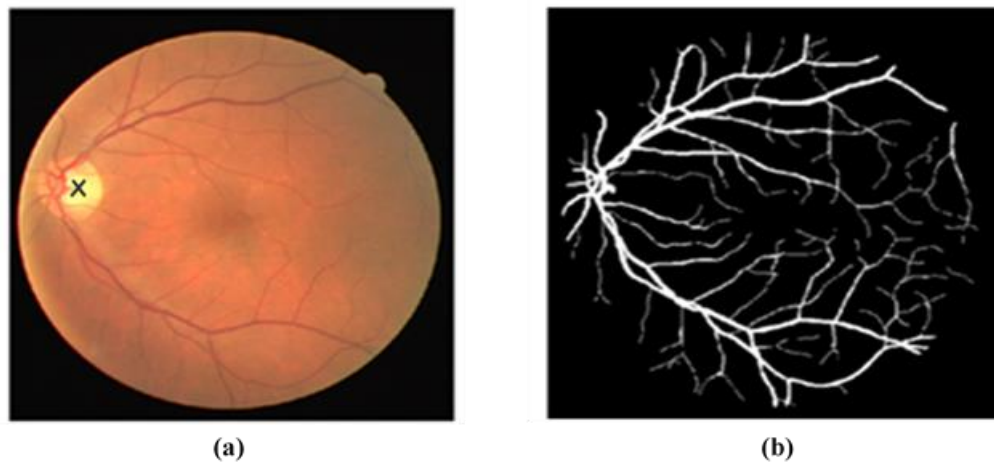


Figure 1.6: Retinal physiological portions (a) optical disc (b) blood vessels

Accurate extraction and segmentation of retinal vasculatures distinguishes between the anatomy and pathology of retinal fundus images. Retinal components like OD and blood vessels are considered as background portions as they are not required for DR anomaly detection [14]. Thus, both these pathological portions are to be removed from the retinal fundus images.

Automated DR lesions detection merely relies on effective segmentation and removal of OD and blood vessels as imprecise detection of these structures may impede the accurate detection of various DR lesions [14, 15]. These anatomical components of the retina are identified by clustering the intensity pixels from the grayscale retinal image.

1.3.2 Lesions in Diabetic Retinopathy

The broad classification of DR lesion lies in two categories namely, yellow/bright and red/dark lesions depending upon the lesion intensity level. Red or deep dark lesion category consists of Microaneurysms (MAs) and Haemorrhages (HEMs), however, yellow, shiny or bright lesion category includes Exudates (EXs) and Cotton Wools (CWs) [16]. Figure 1.7 illustrates the different lesion categories and their identification.

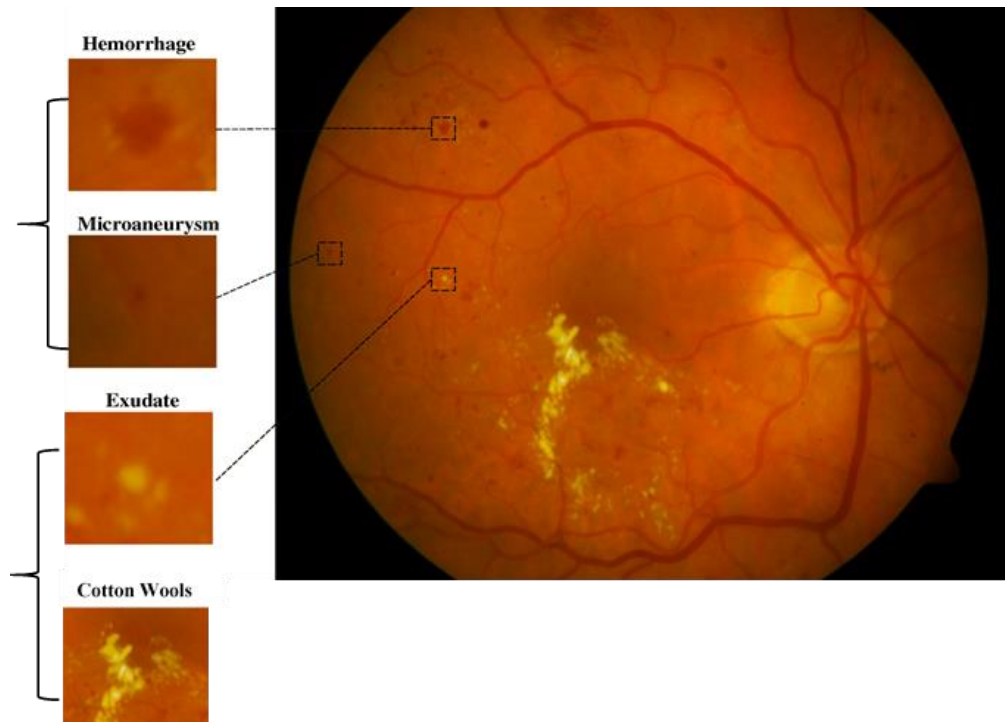


Figure 1.7: Different categories of DR lesions

- i. Microaneurysms (MAs):** MAs are referred to as the dilated blood vessels that appear as tiny red spots in the retinal fundus images. They appear due to swelling in the retinal capillaries which can leak blood or fluid into the retinal surface [17]. MAs are the primary indicator of clinical lesions which are to be targeted first for the DR diagnosis as they are the earliest signs of the ailment.
- ii. Haemorrhages (HEMs):** Loss of blood from retinal vasculatures is indicated by haemorrhages which appear as red-colored patches of varying shapes in the fundus image. Dot and blot haemorrhages are round shaped, like large MAs which exist near the inner nuclear layer of retina or outer plexiform layers. Some flame-shaped haemorrhages are present in the ganglion layer which disappears within a short period [17]. HEMs are the more serious complication related to DR due to its presence in the deep layer of retina.
- iii. Exudates (EXs):** Exudates are yellow-colored deposits of lipids or proteins within the retinal area. This is caused due to increased pressure on thin blood vessels which in turn leaks lipids or proteins. EXs are mainly used for the diagnostic indicators of macular edema as they point out blood vessel permeability or presence of fluid [18].

- iv. **Cotton Wools (CWs):** CWs appear as whitish structures with blurred edges occurring due to the restricted blood supply to the nerve fibers. However, cotton wools individually do not create any visual complications, but they are correlated to the condition affecting the retina. In case of diabetic retinopathy condition, they are of high clinical relevance [18].

Pathology detection is an important part of retinal image processing after the extraction of background anatomical structures (Optical Disc and Blood Vessels). The diseased foreground portion comprising of lesion candidates are extracted via morphological operations. To reduce the chances of false lesion detection, lesion pixel histogram properties are measured for the selection of threshold for lesion candidate identification [17, 19]. The detected pathological symptoms can be graded depending upon the retinopathy severity levels.

1.3.3 Diabetic Retinopathy Grading

Retinal abnormalities can be characterized by an anomalous change in these components of the retina. DR abnormalities can be categorized in two stages, one is Proliferative DR (PDR) stage and other is Non-Proliferative DR (NPDR) stage. Retinal images with no symptoms of DR are considered normal fundus images and NPDR grades can be categorized into mild, moderate and severe grades subject to the number of DR lesions. These retinal complications can cause complete blindness if left untreated for a long time [19]. Figure 1.8 shows a sample fundus image which contains different types of lesions indicating varying DR severity levels.

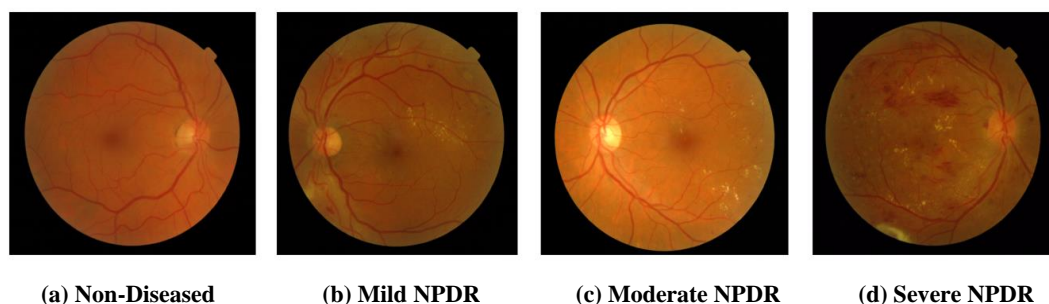


Figure 1.8: Sample fundus images indicating different DR severity levels

Several NPDR grades are elaborated as:

- i. **Mild NPDR Grade:** Mild NPDR grade shown in Figure 1.8 (a) is the earliest stage of DR, with lesions such as MAs, resulting due to the inflammation of the

walls of small blood vessels. The breakdown of these MAs leads to a moderate grade of DR as shown in Figure 1.8 (b).

- ii. **Moderate NPDR Grade:** This situation arises due to mild NPDR continuation which leads to retinal HEMs that are recognized as dark red patches of blood caused by the leakage of MAs on the surface of the retina. EXs and CWs are lipids or fats deposited in retina that emerge in the moderate NPDR stage. They are recognized as yellow lesions unlike HEMs, which are darker red lesions as shown in Figure 1.8 (c).
- iii. **Severe NPDR Grade:** When retinopathy progresses, after a certain time the blood vessels become blocked by micro infarctions in the retina and all of the above abnormalities are fully exposed, this stage is called severe NPDR. The blood vessels are blocked arresting the blood supply to the retinal areas causing the lack of oxygen in the retina as shown in Figure 1.8 (d).

PDR is another classification of DR that occurs when the retina stops the blood flow into the areas of blood vessel closure. In this effort, the retina counters back its blood supply and grows new blood vessels which are potentially weak, leaky and brittle. It further causes blood to leak into the surface of the retina. This stage lead to the bifurcated blood vessel pattern as a result of the abnormally developed new vasculatures. This is the more rigorous DR stage which can also cause retinal detachment with subsequent vision loss [18]. Next section discusses the relevance of feature extraction for DR classification and the significance of statistical analysis for the selection of extracted features.

1.4 STATISTICAL ANALYSIS FOR EXTRACTED FEATURES

Feature extraction provides the accurate description of the complete dataset in quantitative manageable form. The extracted features contain relevant information which can be used for exact classification utilizing the reduced representation instead of the complete dataset. The set of extracted features obtain the useful information about the image such as color, shape, intensity and texture, which can be used to differentiate between the different classes. It provides feature consistency indicative of better classification and confines the relevant features required for the efficient

computation [20]. This work considers four different feature sets; fractal features, intensity features, texture features and geometric shape features for different DR diagnostic tasks and their detailed description is provided in the Appendix 1. Fractal features comprises box-counting dimension, information dimension and correlation dimension. Intensity features consists of minimum intensity, maximum intensity, mean intensity, median intensity, mean absolute difference, standard deviation, inter-quartile range, skewness and kurtosis. Textual features comprise autocorrelation, correlation, contrast, cluster shade, cluster prominence, energy, entropy, homogeneity, inverse difference, inverse difference moment, maximum probability, dissimilarity and information correlations. Shape features include area, perimeter, major axis length, minor axis length, eccentricity, convex area, orientation, equivalent diameter, solidity, extend and compactness.

For effective DR diagnosis, only the prominent features are required from the diverse set of extracted features. Therefore, feature selection is important for significant improvement in the system performance. In this research work, box-plots, Pearson correlation analysis, Analysis of Variance (ANOVA) and t -test statistical tools are used for statistical feature analysis, which are elaborated in the Appendix 2. These statistical feature selection tools form the basis to reduce the feature set which in turn decreases the dimensionality for effectively improving the accuracy of diagnosis [21, 22]. Significant features are selected depending upon the p -value indicative of significance of a particular feature. The significant p -value condition is expressed in Eq. (1.1).

$$p = \begin{cases} p \leq 0.05 & \text{indicative of Strong Significance} \\ 0.01 < p \leq 0.05 & \text{indicative of Moderate Significance} \\ p > 0.05 & \text{indicative of Weak Significance} \end{cases} \quad (1.1)$$

The reduced feature subset obtained after feature selection contain only the relevant information sufficient to discriminate between different classes. The selected significant features are subjected to classification stage for accurate DR prediction. The reduced representation improved the generalization capability of the classification algorithm utilizing reduced number of resources to describe the large fundus image dataset without overfitting. Machine learning classification techniques along with a brief introduction of deep learning modules is discussed further.

1.5 CLASSIFICATION TECHNIQUES

The success of the retinal image processing technique for DR diagnosis relies on successful severity grade classification. Several classifiers are used to distinguish between several classes of the retinal fundus image using the pixel information. The categorization of classifiers is based on the training/learning and testing phases of the classifier [23].

1.5.1 Machine Learning Classifiers

Fundus image discrimination for DR classification is accomplished using various traditional machine learning classifiers reported in the literature. However, in this research, Support Vector Machine, Artificial Neural Network, k-Nearest Neighbour classifiers have been considered for DR classification.

1.5.1.1 Support Vector Machine Classifier

Support Vector Machine (SVM) is supervised discrimination scheme utilizing the learned supervised model to optimally classify the test data using labelled training data [23]. A decision boundary or hyperplane is created using trained data points that better differentiates among class labels. The maximum margin hyperplane is chosen whose distance is highest among the data points close to each class label. This method is practically applicable for both binary as well as multi-class classification [24, 25]. An illustrated representation of the SVM hyperplane is shown in Figure 1.9.

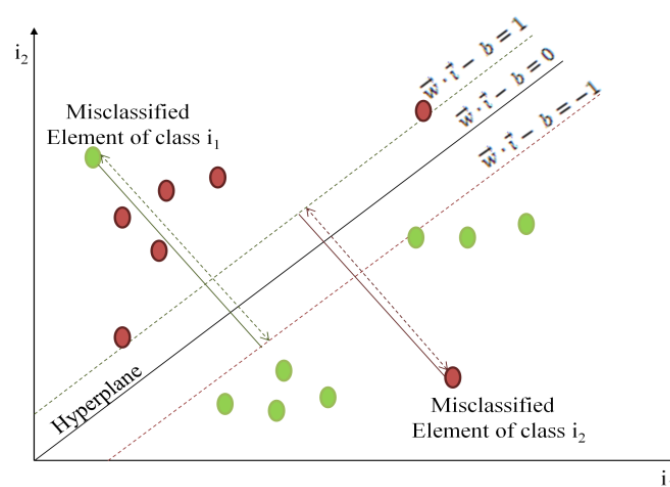


Figure 1.9: Hyperplane representation of SVM classifier

The input data is signified by \vec{i} having a weight vector \vec{w} and bias b , the output equation for hyperplane is represented by Eq. (1.2).

$$\vec{w} \cdot \vec{i} - b = 0 \quad (1.2)$$

However, this output may vary between 1, 0 and -1 depending upon the class it belongs to. Components of class i_1 are represented by green color and red color indicating the components belonging to class i_2 which are separated by a hyperplane. Kernel selection is the utmost important factor on which SVM classification relies for its capability in flexibly mapping the non-linearity among the data separable into a higher dimensional space using hyperplane separability. This work utilizes radial basis function (RBF) Gaussian kernel and linear kernel which are expressed by Eq. (1.3) and Eq. (1.4) respectively.

$$K(i, i') = \sum \vec{w} \cdot \vec{i}, \vec{i}' + b \quad (1.3)$$

$$K(i, i') = \exp \left(-\gamma \times \sum \|i - i'\|^2 \right) \quad (1.4)$$

where i = input vector, i' = support vector, b = bias and γ denotes the width of the Gaussian envelope.

The tuning parameters used to achieve better accurate classification results are regularization parameter (C) and gamma (γ), which are expressed in the error function indicated by Eq. (1.5).

$$C \sum_{i=1}^L (\varepsilon_i^+ + \varepsilon_i^-) + \frac{1}{2} \|w\|^2 \quad (1.5)$$

where ε is the error metric subjected to, $\varepsilon^+ \geq 0$, $\varepsilon^- < 0$ minimization constraint and w is the weight vector.

1.5.1.2 k-Nearest Neighbour Classifier

The k-Nearest Neighbour (kNN) classifier identify the class of a particular data sample depending upon the Euclidian distance of that sample from its k- nearest neighbours in the dataset. The Euclidean distance among the k-nearest training data

point samples acts as the deciding factor for assigning the test data to the most frequently occurring class [23, 26]. Total ‘ n ’ samples are contained in the dataset and the Euclidian distance between training sample x_a and the test sample x_b for ‘ f ’ number of feature vectors is expressed in Eq. (1.6).

$$d(x_a, x_b) = \sqrt{(x_{a1} - x_{b1})^2 + (x_{a2} - x_{b2})^2 + \dots + (x_{af} - x_{bf})^2} \quad (1.6)$$

DR classification problem is solved using kNN algorithms considering $k = 3$ adjacent neighbours, as the reduced number of neighbours yield better classification performance [26].

1.5.1.3 Artificial Neural Network Classifier

Artificial Neural Network (ANN) consists of three layers namely input layer, hidden layer, and output layer. Input features are fed to the neural network via input layer, hidden layer is the processing unit that updates the weights to obtain better network performance and the output layer provides the result of the network in terms of classes. The outcome of the neural network depends upon the propagation function and the learning rule. The inputs to the j^{th} neuron from the output of the preceding neurons are controlled using the propagation function and it is expressed by Eq. (1.7).

$$p_j(t) = \sum_i O_i(t) \times w_{ij} + b \quad (1.7)$$

where $p_j(t)$ is the propagation function, $O_i(t)$ is the output of the preceding neuron, w_{ij} is the weight and b is bias.

The learning rule modifies neural network parameters in a way that the network produces a favorable outcome for a given input set. The learning process modifies the weights within the network for better output computation based upon the learning rule [27].

The artificial neural network uses a large number of neurons whose weights are adjusted to improve the learning rate with extensive training and back propagating the errors. The major strength of neural network is its ability to interpret the

outcome of uncertain data without having previous knowledge of the evenness of the data [27]. This strategy has been applied to several applications [28, 29] and it is an appropriate choice for diagnosis of diabetic retinopathy as it employs weights to determine the ability of input features fitting into a specific output class. These weights are adjustable as per the requirement of the application which makes it a suitable fit for our DR classification problem. The Multilayer Perceptron Neural Network (MLPNN) based classification approach is utilized in this work due to its ability to interpret the outcome of uncertain data without having previous knowledge of the evenness of the data through weight adjustment flexibility.

MLPNN Classifier: MLP is a feed forward neural network that works as an interpreter, and approximates the outcomes from classifier by making use of non-linear activation function for hidden and output layers. An intermediate hidden layer is employed in this network at which neurons process the inputs before providing them to the output layer. The Layer-wise illustration of MLPNN is presented in Figure 1.10 where the input nodes are denoted by green, hidden nodes are indicated by blue and the output nodes are denoted by red and yellow color indicating the type of DR lesions.

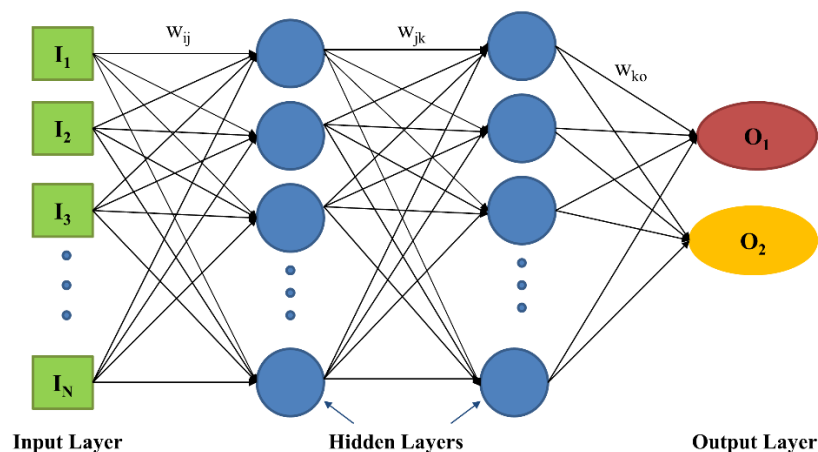


Figure 1.10: Layer-wise description of MLPNN

The initial layer of MLPNN is fed with the input feature vector. The processed information is forwarded to hidden layers for the computation of weight vectors and activation functions as intermediate processing. The back propagation technique is utilized for feature mapping and consistent training to produce classification outcomes [30].

There are many types of activation functions but, in this work, tangent hyperbolic function is used at the intermediate hidden layer as expressed by Eq. (1.8).

$$\tanh(x) = \frac{e^x - e^{-x}}{e^x + e^{-x}} \quad (1.8)$$

Learning speed is improved and the separation capability is enhanced using the tangent hyperbolic function. However, the softmax activation function is used at output layer for deriving the classification outcomes which is stated by Eq. (1.9).

$$F(x) = \frac{e^x}{\sum_{i=0}^k e^x}, \text{ for } i = 0, 1, 2, \dots, k \quad (1.9)$$

The classification outcomes are provided by calculating the softmax activation function probabilities within the range of 0 to 1 where each of the target class is represented with the highest probability value.

Conventional approaches deploy various handcrafted feature extraction techniques to extract clinically relevant features from fundus images. These features are then passed through a specific classifier for DR severity grade classification. These handcrafted features are limited and crafting new effective features is difficult and often does not yield better results. This feature extraction-based process is laborious and may often lead to misclassification. The choice of appropriate handcrafted features requires investigation of various parameter settings with prior expert knowledge.

In the recent advent of technology, Deep Neural Networks have replaced the machine learning-based DR diagnosis systems by achieving significant performance improvement [31].

1.5.2 Deep Neural Networks

Recently, a new advent in technology has evolved with Deep Neural Network (DNN) based methods that have achieved innovative outcomes in various fields especially in medical sciences.

There was a breakthrough in medical image analysis and classification performance when a novel bio-image technique was added to neural networks. Convolutional Neural Network has proven its competence for the interpretation of image and its analysis in medical imaging field.

1.5.2.1 Convolutional Neural Networks

For image classification tasks, convolutional Neural Networks (CNNs) have demonstrated revolutionary performance and thus being exploited for DR diagnosis systems. Unlike other machine learning approaches, CNN based classification methods provide superior performance due to the properties of scale, rotation, and field of view invariance. These properties make it suitable for retinal fundus image-based DR grading, as the acquired fundus images are of varying sizes and different fields of view.

The basic elements of CNN architecture majorly include five layers, namely, input layer, convolution layer, pooling layer, fully connected layer and output layer [32, 33]. The basic architecture of a CNN model is depicted in Figure 1.11.

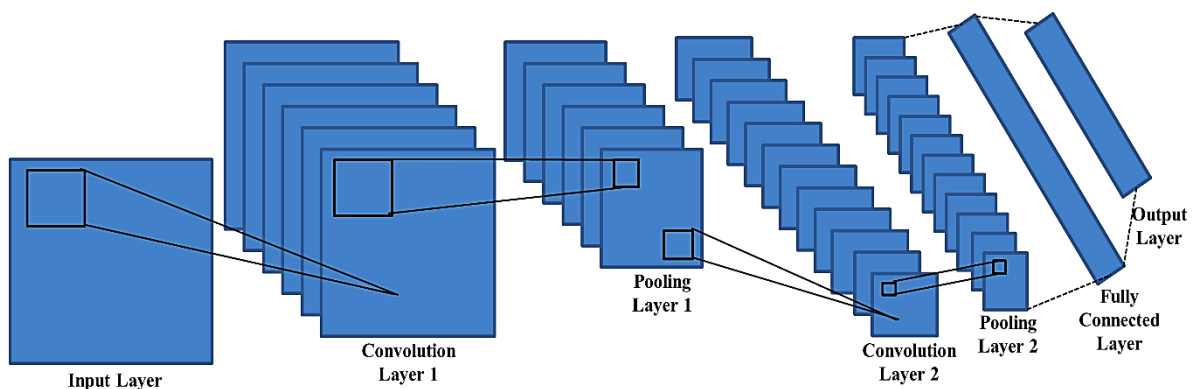


Figure 1.11: A basic CNN architecture

The input layer is responsible for taking the input images and providing them to the CNN architecture to map it to the corresponding class labels in the output layer.

- i. **Convolution Layer:** This layer is the main element of CNN based deep learning model that contains a number of learnable convolution filters. These filters produce two-dimensional maps using the dot product of the input vector and the convolution filter.

For an input image X of size $i \times j \times c$ having size $i \times j$ and c number of channels, the convolutional layer function is expressed by Eq. (1.10).

$$f(X) = \sum_{k=0}^c w_k * X_k + b \quad (1.10)$$

where w = weight vector, b = bias, k = total number of nodes and $*$ denotes convolution operator.

Convolution layer is employed to obtain feature maps by convolving the image with weight vector. The weight vector is adapted during the training phase employing back propagation. Non-linearity is introduced in this layer using the Rectified Linear Unit (ReLU) for the production of constant gradient to all positive input values, instead of its non-differentiability, therefore is a common choice for CNNs. The ReLU function is expressed by Eq. (1.11).

$$ReLU(X) = \begin{cases} 0 & \text{if } X < 0 \\ X & \text{otherwise} \end{cases} \quad (1.11)$$

ReLU function is utilized to achieve better outcomes than the conventional sigmoid or hyperbolic tangent functions by accelerating the training speed [32]. Utilization of ReLU activation function in CNN architectures overcomes the vanishing gradient problem of the traditional neural networks.

- ii. **Pooling layer:** The intermediate layer in between the convolution layers is responsible for down-sampling of the acquired output from the convolution layer and is referred to as the pooling layer. CNN utilizes two types of pooling functions; average pooling and max pooling due to its dimensionality reduction property without compromising the useful information. The convolved image is grouped to non-overlapping sub-parts and the average pooling function produces the average value of each sub-partitions as output. Likewise, max-pooling also functions in the similar way unlike returning the maximum value for each sub-partition. The pooling layer is accountable for intermediate dimensionality reduction between the adjacent convolution layers.

- iii. Fully Connected Layer:** Fully connected layer is the final layer in CNN architecture preceding the output layer. This layer acts as a traditional neural network which comprises large number of parameters and every single node is connected with every other node. The dropout technique is used in this layer to reduce computational complexity by dropping some nodes and connections out from fully connected layer.

The CNN based classification approaches extracts the increasingly complex features increasing the system complexity. Deep Neural Network training from scratch is challenging for medical domain where typically a limited number of annotated data is available, particularly in medical domain. Therefore, to address these issues, another approach proposed in this work employing a transfer learning concept is introduced utilizing various pre-trained CNNs. The main important step for using the pre-trained model weights is fine-tuning of network parameters for the exploitation of the dataset characteristics. Initially, the pre-trained model weights are used as objectives which are further utilized for supervised training of this model on the target data. There exist two types of fine-tuning techniques to make the network task specific; full tuning and fine tuning of pre-trained model. Full tuning is very time consuming as it involves the tuning of complete CNN model which is not specifically necessary for some tasks. However, fine tuning the pre-trained model using the target data can improve the model performance to fit to the specific classification task [33]. Multiple feature learning is accomplished using multiple layers in the CNN model at different levels of hierarchical abstraction. The initial convolutional layers learn the low-level features; however, high level features are learnt by the deeper convolutional layers. Features extracted at every individual convolutional layer are finally used for classification at the fully connected layer.

1.5.2.2 Pre-trained CNN Classifiers

The earliest pre-trained model was given by Lecun *et al.* [34] in 1998 to promote the advancement of deep learning for handwriting recognition. The architecture consists of two subsequent convolutional and pooling layers which are followed by three fully connected layers before the output softmax classification layer. The layered architecture of LeNet is provided in Table 1.1.

Table 1.1: Layer wise description of LeNet architecture

Layer Index	Type	Activations	Learnables		
			Filter Size	Stride	Number of Filters/Pooling type
0	Input data	(32×32×1)	----	----	----
1	Convolution Layer 1	(28×28×6)	(5×5)	1	6
2	Pooling Layer 1	(14×14×6)	(2×2)	2	Avg Pool
3	Convolution Layer 2	(10×10×16)	(5×5)	1	16
4	Pooling Layer 2	(5×5×16)	(2×2)	2	Avg Pool
5	Fully Connected Layer 5	(1×1×120)	----	----	120
6	Fully Connected Layer 6	(1×1×84)	----	----	84
7	Fully Connected Layer 7	(1×1×10)	----	----	10

Spatial features are extracted using convolutional filters and subsampling is achieved by average pooling layer. The activation function used in this architecture is tan hyperbolic function and softmax activation is used at the final classification layer. To deal with the computation complexity, this network utilizes sparse connections between the layers. The other pre-trained networks utilized for various image recognition tasks are AlexNet [35], GoogleNet [36], ResNet [37], VggNet [38] and Inception-V3 [39] which are depicted in Figure 1.12 and are detailed further.

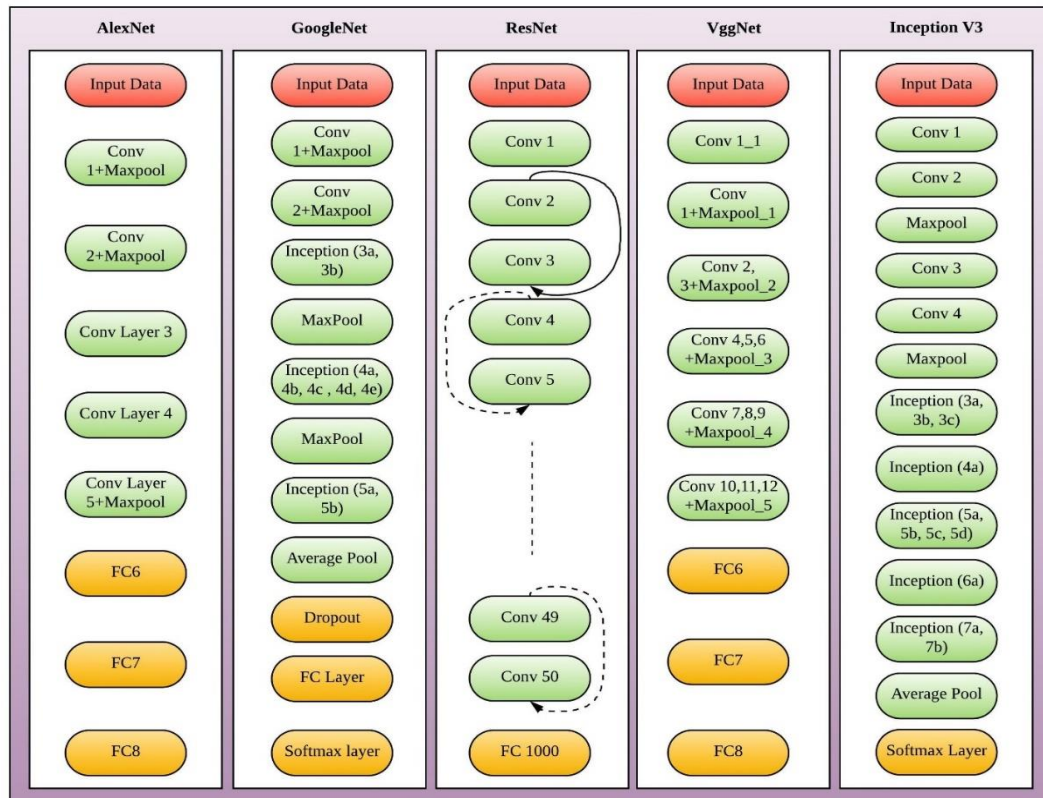


Figure 1.12: Different pre-trained CNN model architectures

- i. **AlexNet:** This network was designed in 2012 and it is similar to the very initial LeNet CNN architecture given by Lecun *et al.* [34], but is much deeper comprising more number of filters per layer. It consists of varying sized convolutional filter (11×11 , 5×5 , 3×3), max pooling and ReLU (Rectified Linear Unit) activations. ReLU activations are used after every convolutional and fully connected layer. AlexNet was the first to implement ReLU activation function to accelerate the training speed while increasing the network accuracy, pooling to reduce the network size and dropout layer to reduce over-fitting. AlexNet has learned a rich feature representation to classify wide range of images into 1000 object categories [35]. But the major limitation of AlexNet is its reduced learning rate during the training process, once the accuracy value plateaus. To overcome this disadvantage, in 2014, GoogleNet was introduced.
- ii. **GoogleNet:** GoogleNet (Inception-V1) [36] was introduced in 2014 which achieved the minimum error rate comparative to the all other available CNN networks. This network is also implemented using a novel inception module

comprising batch normalization and dropout layers. The number of parameters in the architecture is drastically reduced to 60 million using several small convolutions. GoogleNet uses “network in network” concept of building a dense network stacking inception module instead of stacking individual convolutional layers while increasing the network depth. Network accuracy saturates while increasing its depth, thus, in 2015 ResNet came into existence which utilizes skip connections while maintaining the model depth.

- iii. ResNet:** ResNet (Residual Neural Network) [37] was introduced in 2015 with gated skip connections and batch normalization. These skip connections do not have any associated parameter and just adds the output from the previous layer to the adjacent layer ahead. ResNet uses batch normalization and skip connections to design much deeper CNN networks without compromising the generalization capability of the model. Due to its powerful representation ability and better performance, ResNet applications have boosted to various image classification tasks like object detection as well as face recognition tasks. Another CNN variants came into existence in 2015, VggNet having simple implementation and increased depth size.
- iv. VggNet:** Visual Geometry group networks (VggNet) [38] is a multi-layered deep neural network introduced in 2015 due to its simplicity with increased depth level. The convolution filters of size (3×3) are used in this network and volume size is reduced using max pooling operation. Two fully connected layers comprising 4096 neurons is used in VggNet to prepare the feature vector. VggNet is used to improve CNN performance by increasing the network size and using more number of convolutional layers than AlexNet. It consists of a greater number of parameters and uses higher storage space upto 500 MB. It has the constraint of slow training with high storage space making VggNet deployment tedious. This limitation is addressed by another Inception derivative Inception-V3 model.
- v. Inception-V3:** Inception-V3 was initially designed for 1000 object categorization and is a 48 layers deeper neural network trained over a very wide range of images [39]. This model can be retrained on a smaller dataset while maintaining its learned knowledge from the previously trained model.

This concept of feature learning consumes least computational power providing better classification accuracy without the need for much extensive training. Inception-V3 aims at removing the bottleneck representation of adjacent layers which drastically reduces the input dimensions of the next layer having more competent computation using factorization technique.

1.6 DATASET DETAILS

Different publically available benchmark fundus image datasets are used for various image analysis tasks like blood vessel segmentation, abnormality detection, and classification. Table 1.2 describes different fundus image datasets in terms of their size, field of view, image count and usage.

Table 1.2: Dataset description and their usage

Dataset	Size of Image	Field of View (degrees)	Image Count	Usage
DRIVE ¹ [40]	565×584	45	40	Structural analysis of retina
STARE ² [41]	605×700	35	400	Haemorrhages and microaneurysms detection, exudates, abnormal blood vessel
DIARETDB1 ³ [42]	1500×1152	50	89	Position of retinal abnormalities and their detailed labelling
MESSIDOR ⁴ [43]	1440×960, 2240×1488, 2304×1536	45	1200	DR severity grading
IDRiD ⁵ [44]	4288×2848	50	516	DR severity grading

¹DRIVE, Digital Retinal Images for Vessel Extraction, 2004. [Dataset]. Available: <https://drive.grand-challenge.org/>. [Accessed: 04-Jan-2017].

²STARE, Structured Analysis of Retina, 2000. [Dataset]. Available: <http://cecas.clemson.edu/~ahoover/stare/>. [Accessed: 12-July-2018].

³DIARETDB1, 2007. [Dataset]. Available: <https://www.it.lut.fi/project/imageret/diaretdb1/>. [Accessed: 15-Dec-2018].

⁴MESSIDOR, Methods for Evaluating Segmentation and Indexing technique Dedicated to Retinal Ophthalmology, 2014. [Dataset]. Available: <http://messidor.crihan.fr/index-en.php>. [Accessed: 10-Feb-2019].

⁵IDRiD: Indian Diabetic Retinopathy Image Dataset, 2018. [Dataset]. Available: <http://dx.doi.org/10.21227/H25W98>. Accessed: 11-Jan-2020.

All these datasets have been utilized in this research work to accomplish different DR diagnosis tasks. DRIVE [40] and STARE [41] datasets are considered for OD localization and blood vessel extraction, while, STARE [41] and DIARETDB1 [42] dataset images are utilized for anomaly detection. The fundus images from benchmark standard MESSIDOR [43] dataset and latest IDRiD [44] are exploited for the classification and severity grading of NPDR abnormality as it consists of large set of varying images of different resolutions. The detailed description of all these datasets is provided in the following sub-sections.

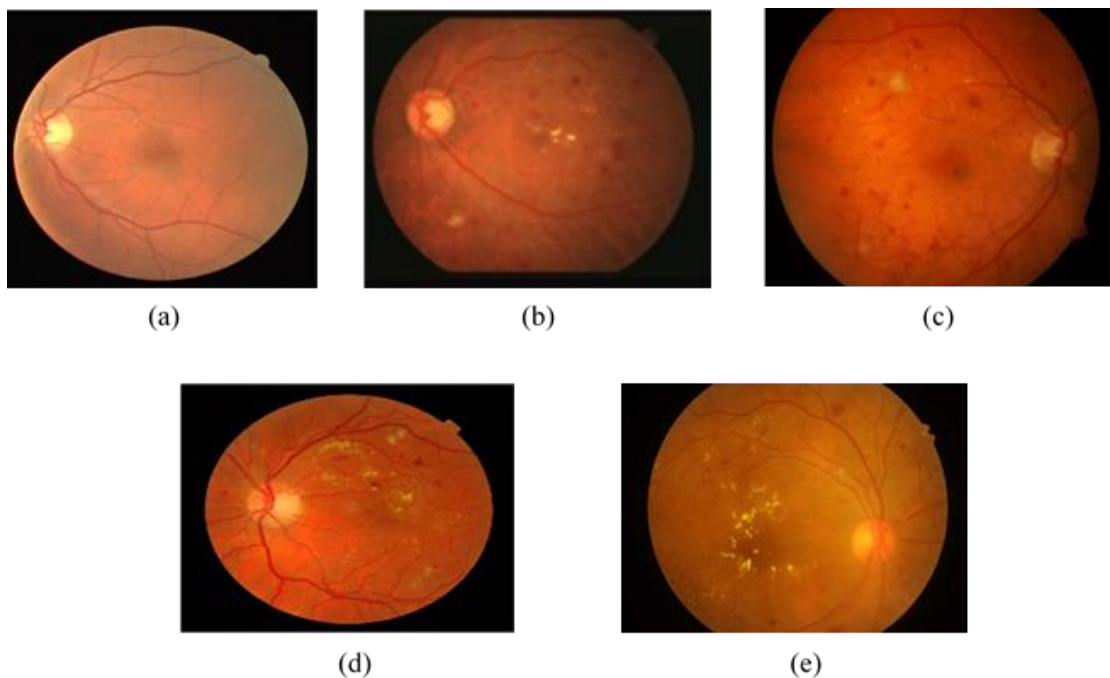


Figure 1.13: Fundus images taken from different datasets: (a) DRIVE (b) STARE (c) DIARETDB1 (d) MESSIDOR (e) IDRiD

1.6.1 DRIVE Dataset

Digital Retinal Images for Vessel Extraction (DRIVE) dataset including 40 colored fundus images using Canon 3CCD (Charge Coupled Device) camera at 45 degrees Field of View (FOV). Individual images comprised in this dataset are of size 565×584 pixels having resolution of 24 bits per pixel [40]. Labelled ground truth vessel segmentations are also present in this dataset along with all these images. The sample of fundus image from DRIVE dataset is presented in Figure 1.13 (a).

1.6.2 STARE Dataset

Structured Analysis of Retina (STARE) dataset comprising 400 raw fundus images digitized using TopCon TRV-50 camera at 35 degrees FOV. Individual images comprised in this dataset are of size 605×700 pixels having resolution of 24 bits per pixel [41]. Ground truth vessel segmentations are present in this dataset for 20 fundus images labeled by professional experts. The sample fundus images of STARE Dataset is illustrated in Figure 1.13 (b).

1.6.3 DIARETDB1 Dataset

A standard DIAbetic RETinopathy DataBase-calibration level 1 (DIARETDB1) includes 89 colored fundus images with 84 containing the symptoms of non-proliferative DR and the remaining 5 containing no DR symptoms. The images were taken using digital fundus camera at 50-degree FOV along with varying imaging-controlled systems in Kuopio University Hospital, Finland. Fundus images were inspected to find hard exudates, haemorrhages, and microaneurysms using special software [42]. The sample fundus image from DIARETDB1 Dataset is represented in Figure 1.13 (c).

1.6.4 MESSIDOR Dataset

Methods for Segmentation and Indexing Techniques Dedicated to Retinal Ophthalmology Retinal Ophthalmology (MESSIDOR) is a benchmark database that consists of 1200 eye fundus color images utilized for evaluating the. Three of the ophthalmologic departments were responsible for gathering images using 3CCD on a Topcon TRC NW6 for non-mydratic retinography at 45 degrees FOV. Varying sized fundus images with 1440×960, 2240×1488 or 2304×1536 pixels were included in this dataset having 8 bits per color plane [43]. The sample of the fundus image from MESSIDOR dataset is represented in Figure 1.13 (d).

1.6.5 IDRiD Dataset

Indian Diabetic Retinopathy Image (IDRiD) dataset [44] comprises of retinal fundus images which were acquired from an Eye Clinic in Nanded, (M.S.), India. These set of images were collected using a Kowa VX-10, a digital fundus camera with the approximate distance of 39 mm between lenses and the eye [44]. Pupil dilation

was performed before capturing the images of all the subjects in the dataset. This dataset consists of 516 images having resolution of 4288×2848 pixels with 50° FOV. In this dataset the total of 454 fundus images contains the symptoms of NPDR severity whereas the rest of 62 fundus images contains symptoms of PDR severity. This dataset consists of clinically relevant images of acceptable quality, collected from the DR and diabetic macular edema tests conducted on thousands of patients during the period 2009–2017.

1.7 COMPUTER-AIDED DIAGNOSIS SYSTEM

Computer-Aided Diagnosis (CAD) has evolved as a major research issue in the field of medical imaging and radiology diagnosis. The medical imaging field deals with evaluation and analysis of abnormality at the earliest, using the image information. CAD systems deal with the improvement of image quality of low contrast raw medical images using various image processing tools which is fit for the interpretation of prominent portions and relevant for disease diagnosis [45]. CAD systems are the computer systems that are specifically designed to assist the detection or diagnosis of diseases by providing the second opinion to the clinical experts. It improves the overall performance of detection and assist the physicians in the early detection of different medical anomalies. CAD systems specifically aim at improving the accuracy of disease diagnosis along with the reduced time computations for the interpretation of image information. It takes into account the equal roles of clinicals as well as computer aided algorithms, thereby providing better diagnostic performance.

CAD has developed as a part of routine clinical diagnosis in some hospitals and it is widely being applied for the detection of many different types of anomalies in different medical imaging modalities. The basic categorization of CAD systems lies into two categories, namely; Computer-Aided Detection (CADe) systems and Computer-Aided Diagnosis (CADx) systems. The CADe systems enable the computer aided processing by assisting the experts in determining the location of disease lesions in the medical images. On the other hand, CADx systems provides a lesion categorization platform by distinguishing between the several classes of the disease to be diagnosed. CAD systems are also helpful in retinal image analysis as they reduce

the chances of severe eye complications upto a large extent by regular screening and timely treatment. The aim of this work is to provide a CADx platform by assisting the ophthalmologists with a second opinion in distinguishing different severity grades of Diabetic Retinopathy [45, 46].

1.8 PERFORMANCE INDICES

Various indices are utilized in this work for the performance evaluation and validation of the proposed techniques based on the extensive study of state of art techniques. Various performance indices calculated in this work are based on four possible events. For deriving the pixel classifications, True Positive (TP) / True Negative (TN) are computed and pixel misclassification is computed from False Positive (FP) / False Negative (FN) values [47, 48]. TP event indicates that the pixel is correctly identified as DR affected fundus image and TN indicates the correctly identified pixel as a normal fundus. FP event indicates that pixel is predicted as a DR affected pixel but it is actually not, and FN event indicates that pixel is predicted as normal pixel but it is actually a DR affected pixel. Based on these 4 predicted events, performance indices are evaluated which are explained below:

- i. **Jaccard Index:** Jaccard similarity coefficient is a comparative statistical index that measures the similarity of data sets. This coefficient is determined as the ratio of the intersection to that of the union of datasets. Its range is between 0 to 1, and the more its value tending towards 1 more similar are the two sets of data. Jaccard Index is expressed by Eq. (1.12).

$$Jaccard\ Index = \frac{A \cap B}{A \cup B} \quad (1.12)$$

- ii. **Dice Coefficient:** Dice coefficient is the measure of similarity between the two sets under evaluation. The dice coefficient is expressed in Eq. (1.13) and it ranges in between 0 to 1, and the more its value tending towards 1, more similar are the two sets of data.

$$Dice\ Coeff. = \frac{2 * Jaccard\ Index}{1 + Jaccard\ Index} \quad (1.13)$$

- iii. **Root Mean Square Error (RMSE):** This performance metric denotes the standard deviation of prediction errors. These prediction errors measure the deviation in the image quality based on the averaging of the squared intensity pixel values. It is expressed by Eq. (1.14).

$$RMSE = \sqrt{\sum \sum \frac{(Prediction\ Error)^2}{Rows \times Columns}} \quad (1.14)$$

- iv. **Structural Similarity Index (SSIM):** Statistical quality of image based on image attributes like luminance, brightness, texture, orientation and contrast. Its value ranges from 0 to 1 and the image quality is considered better if the value approaches toward 1. SSIM is expressed by Eq. (1.15).

$$SSIM = \frac{(2\mu_x\mu_y+c_1)(2\sigma_{xy}+c_2)}{(\mu_x^2+\mu_y^2+c_1)(\sigma_x^2+\sigma_y^2+c_2)} \quad (1.15)$$

where μ_x is the average value of x , μ_y is the average value of y , σ_x^2 is the variance of x , σ_y^2 is the variance of y , σ_{xy} is the covariance of x and y , $c_1 = (k_1L)^2$, $c_2 = (k_2L)^2$ are the stabilization constants where L is the dynamic range of pixels, $k_1=0.01$ and $k_2=0.03$.

- v. **Peak Signal to Noise Ratio (PSNR):** PSNR is an image quality parameter based on the RMSE value. The higher value of PSNR, better is the output image quality. PSNR is expressed by Eq. (1.16).

$$PSNR = 10 \log \frac{(Peak\ value\ (256))^2}{RMSE^2} \quad (1.16)$$

- vi. **Positive Prediction Value (PPV) or Precision:** It considers Positive Prediction Value for the measurement of statistical variability in data that computes the deviation of data entries from its true value. The percentage range of PPV lies from 0% to 100% indicating the data deviation from its actual value and is represented by Eq. (1.17).

$$Precision = \frac{TP}{TP+FP} \quad (1.17)$$

- vii. Sensitivity or Recall rate (SN):** Sensitivity or recall rate is determined as the ratio of true positives to the sum of true positives and false negatives. The recall value provides the measure of model's ability for correct segmentation/classification in order to identify true problematic pixels. It ranges between 0% to 100%, and more the value of recall closer to 100%, more the model becomes capability of correctly detecting abnormal pixels. Sensitivity is represented by Eq. (1.18).

$$SN = \frac{TP}{TP+FN} \quad (1.18)$$

- viii. Specificity (SP):** Specificity is the ratio of true negatives to the sum of true negatives and false positive. It provides the measure of model's capability in terms of segmentation/classification for correctly identifying normal pixels. The specificity ranges from 0% to 100% and it signifies that more is the specificity closer to 100%, more becomes the capability of system for correctly detecting normal pixels. Specificity is represented by Eq. (1.19).

$$SP = \frac{TN}{FP+TN} \quad (1.19)$$

- ix. F-Measure:** F-measure defines the weighted harmonic mean of the outcomes obtained from precision and recall values. This value takes into account both false positives and false negatives. F-measure value ranges from 0% to 100% and more is the value of F-measure closer towards 100%, more becomes the capability of model for correctly predicting the falsely detected pixels. The F-measure is formulated as Eq. (1.20).

$$F - Measure = \frac{(2 * Recall * Precision)}{(Recall + Precision)} \quad (1.20)$$

- x. Accuracy (Acc):** Accuracy is determined as the proportion of the total number of true events to that of the complete set of events. Its range lies in between 0% to 100% and more its value tending towards 100% more is the capability to correctly detect the correctly identified true event pixels and is expressed by Eq. (1.21).

$$Acc = \frac{TP+TN}{TP+FP+TN+FN} \quad (1.21)$$

- xi. Area under the Curve (AUC):** The overall quality of classification performance is indicated by the AUC performance index. More the AUC, better will be the performance of the classifier as each point on the Receiver Operating Characteristics (ROC) curve pointing out the cut-off points of true-positive and false-positive rates.
- xii. Cross-Entropy:** Cross entropy loss measures the classification model performance. The value of this performance measure ranges between 0 to 1, where 1 indicates worst and 0 denotes a perfect classification scenario. The formula of cross-entropy is expressed by Eq. (1.22).

$$\text{Cross - Entropy} = \frac{1}{\sum_{t=1}^M y_{o,t} \log(p_{o,t})} \quad (1.22)$$

where M is the number of classes, t is the true classification for observation o , p is the prediction probability and y is the binary indicator for correct class label.

- xiii. Optical Disc Overlap:** It is defined as the ratio of true positives to the summation of true positives, false negative and false positive expressed by Eq. (1.23).

$$\text{Optical Disc Overlap} = \frac{TP}{TP + FN + FP} \quad (1.23)$$

- xiv. Dice Metric:** Dice Metric computes the similarity between segmentations defined as the ratio of twice the true positives by the sum of all events as expressed by Eq. (1.24).

$$\text{Dice Metric} = \frac{2 * TP}{TP + FN + FP + TN} \quad (1.24)$$

1.9 SOFTWARE PLATFORM

All the experimentation work implemented in this thesis is done using Matrix Laboratory (MATLAB 2018b) environment on a mainframe computer system with configuration of Intel Core i5 processor that offers clock speed of 3GHz and 8GB RAM. For the statistical analysis of derived feature set, IBM Statistical Package for Social Sciences (SPSS) is used.

1.10 MOTIVATION

Diabetes mellitus is a life-threatening disease arising due to the abnormal growth of blood sugar level having adverse effects on human vision, heart, nervous system, kidneys, and other body organs. Diabetes has reached epidemic proportions worldwide and it is the leading cause of severe blindness in the patients between 25 to 74 years of age. More than 10% of diabetic patients suffer from a high risk of developing eye-related disorders. According to the World Health Organization (WHO) survey, 10% of patients develop severe vision defects and 2% of people become blind after 15 years of persistent diabetes [49].

Diabetic retinopathy is the most serious progressive and degenerative retinal complication that has become a serious issue for diabetic patients worldwide. The patients suffering from DR have no initial visible symptoms until it is the very last stage for effective treatment. It is important to regularly examine patients with diabetes for the development of retinal disease as the rate of progression can be fast.

Medical image analysis put emphasis on the diagnosis of progressive diseases like DR as it helps ophthalmologists to take necessary corrective measures before they cause irreversible blindness. The large diabetic population and less number of experienced ophthalmologists have increased the demand for computer-based automated DR diagnostic systems. DR classification is difficult even for ophthalmologists, especially in the presence of various small features. Increasing DR cases have adverse impact on ophthalmologists and require an efficient and accurate method for fundus image evaluation. Based on this motivation and vast literature survey presented in Chapter 2, some research gaps have been formulated which are discussed in the following section.

1.11 RESEARCH GAPS

Depending upon the elaborative study of various DR screening techniques, some of the research gaps are formulated which lead as the foundation for objective framing of this research work.

Research Gap 1: Retinal Physiological Structure Extraction

Insufficient fundus image illumination along with their poor-quality cause inability of analysis in medical domain. Image pre-processing is essential for improving the image features such as contrast and illumination, for the segmentation and extraction of OD and blood vessels. Obtaining a single connected component for Optical Disc localization is still a challenging task as OD has blurred boundaries. Manual vessel estimation approaches are tedious, erroneous, require high skills and time-consuming. Blood vessels possess width disparities; therefore, automated vessel segmentation is required to combat the vessel structure estimation challenge.

Research Gap 2: Development of an efficient Lesion Discrimination Approach

Manual intercession involved in existing DR lesion discrimination approaches are biased, arduous and requires expert human intervention. Manifold possibilities are revealed from the literature to improve the lesion discrimination approach for the removal of fallacious lesion portions. The inability of distinguishing between the background noise, anatomical structures and actual lesion portions is the major constraint of the present DR severity discrimination techniques. Lesion discrimination is a difficult task in the presence of these anatomical structures. Red lesion discrimination is difficult in the presence of retinal blood vessels and similarly, optical disc presence may hamper the performance of the yellow lesion discrimination approach. Thus, initial identification and removal of these anatomical structures are important for true lesion detection.

Research Gap 3: Diagnostic Relevance of DR severity grading

Retinal abnormalities can be characterized by any kind of uneven changes in various retinal components. High clinical relevance of retinal pathologies gives rise to the need for early diagnosis through regular retinal image screening as well as effective severity grading systems. The main constraints that came across for effectual DR severity grading and diagnosis are optimal feature set selection and the choice of finest classifier to maintain the trade-off between accuracy and computation cost. Both these problems are not addressed in the existing research works and therefore, there is the need for devising a reliable retinal image classification scheme to improve the existing DR severity grading systems.

Research Gap 4: Requirement of Deep Learning based DR Diagnostic system

The traditional DR diagnosis methods rely on handcrafted features that are limited and require expert knowledge to devise new handcrafted features. Also, traditional networks become very slow if they must deal with complex tasks involving multiple layers. Unavailability of a large amount of labelled data in the medical domain still prevails as a challenge to researchers. Despite the various advances in CNN based DR diagnosis, these systems still present challenges for clinical applications. Some of these limitations are being addressed in this work using a transfer learning-based CNN approach.

1.12 OBJECTIVES OF RESEARCH WORK

Ophthalmologists highly rely on retinal fundus segmentations for the treatment of abnormalities like glaucoma, strokes, occlusions and diabetic retinopathy. Thus, to extract the diagnostic information of different pathological symptoms reflected in retinal fundus images, image analysis techniques are required. The aim of this research work lies in automated DR characterization assisting ophthalmologists by aiding treatment planning, diagnosis and prognosis. The outline of automated DR detection and severity grading problem addressed in this research work is based on the objectives listed below:

Objective I

Design of an Automated Retinal Blood Vasculature Segmentation Model for Diabetic Retinopathy Detection

Objective II

Developing a Hybrid Lesion Detection Technique for DR Abnormality Discrimination

Objective III

Implementation of a Robust Framework for DR Categorization

Objective IV

Inception of Ensembled Transfer Learning Model for DR Severity Grading

1.13 OUTLINE OF THE THESIS

The research work in this thesis comprises seven chapters including this introduction chapter. It contains the basic introduction along the preliminaries related to this research work. The remaining thesis is structured into the following chapters.

Chapter 2 discusses the literature survey done on various DR detection techniques proposed in the past highlighting the state of the art work done in this field. It also gives the details of the research gaps observed in the current literature and objectives formulated for our research work.

Chapter 3 deals with the objective 1 proposed in this research work. A Circular Hough Transform based OD localization technique and a Hybrid Blood Vessel Extraction Approach using Morphological Reconstruction (HBV-MR) approach are proposed in this chapter to improve the retinal physiological portion extraction while maintaining a trade-off with the computational complexity. The exhaustive performance evaluation illustrates the localization efficiency and viability of the proposed approaches.

Chapter 4 addresses the lesion discrimination problem by designing and implementing a Hybrid Lesion Detection (HLD) scheme for the detection of abnormalities in retinal images. An effective solution is presented to advance DR diagnosis by explicitly locating DR lesions and providing the information about the abnormality location.

Chapter 5 details the Hierarchical Severity Grading (HSG) System proposed in objective 3 which classifies NPDR severity present in retinal fundus images into different stages, to track the disease progression for prognosis and patient referral. The proposed system is generalized through its performance validation for latest dataset.

Chapter 6 deals with the implementation of Deep learning-based methodology for the DR screening and diagnosis. This chapter addresses the two-stage classification into diseased and non-diseased classes by proposing an Ensembled Deep Learning based DR (EDLDR) model. It highlights two different deep learning approaches employed to address DR severity grading: A Prominent Feature based Transfer Learning (PFTL) model and a Quadrant Ensembled Inception-V3 Model (QEIV-3). CNN based classification methods provide superior performance for retinal fundus image acquired at varying field of view and different size, due to its augmentation feature dealing with field of view invariance, scaling and rotation.

Chapter 7 concludes the research outcome of this thesis and provides the future scope for the extension of this research work to make it robust for the real-time DR classification scenario.

CHAPTER 2

LITERATURE REVIEW

CHAPTER 2

LITERATURE REVIEW

From diagnostic point of view, analysis of retinal image is getting more and more important nowadays. This chapter presents a general overview of various image processing techniques developed in the past few years for combating the challenge of DR screening and diagnosis. Many researchers have confronted this challenging job through various methods still this is a daunting challenge and requires more work on finding a robust technique for efficient DR prognosis.

This chapter presents a brief description about existing work in the field of automated DR screening which motivated us to develop a much reliable automated screening solution to aid the ophthalmologists in providing mass DR screening solutions. An extensive literature survey is carried out to outline the initiation of automation in this field and assess the development of various ophthalmic image processing techniques.

Initiatives taken by several researchers in the field of OD localization, blood vessel extraction, lesion discrimination, diabetic retinopathy grading and instigation of deep learning approaches to address severity of DR are detailed in this chapter. The contributory framework of the entire proposed methodology adopted in this thesis is illustrated at the end of this chapter. A block diagram representation of the sequential overview in which literature review is conducted is depicted in Figure 2.1.

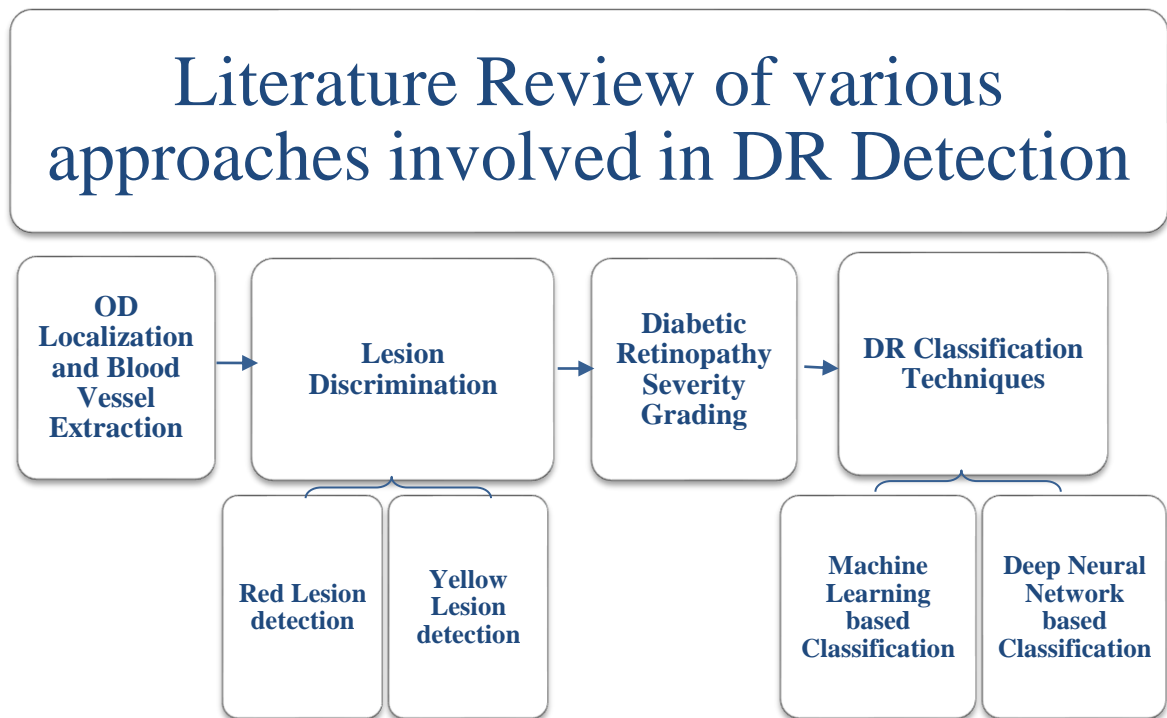


Figure 2.1: Sequential overview of literature review

2.1 OD LOCALIZATION AND BLOOD VESSEL EXTRACTION

Manual vessel segmentation methods require high professional skills and are tedious as well as time consuming. These methods are susceptible to unavoidable errors and demand a lot of training efforts. Thus, automated blood vessel extraction and segmentation systems came into picture for effective computer-aided ophthalmic diagnosis.

In automated retinal image analysis, blood vessels and OD are the most important anatomic location for extraction and removal. The remarkable attempts from various researchers have been noticed towards development and enhancement of screening and diagnosis techniques for blood vessel extraction and optical disc segmentation. Researchers have put lots of efforts in providing better retinal vessel segmentation methods and some of the work done in this field is briefed in the following section.

OD segmentation is important for effectual diagnosis of retina related abnormalities, especially for the accurate identification of yellow (bright) lesions in the DR infected patients as OD and yellow lesions has similar intensity range. The difficulty in OD localization arises when subjected to uneven illumination along with

the large number of pathological abnormalities. It becomes more challenging to extract the OD portion having the shape and size similar to bright lesions (exudates) [50]. A method based on histogram matching was introduced in [51] for OD segmentation in which a template is created by averaging the histogram of each colored component in order to localize the center of OD. The correlation among original image and extracted RGB components are computed to identify the point with maximum correlation as the center of OD. The authors in [52] presented the processing of fundus images providing better lesion clarity for achieving similar quality as of angiogram. Speed up robust features are employed to segment the optical disc using morphological image processing operations. A unique vessel transformation and correction procedure was designed by the authors in [53] based on clustering approach for the automatic detection of OD. The proposed model is integrated with scale space analysis for detecting OD boundaries. High Resolution Fundus image (HRF) dataset is utilized in [54] for OD enhancement which is followed by histogram equalization for enhancing green region of fundus image. The optical disc segmentation is computed using speed up robust features. The Receiver Operating Characteristics (ROC) curves are used for measuring the evaluated results.

Authors in [55] have utilized image filtering and adaptive histogram equalization prior to OD and blood vessel detection. The segmentation and removal of these anatomical structures is carried out through morphological operation and implementing Otsu thresholding technique for improvisation of results. The blood vessel segmentation is further achieved by pre-processing based on histogram equalization and robust distance transformation [56]. Vessel Vector-based Phase Portrait Analysis (VVPPA) is proposed in [57] combining the clustering method with vessel transform to obtain exceptional performance for blood vessel segmentation. Traditional graph cut method along with Markov Random Field (MRF) method is utilized in [58] for extracting retina vascular tree and OD segmentation. The graph cut method was implemented to extract the retinal vascular structures and the two alternative methods MRF and compensation factor method was utilized for optical disc localization which provides a supporting system for non-intrusive diagnosis for modern ophthalmologists. The position of OD is approximated in [59] using graph cut technique for retinal vascular tree extraction and the obtained OD features are further fed to ANN classifier for better performance.

Similar intensity range of blood vessels and red lesion (MAs and HEMs), may lead to misclassification. This problem is addressed by some of the techniques in the literature employing vascular structure masking method [60, 61]. Retinal vessel segmentation methods like line detector, template matching, etc have achieved the segmentation accuracy of 92%, however achieving the segmentation accuracy above 92% while maintaining the low computational complexity is still a challenge to the researchers [62]. Another methods reported in the literature to address this drawback includes a template-based approach for OD segmentation using Circular Hough Transform as OD boundary approximator which can provide a good cooperation between success rate, quality and efficiency [63]. Canny edge detector approach is employed by the authors in [64] to evaluate the vascular structures by producing a better image quality for blockage identification in tiny blood vessels. Various pre-processing and blood vessel feature extraction stages are employed by the authors in [65] to find the biological relevance of this feature set with the previously reported outcomes of early detection of DR. Kirsch's template based Graphical User Interface (GUI) is developed in [66] for retinal blood vessel extraction to accomplish accuracy detection of exudates. This GUI obtains higher performance by incorporating maximum number of image pre-processing methods altogether. Out of a number of segmentation algorithms accessed in [67], the most efficient segmentation outcomes are provided by wavelet filter method for distinguishing retinal blood vessels from other retinal structures. These filters are efficient enough for object identification and segmentation even in the presence of background noise.

Principle Component Analysis (PCA) is utilized in [68] for retinal vessel feature minimization but still all of these features are not useful for providing the effective performance. Hence, Particle Swarm Optimization (PSO) is exploited to provide the better results in terms of entropy, sensitivity, accuracy, etc. Comparative study of automated retinal vessel segmentation and manually labeled fundus images is done using global quality parameters to obtain better comparative results [69]. A supervised blood vessel detection approach was employed in [70] using gray-level and moment invariant features were utilized for effectual pixel representation. Considerably improved results are obtained by authors in [71] using a combination of fundus image registration and multimodal approach for retinal vascular segmentation exploiting Spectral-Domain Optical Coherence Tomography (SD-OCT) volumes. Consistent

blood vessel segmentation accuracy is achieved in comparison with existing supervised segmentation techniques in [72] by utilizing a three-stage segmentation algorithm for extracting major and minor blood vessels. A precise and speedy optic disc detection method was developed in [73] using blood vessel distribution and directional characteristics. When tested on four different publically available dataset, the method provides a robust and efficient solution yielding system accuracy in the range of 83% to 99%. Conventional segmentation techniques are not effective when applied on very thin or elongated blood vessels. This limitation was overcome using conditional random field model and SVM for classification. Authors in [74] presented a fully connected discriminatively trained conditional random field model for effectual blood vessel segmentation. A multi-anatomical fundus segmentation system was presented in [75] to extract the features of retinal vascular structures, optical disc and exudates. This hybrid approach was a combination of adaptive fuzzy thresholding and mathematical morphology to provide robust and accurate segmentation for pathological retinal images. Exceptional performance was achieved compared to the other systems reported in the literature when validated on four benchmark databases. Performance evaluation and validation of different retinal vascular segmentation techniques was done in [76] to improve the trends in retinal vascular segmentation techniques.

An extensive range of evolutionary methods were assessed and reported in [77] to provide a robust CAD for aiding the diagnosis of retinal pathologies. From the study, it was revealed that evolutionary computing algorithms are important in segmentation, feature extraction and selection, dimensionality reduction and classification to achieve an optimized DR-CAD system. Retinal vessel synthesizing problem was addressed in [78] using adversarial learning methods. Synthesized images provided reasonable visual quality providing accurate visual and qualitative results. Adaptive histogram method was utilized for retinal feature extraction by the authors in [79]. This approach uses binary thresholding along with mathematical morphology for small object identification and removal. OD centroid, perimeter and area like geometrical features were evaluated for the diagnostic purpose and the results were compared to the standard techniques. Proliferative diabetic retinopathy featured by retinal vessel overgrowth is encountered using a neo-vascular detection approach [80]. Multi-level Gabor filtering, feature extraction and image classification using SVM were the main

steps involved in this vessel segmentation approach. Out of 42 extracted features, 18 features were utilized for training SVM classifier to yield better outcomes. Image processing and data mining techniques are employed for blood vessel segmentation by Geetharaman, *et al.* [81]. PCA and k-means clustering were exploited for feature extraction and Naïve–Bayes classifier is employed for classification. Faster analysis of blood vasculatures is done on STARE dataset to yield better accuracy. Background noise and uneven illumination of small blood vessel segmentation was addressed in [82] adopting morphological and filtering methods. Anisotropic diffusion was used for blood vessel detection followed by double threshold based region growing methods to obtain improved accuracy.

Dash, *et al.* [83] presented a three- phase computerized blood vessel extraction technique consisting of various steps like contrast limited histogram equalization, mean median filter, C-mean thresholding for segmentation and post processing using morphological cleaning operation. A retinal vasculature extraction approach was proposed by Zafer and Kose [84] using Gabor filter, k- means and Fuzzy C-means clustering to obtain binary vessel map. Post-processing steps were also used in this method to remove falsely segmented isolated regions to obtain acceptable system performance. Independent component analysis was proposed in [85] for automated retinal vessel segmentation method that provides superior performance in comparison with previous state-of-the-art techniques. Technique proposed by authors in [86] involves blood vessel region feature extraction for trimap generation followed by hierarchical image matting model for vessel pixel extraction from the unknown regions. This technique overcomes the computational time limitation outperforming many supervised and un-supervised state of the art approaches.

A comparative analysis of different research initiatives for blood vessel segmentation is illustrated in Table 2.1 along with the image processing techniques employed and performance metrics evaluated.

Table 2.1: Comparison of different optical disc localization and retinal blood vessel segmentation techniques

Year	Algorithm Proposed by	Dataset used to Validate Results	Image Processing Technique Employed	Performance Metrics Employed
2010	Villalobos Castaldi <i>et al.</i> [87]	DRIVE	Gaussian matched filter entropy adaptive thresholding	Accuracy, Specificity, Sensitivity
2011	Abdallah <i>et al.</i> [88]	STARE	Multi-scale based on Anisotropic diffusion	ROC curve
2012	Kaur and Sinha [89]	DRIVE, STARE	Filter Kernel: Gabor filter	ROC curve
2013	Odstrcilik <i>et al.</i> [90]	DRIVE, STARE	Improved T-dimensional Gaussian matched filter	Accuracy, Specificity, Sensitivity
2014	Frucci <i>et al.</i> [91]	DRIVE	Watershed transform Contrast and directional Maps	Accuracy, Precision
2015	Singh <i>et al.</i> [92]	DRIVE	Modified Gaussian matched filter Entropy thresholding	Accuracy, Specificity, Sensitivity
2016	Sharma and Wasson [93]	DRIVE	Grayscale conversion, Gabor filtering, Image Binarization, Principal component analysis, Fuzzy c-means clustering	Accuracy, Specificity, Sensitivity
2017	Jiang <i>et al.</i> [94]	DRIVE, STARE	Global thresholding based on morphological operations	Accuracy, Execution time
2017	Muangnak N., Aimmanee P. <i>et al.</i> [95]	STARE	Vessel vector-based phase portrait analysis (VVPPA), Vessel Transform	Average Sensitivity, Accuracy

Upon comparing various blood vessel segmentation techniques from the year 2010 to 2017 it was found that most of the analysis was done taking two main databases, DRIVE and STARE database. It is revealed that manual blood vessel tracing system is time-consuming and inaccurate, so automatic vessel segmentation is beneficial for ophthalmologists. Even though several OD localization and blood vessel segmentation techniques have been reported in literature, these techniques do have some constraints due to fundus image poor contrast quality and insufficient illumination. Current optical disc localization methods are not able to identify OD boundaries precisely because it has blurred edges. Blood vessel separation is also challenging due to the disparity in

vessel width. Some small blood vessels that have fewer contrasts are not divided by cutting-edge methods. Current methods are not able to overcome these problems of OD localization and blood vessel extraction, thus, there is a need to improve the existing system. It is also accepted that most successful vessel segmentation methods are based on morphological image processing because this method assumes that vascular structures have concave cross sections which yields better outcomes [82, 83]. Thus, the rationale for this research lies in exploring manifold possibilities for the improvement of existing blood vessel extraction techniques and OD segmentation methods.

2.2 LESION DISCRIMINATION

There exist many attempts by the researchers towards devising DR detection techniques for detection of abnormalities and discrimination of fundus image at its initial stage. DR lesion can be broadly classified based on their color and intensity levels into yellow/bright and red/dark lesions. MAs and HEMs belongs to the class of red or dark lesions. On the other hand, EXs and CWs classified as yellow or bright lesions. There exist many approaches which are suitable for DR lesion detection exploiting retinal fundus images. These approaches are reported in literature and divided into two categories based on red and yellow lesion detection methods in this section of the chapter.

2.2.1 Red Lesion Detection

Red lesions (MAs and HEMs) are the initial and undeniable clinical symptoms of DR which are important for early detection of pathology. Some of the existing methods exploited for their detection are detailed in this sub-section. A Curvelet based Edge Enhancement technique using wideband bandpass filtering was proposed by authors in [96] for the detection of dark lesion edges. Parameters were optimized using differential evolution algorithm and morphology based post-processing method was used to exclude the false lesion candidates. Receiver operating characteristics were evaluated for statistical performance analysis and it was revealed that the proposed method is slightly weaker for red lesion detection when the lesions are

indistinguishable from the background. A simple threshold based MA candidate setting technique was provided by authors in [97] that selects the clutter among the candidates by using rejectors in cascaded form. The clutter and MA structures are distinguished using morphological and appearance-based features. Another red lesion detection technique was introduced in [98] based on a new set of dynamic shape features and the evaluation was done on six different databases for MAs and HEMs detection. The robust features obtained using this method make it superior to other state-of-the-art approaches providing high discrimination capabilities at both per-lesion and per-image levels. Directional cross-section profile analysis based method was proposed by the authors in [99] for MA detection. These minute MAs are centered around the candidate pixel of the pre-processed image. A haemorrhage detection approach was proposed by Inbarathi, *et al.* [100] which automates the DR screening process by utilizing features of Splat and Gray-Level Co-occurrence Matrix (GLCM) for machine learning based SVM classification. MESSIDOR dataset was used for experimentation to achieve the improvement in classification accuracy comparative to other techniques. A combination of algorithms was introduced by Habib *et al.* [17] for automated detection of MAs. Gaussian Matched Filter was utilized to find the initial set of candidates and Tree Ensemble classification was employed for the detection of false positives. Consistent performance was achieved using this combination of ensemble classifier in elimination of false positives.

Akram *et al.* [101] used a three-stage strategy comprising pre-processing, feature extraction and classification stages for MA detection. Possible MA regions were extracted and separated based on various features obtained at the feature extraction stage. A combined classifier comprising gaussian mixture model and support vector machine was employed to classify MAs from non-MA regions. A Convolution Neural Network based MA identification method was introduced by Dai, *et al.* [102] where very little supervised information is used to map the images into feature space. Raw fundus image is interleaved with identified MA regions and this information is further provided to the multi-sieving deep mining stage. Niemeijer *et al.* [103] provided two novel contributions in red lesion detection approach; one was candidate detection using pixel classification and another is the introduction of a new feature set which is to be fed to k- nearest neighbour classifier. The results achieved using this approach

were close to the human expert grading providing better performance for red lesion image classification. A lesion detection and characterization framework was given by Quellec *et al.* [104] which provided automatically formed filter generated feature vector using a set of reference image samples. MAs image set provide comparable results to the expert labeled outcomes.

2.2.2 Yellow Lesion Detection

Similarly, for the detection of yellow lesions (EXs and CWs), there exist various techniques which are reported in this sub-section of the chapter. Rocha *et al.* [105] presented an analytical method for red and yellow lesions. This analytical approach uses visual words dictionary framework capable of mapping the feature vector information onto a projection space to yield specific DR class. Five-fold cross-validation was used for performance analysis which provides acceptable performance for both red and yellow lesion classification. Different image processing techniques for identification of EXs regions was provided by Parvoti *et al.* [106] using a subset of 30 colored fundus images. Hue saturation intensity (HSI) space was obtained out of which intensity component is used to extract morphological properties of lesion candidate. Exudates regions were segmented using optimal thresholding operation. Authors in [107] provided a DR screening algorithm for early-stage screening and diagnosis using the combination of image pre-processing, feature extraction and Multilayer Perceptron (MLP) classification steps. Improved classification efficiency was achieved using 16 statistical features for MLP classification process.

A neural network-based approach was proposed by Sadek *et al.* [108] for feature extraction which were further provided to non-linear classifier to obtain fundus image discrimination into normal and abnormal (exudates and drusen). Three different techniques such as SVM, Bayesian classification and Probabilistic Neural Network (PNN) were utilized by authors in [109] for DR diagnosis and SVM provides the highest accuracy out of all the models. An ANN based DR classification system was presented by Paing, *et al.* [110] which maintained a trade-off between system accuracy and computation time when tested on DIARETDB1 benchmark dataset and local databases. Yalcin, *et al.* [111] provided exceptional performance using a deep learning-based early DR detection approach employing CNN yielding remarkable

success rate over other methods. A combined technique for both MA and EX detection using MESSIDOR dataset for Structural and GLCM feature extraction was introduced by authors in [112]. This approach utilizes SVM and k-Nearest Neighbour (kNN) classifiers for obtaining better classification performance. An ensemble classifier based approach utilizing SVM, kNN and Gaussian Mixer Model (GMM) classifiers was introduced by Habib, *et al.* [17]. Feature reduction strategy was also integrated in this approach and the reduced feature set was utilized for the detection and classification of hierarchal lesion. This approach primarily classifies lesion and non-lesion which is followed by classification of EXs and CWs from yellow lesions and classification of MAs and HEMs from red lesions.

Carrera, *et al.* [113] used digital processing to aid early-stage DR detection by isolating various features of blood vessels, exudates, microaneurysms. This approach provided the robustness to change in parameter by utilizing SVM classifier for disease classification. Retinal health assessment method was introduced by Koh, *et al.* [114] utilizing Speeded-Up Robust Features (SURF) and correlated features. These features were subjected to KNN classifier for achieving better outcomes. Karthikeyan and Alli [115] presented a DR disease classification technique on the basis of Genetic Algorithm (GA). Their approach provides an efficient solution by exploiting SVM parameters alongside utilizing Glow-worm Swarm Optimization (GSO). Their work can be extended considering future implications by focusing on adaptability of meta-heuristic techniques as the proposed method lags in dealing with the challenge of computational complexity. Authors in [116] presented a rule-based classification technique that can detect CWs and EXs yellow lesions more accurately. Their approach achieves high accuracy for the detection of bright lesions. Apart from this, the comparison of different red lesion detection methods for the extraction of MAs and HEMs is shown in Table 2.2 detailing the dataset, method and performance metrics employed.

Table 2.2: Comparison of different red and yellow lesion detection methods

Year	Author	Dataset Utilized	Methods Employed	Performance Metrics
2007	Kauppi <i>et al.</i> [42]	DIARETDB1	Pattern Recognition	Recall and Precision
2010	Agurto <i>et al.</i> [117]	MESSIDOR	Modulation Features	Specificity and Sensitivity
2012	Rocha <i>et al.</i> [105]	MESSIDOR, DIARETDB1	SVM and Visual Word Dictionaries	Sensitivity and Accuracy
2014	Decencière <i>et al.</i> [40]	MESSIDOR and DIARETDB1	Evolutional Algorithms	Accuracy and Recall
2014	Akram <i>et al.</i> [118]	DIARETDB	Hybrid Classifiers (m-Mediod, GMM)	Recall, Precision, Accuracy
2015	Mookiah <i>et al.</i> [119]	MESSIDOR, DIARETDB1	k-NN, GMM, AdaBoost and SVM Classifiers	Specificity and Sensitivity
2015	Seoud <i>et al.</i> [98]	MESSIDOR	Random Forest Classifier	Area under ROC curve
2017	Zahoor, <i>et al.</i> [120]	MESSIDOR, DIARETDB1	Mathematical Morphology	Specificity and Sensitivity
2017	Dai <i>et al.</i> [121]	DIARETDB1	Image/Text Mapping, CNN	Recall and Precision
2017	Srivastava <i>et al.</i> [122]	MESSIDOR, DIARETDB1	Kernel Learning	ROC
2018	Orlando <i>et al.</i> [123]	MESSIDOR, DIARETDB1 and E-Ophtha	Deep Learning and CNN	Sensitivity
2018	Ram <i>et al.</i> [124]	DIARETDB1	Hybrid Algorithm, Clustering	Sensitivity and Accuracy
2018	Wahid <i>et al.</i> [125]	DIARETDB1, DIARETDB2	Fuzzy Logic	Specificity and Sensitivity
2020	Carmona <i>et al.</i> [126]	MESSIDOR, DIARETDB1	Evolutional Algorithms	Specificity and Sensitivity

From the conducted literature of various state of art lesion detection approaches, the MAs properties were observed equivalent to blood vessels in terms of color and intensity. This is the reason, many of the approaches mentioned in literature fails in identifying MAs closer to blood vessels. There exists few MAs which are blurred and small in size to be seen through naked eyes. Similarly, the problem of misclassification may arise in EXs detection in the presence of OD due to the similar intensity properties of EXs to that of OD. Thus, it is revealed that lesion discrimination approaches revealed that manifold possibilities lie in the improvement of lesion

discrimination approach for DR detection. After the evaluation of DR lesion detection approaches, it was observed that severity grading is important to track the disease progression. Some of the DR severity grading methods have been reviewed in the next section.

2.3 DIABETIC RETINOPATHY GRADING

Many studies are present in the literature to devise an automated severity grading system for DR detection at the initial stage. Some of the articles are reported in the following section.

Carrera, *et al.* [113] proposed a CAD system for NPDR retinal images grading by separating the blood vessels, exudates, microaneurysms features and grading it using SVM classifier. The method discussed presents better sensitivity and accurate predictive capacity with flexibility of adjusting parameters. Koh *et al.* [114] developed a retinal health observation system that differentiates the diseased fundus image from normal image. Their system uses correlated features and speeded up robust features for providing better severity grade outcomes using kNN classifier. Authors in [116] considers bright fundus image lesions for the classification of normal and abnormal lesions by designing a rule based classification scheme. The proposed system achieves better accuracy for the detection of bright lesion and at the same time it was observed that accurate DR classification is also achieved by considering dark lesions. An automated DR screening method using the concept of visual dictionaries was proposed by Rocha, *et al.* [105] for DR grading. Each image in this process was considered as a collection of regions where point of interest method with SURF extractor was implemented for feature extraction. SVM classifier was employed for anomaly detection in this case.

Akram, *et al.* [127] proposed a filter bank based exudates detection approach including three different stages. Initial stage includes image acquisition and pre-processing followed by OD elimination and EXs pathology detection using Gaussian Bayes Decision rule in the second stage. Feature set formulation along with exudates and non- exudates region classification is adopted in the third stage. Tjandrasa, *et al.* [128] provided a two-level DR severity classification system to grade for moderate

and severe NPDR classes using morphology based approach for EXs segmentation followed by soft margin SVM classifier for disease classification into different severity grades. In series of EXs detection, Akram, *et al.* [129] proposed another macular edema detection approach using the combination of GMM and SVM classifiers. This hybrid classifier improves exudates detection scheme by classifying the retinal images into three different categories: normal category, clinically significant macular edema category and non-clinically significant macular edema category. SVM and kNN classifier based MA and EX detection scheme was proposed by Lachure, *et al.* [112] that considers structural and GLCM feature vectors for classification. Better performance outcomes are achieved for SVM classifier over kNN using MESSIDOR dataset. A number of classifiers such as SVM, kNN, GMM and Adaboost are implemented for DR severity grading system in [25]. The authors in this article presented a better performance hierarchal classification method for the categorization of red lesion to MAs and HEMs and categorization of yellow lesion EXs and CWs. A PDR detection approach was given in [130] using ridge strength measurement and watershed line techniques. A feature set contains 15 different features comprising various attributes such as shape, position, contrast, and brightness was extracted for the classification of normal and abnormal retinal structures.

MA detection scheme using dark object filtering process was proposed by authors in [131] which uses singular spectrum analysis to process cross sectional candidate profiles. Better performance for DR screening was observed employing kNN classifier. Textural features were utilized in [132] for distinguishing healthy and pathological fundus images. Local binary pattern descriptor was employed in this technique for effective DR screening and diagnosis. Publically available dataset from UCI machine learning repository were used by Adekunle, *et al.* [133] for the implementation of DR diagnostic intelligent system for mass screening of DR severity. Feed forward neural network was trained using backpropagation algorithm to aid the physicians in accurate and trouble-free disease diagnosis comparative to the tedious manual computation. Authors in [134] provided an ensemble-based framework for reliability microaneurysms detection using a combination of pre-processing components and candidate extractors for DR and non-DR retinal structure classification. Antal and Hajdu [135] proposed two different diagnosis schemes for

pathological region analysis. Traditional image analysis criteria was used by one of the methods and the other approach deals with 7 pathological features for fundus image classification using statistical analysis approach and pattern classification. Image analysis based technique yields better specificity and sensitivity when compared to the other classification model. Dai, *et al.* [102] used an interleaved deep mining technique to overcome the constraints of existing methods that fails to address inter and intra class variations for MA detection. The objective comparison of various methods developed by the researchers for DR grading is presented in Table 2.3.

Table 2.3: Comparison of different DR grading approaches

Year	Author	Dataset Utilized	Methods Employed	Severity Grading Type
2006	Kahai <i>et al.</i> [136]	Local Database with 143 images	Decision Support System	NPDR
2008	Aptel <i>et al.</i> [137]	Local Database of 79 patients	Single field mydriatic and Three field mydriatic	PDR and NPDR
2010	Dupas <i>et al.</i> [138]	MESSIDOR	Analysis Algorithm for fundus images	NPDR
2014	Ashraf <i>et al.</i> [139]	DIARETDB1	SVM	NPDR
2017	Al-Jarrah <i>et al.</i> [140]	DIARETDB1	ANN	NPDR
2019	Harangi <i>et al.</i> [141]	IDRiD	CNN	DME and DR
2019	Wulandari <i>et al.</i> [142]	MESSIDOR	CNN	NPDR

It is revealed from the literature, that there are some of the challenges in the present work done in this field. The utilization of handcrafted features for DR grading does not show any significant performance improvement in tracking the DR progression. Also, the exploitation of small dataset does not yield satisfactory outcomes as the dataset size influences the machine learning algorithm performance.

2.4 DEEP LEARNING CLASSIFICATION

In the past many years, progress has been made in aiding automated DR diagnosis employing various methods. This subsection of literature review is summarized in two main portions; initially the related works done for automatic DR diagnosis using traditional machine learning based techniques. This is followed by some recent works

in the field of convolutional neural networks for DR severity grading and classification.

2.4.1 Machine Learning based Classification

Three major stages involved in traditional DR classification methods are; image processing, feature extraction and DR severity classification. These practices for automated diagnosis of retinopathy include a feature extraction module before undergoing a specific classification.

Several traditional machine learning methods for DR severity grading are explored in the literature. Eltanboly, *et al.* [143] developed an enhanced Computer Aided Diagnostic system for NPDR severity grading. The segmentation approach was utilized for the localization of 12 different retinal layers from the combination of size, intensity, and spatial information. Normal and DR mild/moderate grades are classified by training the deep fusion classification network. Kumar, *et al.* [144] proposed a CLEAR-DR system to provide clinical decision support to ophthalmologists. A three-phase DR detection and classification system was presented by Tariq, *et al.* [145] for various DR lesions such as MAs, HEMs, EXs and CWs. Lesion extraction was done using filter banks followed by lesion candidate feature extraction and lesion classification. Somasundaram *et al.* [146] presented a Machine Learning Bagging Ensemble Classification (ML-BEC) approach for early stage DR disease classification. This technique includes two phases: first phase comprises feature extraction followed by ensemble based classification in the second phase.

Srivastava *et al.* [147] presented a Frangi filter based method for the detection of red lesions, MAs and HEMs. Filter response yields the feature set, which was used for SVM classifier training in order to predict the presence of lesions. Random forest classifiers exploring shape based features were utilized by Seoud *et al.* [148, 98] for haemorrhages and MA detection indicative of DR severity levels. Sankar, *et al.* [149] proposed a method for classifying non-DR fundus images from mild, moderate and severe DR grades. A meta classification approach was proposed by authors in [150] for DR image recognition at the early stages. This approach is helpful for patient referral to provide immediate healthcare at hospitals using automated screening tool for remote communities. Authors in [151] evaluated various pre-processing methods for effectual MA detection from colored fundus images. The pre-processing

component reliability along with candidate extractors is confirmed for the classification of DR and non-DR retinal structures based on the MAs presence or absence. In the survey article [77], a survey based on the efficiency and accuracy of CAD systems using traditional and evolutionary approaches was conducted. It was found that evolutionary approaches play a vital role specially in pre-processing using enhancement filters, segmentation, dimensionality reduction, feature extraction, selection and DR classification. A deep mining technique for MA detection to overcome the limitations of existing methods was developed using hybrid interleaving concept for MA detection [102]. Rahim *et al.* [152] presented an automatic DR screening system for the early detection of MAs using fuzzy histogram based technique for pre-processing and feature extraction before severity classification. Poddar, *et al.* [153] developed a robust segmentation method for DR and maculopathy grading. Inter and intra image variability was removed using pre-processing steps followed by the segmentation of various part of retina like OD, fovea, MAs, EXs and HEMs. Concentric circular zones are used to classify the pattern and extent of abnormalities in diseased fundus images. An automated grading scheme was introduced by Fleming, *et al.* [154] to remove the shortcomings of human grading systems. They highlighted the importance of contrast normalization for improved capability to distinguish between other noise spots and MAs.

From this literature review it was revealed that the traditional machine learning approaches deploy various handcrafted feature extraction techniques in order to extract clinically relevant pathological features from the fundus images. Further these features are provided to specific classifiers. The handcraft features are limited and crafting of new effective features is difficult and often does not produce better results. This feature extraction-based procedure is laborious and can often lead to misclassification. The choice of appropriate handcrafted features requires validation of various parameter settings with prior expert knowledge. In the modern advent of medical science, Deep Neural Networks have replaced the machine learning based DR diagnosis systems by achieving considerable performance improvement.

2.4.2 Deep Neural Network based Classification

Deep Neural Network has developed as a latest advent to achieve innovative ideas in various fields, especially in medical sciences. Medical image analysis and

classification performance appeared as a breakthrough in technology with a novel bio-image based technique employing CNNs. Some of the techniques for DR classification using DNN approach are reported in the following section. Abbas *et al.* [155] presented a deep visual feature based automated CAD system for DR severity level classification without applying pre-processing steps. This methodology was based on multilayer semi supervised technique that combines the domain knowledge for red lesion detection and retinal images to classify the retinal fundus images using random forest classifier on the basis of severity scale. Wang *et al.* [156] introduced a deep learning technique that uses Regression Activation Maps (RAMs) next to pooling layer for providing better performance in terms of region of interest localization on the basis of severity level grading. Yu *et al.* [157] proposed an image quality classification method. This model attains both supervised and unsupervised features that were further subjected to SVM classifier. Deep Convolutional Neural Network (DCNN) models were implemented by Gao, *et al.* [158] for DR grading localization tested on self-built labeled dataset. Model deployment on the cloud platform was also performed to provide DR diagnostic services to hospitals. Gaussian mixture model was combined with visual geometry group network (VGGNet-19) by the authors in [159]. PCA and Singular value decomposition (SVD) feature selection tools were used at fully connected layers FC7 and FC8 to yield better classification accuracy.

Li *et al.* [160] presented a CNN based transfer learning model which yields better classification results using small dataset by fine-tuning the pre-trained model parameters. CNNs were used on colored fundus images for DR recognition by Lam *et al.* [161] to obtain better validation sensitivity. Pre-trained GoogleNet model yields accuracies of 74.5% for 2-ary, 68.8% for 3-ary and 57.2% for 4-ary classification methodology by employing histogram equalization and dataset fidelity. Yang, *et al.* [162] proposed a two-step deep convolutional neural network for DR severity grading and lesion detection. The similar performance was achieved in comparison to human observations of professional experts. Chandore and Asati [163] presented a system for detecting DR symptoms. The system achieves higher accuracy through dropout layer implementation utilizing large volume of dataset for training CNN model. Gulshan, *et al.* [164] presented an Inception-V3 based CNN scheme for multiple binary decision making to classify the DR severity grades into moderate and severe DR, Diabetic

macular edema and fully gradable DR. 10 layered convolutional network was proposed by M. Melinscak *et al.* [165] for the classification of DR and to obtain higher accuracy by making use of small image patches. Abramoff, *et al.* [166] utilized CNNs specialized on distinguishing normal retinal anatomies from those with haemorrhages, exudates, and neovascularization. It significantly outperforms the existing solutions for DR screening. A customized deep CNN based approach was introduced by Gargeya and Leng [167] for feature extraction to classify between non-DR stage and any stage of DR. The extracted CNN features were combined with retinal image metadata and significantly improved performance was seen using this combination. Quellec *et al.* [168] used a heatmap optimization procedure for CNN training to detect DR cases. Image level and lesion level classification was performed to distinguish hard exudates, soft exudates, small red dots, haemorrhages. Prasad *et al.* [169] introduced two-class categorization for detecting retinal blood vessels, exudates and microaneurysms. PCA based feature extraction and selection technique followed by back propagation in neural networks yields better performance. Du and Li [170] used a textural analysis technique followed by stage deep CNN severity level classification for haemorrhage identification and automatic DR analysis.

Gurudath *et al.* [171] used a three-stage classification for DR identification from colored retinal fundus images. Cao *et al.* [172] used Patch based microaneurysms detection approach employing three different classifiers; SVM, random forest and neural network for five stage DR severity grading. Dimensionality reduction is achieved via PCA and Random Forest Feature Importance (RFFI) to yield better performance. A computer vision system was designed by Nanni *et al.* [173] using a combination of handcrafted and non- handcrafted features. PCA, Compact Binary Descriptor (CBD) and CNN were used for extraction of non-handcrafted features. The extraction of handcrafted features was carried out through local phase quantization, rotated local binary patterns algorithms. Litjens *et al.* [174] used a Google Inception-V3 based DR assessment approach to obtain optimal image classification outcomes comparative to licensed ophthalmologist's grading. Alban and Gilligan [175] used various denoising approaches for retinal fundus image classification using a small dataset. CNN architecture for identification of complex features to classify microaneurysms, haemorrhages and exudates was suggested by Pratt *et al.* [176].

Mansour *et al.* [177] developed a CAD system using AlexNet deep neural network architecture and PCA dimensionality reduction. Their approach presents the classification of fundus images and accurate detection of diseased blood vessels based on severity levels. Goncalves, *et al.* [178] presented a comparative study between the classical machine learning and CNN based deep learning models. It was revealed that CNNs provides comparative performance to the highly trained human grading expert irrespective of the datasets used. The Inception-V3 CNN architecture utilized in this study provides 89% of model accuracy for EyePACS dataset and 81.6% for MESSIDOR dataset. Saranya and Prabakaran [179] provided a DR detection and grading employing CNNs along with the pre-processing and image resizing before providing them to the network. An accuracy rate of 90.9% was achieved for MESSIDOR dataset thereby providing a competent CNN based DR grading approach.

Despite of this literature survey, an objective contribution of several researchers in the field of CNN is tabulated in Table 2.4 to provide a clear comparison of the deep learning based DR classification approaches in terms of method employed, dataset utilized and various performance evaluation metrics involved.

Table 2.4: Comparison of deep convolutional neural network based DR classification approaches

Year	Author	Methods Employed	Dataset Utilized	SN	SP	Acc
2017	Masood, <i>et al.</i> [180]	Pre-trained CNN	EyePACS	-----	-----	48.2%
2017	Yang, <i>et al.</i> [162]	5 Layered CNN	MESSIDOR	97%	96%	96%
2017	Takahashi, <i>et al.</i> [181]	GoogleNet	Private	-----	-----	81%
2017	Ghosh, <i>et al.</i> [182]	CNN	MESSIDOR and EyePACS	94%	97%	96%
2018	Orlando, <i>et al.</i> [183]	Ensemble Approach	MESSIDOR	90%	91%	90%
2019	Zhang, <i>et al.</i> [184]	ResNet, DenseNet	Private	98.1%	98.9%	-----
2019	Yip, <i>et al.</i> [185]	Pre-trained CNN	Private	-----	-----	95.8%
2019	Gao, <i>et al.</i> [186]	Pre-trained CNN	Private	-----	-----	88.7%
2020	Saranya, <i>et al.</i> [179]	CNN	MESSIDOR and IDRiD	-----	96.3%	90.9%

High clinical relevance of DR classification for better interpretation has led to the development of automated DR diagnosis systems. The workload on ophthalmologists is managed by adopting automated disease diagnosis techniques for referable

retinopathy identification and management of the patients requiring critical ophthalmic care along with specialized treatment. Manual grading systems have been surpassed by neural network (NN) based architecture in many applications. CNN model uses a large amount of training data thus ensuring proper learning for task specific applications providing proper convergence without overfitting. CNN has performed revolutionary for various image classification tasks, and thus is being exploited for DR diagnosis systems. The early DR detection prevents visual loss by enabling medication or laser therapy for the treatment of severe eye diseases beforehand.

The comprehensive literature survey done in this work emphasized some pros and cons of the existing state-of-the-art work in DR diagnosis domain. The review of various blood vessel segmentation approaches revealed that the manual blood vessel tracing systems are time-consuming and may lead to inaccuracy due to blood vessel disparities and poor image contrast, so automatic vessel segmentation is required. The literature survey of various state-of-the-art lesion detection and severity grading approaches unveiled that lesion misclassification may arise due to the presence of similar retinal anatomical structures. The existing DR severity grading schemes deploys handcrafted feature extraction techniques which are laborious, require human expertise and can often lead to misclassification. Thus, this literature survey supports the background of the research and all these shortcomings of the existing approaches provides the motivation for this research work. The requirement of a specialized and computer assisted DR progression facility to aid the ophthalmologists in taking necessary corrective measures before the irreversible blindness, is the main motivation behind this study. The aim of this work is to provide a computer-based automated DR diagnostic system overcoming the limitations of other existing approaches.

The exhaustive literature survey of various DR detection and severity grading approaches carried out in this work leads to the formulation of the following research gaps.

Research Gap 1: Retinal Physiological Structure Extraction

Research Gap 2: Development of an efficient Lesion Discrimination Approach

Research Gap 3: Diagnostic Relevance of DR severity grading

Research Gap 4: Need for Deep Learning based DR Diagnostic system

This research work aims at addressing these research gaps by framing the objectives listed below.

Objective I: Design of an Automated Retinal Blood Vasculature Segmentation Model for Diabetic Retinopathy Detection

Objective II: Developing a Hybrid Lesion Detection Technique for DR Abnormality Discrimination

Objective III: Implementation of a Robust Framework for DR Categorization

Objective IV: Inception of Ensembled Transfer Learning Model for DR Severity Grading

To achieve these objectives, a computational framework has been developed which is depicted in Figure 2.2 and the extensive work done in this research is elaborated in the upcoming chapters of the thesis.

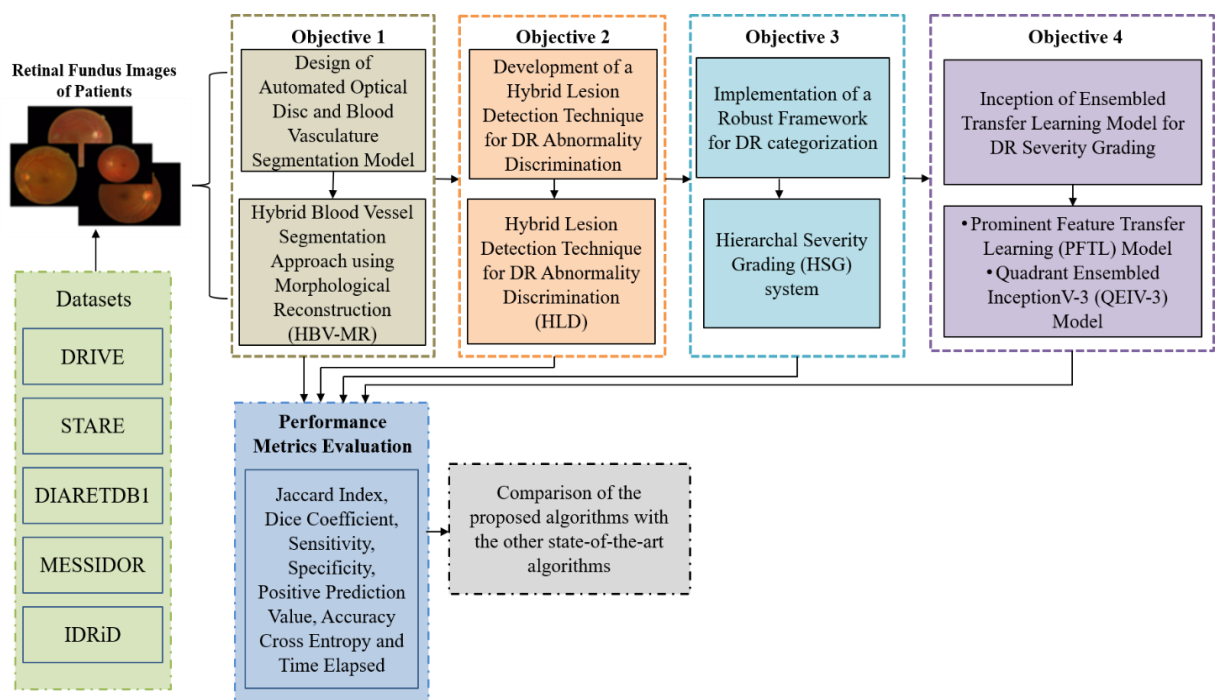


Figure 2.2: The computational framework for DR severity grading

The research methodology of this thesis is divided into four different stages based on the four objectives framed for this work.

CHAPTER 3

**RETINAL BLOOD
VASCULATURE SEGMENTATION
FRAMEWORK**

CHAPTER 3

RETINAL BLOOD VASCULATURE SEGMENTATION FRAMEWORK

3.1 INTRODUCTION

The eye examination is beneficial in mitigating various health concerns including diabetes, hypertension, strokes, occlusion, and many more. According to the statistical analysis done by the International Diabetic Federation (IDF), there are 10 million adults suffering from diabetes and most of them are undiagnosed [6]. In the modern era, retinal vascular analysis methods are widely being used for eye-related complexities like cardiovascular strokes [5], glaucoma, hypertension, and Diabetic Retinopathy, etc. This persistent situation of diabetes arises many other severities, out of which DR is the most common. Patients having prolonged diabetic conditions develop DR, which is a severe eye complication that arises due to change in retinal blood vessels of a diabetic patient. Fundus image analysis is appropriate for inspecting the symptoms of DR and determines the severity grades of pathologies affecting the eye. To reduce the chances of vision loss upto a large extent, regular screening and diagnosis are important, although it requires precise retinal landmark localization and segmentation. High resolution fundus images are useful in disease diagnosis to the ophthalmologists for extraction of various anatomical structures like Blood Vessels, Optical Disc, and Macula [15].

The segmentation of retinal blood vessels, Optical Disc (OD) and other anatomical structures plays a critically important role in the detection of pathological symptoms for DR diagnosis. The brightest portion in retinal fundus image is OD and the entry point of retinal blood vessels and these blood vessels supply blood and nutrition to the eye. For the diagnostic purpose, it is essential to extract OD and blood vessel portions in order to reduce the fallacious detection of pathological symptoms have feature similarity with these physiological landmarks. Image segmentation approaches prove helpful in the removal of retinal anatomical landmarks from the retinal fundus image.

Segmentation yields a set of different image sub-regions that are similar in respect of image pixel characteristics like intensity, color or texture. The different methods of image segmentation are based upon;

- i. Intensity level discontinuity-based region boundary localization
- ii. Threshold based discrimination considering the pixel property distribution
- iii. Direct region identification

However, the adoption of particular image segmentation technique is purely based upon the problem being considered. For this particular application, the intensity level discontinuity-based region boundary localization approach has been adopted as the anatomical landmarks have discontinuous pixel properties.

3.1.1 Retinal Landmark Segmentation

The process of finding out the OD center and localizing the boundary of optical disc portion is known as OD localization. It distinguishes the brightest portion from the other retinal structures for its effectual segmentation from the retinal fundus image. Figure 3.1 depicts retinal fundus image with manually marked OD center and localization of optical disc segment.

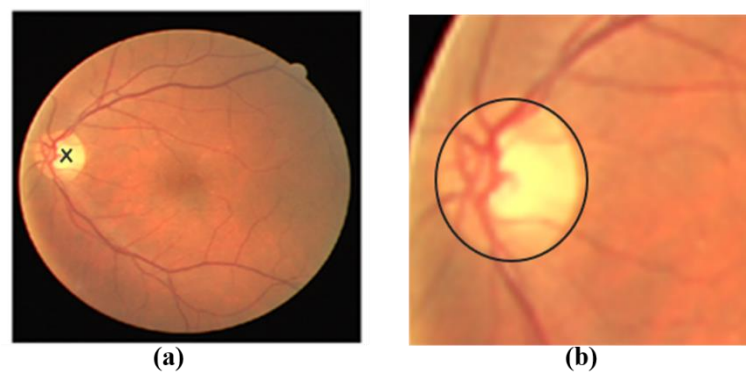


Figure 3.1: (a) Manually marked OD center (b) OD boundary localization

Automated DR lesions detection merely relies on effective segmentation and removal of OD which may hamper the accurate detection of bright lesions like EXs and CWs [14, 15]. OD localization is essential to differentiate it from the other retinal features and observe the changes in OD structure resulting from the disease. However, OD localization possess several challenges due to poor contrast quality of fundus

image and inadequate illumination. A very limited work has been stated in the literature for addressing the identification of exact OD boundaries, as it has blurred edges [82, 83]. This enabled us to address these limitations in order to enhance OD localization methods.

Another retinal landmark required to be segmented for effective DR diagnosis is blood vasculature. The retinal vessels which cover the most of the part of retina, present in the retinal image plays an important role for diagnosing eye related complications. The technique of separating the blood vessels from the retina area in fundus image photography is termed as retinal vasculature segmentation. There are various factors that complicate the process of retinal vessel segmentation such as poor contrast discrimination between the background and blood vasculatures, presence of background noise, varying inadequate illumination, varying contrast features across the fundus image as well as the presence of pathological symptoms [14-16]. These factors may hamper the outcomes obtained using various blood vessel segmentation techniques. The blood vessels separation is very challenging because of disparity in the vessel width. Also, different blood vessel segmentation approaches yield different results and variation in results can be encountered even with the same approach applied on different images.

In blood vasculature segmentations, the blood vessels are considered as white pixels with logic 1 whereas the retinal background pixels are considered as black colored pixels with logic 0 and vice versa. Figure 3.2 represents an image of retinal fundus binary vascular map labelled by ophthalmic experts.

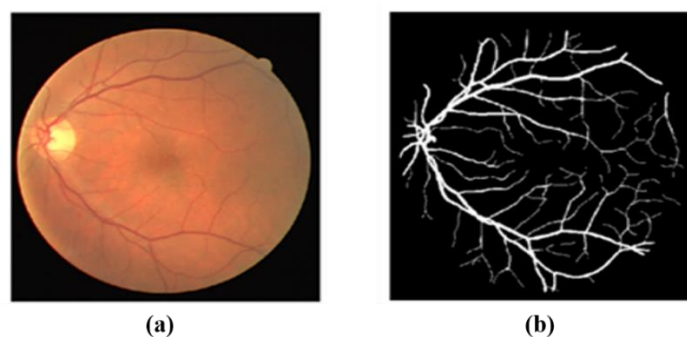


Figure 3.2: (a) Colored retinal fundus image (b) Manually labelled blood vessels

Retinal blood vasculature detection is significant for the identification of retinal field of view, identification of the geometrical relationships between various vasculatures and reduced detection of false lesion having similar properties as that of blood vessel. Due to the discontinuities presents in blood vasculatures, the main approaches for blood vessel segmentation utilizes edge detection and morphological operations because of the simple implementation and accurate extraction.

The most of the image information is enclosed in the boundaries or edges of the image. Thus, boundaries are detected from the image and these discontinuities are enhanced in the image to depict edge information. The image interpretation by a significant reduced data representation, only indicating the sharp boundaries or discontinuities is termed as edge detection. Edges signify the local intensity changes in the image that specifically occurs at different regions in the image. Only the important image information is retrieved and redundant and irrelevant information is discarded using this process. The major steps determining the edge detection process are image smoothing, image enhancement, edge detection and localization [63].

There are various edge detectors such as Laplacian of Gaussian (LoG) and Prewitt Edge detectors, Marr-Hildreth, Robinson and Robert edge detectors, Kirsch, Sobel, and Canny edge detectors. The Robert edge detector computes fast and simpler 2D spatial image measurements by highlighting the high spatial frequency regions. Sobel edge detector finds the edges using derivative approximation and the highest gradient points with maximum spatial frequency are indicated as edges. Prewitt edge detector estimates the edge orientation and magnitude different directions using the highest kernel response. Kirsch edge detector approach is a simpler using mask rotating in the eight compass directions to produce the edges. The magnitude and direction of an edge is examined by the maximum outcome obtained by convolving the mask with image. Robinson edge detector utilizes a symmetrical mask, therefore, the output of first four masks provides the results of other four by negating the outcomes obtained from convolving the image with the initial four masks. Marr-Hildreth edge detector is useful for determining the edges in the digital image with higher variations and image brightness properties. The LoG edge detection approach utilizes the second order derivative of image to locate the zero crossing points as edges. Canny edge detector removes the unwanted noise before edge detection without disrupting the edge features.

This work utilizes Kirsch edge detector due to its simpler implementation and less computational complexity comparative to other edge detection approaches.

Apart from edge detection, another approach for boundary and image attribute extraction is morphology based segmentation. It is suitable for the removal of image imperfections affecting the image shape and texture. Morphological operation performs image segmentation by directly dealing with the extraction of shapes from the image using a structuring element. Structuring element used to define pixel connectivity has varying shape and is used to explore the image properties. Appropriate structuring element is chosen to obtain accurate image details. Morphological dilation operation allows to thicken an object and the extent of its thickness is determined by the structuring element. Dilation is referred as addition of pixels to the boundary elements for object boundary growth. Erosion morphological operation is the complement of dilation operation as it shrinks the object boundaries in a binary image. Erosion operation removes the image structures having smaller size than of structuring element and therefore used to eradicate noisy links between any two objects in the image. Opening operation can be defined as the combination of erosion and dilation to smooth the object outline removing the minor extensions present in the image. Closing morphological operation differs from the opening operation in the order of sequence of dilation and erosion process. This morphological operation blends the small breaks and gaps in the image, smoothing its contours. It eliminates the minute holes in the image by filling the gaps in the object boundaries [19, 20].

Morphological operations are useful in various applications like object boundary extraction, connected component extraction, filling of holes in an image, image thickening and thinning, etc. Properties of retinal vascular structures have become an essential area of research nowadays for the proficient treatment of ophthalmic disorders, exploitation of morphological operations [19]. In this application, morphological operations are used for finding the optical disc boundary and for blood vasculature localization followed by the connected component extraction for locating the actual blood vessels out from a fundus image.

In the literature review, although various OD localization and blood vessel segmentation methods are reported, but these methods do possess certain limitations in

precise identification of OD boundaries and blood vessel. Blood vessel segmentation proves advantageous for determining the branching pattern of blood vessels, their width, density, retinal vessel variability, etc. [15, 16]. Automated vessel segmentation is beneficial for ophthalmologists as manual blood vessel tracing system is time-consuming and erroneous task. Certain small blood vessels having low contrast are not segmented and as per the author's knowledge, existing methods are not able to address problems of OD localization and blood vessel segmentation.

The work done in this research aims at addressing the shortcomings of the existing techniques for enhancement of OD localization and blood vessel segmentation method. The aim of this chapter is to improve the retinal physiological portion segmentation while maintaining a trade-off with computational complexity.

3.2 OD LOCALIZATION AND BLOOD VASCULATURE SEGMENTATION

The OD localization and blood vessel segmentation methodology adopted for achieving better accuracy along with the least complexity employs a three-fold implementation strategy depicted in Figure 3.3.

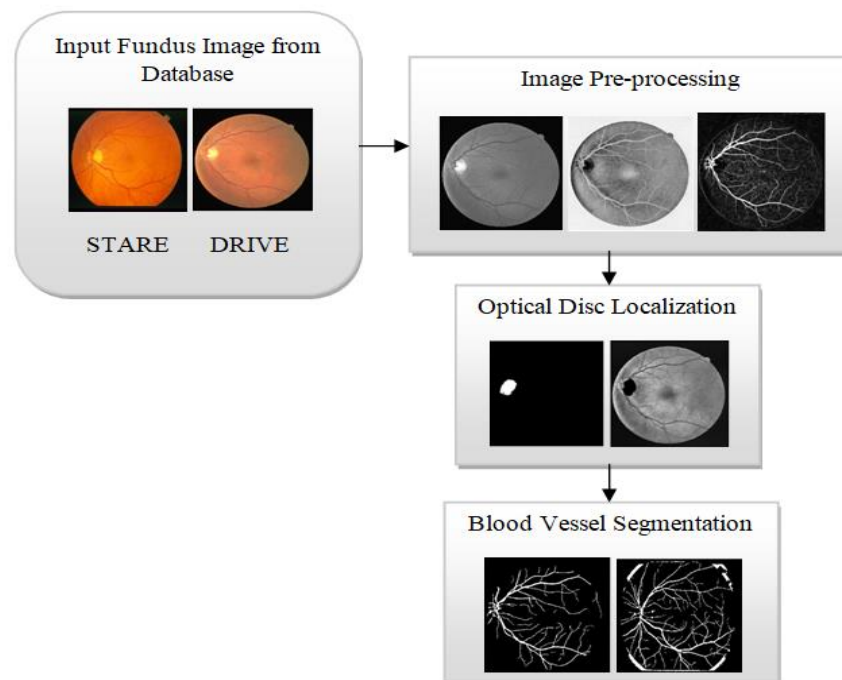


Figure 3.3: Flowchart of OD localization and blood vasculature segmentation

The input images attained from the dataset are pre-processed in the initial stage for removing raw fundus image artefacts. OD localization is performed in the second stage utilizing Circular Hough Transform and morphological operations for boundary localization. Vessel structure estimation is carried out in the third stage for blood vasculature segmentation. The experimental implementation of OD localization and blood vessel segmentation algorithms is carried out for benchmark DRIVE [40] and STARE [41] datasets and various stages adopted are discussed in following sections.

3.2.1 Fundus Image Pre-processing

Raw fundus images cannot be directly used for ophthalmic image processing as they have imperfections, errors, and are prone to noise. The inter and intra pixel variability in the image happens due to numerous reasons like dissimilar iris color of different individuals, varying skin pigmentation, poor positioning of lens, poor camera contrast, etc. These fundus image variations can impede the performance of DR abnormality detection. Image pre-processing suppresses the unwanted image variation without destroying the actual image information. The different image pre-processing steps involved in this work is depicted in Figure 3.4.

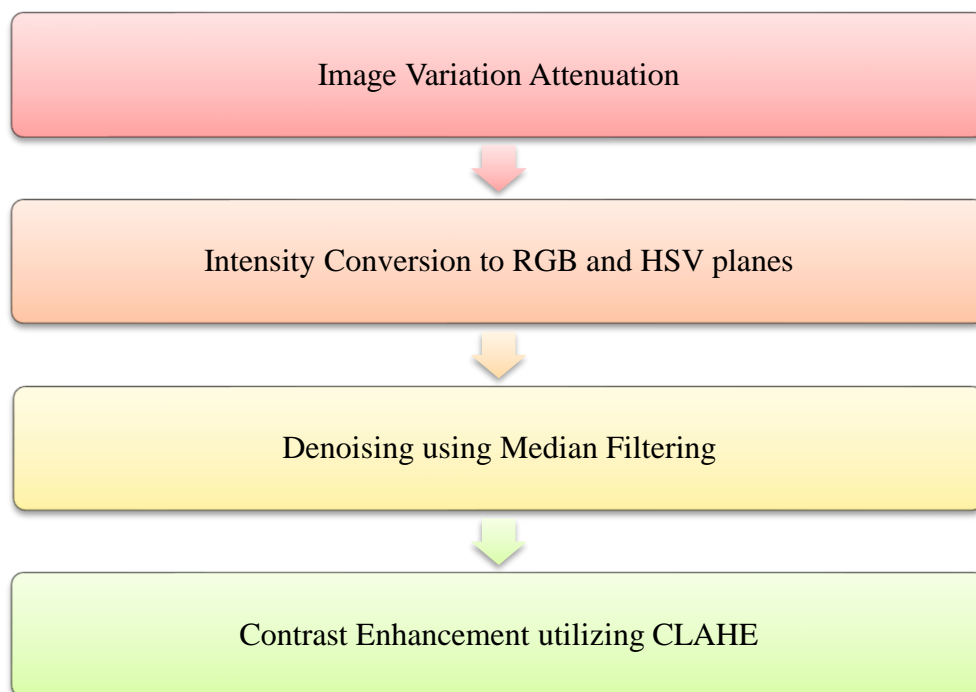


Figure 3.4: Block diagram of image pre-processing steps

- i. Image Variation Attenuation:** It is an image normalization step to eradicate the background pigmentation variation between the retinal structures of different individuals [19, 65]. The fundus image variation methods adopted in this work removes the change in illumination by modelling the colors of fundus image $I(x,y)$ over the mean value of every channel given by Eq. (3.1).

$$\begin{aligned} R_{xi} &= \min \left\{ \frac{R_x}{\text{mean}(R)} \times 255 \right\} \\ G_{xi} &= \min \left\{ \frac{G_x}{\text{mean}(G)} \times 255 \right\} \\ B_{xi} &= \min \left\{ \frac{B_x}{\text{mean}(B)} \times 255 \right\} \end{aligned} \quad (3.1)$$

where R_x , G_x , B_x corresponds to each pixel value in the corresponding channel, R_{xi} , G_{xi} , B_{xi} corresponds to each new pixel value after normalization and RGB values represents the component of red, green and blue channels of fundus image. The output color normalized image ($I(i,j)$) is a combination of (R_{xi} , G_{xi} , B_{xi}) channels.

Differing from other medical domain images, fundus images contain three different channels; red, green and blue, moreover, only a single channel is used for the further processing.

- ii. Intensity Conversion:** The intensity conversion includes segmentation of the green channel from retinal fundus image as it has maximum intensity providing the highest contrast between background and foreground retinal structures. On the contrary, the blue channel is the darkest possessing under-illuminated noisy components and the red channel is oversaturated with lower contrast. So, this work is restricted to the usage of the green channel for further image processing stages of retinal fundus images. All the pathological and physiological regions are evidently visible in green channel comparative to the other two channels of retinal images [65]. The RGB components of the retinal image are converted to Hue, Saturation and Value (HSV) model to extract only the intensity values utilizing the ‘V’ plane for the localization of bright anatomical portions.
- iii. Denoising using Median Filtering:** Retinal fundus images comprises of noise due to inadequate light illumination, sensor temperature and difference of CCD

cameras. Image denoising plays an important role in removing these artefacts from the image. Median image denoising filter replaces each of the pixel with the median value of its neighbourhood, thereby suppressing the isolated noise without blurring the edge information [187]. Thus, making it an appropriate choice for distinction between the legitimate image features and the isolated noise components. The image denoising step using the median filter is expressed by Eq. (3.2).

$$I'(m, n) = \text{median} \{I[i, j]\} \quad , (i, j) \in w \quad (3.2)$$

where $I[i, j]$ is the input intensity converted image to the filter, $I'(m, n)$ is output median filtered image and w signifies the neighbourhood centered around $[m, n]$ locations in the fundus image.

- iv. Contrast Enhancement:** The characteristics of contrast vary across the fundus image making the conventional histogram equalization technique less effective. The contrast of retinal fundus image varies and characterizes higher contrast at center of image and lower contrast at image boundaries. A Contrast Limited Adaptive Histogram Equalization (CLAHE) approach is employed for addressing the varying contrast characteristics and it provides an efficient contrast enhancement without noise amplification. CLAHE contrast enhancement approach operates on smaller data regions unlike other approaches operating on the entire image [187, 188]. The normalized histogram of the original fundus image, which is represented by integer pixel intensities matrix ranges from 0 to $L-1$, is denoted by p_n in Eq. (3.3).

$$p_n = \frac{\text{number of pixels with intensity } n}{\text{Total number of pixels}}, \text{ for } n = 0, 1, \dots, L-1 \quad (3.3)$$

Thus, histogram equalization of the image is represented by Eq. (3.4).

$$f_{i,j} = \text{floor} \left((L-1) \sum_{n=0}^{f_{i,j}} p_n \right) \quad (3.4)$$

where floor function sets the output to its nearest possible integer value by rounding off the value.

The experimental results obtained for retinal image pre-processing are depicted and discussed in section 3.3.1 of this chapter.

After retinal fundus pre-processing, elimination of two pathological structures; Optical Disc and Blood Vessels segmentation from retinal fundus images plays a significant role in severity assessment of pathological retinal portions. Retinal components like OD and blood vessels are the background portions and therefore, removed from retinal fundus images employing the approaches discussed in the following sections.

3.2.2 Optical Disc Localization

The correct diagnosis of the yellow DR lesions (EXs) requires the exact position of the optical disc as it may be wrongly diagnosed as a lesion [15]. The factors hampering OD identification are different FOV of dissimilar fundus images, poor illumination, and increased number of abnormalities. In this work, two OD localization approaches have been adopted: one employing Mathematical Morphology and the other using Circular Hough Transform for OD localization.

3.2.2.1 Mathematical Morphology based OD Localization

OD localization is carried out in two-step involving a pre-processing stage followed by boundary localization. In the pre-processing stage, RGB components are converted to HSV (Hue, Saturation and Value) model to extract the intensity values of the entire image. OD boundary localization is accomplished by mathematical morphology closing operation [15]. The optical disc localization algorithm adopted in this work is based on morphological operations and it is explained in Algorithm 1.

Algorithm 1: Mathematical Morphology based Optical Disc Localization

Input: Input RGB Fundus Image [I_rgb]

Output: Output Image after optical disc removal [OD_seg]

START

Step 1: Separate the RGB channels into HSV color plane extracting the intensity value ‘V’ utilizing the HSV model.

Step 2: Apply pre-processing steps (denoising and contrast enhancement) were applied on ‘V’ plane to extract intensity values.

Step 3: Apply morphological closing operation, a combination of dilation and erosion utilizing disc structuring element [15].

Image A dilation with structuring element B is given by;

$A \oplus B = \{z | (\hat{B})_z \cap A \neq \varphi\}$ Set of all points z obtained by intersection of $(\hat{B})_z$ with A .

Image A erosion with structuring element B is given by;

$A \ominus B = \{z | (B)_z \cap A^c \neq \varphi\}$ Set of all points z obtained by intersection of $(B)_z$ with A 's complement.

Closing operation is given by dilation followed by erosion;

$$A \cdot B = (A \oplus B) \ominus B$$

Step 4: In the intensity plane, the largest circular region is found after contour filling.

Step 5: The region of maximum area is indicated as the OD segment.

Step 6: The complemented image of OD segment $(I_{OD})^c$ is superimposed on the original fundus image to obtain the OD removed fundus image ‘OD_seg’.

$$OD_{seg} = I - (I_{OD})^c$$

END

With this algorithm, the optical disc is localized from the retinal fundus image, however, exact circular boundaries of optical disc portion are not located. Thus, further this algorithm is modified employing Circular Hough Transform for extracting circular region from fundus image.

3.2.2.2 Circular Hough Transform based OD Localization

Circular Hough Transform based OD localization method involves pre-processing stages to extract the intensity values from the ‘V’ plane of HSV color model. This plane is further subjected to denoising and CLAHE for local contrast enhancement

followed by optical disc localization. Morphological closing operation is implemented and contours/gaps are also filled, for discovering the largest circular region out of the intensity plane. The region of the maximum area is specified as the optical disc segment. The flowchart of Circular Hough Transform based OD Localization approach is given in Figure 3.5.

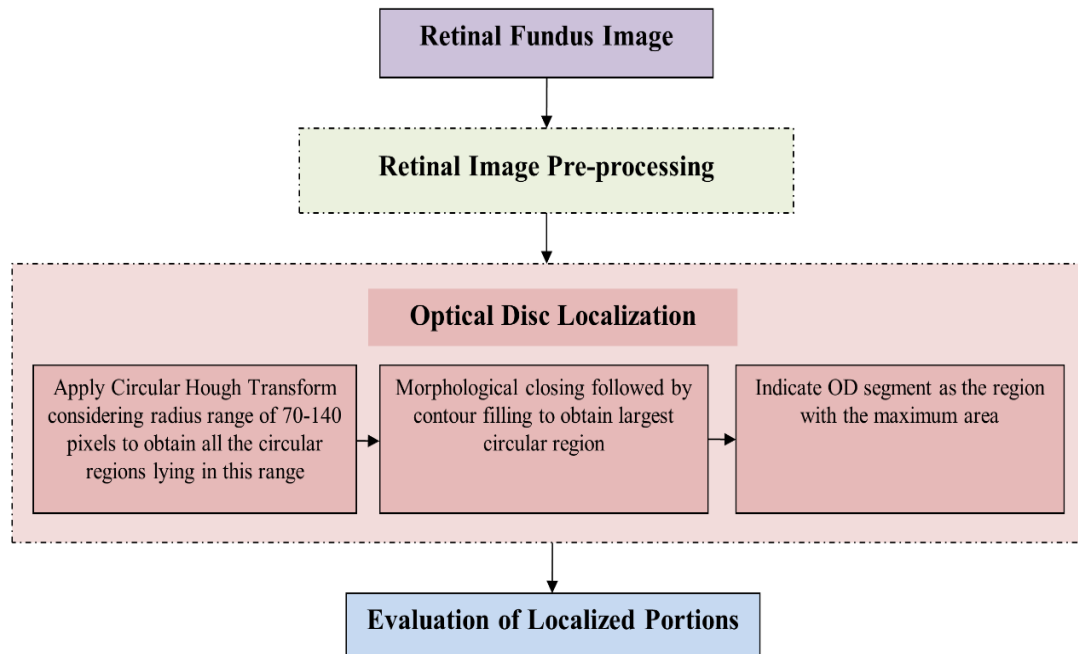


Figure 3.5: Flowchart of Circular Hough Transform based OD localization

Circular Hough Transform: The Circular Hough Transform is utilized for determining circular objects present in an image using the equation of center of circle expressed in Eq. (3.5).

$$(x_i - a)^2 + (y_i - b)^2 = r^2 \quad (3.5)$$

where x_i and y_i are the current pixel positions, a and b represents the center coordinates of the circle and r signifies the radius of the circle.

This is derived from the basic Hough transform which transforms the image into a parameter space constructed to identify a particular shape object [189]. The parameter space is 3D and thus, the three parameters used to define the shape are accumulator, center and radius. For a specific feature point, the votes are collected in the accumulator space using all the parameter combinations. Each of these points

contributes a circular region of radius r to the accumulator space until it reaches the peak where these contributing circles overlap at the center of the original circle [189, 190].

To avoid the false OD detection, the OD localization method is optimized by applying the combination of Circular Hough Transform and morphological closing only considering the circles providing strong circular response. These strong circular response circles are the once corresponding to the OD portions while the other are yellow lesions or some other misleading portions. The results of intermediate OD localization process are provided in section 3.3.2.

OD localization process is followed by the blood vasculature segmentation approach based on mathematical morphology operations.

3.2.3 Blood Vasculature Segmentation

OD segmentation is followed by blood vasculature segmentation approaches; modification in the existing Kirsch's Edge Detection method and implementation of Fuzzy Inference based Blood Vessel Segmentation Approach.

3.2.3.1 Modified Kirsch's Edge Detection

Kirsch's edge detection method identified the points of discontinuity in an image by calculating the intensity difference between all the neighbourhood pixels in the eight compass directions. The magnitude of the intensity difference between the pixels represents an edge or a background depending upon the empirically selected threshold. The Kirsch's edge detection method is modified by implementing post-processing technique for removing the false edges indicated as blood vessels. This step involves denoising and edge enhancement step that yields truly extracted blood vessels by removing the fallacious edge segments. The sequential steps for Modified Kirsch's Edge Detection are provided in Algorithm 2.

Algorithm 2: Modified Kirsch's Edge Detection Method for Blood Vessel Extraction

Input: OD Segmented Image

Output: Blood Vessel Extracted Image

START

Step 1: The pixel intensity information is obtained in the neighbourhood of a particular pixel in the original image $I(x, y)$.

Step 2: A 3×3 kernel mask rotating in 45 degrees increments through all the 8 compass directions (east, west, south, north, northeast, southwest, northwest and southeast) forming eight 3×3 Kirsch's templates is considered [191].

Step 3: Identify the pixel values to get frequent and abrupt changes using the Kirsch's templates.

Step 4: To fine tune the output blood vessel extracted image, a threshold T is selected empirically.

Step 5: The output of edge detection produces an image containing grey pixel values of range 0 or 255.

$I(x, y) > T$; indicates an edge (grey level 255 (white color))

$I(x, y) < T$; indicates background (grey level 0 (Black color))

Step 6: Apply post-processing to remove the fallaciously detected edges.

END

For Modified Kirsch's Edge Detection Approach, the Kirsch template is exploited which is rotated in 8 compass directions at an angle of 45° each in an anticlockwise manner. By convolving the eight directional Kirsch's templates with each pixel of the image, image gradients are obtained. Image gradients are indicative of edges or boundaries. The gradients obtained in all the 8 compass directions are then summed up to obtain the blood vessels [191]. A threshold value is selected empirically and if the difference between the pixel and its

neighbourhood is higher than threshold value, it points towards an edge otherwise it is indicated as background.

Conventional edge detection approaches are decent for fixed edge thickness applications but it is challenging for them to address the varying thickness of blood vessels. For this reason fuzzy inference based blood vessel segmentation approach is implemented for our application.

3.2.3.2 Fuzzy Inference based Blood Vessel Segmentation

The Fuzzy Inference based Blood Vessel Segmentation may prove advantageous for edge detection purpose unlike the classical edge detection techniques as the fuzzy approach deals with uncertainty in the information [192]. In this work, it optimizes the edge information from the given input fundus images to provide the output using fuzzy logic. The algorithm of Fuzzy inference-based blood segmentation approach is provided in this section.

Algorithm 3: Fuzzy Inference based Blood Vessel Segmentation

Input: OD segmented image

Output: Blood vessel segmented image

START

Step 1: Take input image and normalize it using a scaling factor.

Step 2: Image gradients are obtained in x and y direction by applying convolution.

Step3: A fuzzy inference system is defined for blood vessel segmentation and specifying the Gaussian membership function [192].

Step 4: Evaluate the output of the blood vessel segmentation for each row of pixels in $I(x, y)$ using corresponding rows as I_x gradient of image towards x direction and I_y gradient of image towards y direction specified as follows;

$$I(x, y) = \text{white for } I_x = 0 \text{ and } I_y = 0 \text{ ; indicating the background}$$

$$I(x, y) = \text{black for } I_x \neq 0 \text{ and } I_y \neq 0 \text{ ; indicating an edge}$$

END

Retinal fundus image is normalized and fuzzy inference is drawn specifying the Gaussian membership function. Gaussian membership function is utilized in this algorithm due to its symmetric nature. Blood vessels are extracted by parsing fuzzy rule, that compares the pixels in each row of the image with the corresponding row of image gradients I_x and I_y in x and y directions respectively. Precise segmentation of retinal structures that comprises blood vessels, optical disc, and other lesions affects the diagnostic ability and accuracy which consecutively affect the clinical treatment [14, 15]. Thus, we proposed a Hybrid blood vessel segmentation approach for accurate extraction of retinal blood vessels.

3.3 PROPOSED HYBRID BLOOD VESSEL SEGMENTATION

A three-fold blood vessel segmentation approach is realized in this work consisting of pre-processing steps followed by vessel structure estimation along with post-processing steps. The flowchart of the proposed Hybrid Blood Vessel segmentation approach using Morphological Reconstruction (HBV-MR) is depicted in Figure 3.6.

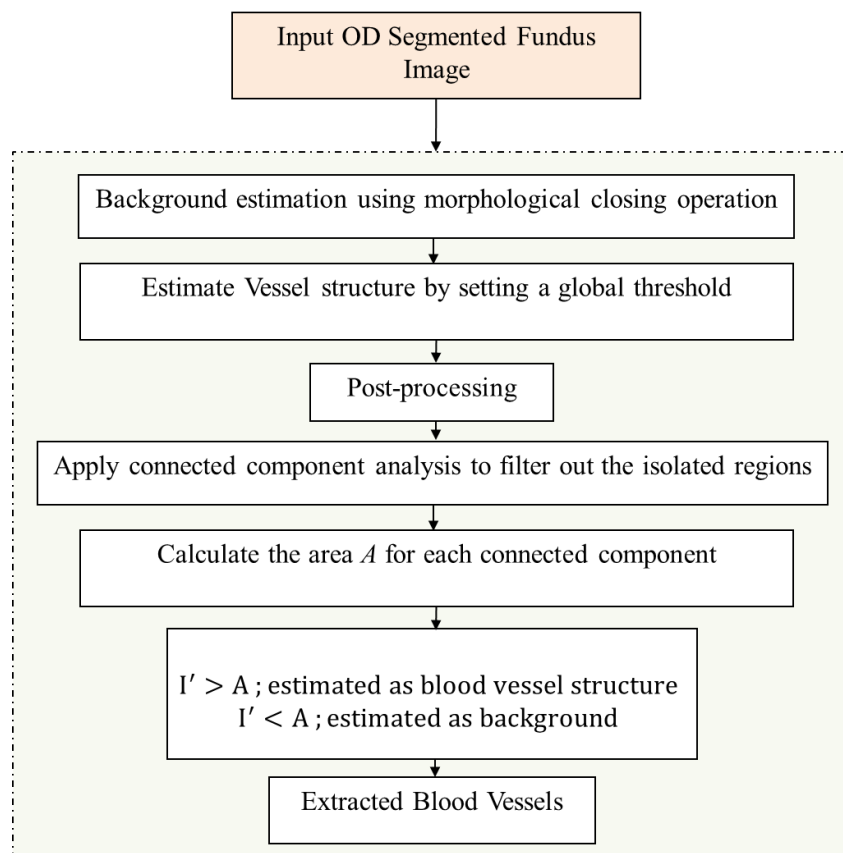


Figure 3.6: Flowchart of the proposed HBV-MR approach

In the proposed HBV-MR approach, retinal image background estimation involves pre-processing steps to suppress the dark image details smaller than the structuring element. Subsequently, background estimation is performed followed by blood vessel estimation and post-processing steps [15]. Vessel structure is estimated by considering a global threshold value after finding the absolute difference among the original image and estimated retinal background. Connected component analysis is used to label the fundus image into different image components depending upon the pixel connectivity (8 connectivity is used). The area of each connected component is the deciding factor for indicating the pixel as a blood vessel or a background. The algorithm of the proposed HBV-MR is explained in Algorithm 4.

Algorithm 4: Proposed HBV-MR Approach

Input: OD Segmented Image

Output: Blood Vessel Segmented Image

START

Step 1: Estimate the retinal fundus image background using morphological closing operation.

Step 2: Subtract the pre-processed fundus image from the estimated background retinal image using morphological closing operation [15].

Step 3: Perform vessel structure estimation by considering a global threshold.

Step 4: Apply post-processing for denoising and contrast enhancement at the estimated vessel structure.

Step 5: Filter out the isolated regions which do not belong to the vascular structure using connected component analysis [15].

Step 6: Final output vessel image is obtained by calculating the area A for each connected component and the condition used is stated as;

$I' > A$; estimated as blood vessel structure

$I' < A$; estimated as background

Step 7: Apply post-processing to remove the fallaciously detected edges.

END

As some isolated background noise is enhanced using the estimation and may lead to misclassification of blood vessel by hampering the localization of exact vessel pixel location. To address this problem, the HBV-MR approach involved post processing step for efficient blood vessel segmentation. Morphological operations along with median filtering and contrast enhancement are applied as post processing steps to remove the fallacious isolated pixels for effectual blood vessel segmentation.

3.3.1 Feature Attribute Selection for Blood Vessel Segmentations

Feature attribute extraction and selection is important after executing pre-processing and retinal landmark segmentation as it helps in accurate description of images in a manageable way. Feature reliability is indicative of better segmentation accuracy; therefore, three diverse feature sets are utilized based on the literature survey and relevance of these features for blood vessel segmentation [20]. A wide range of features comprising shape, pixel intensity, and fractal dimension features were explored from the extracted segmentations. The first set of features includes shape features like blood vessel area, perimeter, eccentricity, major and minor axis length, convex area, orientation, equivalent diameter, solidity, extend and compactness of extracted retinal structures [21, 22]. The second set of features contain pixel-based in intensity features like minimum, maximum intensity, mean, median, standard deviation, skewness and kurtosis are utilized for differentiating the vessel pixels from neighbouring background pixels [22, 23]. The third set of features include fractal dimensional features such as box counting dimensions, information dimensions and correlation dimensions, depictive of self-similarity between the extracted and ground truth blood vessels [193]. The details of these feature sets are given in the Appendix 1.

For the visual representation of the feature sets, box plots are used to represent the statistical data as a rectangular box of quartiles. Box plots visually assess the features in terms of its quartile ranges and outliers for the extracted blood vessel features. Shapiro-Wilk test and Kolmogorov-Smirnov test are used to compare the numerical significant values of the feature sets with standard normal distribution range. The relevant features are selected using Levene's f -test and t -test from SPSS tool detailed in Appendix 2 [194]. Equality of variance is determined using Levene's test commonly known as f -test and equality of means is inferred from t -test. Levene's test provides statistical evidence for estimating whether the variances among two samples are

approximately equal or not. The assumption of homogeneity of variance for Levene's test begins with a null hypothesis (H_0) stated in Eq. (3.6).

$$H_0: \sigma_0 = \sigma_1 \quad (3.6)$$

Null hypothesis rejection (H_1) states that there exists no homogeneity between the variances of the extracted blood vasculature features and this is expressed in Eq. (3.7).

$$H_0: \sigma_0 \neq \sigma_1 \quad (3.7)$$

When the significance value of test is higher than 0.05 then null hypothesis is accepted, otherwise the hypothesis is rejected.

Statistical hypothesis t -test is based on the null hypothesis (H_0'). It states that there is no such significant difference among mean values of the derived feature set and it is expressed in Eq. (3.8). Null hypothesis rejection (H_1') states that there is a substantial difference among means and it is expressed in Eq. (3.9).

$$H_0': \mu_0 = \mu_1 \quad (3.8)$$

$$H_1': \mu_0 \neq \mu_1 \quad (3.9)$$

Descriptives of the derived features are observed by using hypothesis testing to select the optimal feature set for pixel-based classification. The classification step is further followed by performance evaluation of proposed approach. The methodology is investigated using pixel-based classification of the automated segmentation obtained and are compared with the ground truth.

3.4 RESULTS OF OD LOCALIZATION AND BLOOD VASCULATURE SEGMENTATION

This section provides the qualitative and quantitative analysis of the proposed work for pre-processing, OD localization and blood vessels segmentation techniques that are applied on fundus images. The proposed algorithms are applied on all the images from two standard datasets; DRIVE dataset comprising of 40 retinal fundus images with blood vessel ground annotations and STARE dataset comprising 400 images.

3.4.1 Results of Image Pre-processing

The various pre-processing steps are applied on retinal fundus images to mitigate image artefacts prior to OD localization and blood vessel extraction. The original fundus image is subjected to variation attenuation for the removal of inter image variability, green channel conversion to obtain maximum contrast channel, image denoising and contrast enhancement using CLAHE method, as discussed in section 3.2.1. The retinal fundus images from the benchmark datasets after applying sequential pre-processing steps are depicted in Figure 3.7 and Figure 3.8.

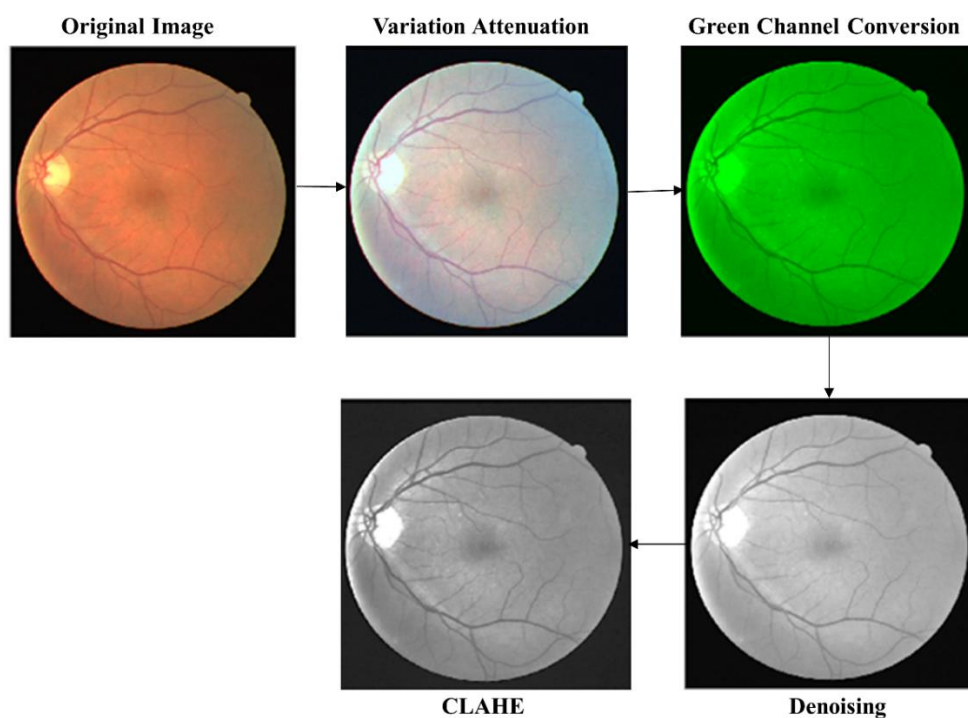


Figure 3.7: Retinal fundus image from DRIVE dataset after applying image pre-processing steps

After applying image variation attenuation, the raw fundus images become invariant to the background illumination. Green channel possesses highest intensity out of all the RGB channels, so green channelled component of fundus images is retained. Further, image denoising and CLAHE are used for local contrast enhancement.

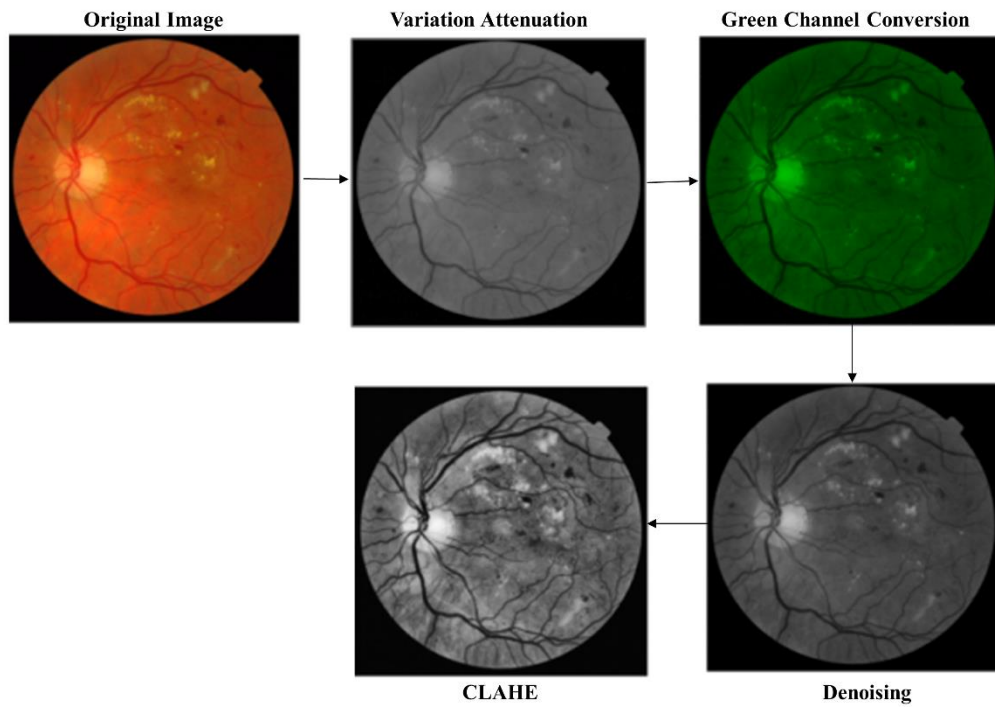


Figure 3.8: Retinal fundus image from STARE dataset after applying image pre-processing steps

The pre-processing step ensures that the retinal fundus image subjected to OD localization and blood vessel segmentation does not possess any image variability, low contrast and other image artefacts. Further, the histogram comparison of denoised image and CLAHE image is shown in Figure 3.9 to get a clear oversight of their histogram distribution involved at this stage.

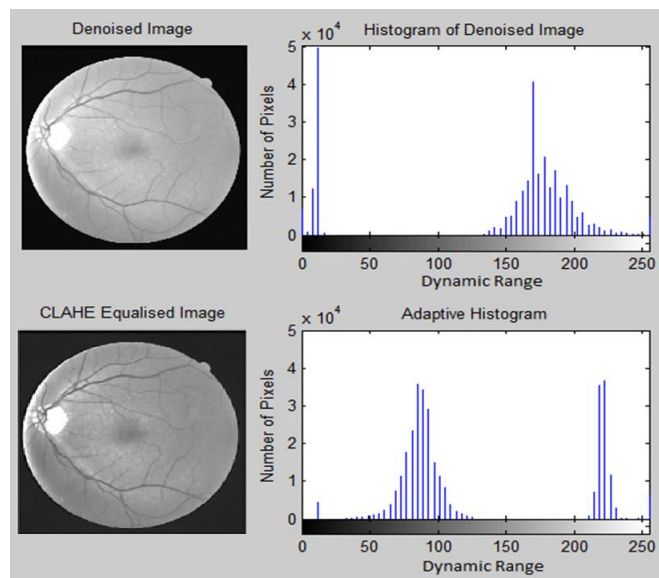


Figure 3.9: Denoised image and contrast limited adaptive histogram equalized image and their respective histograms

It is seen that the peaked and uneven histogram distribution of denoised fundus image is removed using the CLAHE method with Rayleigh distribution. It can be observed that the contrast of overall image is also enhanced using histogram equalization technique.

The pre-processed images after applying pre-processing steps are subjected to image quality analysis by measuring the parameters such as Peak Signal to Noise Ratio (PSNR) values, Structural Similarity Index (SSIM) metrics and Root Mean Square Error (RMSE). Table 3.1 and Table 3.2 depicts the image quality assessment outcomes obtained for 10 images for DRIVE and STARE datasets.

Table 3.1: Quality assessment of images taken from DRIVE dataset

Metrics	DRIVE Dataset			
	Images	RMSE	PSNR (dB)	SSIM
DRIVE_1		0.4187	55.6929	0.9909
DRIVE_2		0.4301	55.4590	0.9924
DRIVE_3		0.4063	55.9533	0.9872
DRIVE_4		0.4082	55.9114	0.9890
DRIVE_5		0.4555	54.9606	0.9848
DRIVE_6		0.5046	54.0705	0.9768
DRIVE_7		0.4172	55.7228	0.9908
DRIVE_8		0.4288	55.4849	0.9981
DRIVE_9		0.4786	54.5305	0.9858
DRIVE_10		0.5126	53.9345	0.9868

From Table 3.1, it is seen that RMSE value for pre-processed images lies in the range of 0.4 to 0.5 which consequently provides the PSNR ranging from 53 dB to 55dB. Another quality assessment parameter, SSIM provides the value ranging from 0.98 to 0.99. Table 3.2 depicts the quality index parameters for pre-processed images acquired from STARE dataset. It provides the RMSE ranging from 0.3 to 0.5, thereby, yielding PSNR values in between 54dB to 58 dB range. The retrieved image structural quality in terms of SSIM ranges between 0.98 to 0.99.

Table 3.2: Quality assessment of images taken from STARE dataset

Metrics	STARE Dataset			
	Images	RMSE	PSNR (dB)	SSIM
STARE_1		0.3880	56.3525	0.9942
STARE_2		0.4073	55.9323	0.9816
STARE_3		0.3442	57.3936	0.9995
STARE_4		0.3883	56.3467	0.9916
STARE_5		0.3453	57.3643	0.9899
STARE_6		0.4091	55.8932	0.9811
STARE_7		0.4156	55.7553	0.9813
STARE_8		0.4288	55.4849	0.9896
STARE_9		0.4600	54.8756	0.9750
STARE_10		0.4279	55.5039	0.9805

From the tabular comparison, it is revealed that lower the value of RMSE provides higher PSNR range indicating better image quality. SSIM value strongly approaching towards 1 indicates improved quality of the pre-processed images for both the datasets under evaluation.

3.4.2 Results of OD Localization

Two OD localization approaches have been adopted in this work: one employing Mathematical Morphology and the other using Circular Hough Transform. The effectiveness of both localization approaches is investigated using the images from standard benchmark datasets.

3.4.2.1 Results of Morphology based OD Localization

The OD portion is identified by clustering the highest intensity pixels from the grayscale retinal image in the mathematical morphology-based OD localization method discussed in section 3.2.2. Image pre-processing is followed by OD segmentation to remove optical disc portion from retinal image that may hamper the identification of brighter lesion features in the retina. The output fundus images for both the datasets after applying OD localization algorithm using mathematical morphology are shown in Figure 3.10.

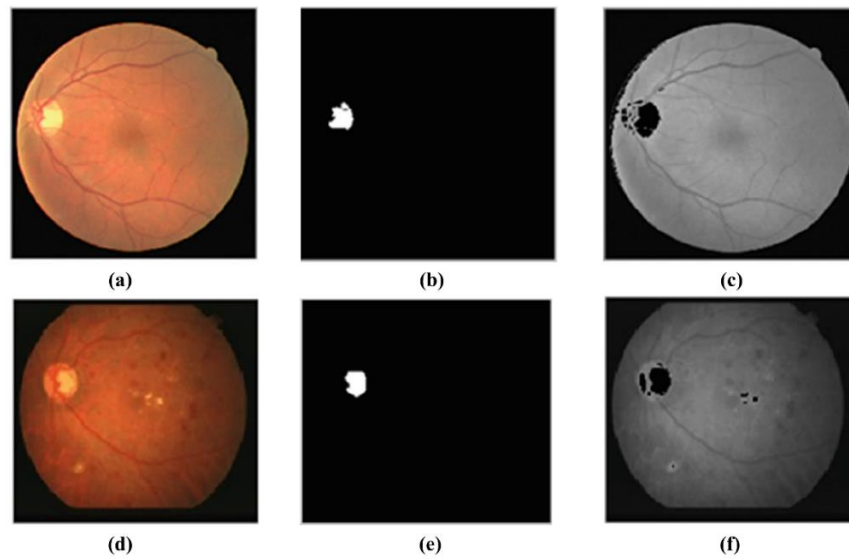


Figure 3.10: (a), (d) Original fundus image from DRIVE and STARE dataset (b), (e) Segmented optical disc (c), (f) Fundus image after OD removal using mathematical morphology based OD localization

Figure 3.10 (a) and (d) shows the original fundus images taken from DRIVE and STARE dataset, Figure 3.10 (b) and (e) provides the output OD segmented portion using mathematical morphology-based OD localization algorithm and Figure 3.10 (c) and (f) depicts the retinal fundus images after OD removal for the benchmark datasets. It is observed from the output fundus images that this approach does not provide satisfactory performance for OD segmentation as it not only localizes the OD portion but also other pathological features in the fundus image having similar intensity range.

3.4.2.2 Results for Circular Hough Transform based OD Localization

This morphology based OD localization technique is capable for distinguishing blurred OD boundaries and the background. Therefore, the Circular Hough Transform is implemented for the identification of circular region with the intensity range of 70-140. The results obtained by Circular Hough Transform based OD localization approach are provided in Figure 3.11 depicting the original fundus images, OD segmented portions and retinal fundus images after OD removal.

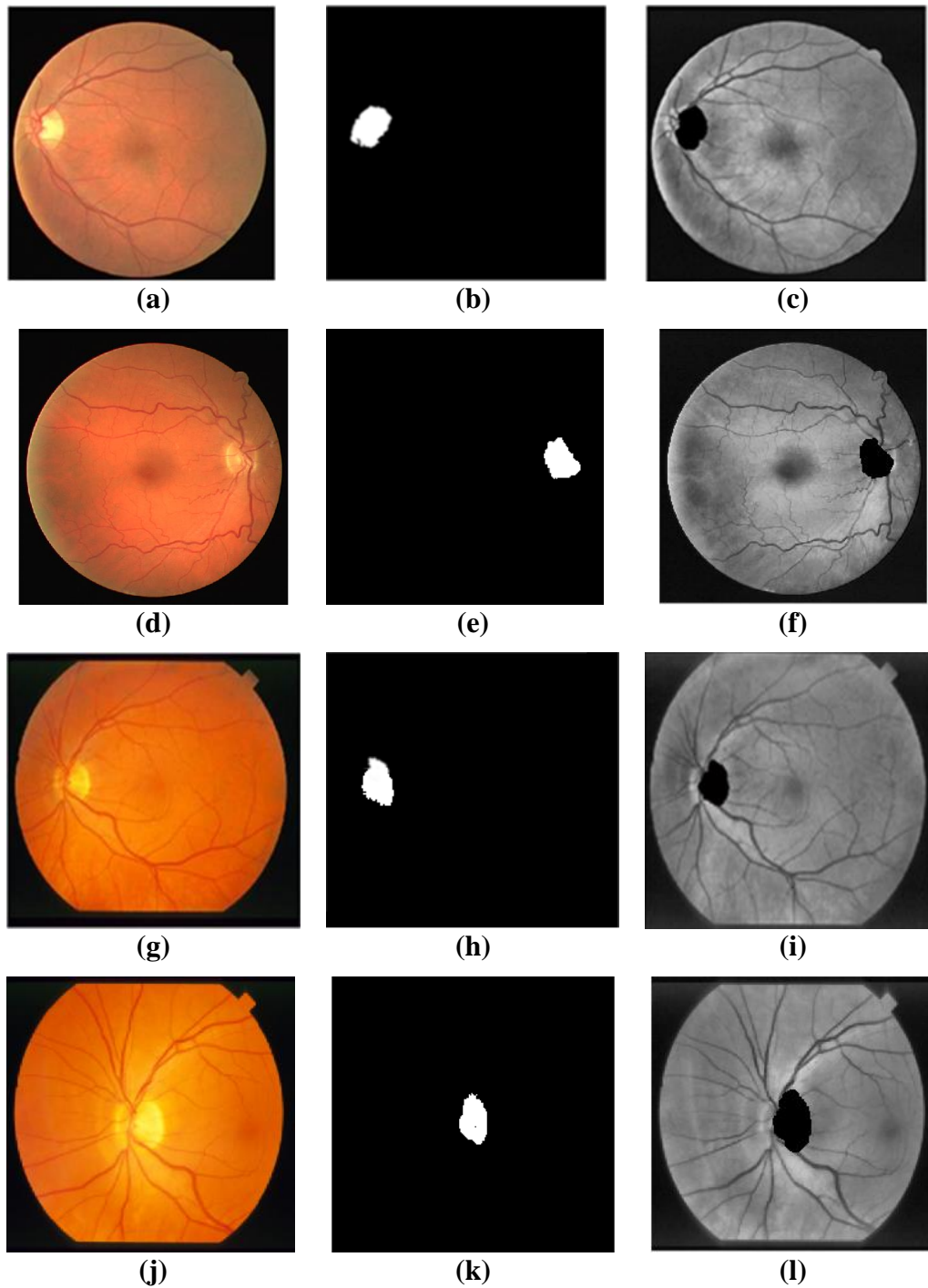


Figure 3.11: Original fundus images (a), (d) from DRIVE dataset (g), (j) from STARE dataset ; (b), (e), (h), (k) Segmented optical disc ; (c), (f), (i), (l) Fundus image database after OD removal using Circular Hough Transform based OD localization approach

The morphological closing operation yields the largest circular region among the intensity plane that is recognized as an optical disc segment. Optical disc boundaries are approximated accurately despite its blurred edges using our OD localization approach.

3.4.2.3 Performance Analysis of OD Localization

The Circular Hough Transform based OD localization approach was compared with mathematical morphology based OD localization approach and another region growing method in terms of two performance evaluation parameter; first is overlap of optical disc and other is dice metric. The region growing based method enables seed point to grow and hence, the circular region is grown by adding equivalent properties of neighbourhood pixels to seed. The center of OD is measured as a seed point and the difference among the seed point and pixel values is considered as the stopping condition for region growing. The comparison drawn is shown in Table 3.3.

Table 3.3: Performance evaluation of OD localization approach

Approaches Parameters	Region growing OD Localization Method [195]	Mathematical Morphology based OD Localization	Circular Hough Transform based OD Localization	Percentage Improvement from Region growing OD Localization	Percentage Improvement from Morphology based Approach
Optical Disc Overlap	0.9565	0.9652	0.9872	3.21%	2.27%
Dice Metric	0.9489	0.9541	0.9931	4.65%	4.08%

The comparative analysis reveals that the Circular Hough based OD localization approach provides 3.21% improvement comparative to the region growing OD localization method and 2.27% improvement from mathematical morphology based OD localization approach, in terms of optical disc overlap. The improvement of 4.65% and 4.08% is seen for and dice metric parameter employing region growing OD localization method and mathematical morphology based OD localization approach respectively. The outcomes obtained for performance evaluation of OD localization demonstrates the viability of the OD localization approach and validates its localization efficiency.

After the OD localization, retinal blood vessel extraction is essential for diagnosing of DR. Blood vessels are segmented for obtaining the image background and foreground portions for lesion discrimination.

3.4.3 Results of Blood Vasculature Segmentation

Blood vessel extraction is beneficial in finding the geometrical relationships between the vasculatures and also aids in the identification of retinal field of view [196]. The output blood vessels obtained employing Modified Kirsch's Edge Detection and Fuzzy Inference based segmentation approach along with the ground truth blood vessels are depicted in Figure 3.12.

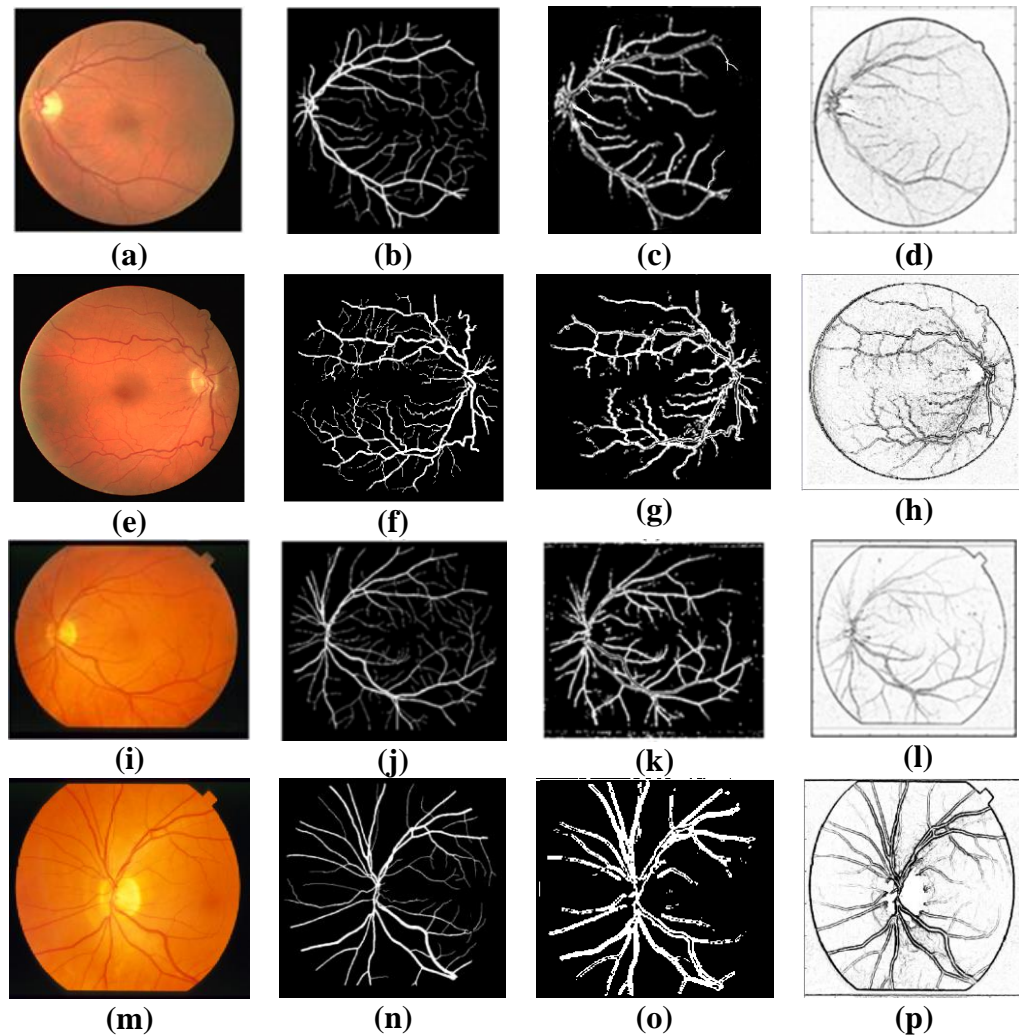


Figure 3.12: (a), (e), (i), (m) Original fundus images ; (b), (f), (j), (n) Ground truth blood vessels labeled by experts ; Extracted blood vessel output using (c), (g), (k), (o) Modified Kirsch's Edge Detection and (d), (h), (l), (p) Fuzzy Inference based Blood Vessel Segmentation respectively

Kirsch's Edge Detection outputs depicted in Figure 3.12 (c), (g), (k) and (o) shows the empty areas that are still evident in the blood vessel images extracted by matching Kirsch's template. This method highlights the edges of blood vessels but unwanted noise is also enhanced which are indicated as small dots in the output images. Figure

3.12 (d), (h), (l) and (p) depicts the output of fuzzy based blood vessel extraction technique and the blood vessels are more clearly visualized in this segmentation approach. Comparing the visual results of both the methods, fuzzy based approach overcomes the disadvantages of Kirsch's edge detection technique and provides the output blood vasculatures comparable to the ground truth.

3.4.3.1 Performance Analysis of Segmented Blood Vessels

After qualitative analysis, the segmented blood vessels are compared quantitatively in terms of various performance indices: Jaccard's index, dice coefficient, sensitivity, precision, specificity and accuracy as depicted in Table 3.4.

Table 3.4: Performance parameters for Blood vessel Segmentation techniques

Blood Vessel Extraction Techniques Employed	Modified Kirsch's Edge Detection		Fuzzy Inference based Blood Vessel Segmentation	
	DRIVE	STARE	DRIVE	STARE
Dataset				
Parameter				
Jaccard's Index	0.3193	0.3091	0.5942	0.5831
Dice Coefficient	0.4827	0.4729	0.6665	0.6527
Sensitivity	0.5884	0.5378	0.6340	0.5845
Precision	0.6682	0.6327	0.7199	0.6894
Specificity	0.9207	0.9175	0.9510	0.9476
Accuracy	0.8911	0.8831	0.9236	0.9102

It is revealed from the tabular comparison that the results obtained from fuzzy inference based blood vessel segmentation provides better performance comparative to the modified Kirsch's edge detection method, thereby justifying the visual qualitative analysis. The fuzzy inference based method yields better accuracy of 92.36% and 91.02% for DRIVE and STARE datasets respectively. The fuzzy

based approach has a drawback of somewhat poor visualization of thin blood vessels in the retinal area when compared with ground truth blood vessels. The HBV-MR approach overcomes the limitations of both these methods while providing effectual blood vasculature segmentation.

3.5 RESULTS OF PROPOSED HBV-MR APPROACH

The visual qualitative comparison of proposed HBV-MR with the ground truth blood vessels labelled by professional experts for both DRIVE and STARE database images is depicted in Figure 3.13.

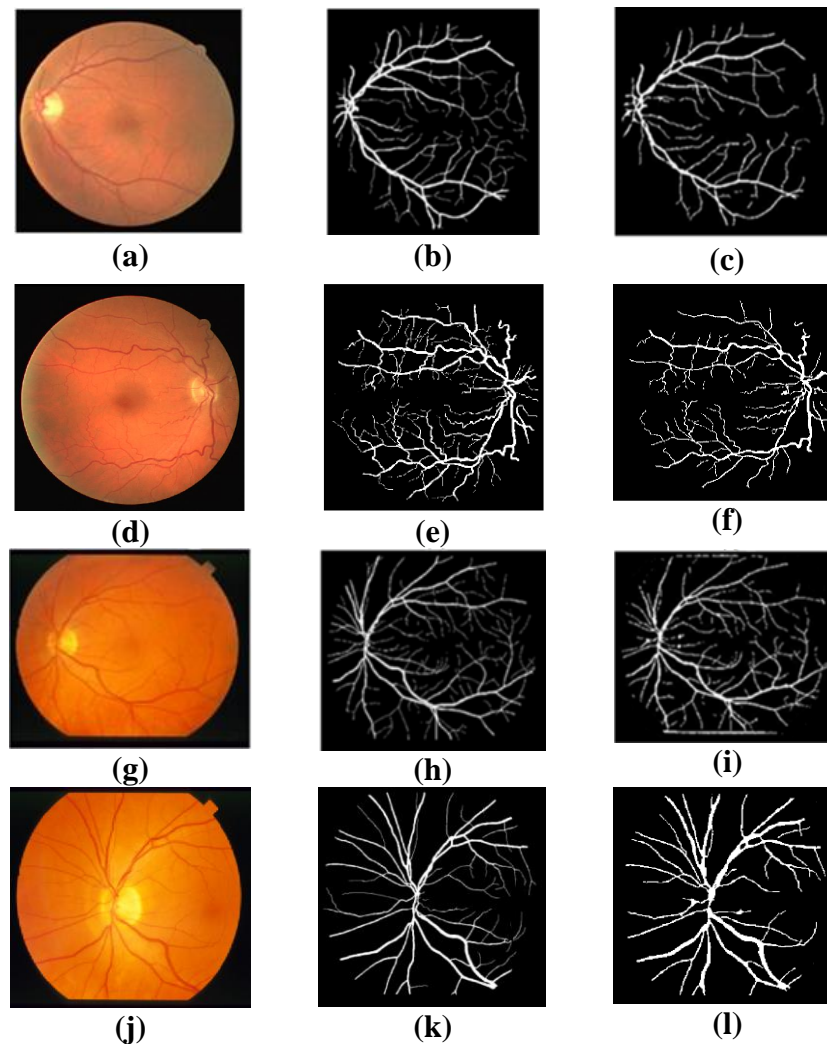


Figure 3.13: (a), (d), (g), (j) Original fundus images ; (b), (e), (h), (k) Ground truth blood vessels labeled by experts ; (c), (f), (i), (l) Extracted blood vessels using the proposed HBV-MR respectively

Figure 3.13 reveals that the blood vessel segmentations obtained after employing HBV-MR are comparable to the ground truth blood vessels. The proposed approach yields better results, overcoming the limitations of the previously reported blood vessel segmentations. Challenge of both modified Kirsch's edge detection and fuzzy inference based blood vessel segmentation lies in fairly poor visualization of thin blood vessels in the retinal area which is addressed by HBV-MR technique. The qualitative comparison of three blood vessel segmentation methods reveals that the proposed HBV-MR technique delivers better visual outcomes compared to other two techniques. HBV-MR approach used is proficient for identifying small blood vessels and the satisfactory performance is achieved which is closer to the ground truth blood vessels.

After performing blood vasculature segmentation, feature extraction is the main focus to understand the statistical relevance of the extracted blood vessels. After the exhaustive literature survey, the prominent image features are investigated and chosen depending upon the applicability for this research work. Features comprising of shape, intensity and fractal dimensions of blood vessels are taken into consideration. Blood vessel feature-based comparison of extracted fundus images with the ground truth images is done for performance validation of the proposed technique.

3.5.1 Statistical Analysis of HBV-MR

The three set of features including shape features, intensity features and fractal dimension features are extracted for the statistical analysis of the extracted blood vessels. Shape features are used to determine the geometric properties of extracted retinal structures, the pixel-based intensity features are useful in distinguishing the vessel pixels from neighboring background pixels and fractal dimensions is helpful in blood vessel bifurcation diagnosis.

The box plots are observed for all the three feature sets to analyze their normality visualization in terms of quartiles and outliers. The box plots of shape and intensity are depicted in Figure 3.14, Figure 3.15 respectively.

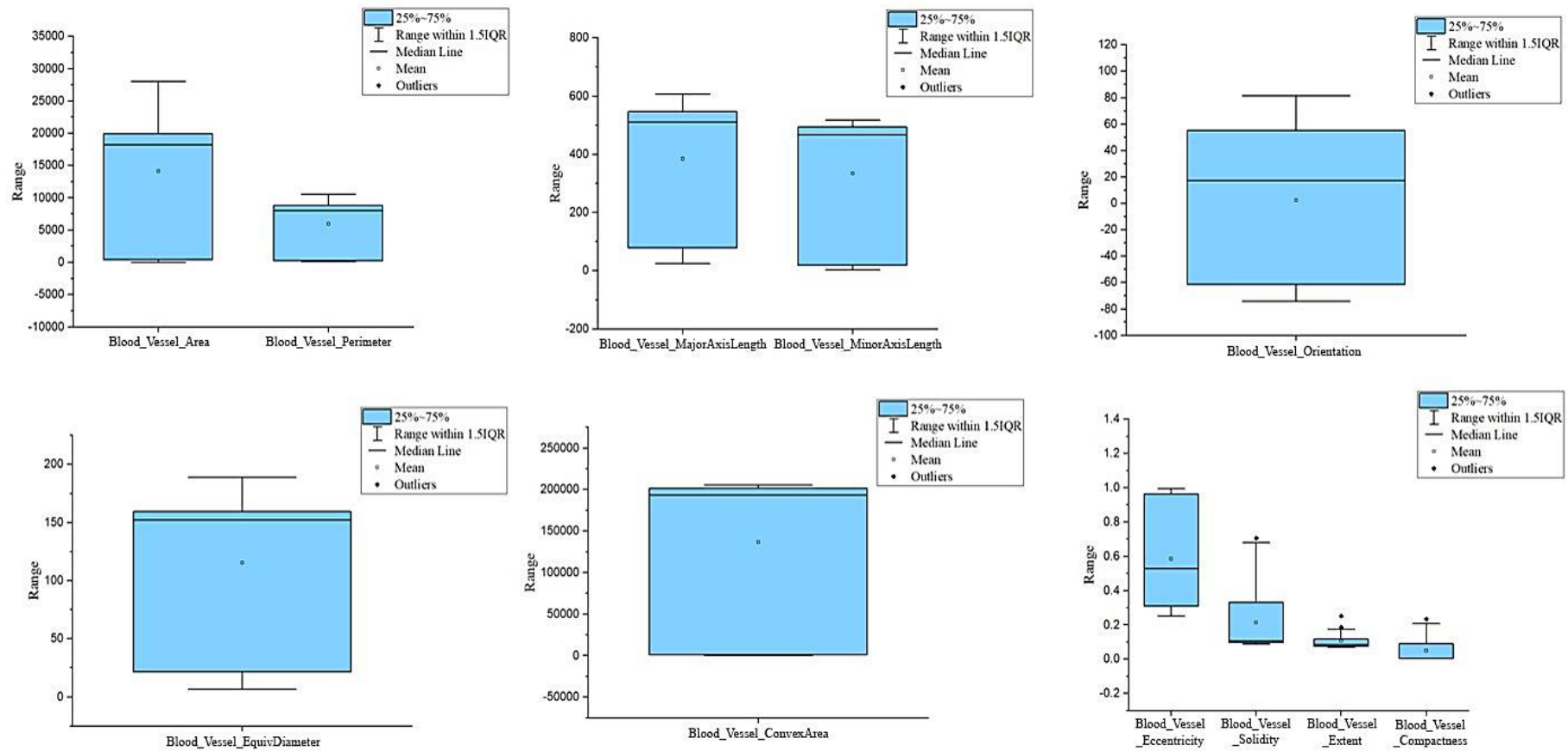


Figure 3.14: Box plots of shape features for proposed HBV-MR

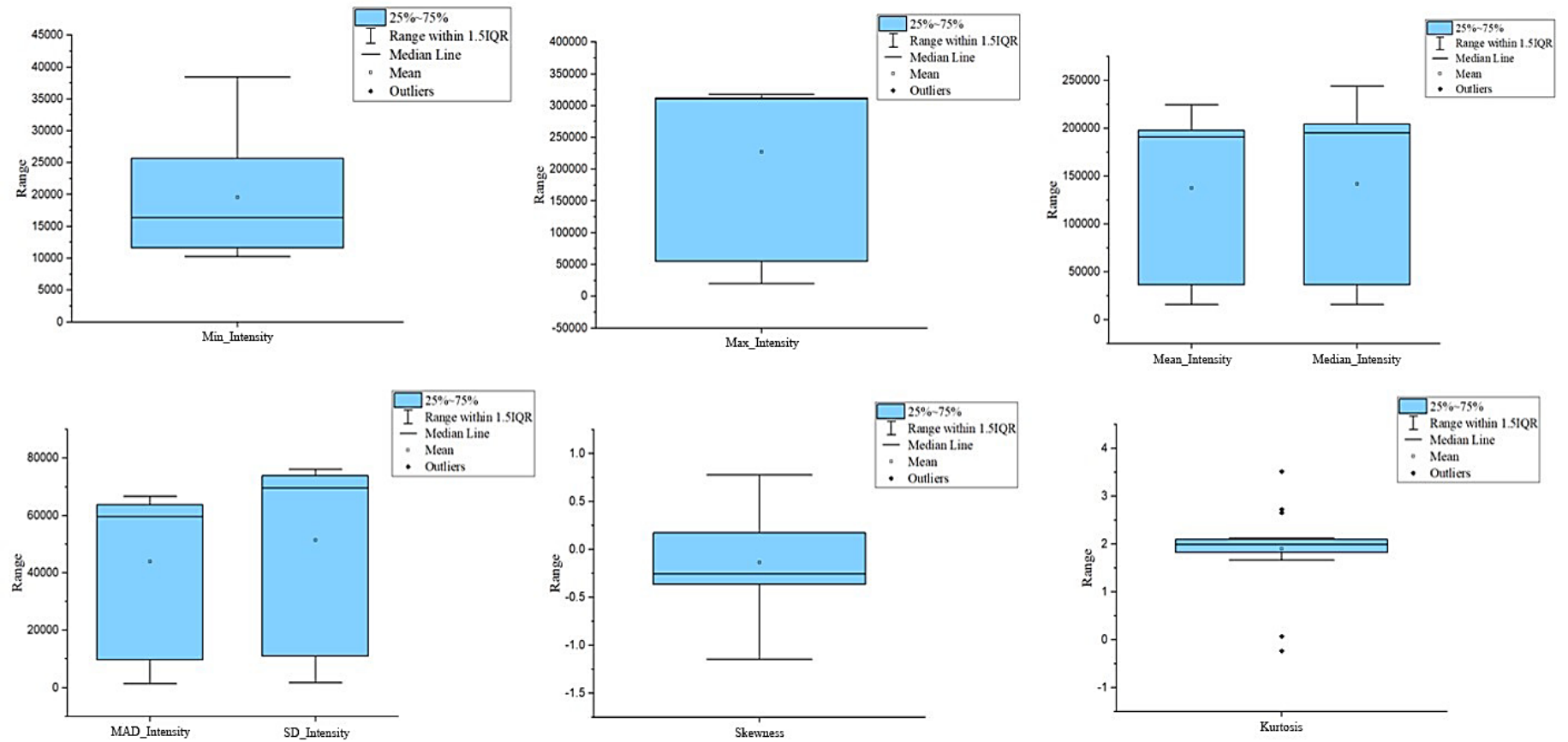


Figure 3.15: Box plots of intensity features for proposed HBV-MR

The box plot descriptive depicted in Figure 3.14 and Figure 3.15 shows that the shape and intensity features are not substantial for pixel-based classification of extracted blood vessels due to their undistinguishable quartile ranges. However, literature reveals that fractal dimensional features explored are significant for Proliferative Diabetic Retinopathy (PDR) diagnosis as the high value of fractal dimensions implies more bifurcated abnormal blood vessel overgrowth indicative of a higher degree of PDR [197]. Thus, for further statistical analysis, fractal dimensions are utilized. To estimate the self-similarity of extracted blood vessels from the ground truth vessels, box plots of the fractal dimensions; Box count, information and correlation, are observed for vascular branching patterns.

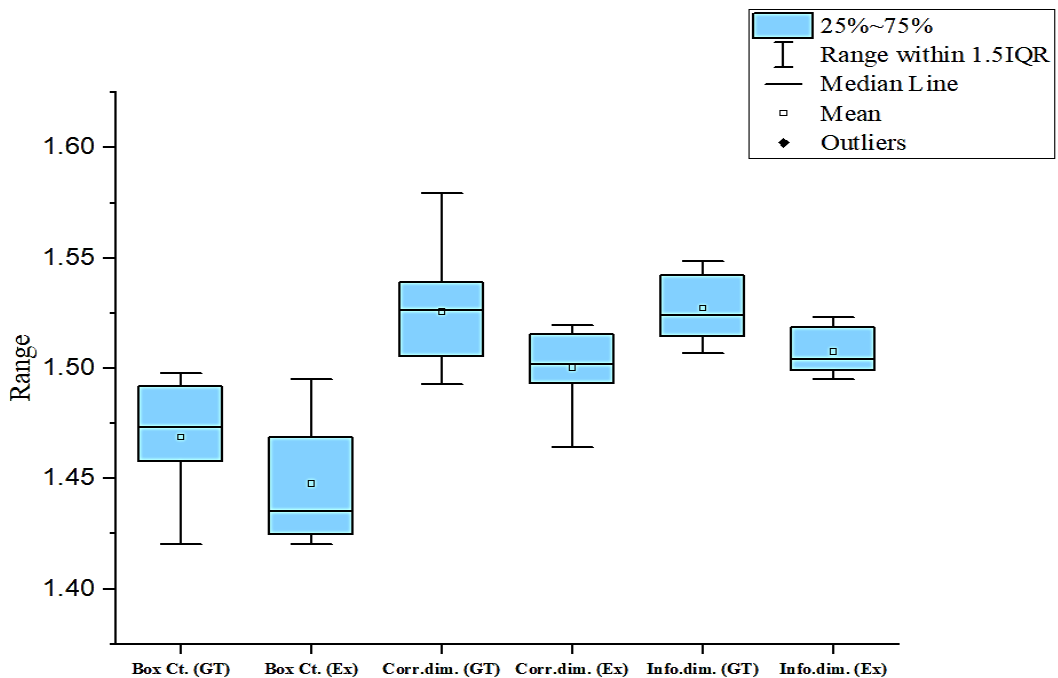


Figure 3.16: Box plots comparison of fractal features for Ground Truth (GT) blood vessels and Extracted (Ex) vessels using the proposed approach

It is seen from Figure 3.16 that the box plots that the dimensions of the extracted blood vessels using the HBV-MR approach lies in a similar range as that of ground truth fractal dimensions. Also, the different quartile ranges of all the fractal features indicates their significance which is numerically validated using various test from SPSS statistical package. The p -values of Shipro-Wilk test and Kolmogorov-Smirnov test are computed to check the normality of the feature set in terms of significant p -values.

Table 3.5: p -value for normality check of fractal feature set

Fractal Features	Shapiro-Wilk Test	Kolmogorov-Smirnov Test
	p -value ($p > 0.05$)	p -value ($p > 0.05$)
Box Count (GT)	0.944	0.155
Box Count (Ex)	0.835	0.166
Inf. Dim. (GT)	0.984	0.103
Inf. Dim. (Ex)	0.850	0.179
Corr. Dim. (GT)	0.980	0.085
Corr. Dim. (Ex)	0.846	0.207

For a normally distributed feature set, p -values should be greater than 0.05 and from the Table 3.5, it is clear that the fractal feature set is normally distributed as the p -value for every extracted feature is greater than 0.05. Further, feature selection is done on the basis of correlation analysis, Levene's f -test and t -test. Pair-wise linear correlation is executed utilizing Pearson and Spearman's correlation coefficients for quantifying the relationship among feature variables. Equality of variance is determined using Levene's test commonly known as f -test and equality of means is inferred from t -test. The f -test test provides statistical evidence for variance analysis among two feature sets are approximately equal or not. The null hypothesis assumptions considering the homogeneity of variance for Levene's test and homogeneity of means for t -test are provided in the Appendix 2.

Table 3.6 and Table 3.7 gives the correlation comparison of fractal features using Person and Spearman methods respectively for extracted blood vessels with that of ground truth blood vessels labelled by ophthalmic experts.

Table 3.6: SPSS Pearson correlation analysis of fractal features observed for Extracted (Ex) vessels and Ground Truth (GT)

Pearson Correlation Coefficients						
Fractal Features	Box Count (GT)	Box Count (Ex)	Inf. Dim. (GT)	Inf. Dim. (Ex)	Corr. Dim. (GT)	Corr. Dim. (Ex)
Box Count (GT)	1	0.618**	0.970**	0.652**	0.971**	0.663
Box Count (Ex)	0.618**	1	0.558*	0.993**	0.524*	0.992**
Inf. Dim. (GT)	0.970**	0.558*	1	0.613**	0.990**	0.608**
Inf. Dim. (Ex)	0.652**	0.993**	0.613**	1	0.579**	0.995**
Corr. Dim. (GT)	0.971**	0.524*	0.990**	0.579**	1	0.585**
Corr. Dim. (Ex)	0.663**	0.992**	0.608**	0.995**	0.585**	1

** Correlation is significant at 0.01 level

* Correlation is significant at 0.05 level

Table 3.7: SPSS Spearman's correlation analysis of fractal features observed for Extracted (Ex) vessels and Ground Truth (GT)

Spearman's Correlation Coefficients						
Fractal Features	Box Count (GT)	Box Count (Ex)	Inf. Dim. (GT)	Inf. Dim. (Ex)	Corr. Dim. (GT)	Corr. Dim. (Ex)
Box Count (GT)	1	.507*	.955**	.568	.965*	.529**
Box Count (Ex)	.507*	1	.445*	.970*	.445	.974*
Inf. Dim. (GT)	.955**	.445*	1	.528**	.991*	.478
Inf. Dim. (Ex)	.568**	.970**	.528*	1	.526**	.976*
Corr. Dim. (GT)	.965**	.445*	.991**	.526**	1	.492**
Corr. Dim. (Ex)	.529*	.974**	.478*	.976*	.492**	1

** Correlation is significant at 0.01 level

* Correlation is significant at 0.05 level

From the tabular depiction of correlation coefficients done in Table 3.6 and Table 3.7, it is clear that information dimensions and correlation dimensions are highly correlated to each other having a correlation coefficient of 0.995. The lower correlation was found between box-counting dimensions and correlation dimensions yet higher enough (> 0.5) considering the features in strong association to each other.

Table 3.8: Levene's test and t -test results for the fractal feature set

Fractal features				
Features	Levene's Test		t -test	
	F	Sign.	t	Sign. (2-tailed)
Box Dim.	24.975	0.000	2.730	0.010
Inf. Dim.	15.545	0.000	2.991	0.005
Corr. Dim.	23.674	0.000	2.938	0.006

From Table 3.8, it is revealed that the experimental results obtained for both Levene's test as well as 2-tailed t -test for the feature set are significant as the significance value is lesser than 0.05. Therefore, rejecting null hypothesis (H_0), it is observed that there is not much difference among the mean and variance values. Features comprising of relevant information are selected for classification using reduced representation instead of complete data. Thus, all the fractal features are selected for analysis after evaluating their contribution for the detection of vascular structures. This feature set can be further used for classification of blood vessels so as to diagnose PDR symptoms at the early stage by estimating the bifurcated vascular patterns at the early stage.

Efficiency of three diverse blood vessel segmentation approaches discussed in section 3.2.3 are checked in terms of various performance indices.

3.5.2 Performance Analysis of HBV-MR

Performance analysis of the proposed HBV-MR blood vessel segmentation approach is done in terms of Jaccard index, dice coefficient, precision, accuracy,

sensitivity and specificity. The performance results attained for two datasets are tabulated in Table 3.9.

Table 3.9: Performance parameter analysis of Proposed HBV-MR approach for benchmark datasets

Blood Vessel Extraction Techniques Employed	Proposed HBV-MR	
Dataset Parameter	DRIVE	STARE
Jaccard's Index	0.8126	0.7986
Dice Coefficient	0.8957	0.8880
Sensitivity	0.7833	0.7120
Precision	0.8684	0.8320
Specificity	0.9919	0.9897
Accuracy	0.9550	0.9480

The proposed HBV-MR approach provides average accuracy of 95.50% for the DRIVE database and comparable results are obtained for STARE database with the average accuracy of 94.80%. The average specificity values of 98.97% and 99.19% are achieved for STARE and DRIVE datasets respectively.

3.6 COMPARITIVE ANALYSIS OF PROPOSED HBV-MR

The proposed HBV-MR approach is compared with the other state of art approaches in terms of accuracy for both the benchmark datasets. The comparison of proposed segmentation approach for blood vessels with currently existing techniques is depicted in Table 3.10.

Table 3.10: Comparison of proposed HBV-MR with the existing approaches

Technique used	Accuracy for DRIVE Database	Accuracy for STARE Database	Complexity
Jiang & Mojon, 2003 [198]	92.13%	90.09%	High
Martinez-Perez, <i>et al.</i> , 2002 [199]	93.45%	94.11%	High
Naguyen, <i>et al.</i> , 2013 [200]	94.01%	93.00%	High
Ana Salazar-Gonzalez <i>et al.</i> , 2010 [201]	94.12%	94.40%	Moderate
Fraz, <i>et al.</i> , 2012 [202]	94.30%	94.42%	Moderate
Bandara, <i>et al.</i> , 2017 [203]	94.11%	94.78%	Moderate
Li, <i>et al.</i> , 2018 [204]	83.47%	----	Moderate
Roy, <i>et al.</i> , 2019 [205]	94.88%	92.95%	High
Adapa, <i>et al.</i> , 2020 [206]	94.50%	84.86%	Moderate
Proposed HBV-MR	95.50%	94.80%	Low

It is observed from the experimentation that the proposed method outperforms the existing methods providing less run-time computational complexity. The accuracy value of the proposed model indicates the exact marking of the vessel and non-vessel pixels. The results obtained validate the improvement over previously reported outcomes in state-of-the-art methods.

3.7 CONCLUSION

The implementation of OD localization and blood vessel segmentation approaches are able to differentiate the anatomical structures from other retinal features. Discrepancies due to presence of background noise, varying inadequate illumination, varying contrast between the background and blood vasculatures are removed utilizing the proposed HBV-MR approach. The OD segmentation approach is effective in detecting optical disc for effective blood vessel segmentation close to the OD area. Remarkable improvement is seen for Circular Hough based OD localization approach

in terms of OD overlap parameter and dice metric, thereby demonstrating its feasibility and localization efficiency.

The OD localization and blood vessel segmentation results depicted in this work reveals the robustness of the proposed technique for the statistical, visual, and performance analysis. The results obtained using the proposed HBV-MR approach provide average accuracies of 95.50% and 94.80% and average specificity values of 99.19% and 98.97% for DRIVE and STARE datasets respectively. Visual, statistical, and performance analysis provides a robust solution for the DR detection at its early-stage by reducing the fallacious detection of pathological symptoms having similar features as OD or blood vessels. The next chapter of this thesis focuses on anomaly identification after the efficient blood vessels segmentation to aid the DR diagnosis process.

CHAPTER 4

**A HYBRID LESION DETECTION
TECHNIQUE FOR DR
ABNORMALITY
DISCRIMINATION**

CHAPTER 4

A HYBRID LESION DETECTION TECHNIQUE FOR DR ABNORMALITY DISCRIMINATION

4.1 INTRODUCTION

Automated DR discriminatory diagnostic systems have globally become an integral part of disease detection and pathology identification. Concerning the medical science field, automatic pathology detection plays an important role in assisting the interpretation of disease. It analyses the level of disease severity, thereby assisting the patients in timely treatment and routine follow-up.

Traditionally when the technology was not sophisticated enough, DR was diagnosed using ophthalmoscopy and pupil dilation by the ophthalmic experts. Although, imaging modalities like retinal photography and OCT scans can provide improved detection accuracy with regular monitoring of the risk factors associated with the disease. DR screening and diagnosis depend upon fundus photography-based strategies that uses specialized fundus cameras able to capture a magnified view of interior of the eye having high-resolution. Retinal photography can provide advanced DR diagnosis by explicitly locating DR lesions in the retinal fundus image and thus providing the useful information about abnormality location and disease severity level. This can be accomplished by utilizing binary classification approach for classifying each pixel in the image. However, the issue associated with these approaches are their varying feature characteristics like color and size for different types of DR lesions. Furthermore, in the real time scenario, doctors are unable to identify each part of the fundus image as healthy or belonging to one of the lesion class. Instead, they rely on ground-truth annotation containing the pixel probabilities defining each pixel in the image as a part of diseased or non- diseased portion.

For a normal/healthy fundus image, the visual components are blood vessels, macula, and optical disc. DR could be a progressive disease that has no initial symptoms but as the stage progresses it shows mild vision problems such as fluctuating, impaired, or blurred vision. These symptoms are characterized through

lesions such as MAs, HEMs, EXs and CWs [16]. The information about the types of DR abnormalities is required for determining the different stages of the disease development.

4.1.1 Diabetic Retinopathy Abnormalities

The development of Diabetic Retinopathy can be distinguished into two major stages: NPDR and PDR. In the NPDR stage of retinal abnormality, the damaged blood vessels leak blood or fluid forming lesions on the retinal surface. DR lesions can be broadly differentiated into yellow/bright and red/dark lesions depending on their color and intensity level. MAs and HEMs fall into the category of red lesions, and EXs and cotton wool are known as yellow lesions [17]. Tiny MAs are the first visible clinical symptoms of DR. MAs are formed by inflammation in blood vessels and indicated as small red dots of color and intensity similar to blood vessels. The rupture of microaneurysms causes haemorrhage that is indicated as a dark red mark on the surface of the retina. EXs are indicated as visible yellow spots with different shapes formed by lipoprotein leakage in the retinal region. The advanced stage of NPDR is indicated by CWs appearing as white fluffy lesions present inside the eye. Different lesions present in DR affected fundus image are depicted in Figure 4.1.

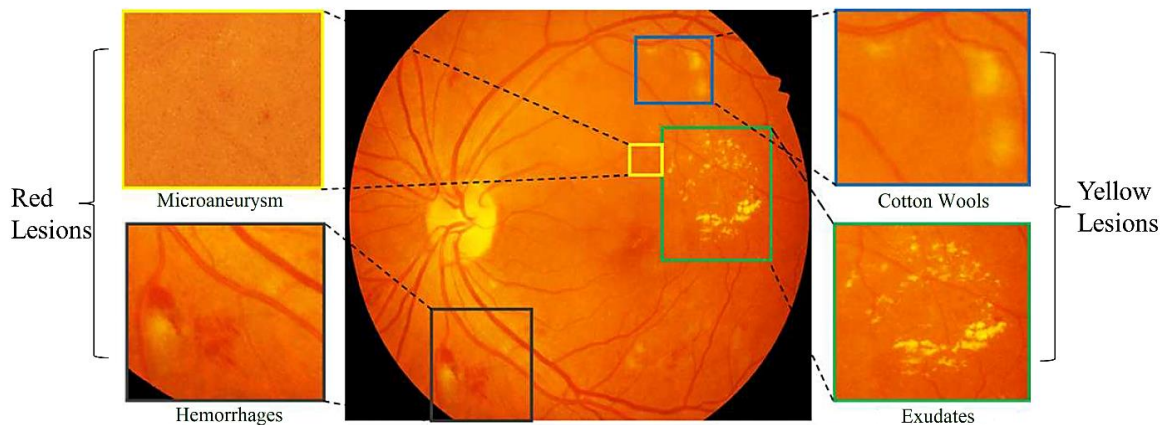


Figure 4.1: Lesions present in DR affected fundus image

Human interventions involved in manual DR diagnostic systems are subjective, laborious, and require human expertise. Also, the major challenge for lesion discrimination is the lack of ability to distinguish between the actual problematic area from background noise and other anatomical structures. From the image processing perspective, MAs and HEMs have color and size similarity as the blood vessels,

challenging their automated detection. The MAs have size variability and sometimes their size are considerably very small that can easily be perplexed with background noise or retinal tissue pigmentation [16, 17]. Optical disc also has color, intensity, and shape similarity with EXs and CWs, therefore altering the automated detection of these yellow lesions. However, OD and blood vessels have certain features differentiating the anatomical structures from DR lesion. Thus, there is a need for more accurate automated algorithms producing the desirable image pixel information as the output serving the need of the ophthalmologists. An efficient DR screening approach is proposed in this chapter for fundus image discrimination and DR lesion detection.

4.2 PROPOSED METHODOLOGY

The work in this research focuses on providing a screening solution for the diagnosis of DR by the detection, localization, and classification of red and yellow lesions. A three-stage implementation strategy is performed for fundus image discrimination and DR lesion detection. The first stage of the proposed methodology involves background segmentation accomplished by using HBV-MR approach proposed in Chapter 3 comprising fundus image pre-processing and removal of the background (OD and blood vessel) portions. The second stage involves the identification of foreground portions indicating diseased and non-diseased retinal fundus images. A Hybrid Lesion Detection (HLD) algorithm is proposed to detect abnormalities in retinal images and distinguish DR lesion into red and yellow lesions. After exhaustive literature review, geometrical shape, intensity, and texture features (detailed explanation in Appendix 1) are extracted from diseased and non-diseased fundus images, which are subject to statistical analysis-based feature set reduction strategy to select optimal features. DR discrimination strategy involved in the proposed methodology comprises fundus image discrimination into diseased/non-diseased followed by DR lesion discrimination into red and yellow lesions, utilizing different machine learning techniques. The flowchart of the proposed methodology is depicted in Figure 4.2.

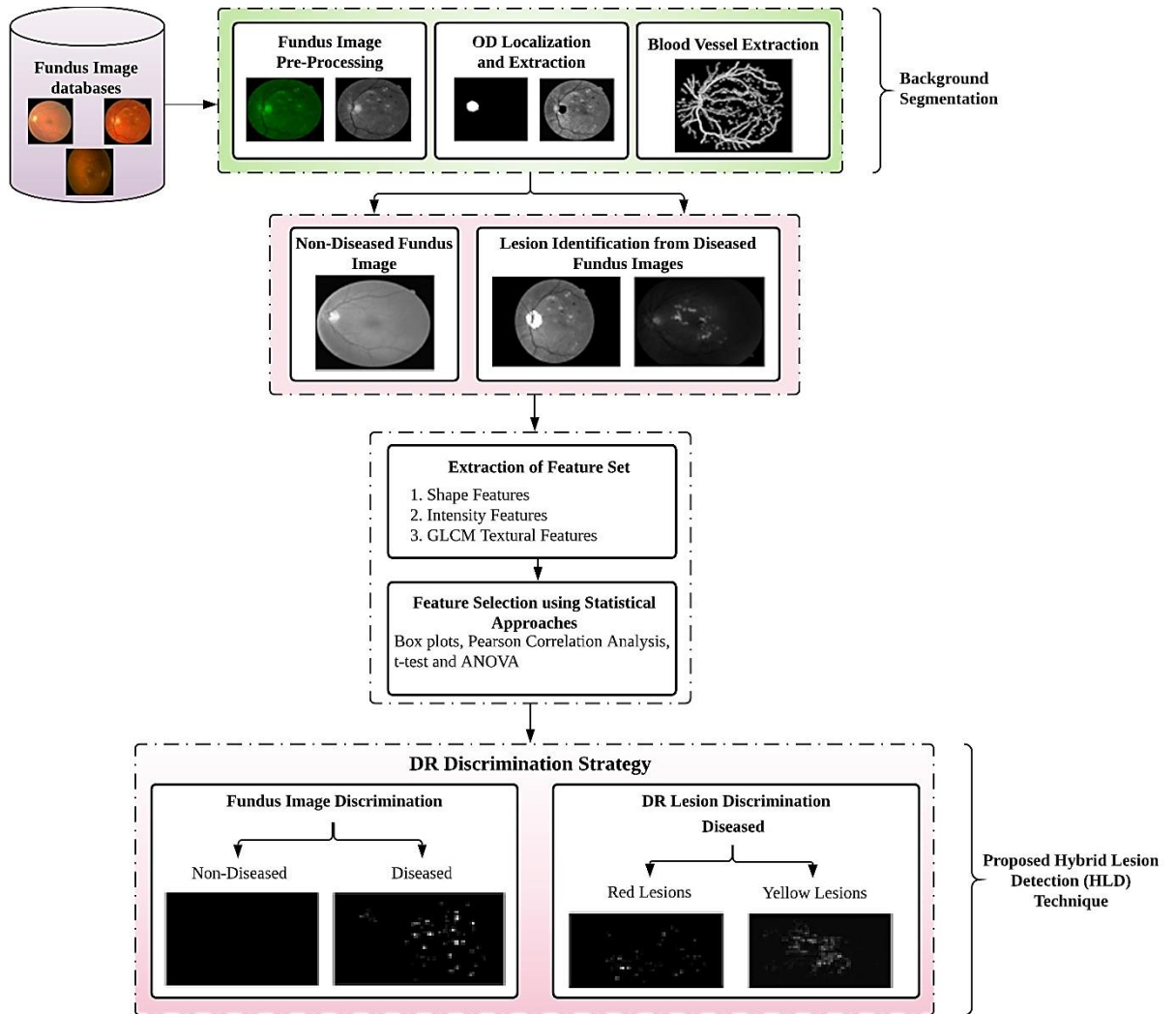


Figure 4.2: Block diagram of the proposed methodology for DR abnormality discrimination

The proposed algorithm is evaluated on benchmark Structured Analysis of the Retina (STARE) [41] and DIARETDB1 [42] datasets, which have different field of view and a varying number of images with different resolutions. For this research work, all the images from both the dataset are considered and the visual results have been presented for few images. The following subsections detail the stepwise description of the proposed methodology.

Background segmentation is accomplished by utilizing the retinal landmark segmentation methodology adopted in Chapter 3. It involves fundus image pre-processing and background (OD and blood vasculature) removal steps [195, 207, 208]. The pre-processing step consists of image variation attenuation, green channel conversion, denoising and CLAHE for image contrast enhancement.

OD and blood vessel components of retinal image are considered as background portions as they are not essential for DR anomaly detection. The OD is undesirable anatomy for DR diagnosis because it has the same intensity value as the yellow lesion. OD boundary localization is accomplished using the combination of Circular Hough Transform along with morphological closing operation and the largest circular region is identified as the OD portion as discussed in Chapter 3 [187, 188, 208].

The blood vessel is another background portion, which is eliminated employing HBV-MR approach. In order to filter out some discrete regions that are not considered as vascular regions, associated component analysis is used. Eight connected pixel connectivity is used to distinguish between the vessel and non-vessel pixels [209]. Background elimination steps, including blood vessel removal using OD localization and morphological reconstruction (I_{Mrph}), is expressed by Eq. (4.1).

$$I_{BV} = I - I_{Mrph} \quad (4.1)$$

where I is the original fundus image, I_{Mrph} is a morphologically reconstructed image and I_{BV} is the background removed fundus image.

The foreground region is obtained by subtracting the original fundus image from the identified background. After removal of the background, the non-diseased fundus image does not contain any foreground lesions and the lesion portions are only visible in the diseased fundus images.

4.2.1 Diabetic Retinopathy Discrimination

The two types of DR discrimination strategies utilized in this research work are; fundus image discrimination strategy for differentiating diseased and non-diseased images, and DR lesion discrimination strategy for distinguishing between red and yellow DR lesions.

4.2.1.1 Fundus Image Discrimination

Fundus image discrimination strategy allows to differentiate between the diseased and non-diseased fundus images after background segmentation followed by retinal landmark extraction.

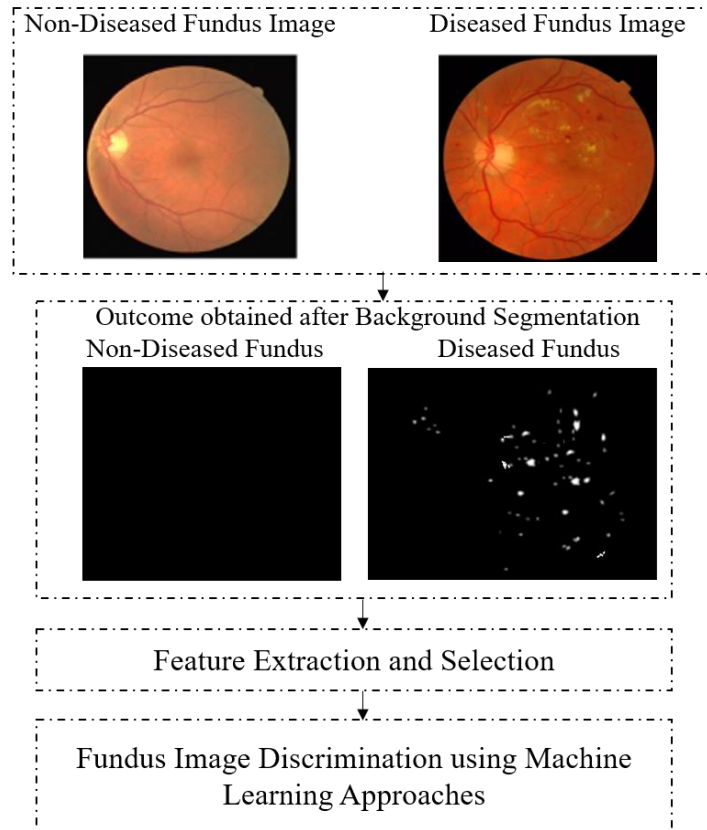


Figure 4.3: Adopted methodology for fundus image discrimination

Figure 4.3 shows the methodology adopted for fundus image discrimination. Initially background segmentation is done for the identification of Diseased and Non-Diseased Fundus image. Then, the feature set is extracted for both diseased and non-diseased fundus image sets to obtain the derived features which are informative and non-redundant. This step ensures the subsequent learning leading to better human interpretation of DR and non- DR classes. Feature extraction is followed by statistical feature selection strategy utilizing the SPSS package tool [194] to transform the extracted features into reduced feature set. This reduced feature subset obtained after feature selection contain only the relevant information sufficient to discriminate the fundus images into diseased and non-diseased. Feature selection is followed by fundus image discrimination using machine learning approach. The reduced representation improved the generalization capability of the machine learning algorithm utilizing less number of resources to describe the large fundus image dataset without overfitting.

Fundus image discrimination is trailed by DR Lesion discrimination for identifying and detecting pathological symptoms in diseased fundus.

4.2.1.2 DR Lesion Discrimination

Discrimination between different types of anomalous patterns or lesions is of great interest to improve the automated screening performance for useful clinical application. The goal of this research work is to distinguish a healthy fundus images from those containing the pathological symptoms considering both red and yellow lesion detection and employing a unique feature vector that is able to discrimination between the two classes.

DR lesion discrimination is accomplished utilizing the HLD technique for pathology identification followed by feature extraction, selection and DR discrimination using different machine learning approaches.

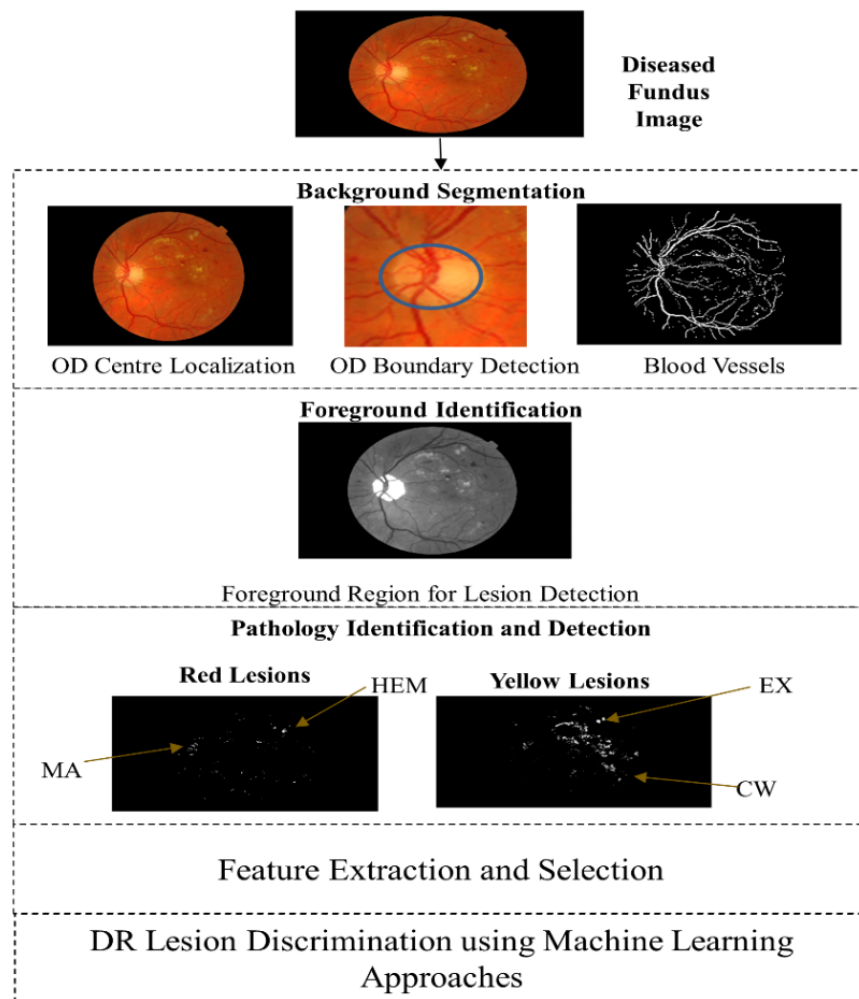


Figure 4.4: DR lesion discrimination methodology

The methodology depicted in Figure 4.4 for DR lesion discrimination is initiated by the identification of pathological symptoms in Diseased Fundus image after Background Segmentation. The DR pathologies are identified using proposed Hybrid Lesion Detection technique which is detailed in the upcoming subsection. The identified foreground is subjected to feature extraction in order to increase the classification accuracy of the machine learning model. Followed by lesion detection is a feature extraction step for accurate disease detection utilizing geometrical, intensity, and textural features. Feature set extraction of the identified pathologies is accomplished along with statistical feature selection. DR Lesion Discrimination is achieved using Machine Learning approaches.

4.2.2 Proposed Hybrid Lesion Detection Technique

A Hybrid Lesion Detection (HLD) technique is proposed in this work that aims at providing the assistance to the ophthalmologists for the detection of DR abnormalities present in the retinal fundus images. Background segmentation step clearly indicates non-diseased and diseased fundus images, as the lesion portions are observable in the diseased retinas. Diseased foreground retinal fundus images after removal of the background include two types of lesions (red and yellow). Thus, for the identification of these pathological symptom, HLD technique is proposed in this work whose sequential steps are detailed in Figure 4.5.

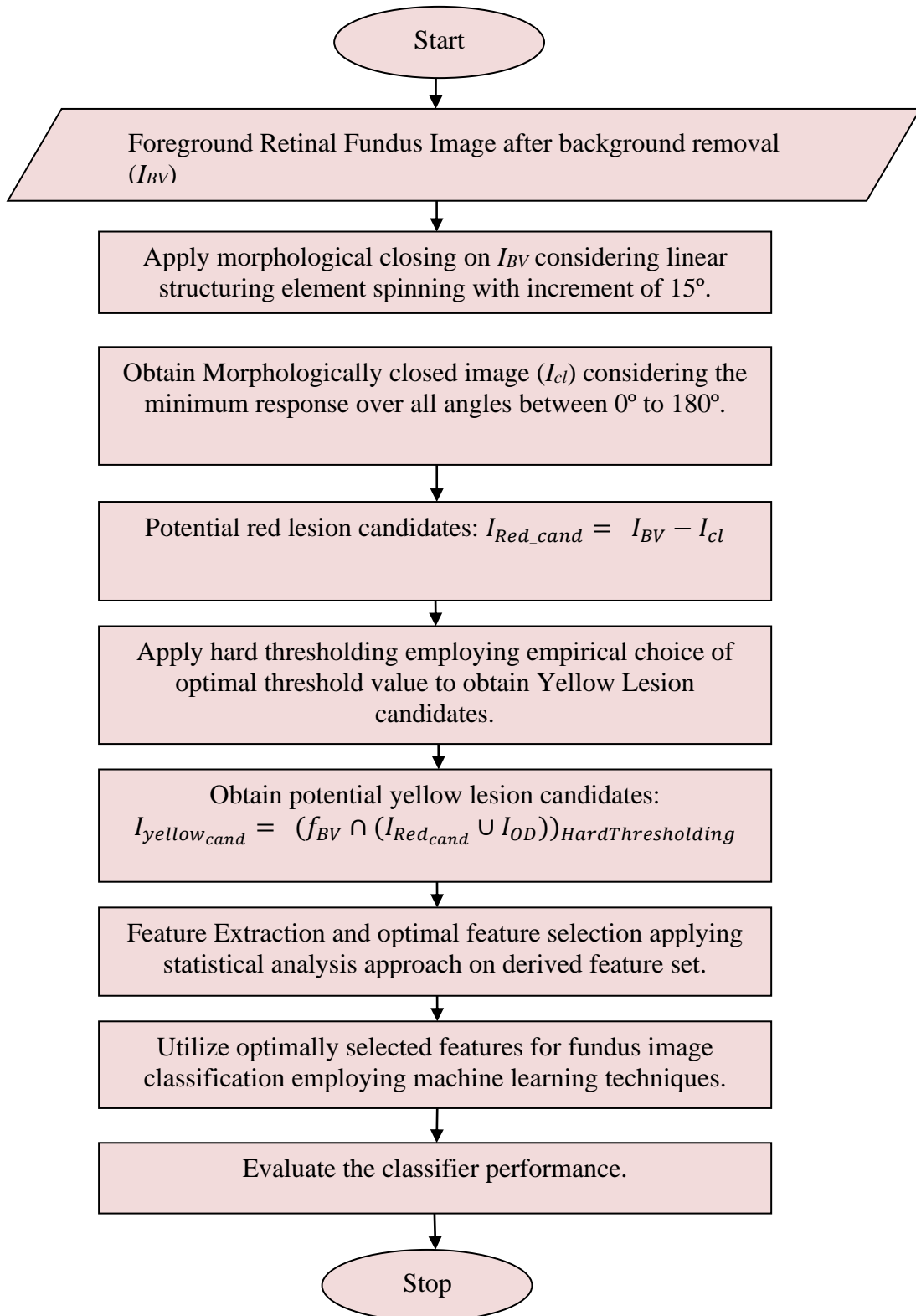


Figure 4.5: Flowchart for Proposed Hybrid Lesion Detection

To identify red lesions, a minimally angular response is considered, adding a morphologically closed image. Yellow lesions are extracted by the use of a hard

thresholding operation, which is empirically selected by choosing the optimal threshold value [7]. Lesion histogram properties were also considered for threshold selection to identify lesion candidates [123, 210].

Statistical Analysis:

The Lesion identification step is followed by optimal feature selection using attribute extraction and statistical analysis. Extensive literature survey and exploitation of wide range of features, reveals that majorly three types of features sets are considered relevant for DR lesion discrimination [211, 212]. The feature set includes shape, intensity and textural attributes which comprises a totality of 34 features extracted consisting of 11 shape features, 9 pixel based intensity features, and 14 GLCM features (detailed explanation in Appendix 1) [21, 98]. Eleven shape features exploiting the geometric properties of the lesions includes area, convex area, perimeter, major and minor axis length, eccentricity, orientation, diameter, solidity, extent, and compactness. Nine pixel based intensity features were exploited including maximum intensity, minimum intensity, mean, median, Standard Deviation (SD), Inter-quartile Range (IQR), Mean Absolute Difference (MAD), skewness and kurtosis. These pixel-based features help to distinguish between lesion candidates and non-lesions. Fourteen Gray-Level Co-occurrence Matrix (GLCM) features including autocorrelation, correlation, contrast, energy, entropy, homogeneity, dissimilarity, cluster shade, cluster prominence, maximum probability, inverse difference normalized, inverse different moment normalized, information measure of correlation1 and information measure of correlation2 were exploited [21]. These GLCM features provide the texture based properties considering the spatial relationships of pixels in the image.

These handcrafted features are utilized by various researchers to obtain relevant information for accurate classification. All these features are subjected to statistical feature extraction utilizing the SPSS package tool [194] in order to facilitate dimensionality reduction. This reduced representation contains only the relevant information sufficient to discriminate between the fundus images as well as different DR lesions. The statistical significance of features equality of means (μ) is inferred from t -test based on hypothesis testing. The null hypothesis (H_0) for t -test is expressed by Eq. (4.2) and it state that there is no significant difference between the mean values

of features differentiating the two classes. The null hypothesis rejection (H_1) is expressed by Eq. (4.3) and it state the significant difference between the means of features of two separate classes of DR abnormality.

$$H_0: \mu_0 = \mu_1 \quad (4.2)$$

$$H_1: \mu_0 \neq \mu_1 \quad (4.3)$$

From the t -test descriptive, it is indicated that the null hypothesis is accepted if significance values for the feature set are greater than 0.05 otherwise the hypothesis is rejected.

Similarly, for ANOVA, the null hypothesis defines the significant difference between the variances (σ) of feature set distinguishing between DR abnormality classes. The null hypothesis and its rejection for ANOVA test are presented in Eq. (4.4) and Eq. (4.5) respectively.

$$H'_0: \sigma_0 = \sigma_1 \quad (4.4)$$

$$H'_1: \sigma_0 \neq \sigma_1 \quad (4.5)$$

The final phase of the proposed methodology involves the classification of diseased and non-diseased fundus images and DR lesion detection using machine learning techniques utilizing optimally selected features after exhaustive statistical analysis to achieve better performance.

The literature highlights several classifier approaches in order to classify DR abnormalities. The common choice of utilizing Support Vector Machine (SVM) for binary classification make this classifier suitable for our problem [23]. The SVM based classification approach is utilized as it incurs low computational complexity for binary classification. The strength of SVM classifier lies in its ability of handling the imbalanced distribution of true and false samples [24, 25]. This research work also utilizes Multi-Layer Perceptron Neural Network (MLPNN) classifier are employed for lesion detection. The multi-class classification of DR abnormalities into red and yellow lesions employs MLP neural network-based classification approach, due to its ability to interpret the outcome of uncertain data without having previous knowledge of the evenness of the data through weight adjustment flexibility [30].

4.3 RESULTS OF DIABETIC RETINOPATHY DISCRIMINATION

The results of the proposed HLD technique are evaluated using three-fold analysis in terms of visual, statistical and performance assessment. The research work is performed on two benchmark datasets to establish the generalization competence of the proposed methodology irrespective of image resolution. The classification approach used in this work for abnormality detection utilizes 70%-30% training and testing criteria with 10-fold cross validation. Primarily, the outcomes for background segmentation are presented followed by the results of fundus image discrimination and DR lesion discrimination.

Physical and pathological regions of raw fundus images are improved using image pre-processing and background segmentation steps to remove its poor contrast and insufficient illumination effects [48]. Therefore, the proposed methodology includes image variation attenuation, green channel conversion, contrast enhancement followed by the segmentation of OD and blood vessel removal steps which are illustrated for DIARETDB1 dataset in Figure 4.6 and STARE dataset in Figure 4.7.

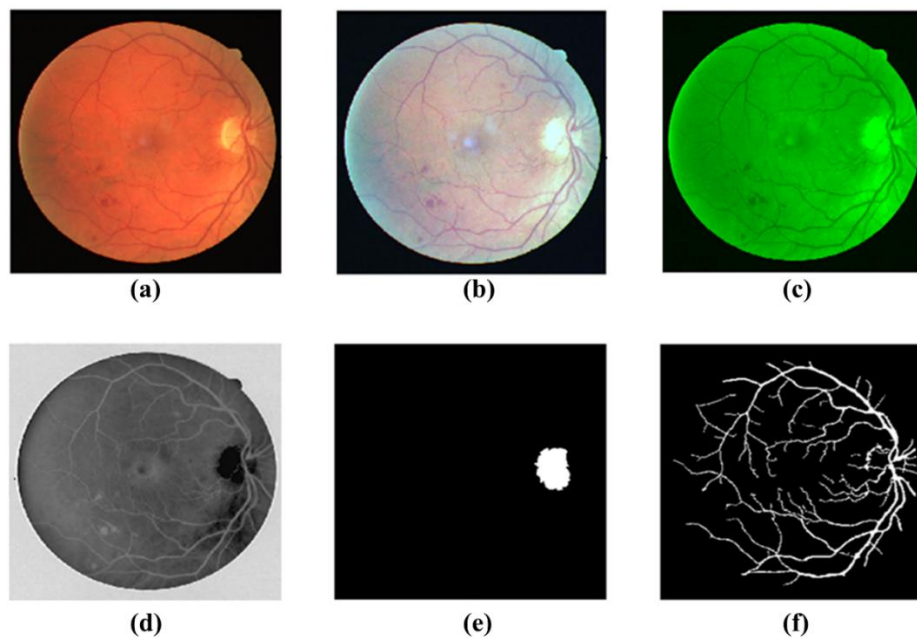


Figure 4.6: Image pre-processing stages for DIARETDB1 dataset image: (From left to right) (a) Original fundus image, (b) Variation attenuated fundus image, (c) Green channeled fundus image, (d) Contrast-enhanced fundus image, (e) Segmented OD portion, (f) Extracted blood vessels.

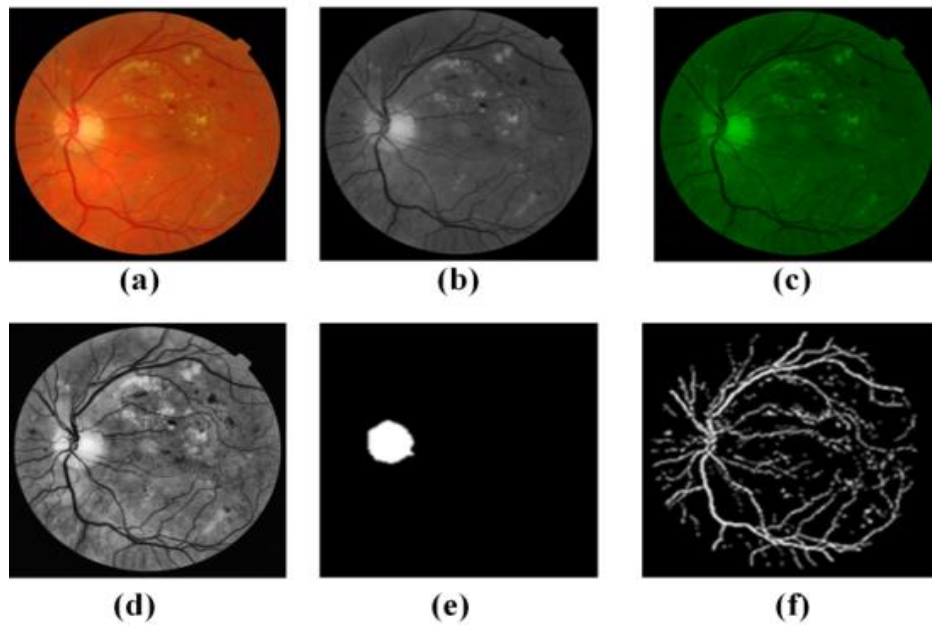


Figure 4.7: Image Pre-processing stages for STARE dataset image: (From left to right) (a) Original fundus image, (b) Variation attenuated image, (c) Green channeled fundus image, (d) Contrast-enhanced fundus image, (e) Segmented OD portion, (f) Extracted blood vessels.

OD can be misclassified as lesion portions because of its similar intensity properties like yellow lesions. Therefore, this physiological portion is needed to be removed before proceeding to the lesion recognition phase. Blood vessels can also be considered as pathological symptoms and can be misclassified as MA and HEMs red lesions. These unwanted anatomical region and artifacts are eliminated utilizing the pre-processing steps so that they do not impede the DR diagnosis. After applying background segmentation, it is interpreted that foreground lesion portions can only be seen in the diseased fundus images and no such portions are observed in non-diseased images.

The investigation of background segmentation yields the foreground fundus images for DR abnormality detection. Therefore, statistical and performance analysis of diabetic retinopathy discrimination strategies: Fundus image discrimination and DR lesion detection for abnormality discernment, is done in the following section.

4.3.1 Statistical Analysis and Discrimination of Fundus Images

Fundus image discrimination distinguishes between the diseased and non-diseased fundus images using the descriptive of derived feature set. This is

accomplished using two-fold scheme; statistical feature analysis for the selection of relevant features followed by fundus image classification.

4.3.1.1 Statistical Analysis of Derived Feature set

The feature set briefed in section 4.2.2 is derived for fundus image discrimination and statistical analysis of the derived feature set is done using the SPSS statistical package. The statistical analysis of the descriptive feature set is normalized using box plot analysis. Box plot analysis is graphical representation of normality visualization of the feature set and the box plots for selective shape, intensity and GLCM features are shown in Figure 4.8.

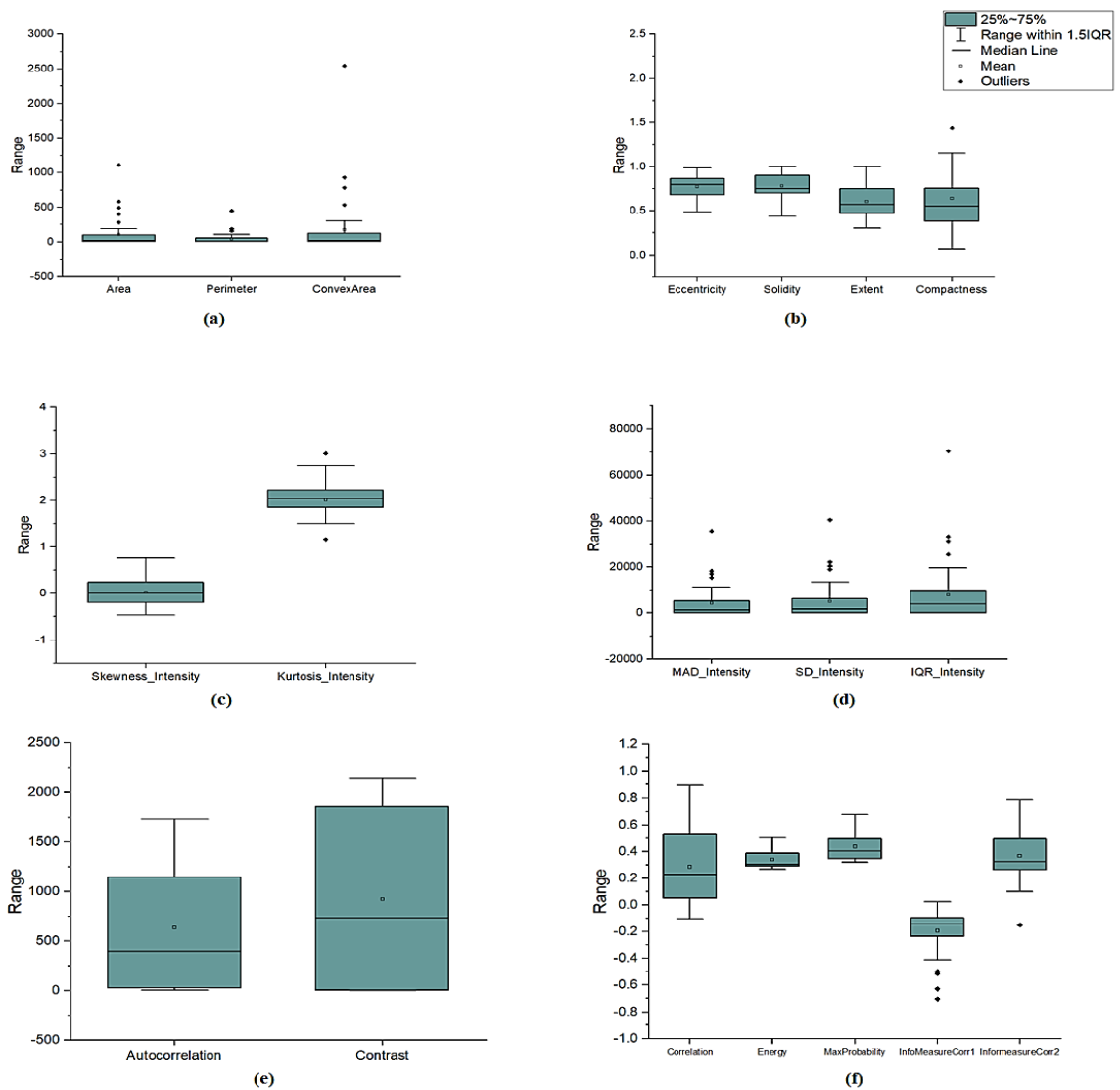


Figure 4.8: Box plots of some of the Extracted Feature Set: (a) and (b) Shape features, (c) and (d) Intensity features, (e) and (f) GLCM features

Box-plots indicates the quartile ranges specifically pin-pointing the outliers [195]. The outliers are those feature values which do not fit in the normalized feature set range and they can be discarded for further computation and are indicated by individual points outside the rectangular box. Outliers are correctly pointed with the cross marks and the feature significance is indicated by different quartile ranges. The quartile ranges of individual features show the significant variations, distinguishing between the features of diseased and non-diseased fundus images.

Optimally selected features are obtained using exhaustive statistical analysis done employing ANOVA and *t*-test statistical tools as tabulated in Table 4.1. This step of feature reduction ensures the reduced dimensional complexity along with increased accuracy rate improving the diagnosis. A significant value (*p*-value) analysis is performed to obtain the most prominent features from the entire feature set. Features having a *p*-value less than 0.05 are the prominent ones, however the features with *p*-value greater than 0.05 are discarded.

From the tabular representation, the *p*-values for two features namely; *eccentricity* and *orientation* came out to be greater contributing least in the feature selection process, therefore, these two features are discarded and are not used for classification.

Table 4.1: Statistical analysis of extracted feature set using *t*-test and ANOVA

Geometric Features			Intensity Features			GLCM Textural features		
Features	<i>t</i> -test (Sig.)	ANOVA (Sig.)	Features	<i>t</i> -test (Sig.)	ANOVA (Sig.)	Features	<i>t</i> -test (Sig.)	ANOVA (Sig.)
<i>Area</i>	0.019	0.019	<i>Min. Int.</i>	0.003	0.000	<i>Auto Correlation</i>	0.001	0.001
<i>Perimeter</i>	0.040	0.033	<i>Max. Int.</i>	0.000	0.000	<i>Correlation</i>	0.000	0.000
<i>Major_Axis_Length</i>	0.033	0.003	<i>Mean Int.</i>	0.000	0.000	<i>Contrast</i>	0.000	0.000
<i>Minor_Axis_Length</i>	0.011	0.005	<i>Med. Int.</i>	0.000	0.000	<i>ClusterShade</i>	0.005	0.007
<i>Eccentricity</i>	0.062	0.062	<i>MAD Int.</i>	0.000	0.000	<i>ClusterProminance</i>	0.000	0.000
<i>Convex_Area</i>	0.005	0.002	<i>SD Int.</i>	0.000	0.000	<i>Energy</i>	0.002	0.000
<i>Orientation</i>	0.102	0.102	<i>IQR</i>	0.000	0.000	<i>Entropy</i>	0.001	0.000
<i>Equiv_dia</i>	0.002	0.002	<i>Skewness</i>	0.012	0.015	<i>Homogeneity</i>	0.000	0.000
<i>Solidity</i>	0.015	0.007	<i>Kurtosis</i>	0.005	0.005	<i>InverseDiffNorm</i>	0.000	0.000
<i>Extent</i>	0.033	0.030				<i>InvDiffMoment</i>	0.007	0.007
<i>Compactness</i>	0.002	0.000				<i>Dissimilarity</i>	0.000	0.000
						<i>MaxProb</i>	0.000	0.000
						<i>InfoCorr1</i>	0.002	0.000
						<i>InfoCorr2</i>	0.005	0.005

4.3.1.2 Fundus Image Discrimination

The reduced feature set with thirty-two features is used for SVM and MLPNN classification to perform fundus image and lesion discrimination in the next stage. Figure 4.9 provides the performance metrics for non-diseased and diseased fundus image discrimination in terms of sensitivity, specificity, accuracy, and PPV.

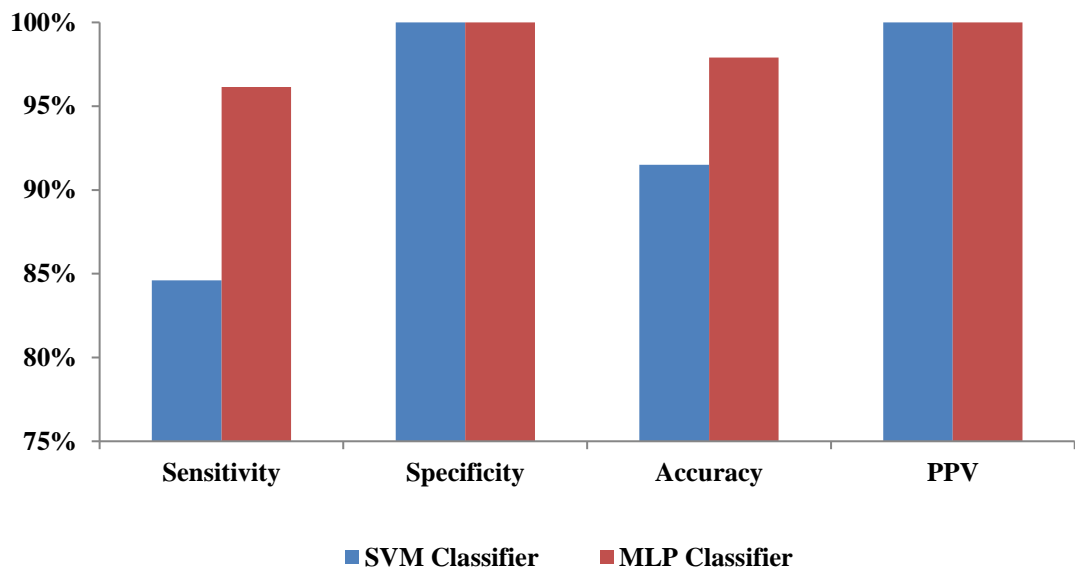


Figure 4.9: Performance metrics for fundus image discrimination

The overall performance is measured considering two different classification schemes; SVM classifier utilizing Gaussian RBF kernel and MLPNN based classification. The accuracy, 91.50%; sensitivity, 84.61%; specificity and PPV, 100% each are observed for diseased and non-diseased fundus image discrimination using SVM classifier. On the other hand, overall accuracy of 97.90% is observed for MLPNN classifier-based fundus image discrimination. MLPNN provides better performance for two class image discrimination comparatives to the SVM classifier utilized in this work. Sensitivity, 96.15%; specificity, 100%, and PPV, 100% values are obtained using MLPNN classifiers. After fundus image discrimination, DR lesion detection is important to aid the ophthalmologists for accurate DR screening and diagnosis.

4.3.2 Results of Proposed HLD Technique

DR lesion detection is served by lesion candidate extraction applying the proposed HLD technique, then the identified lesions are subjected to feature extraction and selection followed by the classification of DR pathologies.

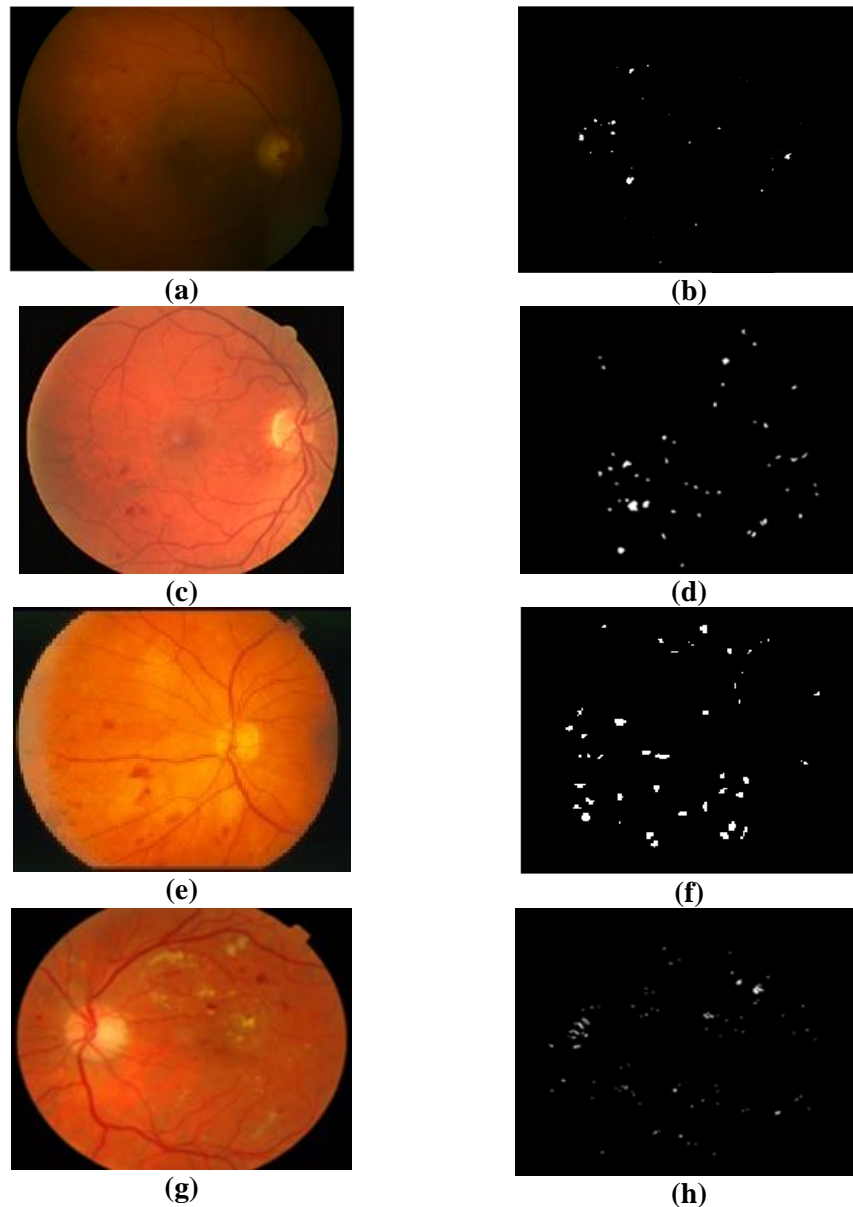


Figure 4.10: Experimental results of Red Lesion Detection: (a), (c), (e), (g) Original fundus image; (b), (d), (f), (h) Detected red lesion candidates from DIARETDB1 and STARE datasets respectively

The diseased fundus images are subjected to lesion candidate extraction by applying the proposed HLD technique. This is a hybrid technique employing morphological operations for candidate identification and thresholding function is

utilized for the removal of false candidates. The experimental results of the extraction of the red and yellow lesion are depicted in Figure 4.10 and Figure 4.11, respectively.

Figure 4.10 depicts the original fundus and the final red lesion candidate images collected from the benchmark dataset. The experiment is performed to detect true lesion but still, there may exist some false lesion candidates which may be some crossing points of the blood vessels, old scar in retina or some black spots. The results obtained shows that true exudates are clearly distinguished and identified using proposed HLD technique.

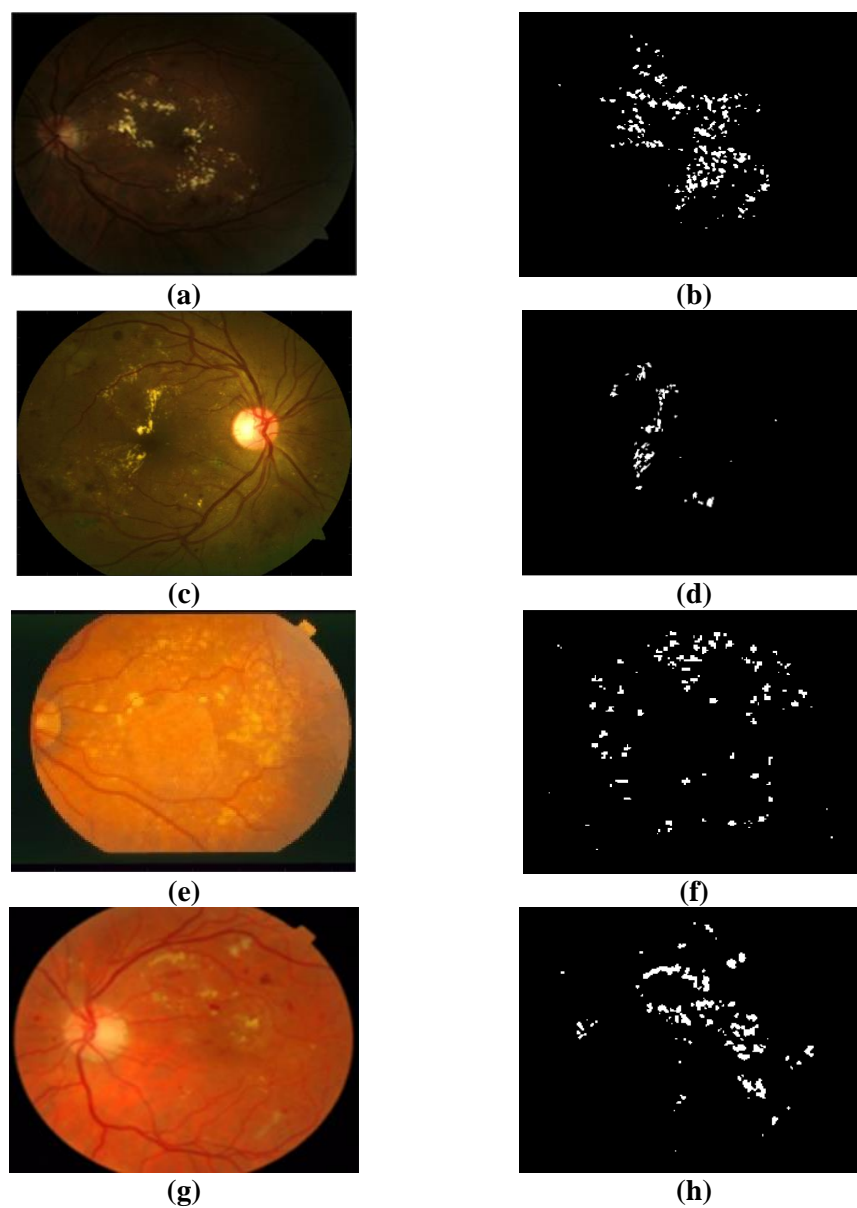


Figure 4.11: Experimental results of Yellow Lesion Detection: (a), (c), (e), (g) Original fundus image; (b), (d), (f), (h) Detected yellow lesion candidates from DIARETDB1 and STARE dataset respectively

The yellow lesion candidate detection results obtained for the retinal fundus images acquired from different datasets are shown in Figure 4.11. The pixels values in the output image are based on the comparison of corresponding pixels in the input fundus image with its neighbourhood pixels. Lesion candidates are separated by using thresholding operation to eliminate the noisy pixels from the fundus image removing the unnecessary details and extracting only the lesion information. Empirical threshold selection is done experimentally for the separation of candidate objects from the noisy background pixels. The selection of threshold is based on the features of background noise and retinal landmarks (OD and blood vessels) using connected component analysis. Depending upon this criteria, red and yellow DR lesion are detected based upon their circulatory. The visual DR lesion detected using the proposed HLD technique are further subjected to feature extraction and the derived feature set is statistically analyzed. The pathological features suitable for disease severity classification are provided by using the relevant feature set in order to serve DR lesion discrimination.

4.3.2.1 Statistical analysis for Feature selection

Exhaustive statistical analysis done for the reduction of feature set and to obtain the prominent features utilizing pair-wise correlation test, ANOVA and *t*-test statistical tools. To quantify the relationship between feature variables, pair-wise correlation test is performed and Pearson correlation coefficients are obtained which are tabulated in Table 4.2, Table 4.3 and Table 4.4 for Shape, Intensity, and GLCM features respectively.

From the pair-wise Pearson correlation coefficients obtained for shape features (represented in Table 4.2), it is analysed that *eccentricity* and *orientation* features are least correlated to all other shape features. Negative values of the Pearson correlation coefficient signify the negative correlation of feature sets.

Table 4.2: SPSS Pearson Correlation analysis of Shape features

Shape Features	Pearson Correlation Coefficients										
	Area	Perimeter	Major Axis Len.	Minor Axis Len.	Eccentricity	Convex Area	Orientation	Equiv. Dia.	Solidity	Extent	Compactness
Area	1.000	0.980	0.903	0.940	0.182	0.977	-0.067	0.954	-0.715	-0.609	-0.582
Perimeter	0.980	1.000	0.890	0.929	0.178	0.993	-0.002	0.923	-0.761	-0.627	-0.597
Major Axis Len.	0.903	0.890	1.000	0.821	0.328	0.862	-0.079	0.927	-0.779	-0.673	-0.667
Minor Axis Len.	0.940	0.929	0.821	1.000	-0.009	0.904	-0.092	0.958	-0.768	-0.601	-0.693
Eccentricity	0.182	0.178	0.328	-0.009	1.000	0.180	0.038	0.153	-0.226	-0.231	-0.176
Convex Area	0.977	0.993	0.862	0.904	0.180	1.000	0.008	0.891	-0.703	-0.583	-0.518
Orientation	-0.067	-0.002	-0.079	-0.092	0.038	0.008	1.000	-0.131	-0.044	0.031	-0.035
Equivalent Diameter	0.954	0.923	0.927	0.958	0.153	0.891	-0.131	1.000	-0.778	-0.650	-0.733
Solidity	-0.715	-0.761	-0.779	-0.768	-0.226	-0.703	-0.044	-0.778	1.000	0.860	0.816
Extent	-0.609	-0.627	-0.673	-0.601	-0.231	-0.583	0.031	-0.650	0.860	1.000	0.660
Compactness	-0.582	-0.597	-0.667	-0.693	-0.176	-0.518	-0.035	-0.733	0.816	0.660	1.000

Table 4.3: SPSS Pearson Correlation analysis of Intensity features

Intensity Features	Pearson Correlation Coefficients								
	Min. Intensity	Max. Intensity	Mean Intensity	Median Intensity	MAD Intensity	SD Intensity	IQR Intensity	Skewness	Kurtosis
Min. Intensity	1.000	0.990	0.997	0.997	0.565	0.577	0.552	0.379	0.387
Max. Intensity	0.990	1.000	0.997	0.997	0.676	0.687	0.662	0.399	0.409
Mean Intensity	0.997	0.997	1.000	1.000	0.624	0.636	0.612	0.383	0.394
Median Intensity	0.997	0.997	1.000	1.000	0.623	0.634	0.611	0.379	0.391
MAD Intensity	0.565	0.676	0.624	0.623	1.000	0.999	0.997	0.303	0.307
SD Intensity	0.577	0.687	0.636	0.634	0.999	1.000	0.993	0.320	0.327
IQR	0.552	0.662	0.612	0.611	0.997	0.993	1.000	0.276	0.264
Skewness	0.379	0.399	0.383	0.379	0.303	0.320	0.276	1.000	0.510
Kurtosis	0.387	0.409	0.394	0.391	0.307	0.327	0.264	0.510	1.000

Table 4.4: SPSS Pearson Correlation analysis of GLCM features

GLCM Features	Pearson Correlation Coefficients													
	Auto Corr.	Corr.	Contrast	Cluster Shade	Cluster Prom.	Energy	Entropy	Homo.	Inv.Diff.Norm.	Inv.Diff.Mom.	Diss.	Max Prob.	Inf. Corr. 1	Inf. Corr. 2
Auto Correlation	1.000	-0.718	0.909	-0.459	0.969	-0.693	0.569	-0.791	-0.902	-0.498	0.906	-0.697	0.548	-0.480
Correlation	-0.718	1.000	-0.839	-0.021	-0.738	0.646	-0.486	0.963	0.860	0.549	-0.851	0.603	-0.819	0.815
Contrast	0.909	-0.839	1.000	-0.075	0.939	-0.722	0.585	-0.915	-0.997	-0.557	0.999	-0.769	0.548	-0.524
ClusterShade	-0.459	-0.021	-0.075	1.000	-0.286	0.100	-0.093	-0.012	0.063	0.026	-0.069	0.038	-0.093	0.009
ClusterProm.	0.969	-0.738	0.939	-0.286	1.000	-0.722	0.599	-0.817	-0.930	-0.513	0.935	-0.723	0.582	-0.517
Energy	-0.693	0.646	-0.722	0.100	-0.722	1.000	-0.576	0.790	0.743	0.579	-0.734	0.948	-0.657	0.405
Entropy	0.569	-0.486	0.585	-0.093	0.599	-0.576	1.000	-0.542	-0.578	0.225	0.582	-0.515	0.465	-0.314
Homogeneity	-0.791	0.963	-0.915	-0.012	-0.817	0.790	-0.542	1.000	0.937	0.619	-0.927	0.769	-0.761	0.707
InverseDiffNorm	-0.902	0.860	-0.997	0.063	-0.930	0.743	-0.578	0.937	1.000	0.580	-0.999	0.777	-0.581	0.548
InvDiffMoment	-0.498	0.549	-0.557	0.026	-0.513	0.579	0.225	0.619	0.580	1.000	-0.570	0.606	-0.433	0.397
Dissimilarity	0.906	-0.851	0.999	-0.069	0.935	-0.734	0.582	-0.927	-0.999	-0.570	1.000	-0.774	0.565	-0.537
MaxProb	-0.697	0.603	-0.769	0.038	-0.723	0.948	-0.515	0.769	0.777	0.606	-0.774	1.000	-0.475	0.304
InfoCorr1	0.548	-0.819	0.548	-0.093	0.582	-0.657	0.465	-0.761	-0.581	-0.433	0.565	-0.475	1.000	-0.867
InfoCorr2	-0.480	0.815	-0.524	0.009	-0.517	0.405	-0.314	0.707	0.548	0.397	-0.537	0.304	-0.867	1.000

Intensity feature correlation analysis presented in Table 4.3 reveals that all the intensity features are correlated to each other. However, skewness and kurtosis features are less correlated as compared to other intensity features, but significant enough to be used in the classification stage. Table 4.4 shows that all the GLCM features except *Cluster shade* are prominent. Further analysis using other statistical techniques is required to check less related features for DR classification.

Further investigation is done in terms of descriptive statistical analysis using *t*-test and ANOVA for optimal feature selection. To determine the statistical significance of features equality of means (μ) and variances (σ) are inferred from *t*-test for the two classes of lesions (red lesion and yellow lesion) based on hypothesis testing described in section 4.2.2.

From the descriptive of *t*-test and ANOVA, it is indicated that the null hypothesis is accepted if significance values for the feature set are greater than 0.05 otherwise the hypothesis is rejected. The optimal feature selection process using descriptive statistical analysis through *t*-test and ANOVA is depicted in Table 4.5.

Table 4.5: Statistical analysis of extracted feature set using *t*-test and ANOVA

Geometric Features			Intensity Features			GLCM Textural features		
Features	<i>t</i> -test (Sig.)	ANOVA (Sig.)	Features	<i>t</i> -test (Sig.)	ANOVA (Sig.)	Features	<i>t</i> -test (Sig.)	ANOVA (Sig.)
<i>Area</i>	0.001	0.000	<i>Min. Int.</i>	0.000	0.029	<i>Auto Correlation</i>	0.000	0.000
<i>Perimeter</i>	0.001	0.000	<i>Max. Int.</i>	0.000	0.000	<i>Correlation</i>	0.000	0.014
<i>Major_Axis_Length</i>	0.000	0.000	<i>Mean Int.</i>	0.000	0.001	<i>Contrast</i>	0.000	0.000
<i>Minor_Axis_Length</i>	0.000	0.001	<i>Med. Int.</i>	0.000	0.001	<i>ClusterShade</i>	0.584	0.421
<i>Eccentricity</i>	0.275	0.411	<i>MAD Int.</i>	0.000	0.000	<i>ClusterProminance</i>	0.000	0.000
<i>Convex_Area</i>	0.007	0.000	<i>SD Int.</i>	0.000	0.000	<i>Energy</i>	0.000	0.000
<i>Orientation</i>	0.650	0.559	<i>IQR</i>	0.000	0.000	<i>Entropy</i>	0.000	0.005
<i>Equiv_dia</i>	0.000	0.000	<i>Skewness</i>	0.013	0.048	<i>Homogeneity</i>	0.000	0.036
<i>Solidity</i>	0.000	0.004	<i>Kurtosis</i>	0.005	0.026	<i>InverseDiffNorm</i>	0.000	0.024
<i>Extent</i>	0.001	0.038				<i>InvDiffMoment</i>	0.048	0.007
<i>Compactness</i>	0.000	0.020				<i>Dissimilarity</i>	0.001	0.000
						<i>MaxProb</i>	0.000	0.000
						<i>InfoCorr1</i>	0.000	0.000
						<i>InfoCorr2</i>	0.001	0.005

It is observed that the significance values of t -test and ANOVA provides p -values greater than 0.05 for three features; eccentricity, orientation and cluster shade. Therefore, out of the totality of thirty-four features, thirty-one are selected for the DR discrimination process at the classification stage.

4.3.2.2 Discrimination of DR pathologies

The remarkable performance of MLPNN classifier for fundus image discrimination, as suggested in the literature, makes it suitable for DR lesion discrimination. For every training sample, hidden layer weights are updated using error propagation in the backward direction for weight updation. The sensitivity, specificity, accuracy and PPV performance parameters are calculated to observe the clinical relevance of the detected pathological symptoms. Various performance indices observed for DR lesion discrimination are depicted in Figure 4.12.

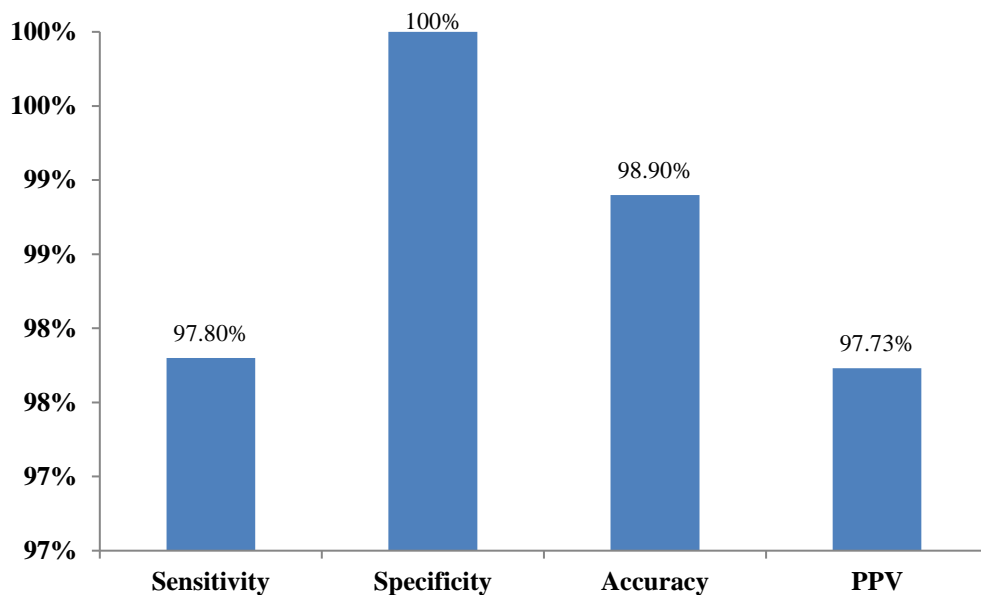


Figure 4.12: MLPNN classification performance for DR lesion detection

A mass screening solution is provided with 98.90% accuracy performance by the proposed system for DR lesion detection with less computational complexity. The other performance measures computed for MLPNN classification approach yields sensitivity, 97.80%; specificity, 100% and PPV of 97.73%.

4.4 DISCUSSION

The proposed method provides successful discrimination ability between diseased and non-diseased fundus images simultaneously providing better categorization of red and yellow lesions. Most of the accurate lesions are detected employing the HLD technique and some of the fallacious lesion portions, if exists, are due to the branched blood vessels scars or blood spots from the patient's previous medical history. When histogram properties of red and yellow lesions are observed, it is revealed that red lesions have darker intensity histogram range comparative to yellow lesions with brighter intensity ranges [123]. Very tiny and small false red and yellow lesion candidates are difficult to identify and fallacious lesion due to reflection of nerve fibre layers, blood spots and scars are discarded and are not considered as lesion candidates [30]. Various features were analysed after lesion identification from the diseased fundus images.

Abnormality identification and lesion discrimination are followed by feature attribute extractions which are further provided to statistical analysis for optimal feature selection. Features providing significance value less than 0.05 are selected and out of thirty-four extracted features, only two features: eccentricity and orientation do not provide significance. Thirty-two features providing a significant difference between the mean values of non-diseased and diseased DR fundus images are statistically selected and are provided to the classification stage. SVM and MLPNN classifiers are used for fundus image discrimination into diseased and non-diseased classes. Accuracy value of 91.50% is obtained by SVM classifier and to improve the classification performance along with less complexity, a neural network-based MLPNN classifier is used which enhances the classification accuracy by 97.90% for fundus image discrimination. Continuous training and weight updation using backpropagation are employed for error function minimization.

4.4.1 Comparative analysis with the existing techniques

The comparative analysis of the proposed fundus image discrimination approach over another state-of-the-art methods employing the same standard dataset is shown in Figure 4.13.

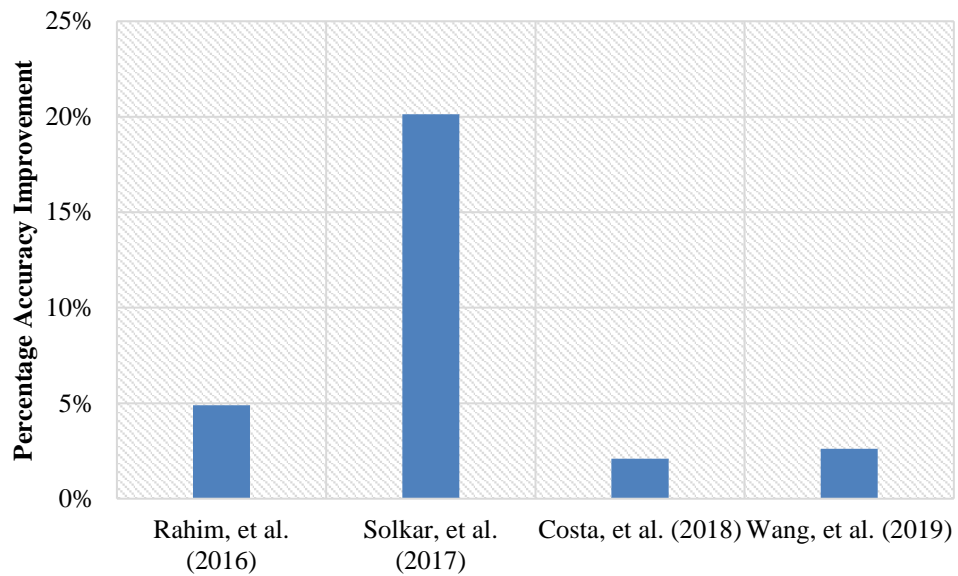


Figure 4.13: Percentage accuracy improvement of fundus image discrimination approach over the other approaches for classification of non-diseased and diseased fundus images

The proposed approach provides a maximum 20.13% improvement with Solkar, *et al.* [213] outperforming the state of art methods in terms of accuracy for diseased and non- diseased fundus classification, as indicated in Figure 4.13. Other methods provide percentage accuracy improvement of 4.90% with Rahim, *et al.* [209], 2.10% with Costa, *et al.* [214] and 2.61% with Wang, *et al.* [219] providing an effective screening solution for fundus image discrimination to facilitate automated detection of diabetic retinopathy. The diseased images containing different lesions can be discriminated based on the lesion intensity range after fundus image discrimination. Red lesions belong to darker intensity regions; however, yellow lesions belong to the brighter side of the dynamic range. The presence of DR abnormalities is detected using these lesions which identify the patients requiring immediate ophthalmic care thus reducing the burden of ophthalmologists. Accuracy value of 98.90% is provided by the MLPNN classifier for lesion classification into red and yellow lesions. MLPNN classifier is flexible for image processing based applications due to its ability to learn from experience.

Unlike other classification techniques, MLPNN is preferred for DR lesion discrimination due to the technical functionality of no restriction to the input data distribution. Accuracy value of 98.90% is obtained for the generalized MLPNN classifier with significantly better performance than the existing approaches. Table 4.6

provides the comparative percentage accuracy improvement of the proposed approach with state-of-the-art techniques.

Table 4.6: Accuracy improvement of lesion detection approach with the existing state of the art approaches

Techniques	Accuracy	% age Accuracy Improvement
Nayak, <i>et al.</i> (2008) [215]	93.00%	5.90%
Priya, <i>et al.</i> (2013) [109]	95.38%	3.52%
Paing, <i>et al.</i> (2016) [216]	96.00%	2.90%
Saha, <i>et al.</i> (2018) [217]	95.13%	3.77%
Fan, <i>et al.</i> (2018) [218]	96.00%	2.90%
Wang, <i>et al.</i> (2019) [219]	95.41%	3.65%

Maximum 5.90% accuracy improvement is provided by the proposed lesion detection approach with state-of-the-art technique provided by Nayak, *et al.* [215]. Comparison with other techniques provides accuracy improvements of 3.52%, 2.90%, 3.77%, 2.90% and 3.65% with Priya, *et al.* [109], Paing, *et al.* [216], Saha, *et al.* [217], Fan, *et al.* [218] and Wang, *et al.* [219] respectively providing the suitable evidence of its outperformance with state-of-the-art approaches.

4.5 CONCLUSION

This chapter presents fundus image discrimination strategy to distinguish between diseased and non-diseased images and DR lesion discrimination approach for differentiating between red and yellow lesions. HLD technique is employed for DR lesion detection using SVM and MLPNN classifiers, to assist ophthalmologists in detecting DR severity. A totality of thirty-four features are extracted based on the geometry, intensity, and texture of the fundus images and identified anomalies. This feature set is subjected to exhaustive feature selection to obtain the optimal set of features for both the scenarios. Fundus image discrimination yields overall accuracies

of 91.50% and 97.90% using SVM and MLPNN classifiers while utilizing the optimized feature set comprising 32 features out of total 34 features. While for DR discrimination task, 31 features are selected after statistical analysis that provides 98.9% accuracy value utilizing the efficient MLPNN classifier. The proposed system outperforms existing work by showing significant accuracy improvement of 5.90% to provide a less complex and cost-effective DR screening solution for lesion discrimination. The novelty of our proposed approach lies in the statistical analysis performed on a comprehensive feature set for optimal feature selection. Another contribution of this research work is significantly improved candidate classification scheme using multi-layer perceptron networks that provide better accuracy and minimal run-time complexity. A robust alternative solution is achieved using the proposed approach for automated DR screening with optimally improved categorization ability of red and yellow lesions. This approach will aid automatic DR detection by integrating ophthalmic processing with optimal feature sets providing successful discrimination ability between healthy and DR symptomatic fundus images. Further, after pathology detection and discrimination, tracking the appearance and progression of disease is of utmost importance in order to aid the ophthalmologists in understanding the likelihood of vision loss for referral and treatment. Therefore, the next chapter of this thesis is dedicated to the recognition of retinal feature patterns yielding the DR severity grading based on the identified lesions.

CHAPTER 5

**DIABETIC RETINOPATHY
CATEGORIZATION AND ITS
SEVERITY GRADING**

CHAPTER 5

DIABETIC RETINOPATHY CATEGORIZATION AND ITS SEVERITY GRADING

5.1 INTRODUCTION

The majority of patients with DR may not feel any vision changes in the early stages, but as the condition prevails, vision loss becomes severe. The rate of DR progression may increase rapidly making it important to monitor the retinal disease development. This condition gives rise to the need for early diagnosis through regular retinal image screening as well as continuous periodic eye tests. The identification of DR pathological symptoms is followed by disease severity grading in order to track its appearance and progression.

DR categorization and grading plays a vital role in the recognition of retinal features enabling the measurement and monitoring of appropriate severity levels. Every DR patient has a unique combination of symptoms and rate of disease progression that requires significant treatment approach to preserve the vision loss. Occurrence of a particular DR feature increases the likelihood of vision loss and if this situation is not tackled at its early stage, vision loss becomes inevitable. Particular retinal features indicate the disease progression and recognition of these patterns are used to grade retinopathy. DR grading provides a consistent retinopathy classification for providing appropriate level of service planning and evaluating quality of service provision. Thus, it is important to grade individual person's retinopathy making the likelihood of vision loss understandable to aid appropriate management by Ophthalmologists for patient referral and treatment [220].

Retinal abnormalities can be characterized by any kind of uneven changes in various retinal components [17]. Retinal images with no symptoms of DR are considered Non-Diseased fundus images and Non-Proliferative DR (NPDR) can be classified into mild, moderate, and severe stages based on the number of DR lesions. It is very difficult to differentiate between diabetic eye with no DR symptoms and those with the mild DR symptoms, as the only difference is the presence of very tiny MAs.

Both of them have very low risk to develop the progression to severe case of DR abnormality, however, yearly follow up is still required for these patients also. Moderate NPDR stage contains HEMs along with MAs but less than the severe NPDR case. The Severe grade of NPDR comprises 20 or more HEMs with prominent Intra-Retinal Microvascular Abnormality (IRMA) [221]. Patients suffering from severe NPDR condition are at high risk (more than 17%) [222] of developing Proliferative Diabetic Retinopathy (PDR) within one year, requiring routine follow-ups in every 2-4 months [220]. Figure 5.1 shows the difference between the normal retina having no DR symptoms and DR affected retina to provide a clear oversight of abnormality.

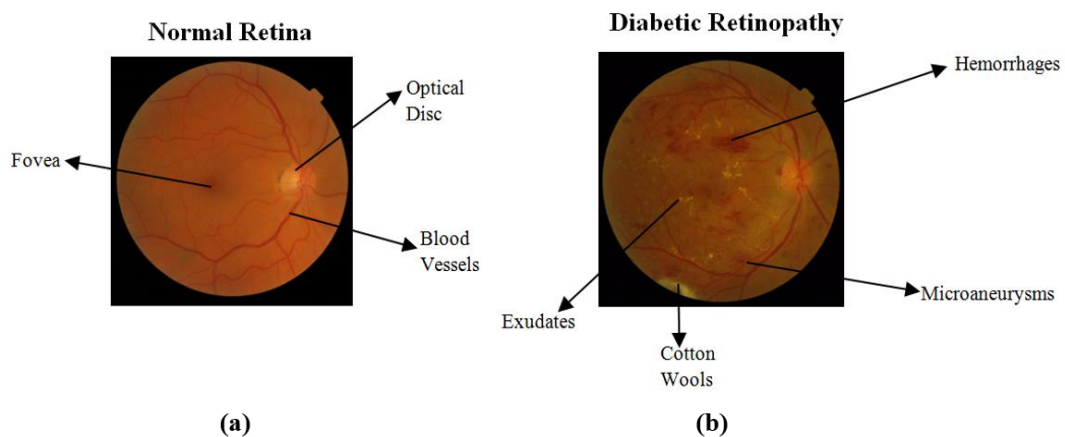


Figure 5.1: Differentiation of normal and DR affected retina

5.2 DR SEVERITY GRADING

The International Clinical Diabetic Retinopathy Disease Severity Scale [223] provides the DR grading from 0 to 4 severity levels. In this grading specification, grade 0 is indicated as non-DR, mild NPDR signs are indicated by grade 1, moderate NPDR are indicated by grade 2, severe NPDR are designated as grade 3 and PDR symptoms in fundus image. The occurrence of NPDR severities depends upon the presence of MAs, HEMs and IRMA, however, the PDR is indicated by neo-vascularization and vitreous haemorrhage. The detailed DR grading provided by International Clinical Diabetic Retinopathy Disease Severity Scale is given in Table 5.1.

Table 5.1: Illustration of International clinical DR severity scale

Disease Severity Scale	DR Grade	Description
0	Non- DR Grade	No retinopathy abnormalities are present
1	Mild NPDR grade	Only microaneurysms are present
2	Moderate NPDR grade	Number of microaneurysms increases but still less than severe NPDR grade
3	Severe NPDR grade	More than 20 intra-retinal microaneurysms or haemorrhages Occurrence of intra-retinal microvascular abnormalities (IRMA)
4	PDR grade	Presence of either neovascularization or pre-retinal vitreous haemorrhage

In this work, we have taken into account the grading of NPDR severities for early stage classification and prognosis. The NPDR grades ranges from severity scale 0 to 3 referring to the DR categorization using the standard guidelines for two discrepancies of DR: MAs and HEMs. Based upon the presence of DR abnormalities, ophthalmic experts rank the retinal fundus images into several severity grades. Table 5.2 depicted the DR severity grades along with their description.

Table 5.2: DR severity grades and their description

Retinopathy Grades	Grading Description
Grade 0	$(N_{MA} = 0)$ and $(N_{HEM} = 0)$
Grade 1	$(0 < N_{MA} \leq 5)$ and $(N_{HEM} = 0)$
Grade 2	$(5 < N_{MA} < 15)$ or $(0 < N_{HEM} \leq 5)$
Grade 3	$(N_{MA} \geq 15)$ or $(N_{HEM} \geq 5)$

N_{MA} = number of microaneurysms, N_{HEM} = number of haemorrhages

The Non-Diseased fundus images designated as Grade 0 with no DR symptoms. NPDR grade 1 can be characterized by 0 to 5 MA anomalies and no sign of HEM. Increased number of MAs (5 to 15) and 0 to 5 HEMs characterizes moderate NPDR grade as grade 2 while the presence of more number of MA and HEM (more than 20) anomalies signifies the NPDR grade 3. NPDR grade 3 is the highest retinopathy grade which comprises fundus images with more than 15 MAs or more than 5 HEMs. Similarly, IDRiD dataset consists of 168 images having retinopathy grade 0, 25 images with grade 1, 168 grade 2 images and 93 images are indicated as grade 3.

Serious efforts have been made by the researchers are to explore various DR screening methods to detect abnormalities at an early stage. However, studies revealed that the early stage DR diagnosis requires systematic and extensive screening due to the asymptomatic nature of retinopathy [17]. The major impediment in the current methodology lies in the actual lesion discrimination from the background noise as well as poor discrimination between blood vessels and other anatomical structures such as OD [14, 15]. The deficiency of qualified professionals for effective screening of vision threatening DR poses further challenges. Other constraint lies in the selection of feature set as well as the optimal choice of classifiers that can place a trade-off between classification accuracy and the high cost of manual computation. The purpose of this work is to address the shortcomings of the existing methods for the enhancement of DR classification and severity grading techniques. In this chapter, a novel Hierarchical Severity Grading (HSG) system is proposed to classify NPDR severities of retinal fundus images to help the ophthalmologists in effectual diabetic retinopathy detection and grading.

5.3 PROPOSED METHODOLOGY

A hierarchal DR grading system is proposed in this work for fundus image categorization on the basis of retinal pathological abnormalities. The challenges of retinal contextual landmark segmentation, retinal lesion discrimination and challenges of DR severity grade categorization are extensively eradicated in this research work. The steps involved in the proposed HSG system comprises retinal contextual landmark segmentation, anomaly detection, feature extraction, feature set reduction using statistical analysis, and DR severity grade classification.

Figure 5.2 depicts the step-wise implementation strategy of the proposed system.

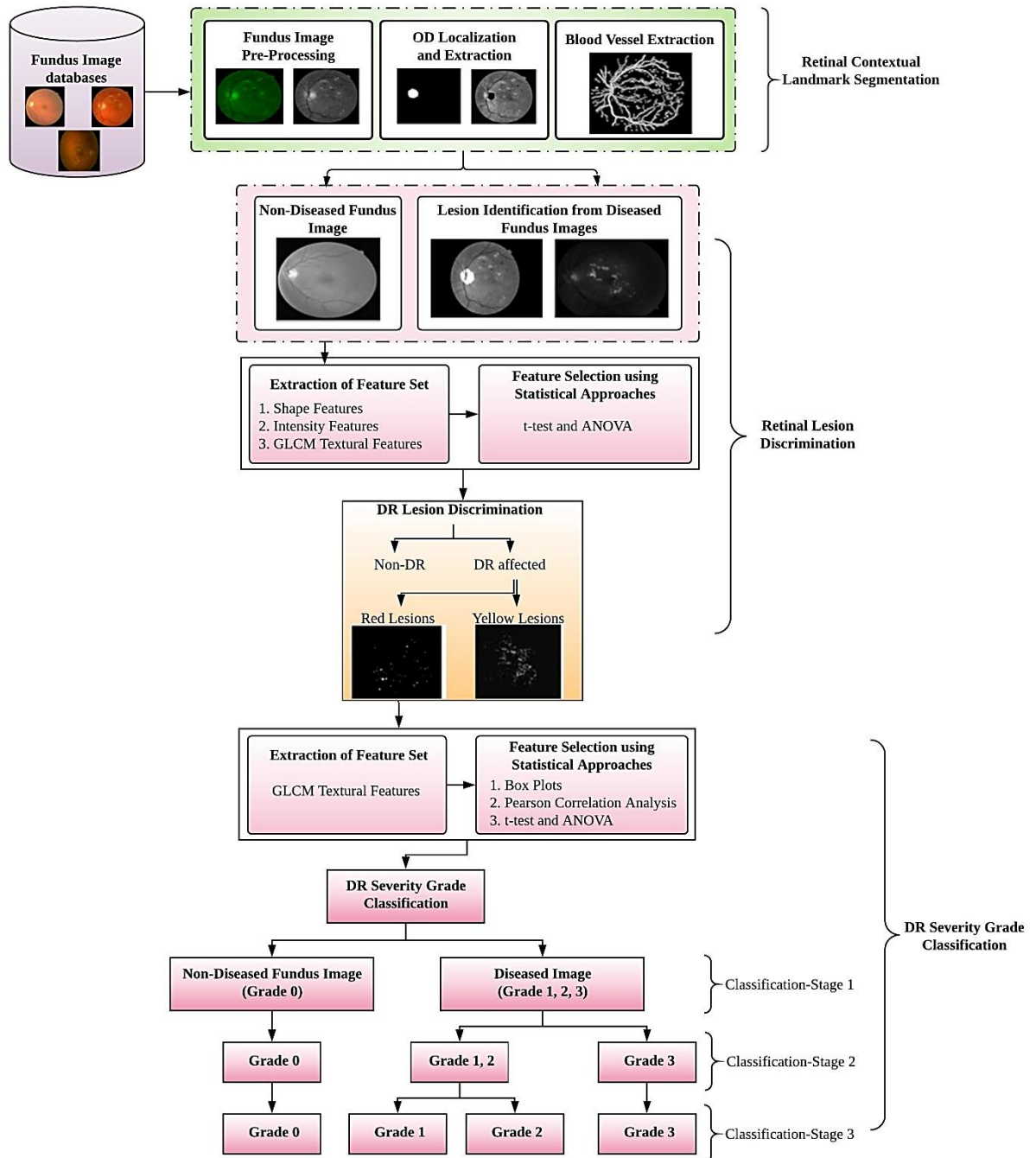


Figure 5.2: Block diagram of the proposed HSG grading system

Undesirable retinal components are masked using retinal contextual landmark segmentation in first stage of the proposed HSG grading system. Retinal Lesion discrimination is done using the foreground retinal image portion and the identified anomalies are subjected to Image Feature Vector (IFV) extraction. Statistical analysis of IFV resulted into optimally Reduced Image Feature Vector (RIFV) comprising of

selected feature set for DR classification. The individual effects of IFV and RIFV are determined on the classification accuracy in the context of different performance indices. The significant contribution of the HSG framework lies in critical evaluation of the derived attributes along with determining the capabilities of numerous classifiers to find the ideal characterization strategy for detection and grading of DR severity. The significance of the reduced feature set is validated by comparing its outcomes with the extracted feature set for severity grade classification. The proposed framework outperforms the existing techniques for NPDR severity grade classification when tested on a benchmark MESSIDOR [43] dataset. Latest IDRiD [44] dataset is used to validate the uniformity in the outcomes of the proposed system, justifying its generalization capabilities for DR severity grading.

Retinopathy grade-based description is considered for determining different severity grades which are given in Table 5.3. It specifies the diverse severity grades liable to the presence of MAs and HEMs accompanied by the number of images in each retinopathy grade.

Table 5.3: NPDR grades distribution for MESSIDOR and IDRiD datasets

Diabetic Retinopathy Grades	Number of Images in MESSIDOR Dataset	Number of Images in IDRiD Dataset
Grade 0	546	168
Grade 1	153	25
Grade 2	247	168
Grade 3	254	93

The flowchart of complete step-wise description of the proposed HSG system is shown in Figure 5.3.

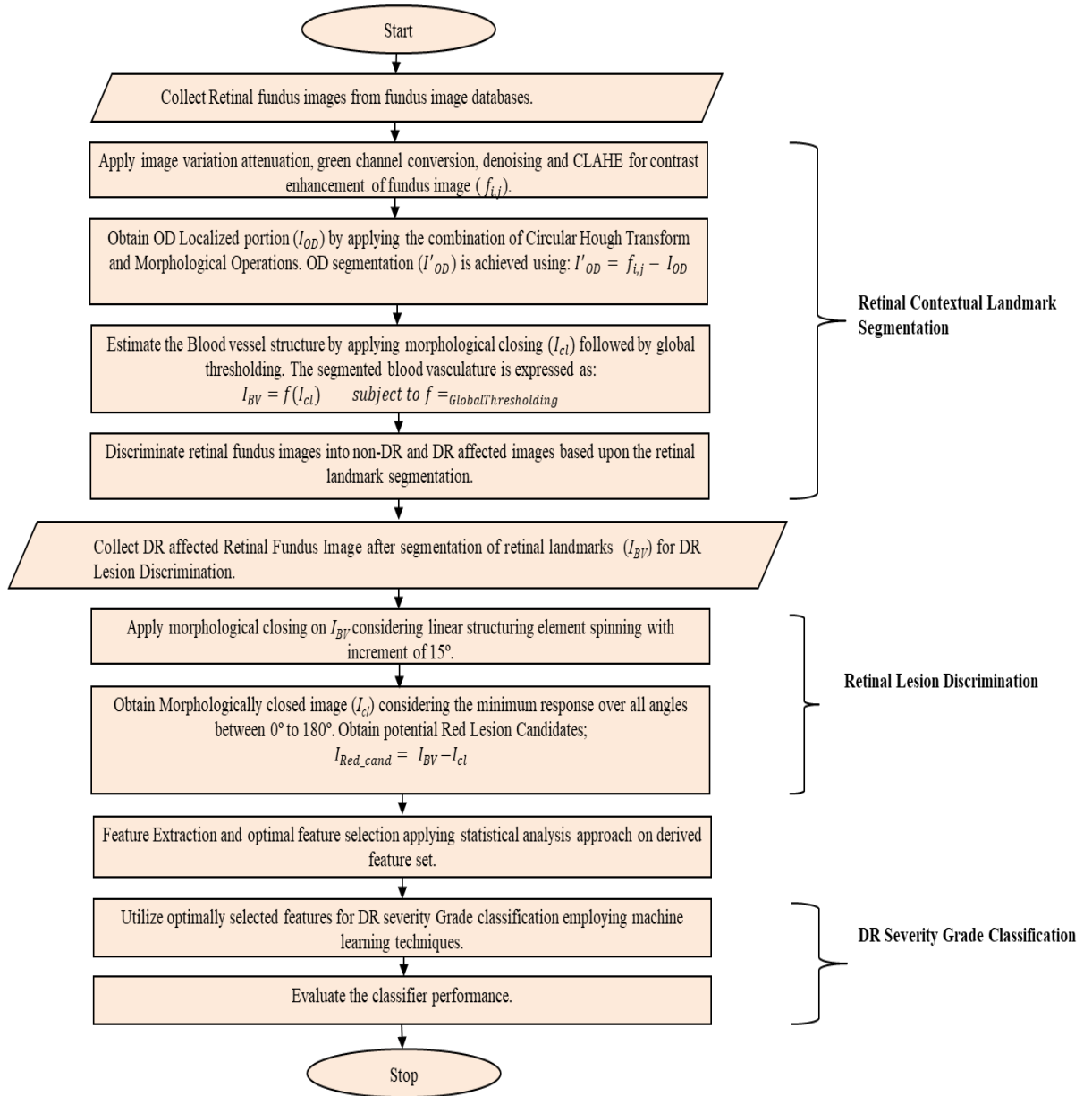


Figure 5.3: Flowchart of the proposed HSG system

The framework of the proposed scheme consists of three fundamental phases: first phase is retinal contextual landmark segmentation, second phase is discrimination of retinal lesion and third phase is categorization of DR severity. The identification of background portion and distinction of DR affected and non-DR retinal fundus images is facilitated using retinal contextual landmark segmentation stage. Discernment of different DR lesions is done by enabling retinal lesion discrimination strategy. The last phase of the proposed framework includes fundus image categorization into various DR grades on the basis of the rules obtained from the International Clinical Diabetic

Retinopathy Disease Severity scale. A detailed stepwise description of the proposed algorithm is done in the following sub-sections.

5.3.1 Retinal Contextual Landmark Segmentation

Retinal contextual landmark segmentation is implemented for removing unwanted retinal components: Optical Disc components and blood vasculatures. Artifacts like image variation, noise, and poor contrast are mitigated prior to background segmentation using various pre-processing steps such as attenuation variation, conversion of green channel to green channel, image denoising, and enhancement of contrast utilizing CLAHE. Circular Hough transform and morphological operations detailed in Chapter 3, are used for OD boundary localization and the circular region in the intensity plane is identified as the OD portion. HBV-MR approach is proposed for blood vessel segmentation in Chapter 3 which includes combination of morphological closing and global thresholding. Vessel and non-vessel pixels are labelled after separating the true vessel pixels from the noisy background [195, 208]. Chances of false detection of OD pixels as exudates lesions and blood vessel pixels as red lesions (microaneurysms or haemorrhages) are reduced by masking the background anomalies. The visual illustration of background segmented portions is depicted in Figure 5.4.

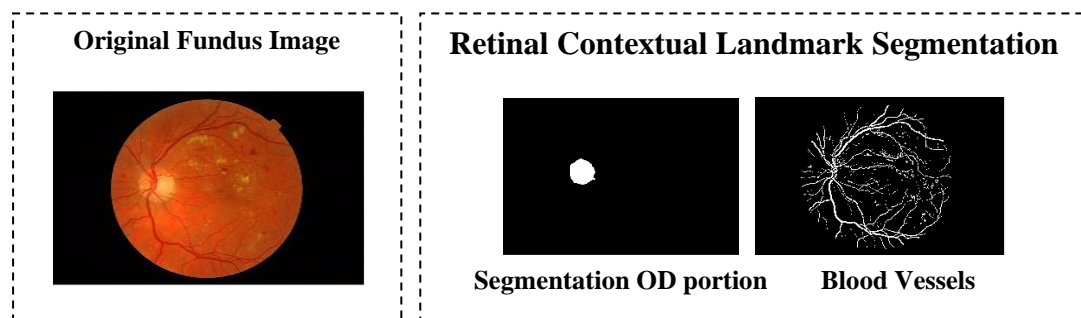


Figure 5.4: Representation of retinal contextual landmark segmentation

This step ensures the OD boundary approximation and localization despite of its blurred edges demonstrating the viability of the OD localization approach proposed in Chapter 3 and validates its localization efficiency. Proficient HBV-MR approach is capable of identifying the small blood vessels by approximate marking of the vessel and non-vessel pixels which are comparable to the ground truth.

The foreground region is obtained by subtracting the retinal contextual segmentations from that of the original image and this foreground portion is used in the anomaly identification stage.

5.3.2 Retinal Lesion Discrimination

DR severity grading in the proposed HSG system considers two anomalies: MAs and HEMs. HLD technique proposed in Chapter 4 is utilized for DR lesion discrimination. To detect the red lesions ($I_{\text{Red_Cand}}$) including MAs and HEMs the morphologically closed (I_{cl}) image from background removed fundus image (I_{BV}). Figure 5.5 depicts the visual illustration of identified foreground MAs and HEMs.

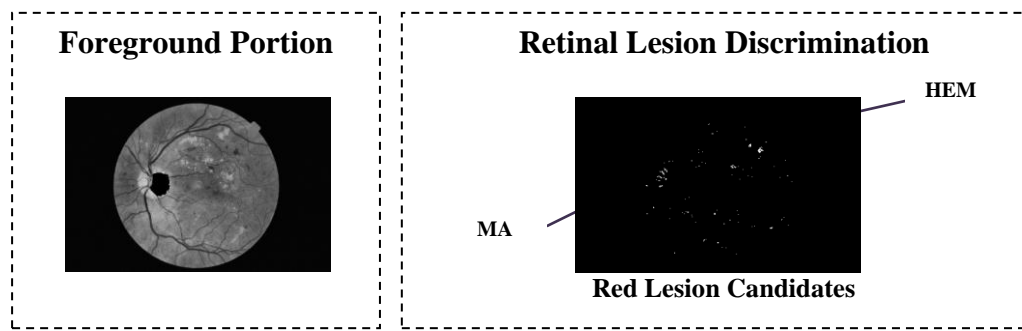


Figure 5.5: Identified anomalies from the foreground portion (MA-Microaneurysms, HEM-Haemorrhage)

Automatically detected lesions are compared with the manual ground truth annotations done by ophthalmic experts to identify the true anomalies [123, 209]. Non-lesion candidates are identified using automated lesion detection techniques and are not marked as true lesions if they are absent in the annotations provided by the experts. The distinguished false lesions may correspond to some dark spots or scars because of patients' past clinical records. After discarding the false lesions, identified true anomalies are subjected to feature extraction to differentiate the diseased and non-diseased fundus images and distinguish between various severity grades.

5.3.3 Reduced Image Feature Vector Selection

DR severity grade classification involves feature attribute extraction and selection before passing the selected features for DR severity grading. Based on the literature review, textural features of Gray-Level Co-occurrence Matrix (GLCM) are found the most relevant feature set for DR severity grade classification [21, 98]. These GLCM

features consider the spatial inter-pixel dependency and different spatial orientations in an image [211, 224]. For the computation of relevant IFV comprising 14 GLCM features, co-occurrence matrix $X_{i,j}$ of size $N \times N$ is considered in which each pixel of i_{th} gray level is spatially related to every pixel with j_{th} gray level. The formulated GLCM textural features are tabulated in Table 5.4.

Table 5.4: GLCM Textual Features

GLCM Textural Features	Formulas
Autocorrelation	$\sum_{i,j=0}^{N-1} X_{i,j} \left[\frac{(i,j - \mu_{i,j})^2}{\sqrt{\sigma_{i=j}^2}} \right]$
Correlation	$\sum_{i,j=0}^{N-1} X_{i,j} \left[\frac{(i - \mu_i)(j - \mu_j)}{\sqrt{\sigma_i^2 \sigma_j^2}} \right]$
Contrast	$\sum_{i,j=0}^{N-1} X_{i,j} (i - j)^2$
Energy	$\sum_{i,j=0}^{N-1} X_{i,j}^2$
Entropy	$\sum_{i,j=0}^{N-1} X_{i,j} (-\ln(X_{i,j}))$
Homogeneity	$\sum_{i,j=0}^{N-1} \frac{X_{i,j}}{1 + (i - j)^2}$
Dissimilarity	$\sum_{i,j=0}^{N-1} X_{i,j} i - j $
Cluster Shade	$Sgn(A A ^{1/3}) \text{ where } A = \sum_{i,j=0}^{N-1} \frac{(i+j-2\mu)^3 \times X_{i,j}}{\sigma^3 (\sqrt{2(1+Correlation)})^3}$
Cluster Prominence	$Sgn(B B ^{1/4}) \text{ where } B = \sum_{i,j=0}^{N-1} \frac{(i+j-2\mu)^4 \times X_{i,j}}{4 \times \sigma^4 (1+Correlation)^2}$
Maximum Probability	$\max(X_{i,j})$
Inverse Difference Normalized	$\sum_{i,j=0}^{N-1} \frac{C(i,j)}{1+ i-j } \text{ where } C(i,j) = \frac{X_{i,j}}{\sum_{i,j=1}^{N-1} X_{i,j}}$
Inverse Difference Moment Normalized	$\sum_{i,j=0}^{N-1} \frac{C(i,j)}{1 + i - j ^2}$
Information Measure of Correlation1	$\frac{H_{XY} - H_{XY1}}{\max(H_X H_Y)}$
Information Measure of Correlation2	$(1 - \exp[-2(H_{XY2} - H_{XY})^{1/2}])$

These textural features are subjected to exhaustive statistical analysis for optimal selection of prominent RIFV providing better performance for DR severity classification problem.

Statistical Feature selection

Feature descriptive are represented using box plots and feature vector reduction is accomplished using t -test and ANOVA statistical tools from the SPSS package [211, 212]. These tests provide inferential significance to the extracted feature set by analysing the mean value variation in IFV. The statistical inference for a normally distributed continuous set of data depends upon the hypothesis testing. The hypothesis (H_0) for t -test is given by Eq. (5.1) and the rejection of hypothesis is provided in Eq. (5.2).

$$H_0: \mu_0 = \mu_1 \quad (5.1)$$

$$H_1: \mu_0 \neq \mu_1 \quad (5.2)$$

This hypothesis defined the GLCM feature set significance in terms of equality of means (μ) for different DR severity grades. The null hypothesis of ANOVA test signifies the deviation of feature set variances (σ). Null hypothesis and its rejection are stated by Eq. (5.3) and Eq. (5.4) respectively.

$$H'_0: \sigma_0 = \sigma_1 \quad (5.3)$$

$$H'_1: \sigma_0 \neq \sigma_1 \quad (5.4)$$

The statistical relevance of ANOVA and t -test are provided using significance value (p -value) of the test that should provide a value less than 0.05 to prove any feature statistically significant to reject the hypothesis. Optimum attribute selection utilizing the SPSS statistical analysis tool resulted in prominent RIFV for effectual DR severity classification.

Classifiers for DR severity grading

DR severity classification is the final stage of the proposed methodology that grades the NPDR severities into grade 0, 1, 2 and 3. There are numerous classifiers reported in the literature to attain better classification accuracy [23-27]. Efficient Support Vector Machine (SVM), k-Nearest Neighbour (kNN) and Artificial Neural Network (ANN) classifiers detailed in Chapter 1, are chosen for this research work to accomplish DR severity grade classification.

The SVM classifier falls into the category of kernel based supervised machine learning algorithms which are particularly designated to perform binary classification. However, SVM can also be used effectively for non-linear classification problem. During the training phase of SVM model, the training samples are mapped on the basis of a decision boundary for each for the class separated by a hyperplane. Another machine learning based classification approach used in this work is kNN classifier. The kNN classifier is an instance based machine learning method that classifies the data samples based on the closest training example already present in the learned feature space. The majority votes of the neighbourhood learned data samples decides the class of the test sample. The test sample is assigned to that particular class which is most common among its k neighbours (where k is a positive integer). kNN algorithms is implemented using the Euclidian distance metric to locate the k-nearest neighbours. SVM is computationally less complex algorithm than kNN and is easier to implement as well as interpret. But, the SVM classifier has limited capabilities to interpret a limited set of patterns. Alternately, kNN provides effective outcomes for multi-class classification while providing a reduced misclassification error. kNN is able to find the complex patterns also but the interpretation of its output is much challenging. Both these algorithms are applied in this work to illustrate their classification and prediction capabilities for binary as well as multi-class classification. ANN supervised learning algorithm is also utilized in this work due to its improved capabilities for different classification and regression problems. ANN uses an inbuilt optimization process by incorporating the backpropagation algorithm to achieve minimum error and comparatively reduced computational cost. This leads to an improvement in the classification performance of the network as compared to the other supervised learning algorithms [23-27].

The performance results are obtained for all of these classifiers and a comparison is drawn to observe the most significant classification outcomes for the DR classification problem.

5.4 RESULTS AND DISCUSSION

For the experimentation, MA and HEM lesions after anomaly identification are combined using the standard guidelines. IFV is extracted for lesion candidates belonging to the diseased class and non-lesion candidates belonging to the non-diseased class. Statistical feature reduction strategy is applied utilizing SPSS statistical analysis tool on IFV to reveal the statistical relevance of extracted feature set resulting in RIFV. In the proposed work, the non-diseased and diseased DR stage classification is accomplished by annotating the feature vector of non-diseased fundus images with 0 label and feature vector of diseased class with label 1 liable to the results obtained for automated lesion discrimination along with annotated ground truths. The diseased class is further graded into three different retinopathy grades; 1, 2, 3. Three different classification cases are considered and the feature vector annotations considering different cases of classification are specified in Table 5.5.

Table 5.5: Annotations for different classification cases

Classification Case 1		Classification Case 2		Classification Case 3	
Grades	Annotations	Grades	Annotations	Grades	Annotations
Grade 0	0	Grade 0	0	Grade 0	0
Grade 1,2,3	1	Grade 1 and 2	1	Grade 1	1
		Grade 3	2	Grade 2	2
				Grade 3	3

The proposed system is assessed using MATLAB software considering the benchmark MESSIDOR dataset for retinopathy grading evaluation and IDRiD dataset for performance validation. The 70%-30% training/testing criteria is used to partition the complete arrangement of images to training set and testing set. The training set is divided into 10 distinct classes and each of these subsets are trained against every other (10-1) validation set for the 10-fold cross validation scheme. The validation strategy results in providing the favourable outcomes for the DR classification phase.

5.4.1 Statistical analysis

Statistical analysis of IFV is done to obtain a reduced optimal RIFV after feature selection. IFV includes 14 GLCM features whose statistical significance is analysed using box plots, t -test and ANOVA descriptive statistical tests. The box plots of some extracted features of GLCM are depicted in Figure 5.6.

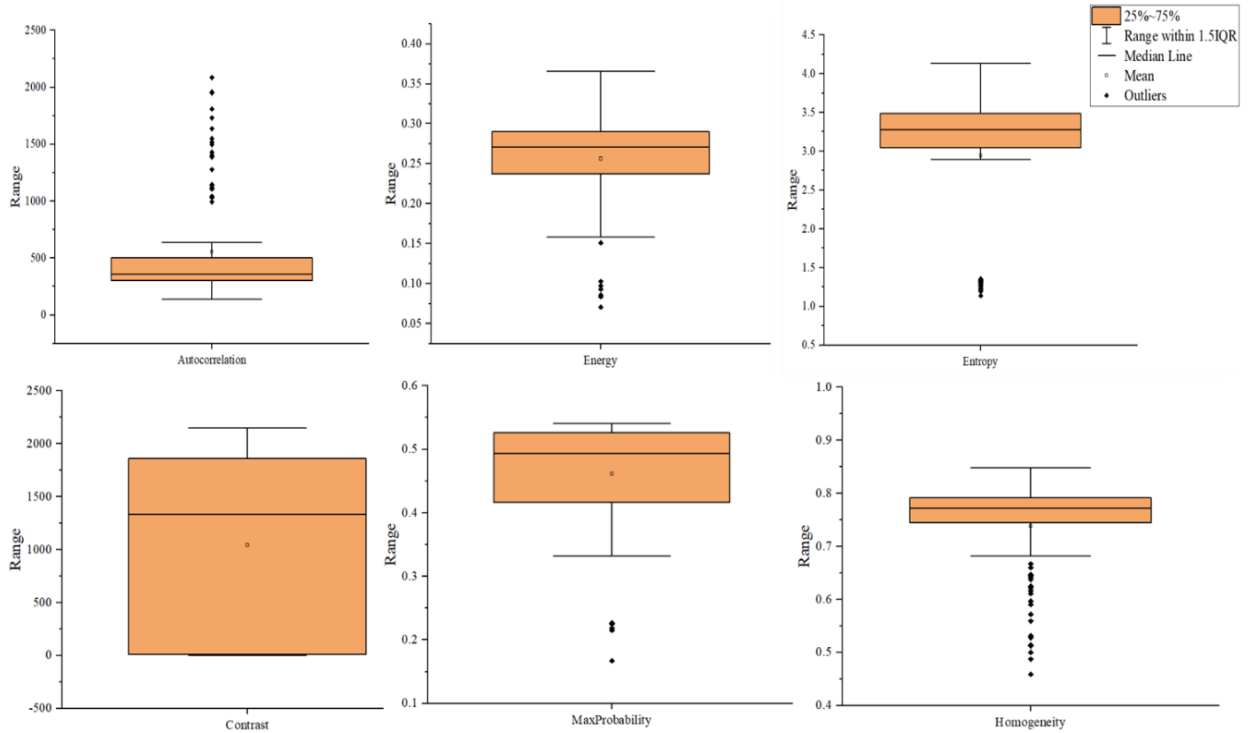


Figure 5.6: Box plots of some extracted GLCM textural features

The box-plots for GLCM textural features shows their quartile ranges while point out the outliers with dots indicated outside the quartile box [195]. These outlier feature values are not considered for feature selection process, thereby yielding better performance. The different quartile ranges of individual textural features imply their importance for differentiating different DR severity grades.

Further, statistical feature selection is done using t -test and ANOVA which are based upon hypothesis tests discussed in section 5.3.3 for the equality of means and variances. The null hypothesis test presents that, there is no considerable disparity among GLCM features of diseased and non-diseased DR classes. Rejection of the null hypothesis points to a significant difference between diseased and non-diseased DR classes. The outcomes obtained for t -test and ANOVA for the extracted IFV are

summarized in Table 5.6 to distinguish between diseased and non-diseased DR severity levels.

Table 5.6: Levene's test and t -test for IFV set comprising GLCM features

Features	t -test	ANOVA
	Significance (2-tailed)	One-way ANOVA (Significant value)
Auto Correlation	0.000	0.001
Correlation	0.001	0.000
Contrast	0.001	0.001
ClusterShade	0.458	0.458
ClusterProminance	0.000	0.000
Energy	0.295	0.295
Entropy	0.017	0.017
Homogeneity	0.000	0.001
InverseDiffNormalized	0.000	0.000
InverseDiffMoment	0.001	0.001
Dissimilarity	0.001	0.001
MaxProbability	0.000	0.001
InfoCorr1	0.000	0.000
InfoCorr2	0.001	0.001

The significance (p -value) of t -test and ANOVA is presented in Table 5.6 should be less than 0.05 to reject the null hypothesis representing the presence of significant disparity among means of diseased and non-diseased DR classes. From the p -value significance test, 12 prominent features are selected for the classification cases.

Two insignificant GLCM features *cluster shade*, *energy* feature indicates p -value deviation to a greater value than 0.05 significant level indicative of more deviation among the mean values. Therefore, RIFV chosen for the DR severity grade classification consisting 12 GLCM features.

5.4.2 Results for DR Severity Grade Classification

Both IFV and RIFV feature sets are used for the classification of DR severity to observe the effect of both feature vectors in severity grading. After exhaustive literature survey, the three classifiers utilized for severity grade classification are SVM [23-25], kNN [112, 123, 152], and ANN Classifier [27-29] to obtain robust performance demonstrating the practicability of the proposed HSG grading framework. The following subsections provide the results of classification cases considered for DR severity grading utilizing the standard benchmark MESSIDOR and IDRiD datasets.

5.4.2.1 Classification-Case 1

Classification- case 1 categorizes the retinal fundus images into non-DR category comprising retinopathy Grade 0 images and DR affected category including Grade 1, 2, 3 (collectively). Non-diseased retinal fundus images are separated from the diseased fundus images using different classifier combinations. Classification performance is evaluated for Positive Prediction Value (PPV), Sensitivity, Specificity and Accuracy. The results for all the performance indices are computed for both IFV and RIFV sets.

Table 5.7: Performance indices of HSG system for classification-Case 1

GLCM Feature Sets		IFV set			RIFV set	
Classifier	SVM Classifier	kNN Classifier	ANN classifier	SVM Classifier	kNN Classifier	ANN classifier
Indices						
PPV	93.93%	98.91%	100%	97.06%	100%	100%
SN	93.93%	99.89%	80.80%	100%	100%	100%
SP	90.47%	99.99%	100%	95.23%	100%	100%
Acc.	92.60%	99.78%	90.71%	98.10%	100%	100%

PPV- Positive Prediction Value, SN- Sensitivity, SP- Specificity, Acc.- Accuracy

Performance indices tabulated in Table 5.7 revealed the significance of feature set reduction in classifier performance. Feature set reduction advances the performance of SVM classifier improving the classification accuracy from 92.60% to 98.10%. However, it should be noted that feature set reduction does not affect the performance of the kNN classifier, and 100% accuracy value is achieved for both IFV and RIFV feature sets. In ANN classification, feature set reduction plays a vital role with IFV set providing 80.8% sensitivity, 90.71% accuracy, and 100% specificity and PPV rate. However, on the contrary, all the indices provide 100% performance utilizing RIFV as the feature set disparities are removed after removing insignificantly irrelevant features.

ROC curve and area under the curve computes the overall classification quality to discriminate between the Non-Diseased and Diseased classes. The ideal classification outcome with no misclassification is seen at the top left corner of the ROC curve. ROC performance curves for SVM, kNN, and ANN classifiers to differentiate the Non-Diseased and Diseased stages are depicted in Figure 5.7, 5.8, and 5.9, respectively.

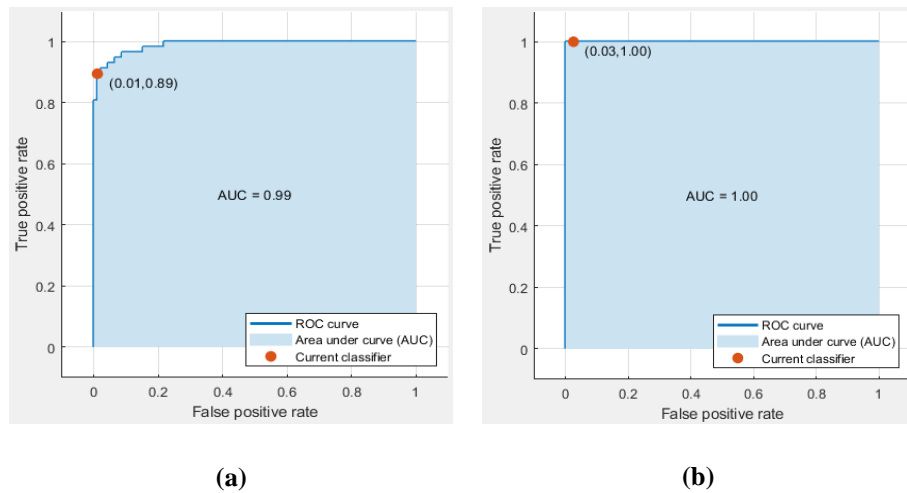


Figure 5.7: ROC curves for classification- Case 1 (a) SVM classifier using IFV, (b) SVM classifier using RIFV

The AUC curve comparison provides the proper justification of classification performance in terms of the true positive and false positive rate cut off points. SVM classifier provides AUC of 0.99 for IFV and 1 for RIFV showing the dependency of its performance on the feature set.

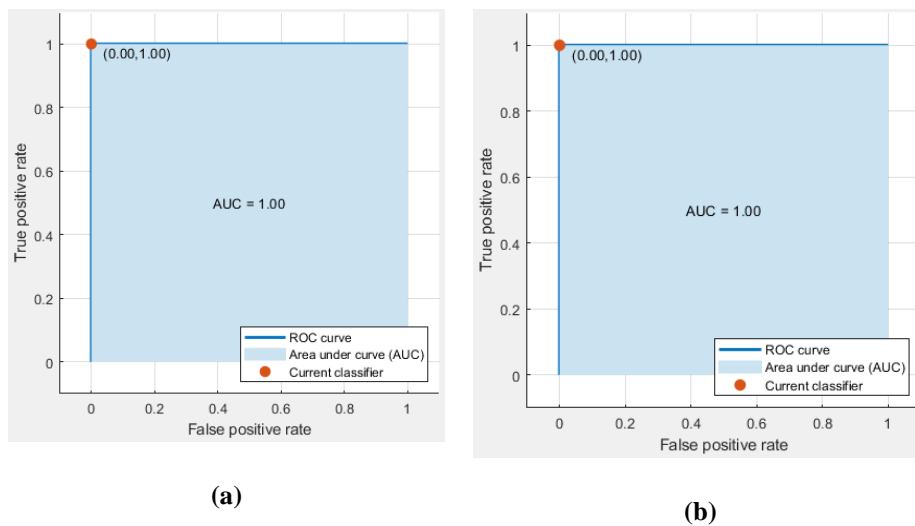


Figure 5.8: ROC curves for classification- Case 1 (a) kNN classifier using IFV, (b) kNN classifier using RIFV

However, kNN classifier performance is irrespective of feature selection providing AUC of 1 using IFV as well as selected RIFV. Better classification outcomes are obtained for kNN classifier utilizing both IFV and RIFV due to its

dependency on Euclidean distance of k-nearest neighbours and not much on feature selection.

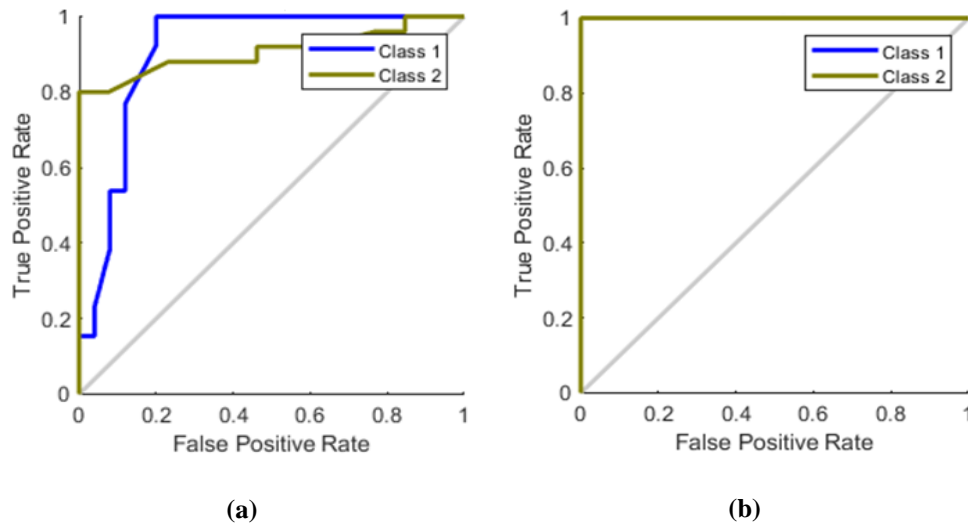


Figure 5.9: ROC curves for classification- Case 1 (a) ANN classifier using IFV, (b) ANN classifier using RIFV

On the contrary, the performance of the ANN classifier is highly affected by the feature selection process. It provides AUC of 0.84 and 1 for classification using IFV and RIFV. The following sub-sections provide the DR severity grade classification outcomes for case 2 and case 3.

5.4.2.2 Classification-Case 2

In this classification case, grade 0 images are annotated as 0 class, grade 1 and grade 2 severity levels collectively as individual category that is marked as class 1, and grade 3 annotated as class 2 is considered as another severity category as depicted in Table 5.5. The lesion properties of grade 1 and 2 comprising of mild and moderate DR symptoms are similar and are less severe than grade 3 DR abnormality. Therefore, in this classification case, they are treated collectively for severity grade classification. The classification-case 2 results considering both sets of GLCM features; IFV and RIFV are tabulated in Table 5.8.

Table 5.8: Performance indices of HSG system for classification- Case 2

GLCM Feature Sets		IFV set			RIFV set		
Classifier	Indices	SVM	kNN	ANN	SVM	kNN	ANN
		Classifier	Classifier	Classifier	Classifier	Classifier	Classifier
PPV _x	PPV ₀	87.52%	100%	91.76%	100%	100%	96.32%
	PPV ₁	86.65%	87.51%	93.81%	100%	100%	100%
	PPV ₂	95.85%	100%	100%	92.86%	96.29%	99.98%
SN _x	SN ₀	100%	100%	91.41%	100%	100%	92.88%
	SN ₁	92.88%	100%	86.23%	85.71%	92.86%	99.89%
	SN ₂	88.45%	92.32%	100%	100%	100%	100%
SP _x	SP ₀	97.52%	100%	100%	100%	100%	97.08%
	SP ₁	93.94%	93.95%	94.71%	100%	97.06%	99.99%
	SP ₂	95.25%	100%	98.31%	90.47%	100%	100%
Acc _x	Acc ₀	97.88%	100%	97.91%	100%	100%	97.87%
	Acc ₁	93.63%	95.93%	97.65%	95.74%	97.87%	100%
	Acc ₂	91.48%	95.74%	95.24%	95.74%	97.87%	97.86%
Overall Accuracy		91.52%	95.73%	95.35%	95.68%	97.90%	97.85%

PPV- Positive Prediction Value, *SN_x* - Sensitivity, *SP_x*- Specificity, *Acc_x* – Accuracy, *x*-(Severity Grading: 0,1,2)

For DR classification-case 2, the IFV offers accuracies of 91.52%, 95.73% and 95.35% for SVM, kNN and ANN classifiers respectively. Advancement in the classifier performance is evident by adopting the feature set reduction strategy while improving the accuracy outcomes to 95.68%, 97.90% and 97.85% correspondingly for SVM, kNN and ANN classifiers. kNN and ANN classifiers provide comparable outcomes of all the performance indices justifying their capabilities for non-linear classification problem.

Classifier performance in terms of ROC curves is also computed to evaluate the overall classification quality of case 2 for SVM, kNN, and ANN classifiers as depicted in Figure 5.10.

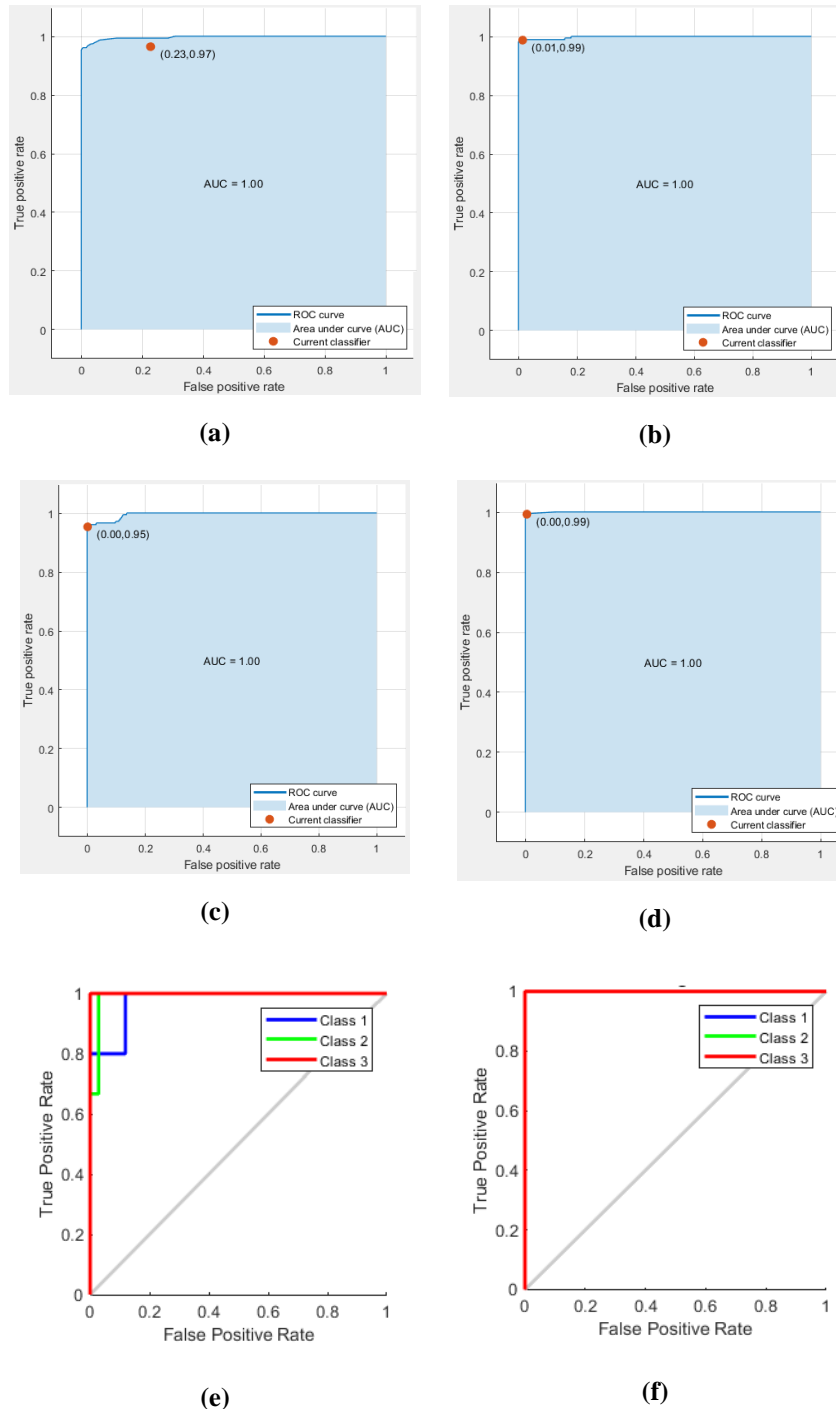


Figure 5.10: ROC curves for classification- Case 2 (a) SVM classifier using IFV, (b) SVM classifier using RIFV, (c) kNN classifier using IFV, (d) kNN classifier using RIFV, (e) ANN classifier using IFV, (f) ANN classifier using RIFV

A complete justification of classification performance in terms of true positive and false positive rate cut off points is provided by AUC curve assessment of SVM, kNN, and ANN classifiers. AUC of 1 is observed for all the classifier combinations using both IFV and RIFV sets. However, the dependency of classifier performance on the feature set is provided by the deviation in true positive and false positive cut off rates which are improved for RIFV. ANN classification approach provides AUC of 1 for both the sets and an overlapping behaviour of the receiver operating characteristics is observed for RIFV evidencing the effect of feature selection.

5.4.2.3 Classification-Case 3

Severity grade classification involved in classification-case 3 distinguishes between different DR abnormality grades entirely depending upon GLCM feature space. Classification-case 3 is introduced in the proposed system to categorize DR into different abnormalities by separating grade 0, 1, 2 and 3 into individual classes. Table 5.9 provides the performance indices comparing the classification results for SVM, kNN, and ANN using IFV and RIFV sets.

Table 5.9: Performance indices of HSG system for classification- Case 3

GLCM Feature Sets		IFV set			RIFV set		
Classifier	Indices	SVM	kNN	ANN	SVM	kNN	ANN
		Classifier	Classifier	Classifier	Classifier	Classifier	Classifier
PPV _x	PPV ₀	96.36%	96.90%	91.40%	98.07%	100%	97.10%
	PPV ₁	85.71%	91.41%	100%	87.28%	91.71%	98.21%
	PPV ₂	95.00%	88.52%	79.31%	95.65%	100%	96.50%
	PPV ₃	100%	79.21%	86.72%	89.47%	93.81%	100%
SN _x	SN ₀	92.98%	91.40%	100%	89.47%	91.42%	100%
	SN ₁	96.00%	96.42%	87.31%	96.00%	100%	96.41%
	SN ₂	82.61%	88.51%	85.22%	95.65%	86.21%	96.50%
	SN ₃	94.74%	93.91%	96.31%	89.47%	100%	100%
SP _x	SP ₂	97.83%	99.11%	97.41%	98.91%	100%	99.11%
	SP ₁	91.92%	94.71%	100%	92.93%	94.70%	98.92%
	SP ₂	98.20%	97.62%	95.13%	97.62%	100%	99.20%
	SP ₃	100%	99.11%	96.72%	100%	98.31%	100%
Acc _x	Acc ₀	95.97%	97.32%	97.91%	95.30%	97.91%	99.31%
	Acc ₁	93.29%	95.30%	94.60%	93.96%	96.63%	97.92%
	Acc ₂	92.37%	95.90%	93.30%	97.31%	97.32%	98.61%
	Acc ₃	95.33%	97.91%	96.61%	98.66%	98.71%	100%
Overall Accuracy		91.20%	93.30%	91.30%	92.60%	95.30%	98.00%

PPV- Positive Prediction Value, *SN_x* - Sensitivity, *SP_x* - Specificity, *Acc_x* – Accuracy, *x*-(Severity Grading: 0,1,2,3)

The SVM classifier results in an accuracy of 91.20% for IFV, however, when the RIFV is utilized the classifier accuracy increased to 92.60% providing better performance. Accuracy, 93.30%; sensitivity, 92.51%; specificity, 97.62% and positive prediction value, 89% are provided by kNN classifier for IFV set, while utilization of RIFV yields PPV, sensitivity, specificity and accuracy of 96.40%, 94.52%, 98.31% and 95.30% respectively. Accuracy of 91.30%, the sensitivity of 92.22%, the specificity of 97.31% and positive prediction value of 89.35% are obtained for ANN classification for IFV set and 97.90%, 98.21%, 99.31% and 98.00% of PPV, sensitivity, specificity and accuracy values respectively for RIFV. ANN provides the optimal classification performance for statistically selected RIFV set consisting of 12 GLCM features, as compared to the other two classification approaches. These results depict the evident role of optimal classification providing optimal performance for ANN classifier due to robustness for non-linear classification problems.

Figure 5.11 provide ROC performance curves for SVM, kNN, and ANN classifiers showing the significance of true positive and false positive rate cut off points for reduced feature set in accordance with originally extracted feature set. For DR classification-case 3, SVM classifier shows the performance dependency on the feature set providing AUC of 0.89 for IFV and 0.99 for RIFV. The ROC curves obtained for the kNN classifier for both IFV and RIFV feature sets provide somewhat similar results as the target class is allocated while considering the neighbourhood distance. On the contrary, the ROC curve results obtained for the ANN classifier depicted in Figure 5.11 (e) and 5.11 (f) indicates the deviation in AUC.

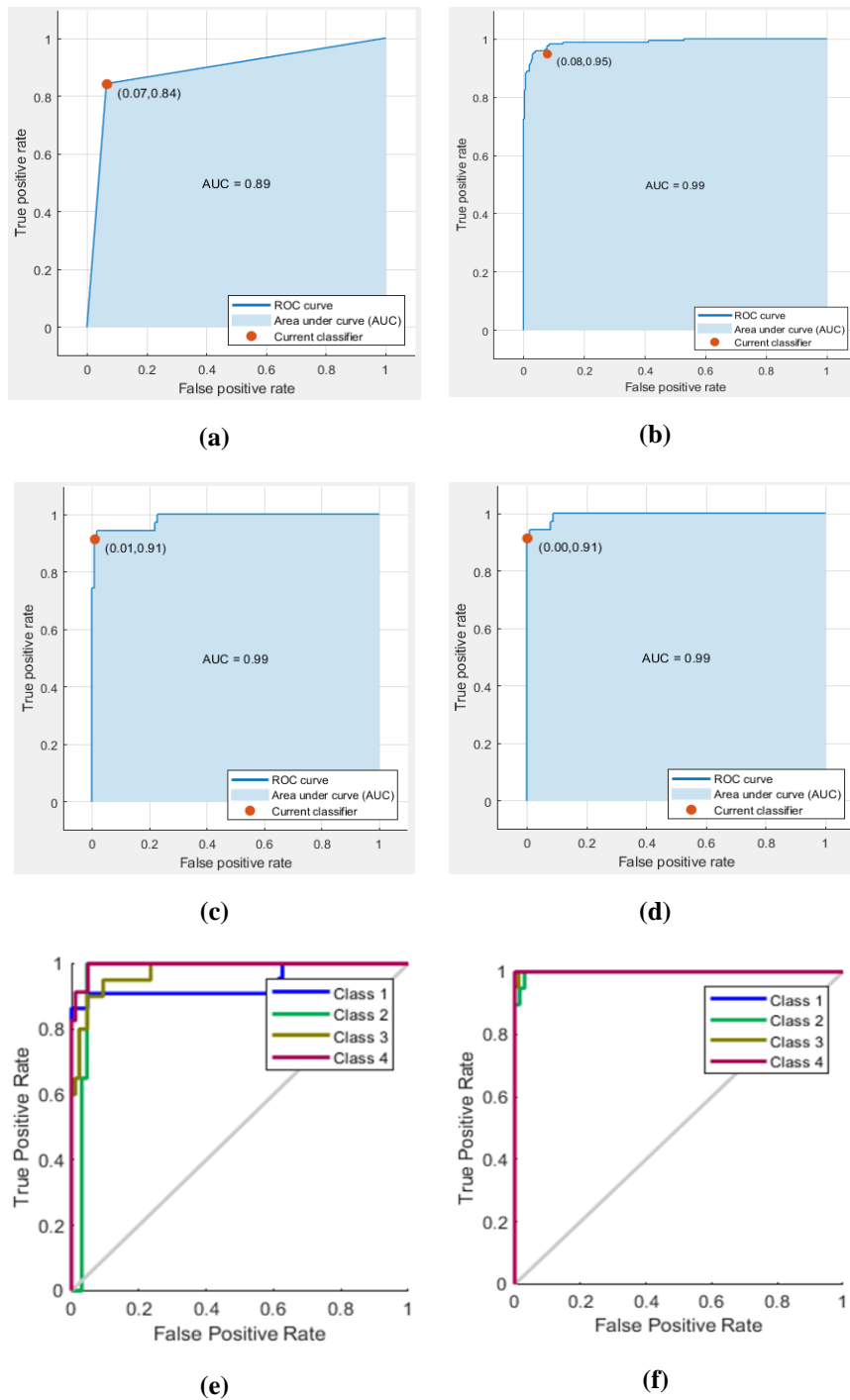


Figure 5.11: ROC curves for classification- Case 3 (a) SVM classifier using IFV, (b) SVM classifier using RIFV, (c) kNN classifier using IFV, (d) kNN classifier using RIFV, (e) ANN classifier using IFV, (f) ANN classifier using RIFV

The effect of feature selection shown in Figure 5.11 reveals that more area under the ROC curve is obtained while utilizing RIFV set. A noteworthy percentage improvement is noticed for the diagnosis of diabetic retinopathy utilizing RIFV, which is depicted in Figure 5.12.

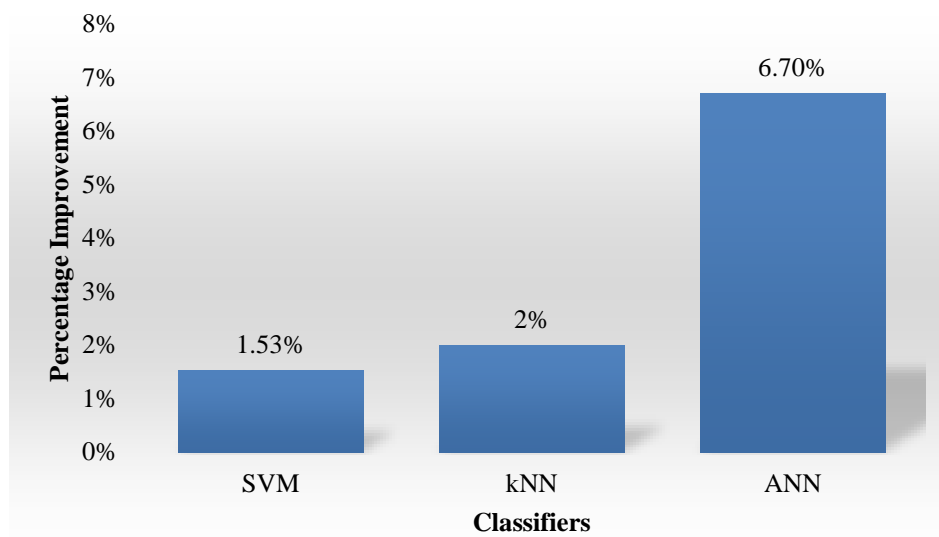


Figure 5.12: Percentage improvement in classification performance of RIFV over IFV

The performance improvement of 1.53% and 2% is seen for SVM and kNN classifiers after feature set reduction. However, a significant improvement of more than 6.70% is seen for ANN classification. The feature set disparities are removed after the feature selection process providing weight adjustment flexibility to ANN classifier as per application requirements.

5.5 VALIDATION AND COMPARATIVE ANALYSIS OF HSG SYSTEM

For the validation of HSG system, the latest IDRiD dataset (2018) is used to improve its generalization capabilities. The clinically relevant images present in IDRiD are acquired after the routine examination performed on diabetic patients from the year 2009 to 2017. The validation results are presented in the following section.

5.5.1 Performance validation of the proposed system employing IDRiD dataset

The main aim of this work is DR severity grading, so the proposed HSG system is validated for classification case 3 utilizing IDRiD dataset. For proper validation of the proposed system, the same set of classifiers are used. This validation scheme increases the samples and help ophthalmologists in tracking the appearance and progression of the disease. The performance metric analysis of different classifiers is given in Table 5.10 for SVM, kNN and ANN classifiers for severity grading into 3 classes.

Table 5.10: Performance indices of HSG system for classification- Case 3 utilizing IDRiD dataset

Classifier	Indices	IFV set			RIFV set		
		SVM	kNN	ANN	SVM	SVM	kNN
PPV	PPV ₀	96.96%	96.96%	96.85%	94.12%	97.06%	93.15%
	PPV ₁	91.38%	91.38%	89.12%	92.59%	93.10%	97.10%
	PPV ₂	88.46%	88.46%	91.43%	82.75%	88.46%	96.47%
	PPV ₃	96.87%	96.87%	96.56%	96.87%	96.77%	88.74%
SN	SN ₀	91.42%	91.42%	92.12%	91.42%	94.28%	98.28%
	SN ₁	96.36%	96.36%	96.45%	90.91%	98.18%	94.25%
	SN ₂	88.46%	88.46%	89.47%	92.31%	88.46%	90.48%
	SN ₃	93.93%	93.93%	94.04%	93.93%	90.91%	88.91%
SP	SP ₀	99.12%	99.12%	98.99%	98.24%	99.12%	95.32%
	SP ₁	94.68%	94.68%	94.78%	95.74%	95.74%	99.78%
	SP ₂	97.56%	97.56%	97.67%	95.93%	97.56%	99.54%
	SP ₃	99.13%	99.13%	98.89%	99.13%	99.13%	97.25%
Acc.	Acc ₀	97.31%	97.31%	97.47%	96.64%	97.98%	96.88%
	Acc ₁	95.30%	95.30%	95.38%	93.96%	96.64%	97.74%
	Acc ₂	95.97%	95.97%	95.79%	95.30%	95.97%	95.57%
	Acc ₃	97.98%	97.98%	97.86%	97.98%	97.31%	97.38%
Overall Accuracy		90.60%	93.31%	93.76%	91.90%	94.00%	94.87%
AUC		0.95	0.98	0.99	0.97	0.99	1.00

PPV- Positive Prediction Value, *SN_x* - Snsitivity, *SP_x* - Specificity, *Acc._x* – Accuracy, *x*-(Severity Grading: 0,1,2,3)

The feasibility of proposed HSG system is observed through performance evaluation with IDRiD dataset and maximum accuracy of 94.87% is achieved for ANN classifier while utilizing RIFV. The accuracy of SVM classifier rises from 90.60% to 91.90% and kNN classifier accuracy value improves from 93.31% to 94.00%, when RIFV is used instead of IFV.

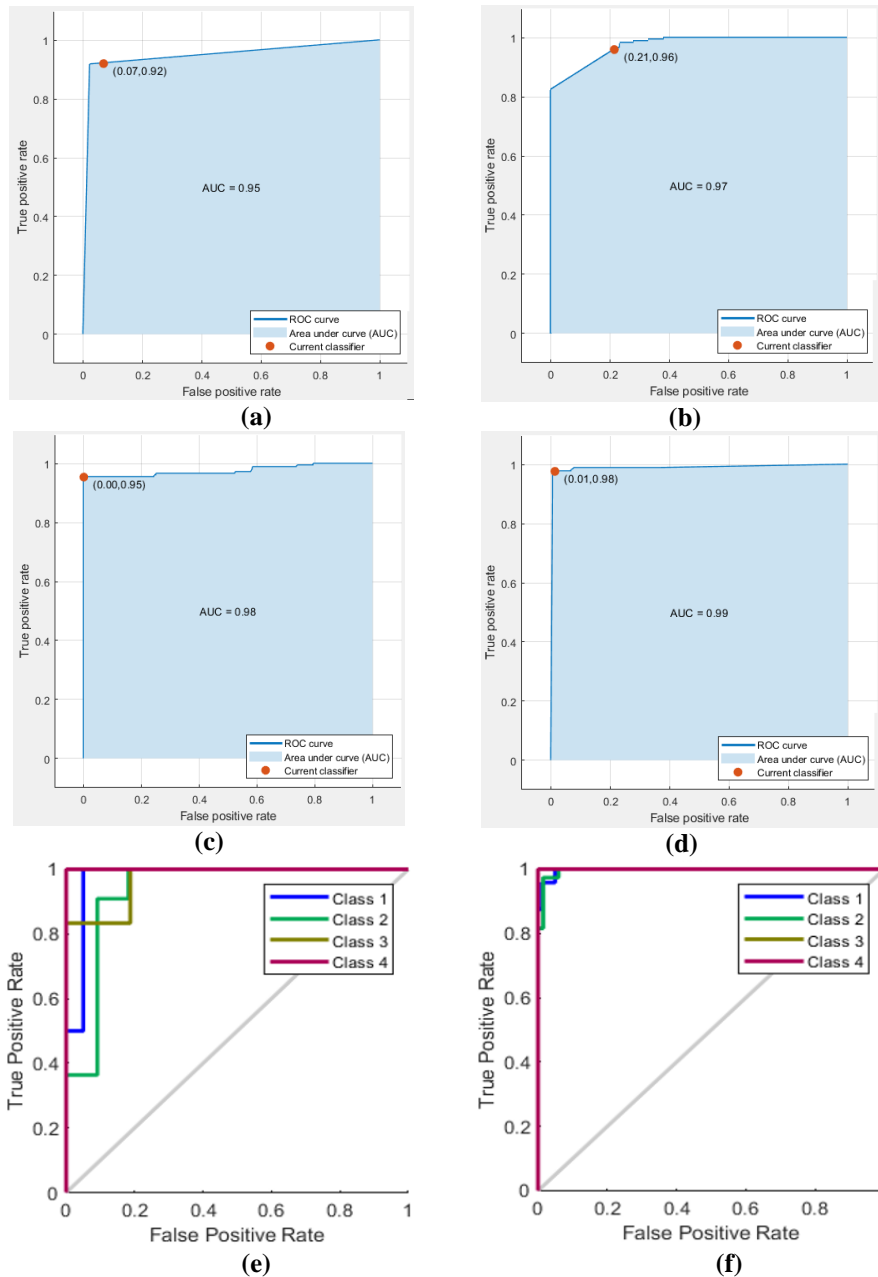


Figure 5.13: ROC curves for HSG classification- Case 3 utilizing IDRiD dataset (a) SVM classifier using IFV, (b) SVM classifier using RIFV, (c) kNN classifier using IFV, (d) kNN classifier using RIFV, (e) ANN classifier using IFV, (f) ANN classifier using RIFV

The AUC depicting the receiver operating characteristics for SVM, kNN, and ANN classifiers utilizing IDRiD dataset are shown in Figure 5.13. These curves signify the feature selection dependency on the classifier performance. SVM and kNN classifiers provide AUC of 0.95 and 0.98 for IFV which improves to 0.97 and 0.99 respectively, utilizing RIFV. The ANN classifier yields AUC value of 0.99 for IFV and an improvement is seen for RIFV providing AUC value of 1. The preeminent attempts have been made by ANN classification approach to address and simplify the grading capability of proposed framework yielding improved performance.

The proposed HSG system validation with IDRiD dataset for accuracy and computational time is depicted in Figure 5.14.

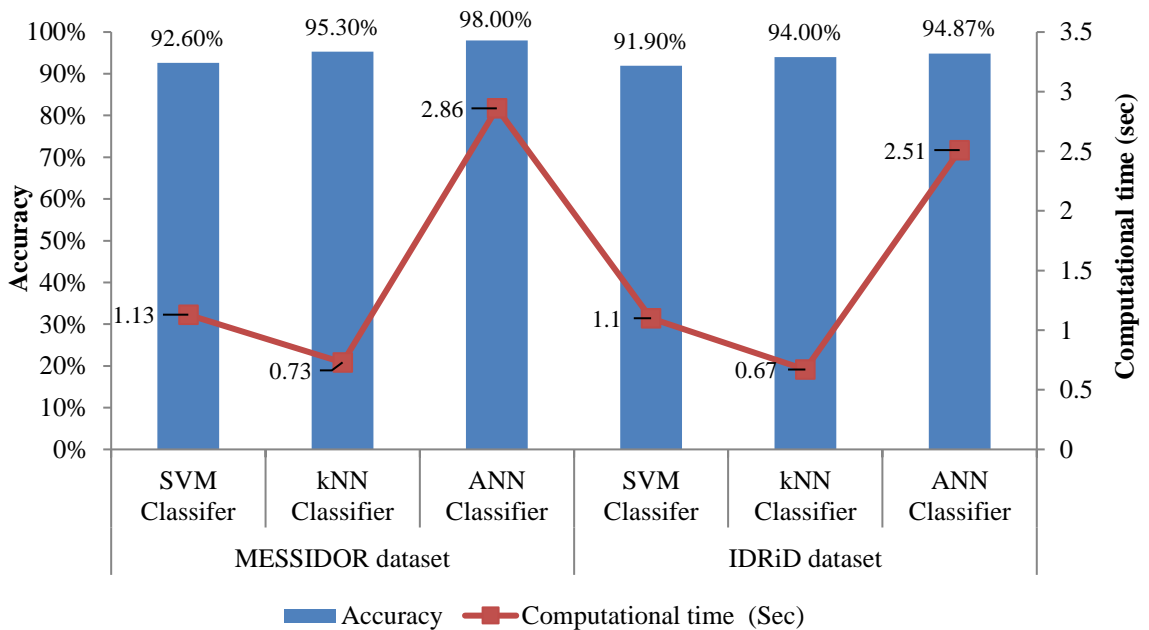


Figure 5.14: Validation of the proposed HSG system in terms of accuracy and computational time with MESSIDOR and IDRiD datasets

The assessment of MESSIDOR and IDRiD datasets reveals that the kNN classifier yields improved accuracy while maintaining less computational time. An evident increase is seen in the performance of ANN classifier upholding a trade-off with time. The accuracy value of 95.30% is achieved implementing kNN classifier, maintaining 0.73 seconds of computational time for training which is comparatively better than SVM classifier yielding 92.60% accuracy at 1.13 seconds and ANN classifier with

98.00% accuracy and 2.86 seconds computational time, utilizing MESSIDOR database.

The training of fundus images from IDRiD dataset takes 2.51 seconds, 0.67 seconds for training of kNN classifier and 1.10 seconds for SVM classifier training. It is observed that a significant accuracy improvement is evident upon exploiting ANN classifier compensating to the computational time. The substantial improvement in the system performance along with a trade-off to the computation time rationalizes the ANN classifier utilization for the classification of DR severity. The proposed HSG scheme delivers uniform results, regardless of dataset being utilized, thereby, establishing its generality.

5.5.2 Comparative Analysis with other state-of-the-art methods

Various researchers have made serious attempts and came up with numerous advancements in the field of automated DR classification to address diverse DR abnormalities as well as severity grading. Thus, a comparative study of the proposed system is done with the other existing methods. Table 5.11 illustrates the comparison of our proposed system with other severity grading systems using the same benchmark MESSIDOR dataset.

Table 5.11: Comparison of different DR severity grading methods with the proposed HSG system

Dataset used	Accuracy	AUC
MESSIDOR		
	Technique	
	Seoud, <i>et al.</i> (2015) [148]	74.10% 0.73
	Navarro, <i>et al.</i> (2016) [225]	84.00% ----
	Thammastitkul and Uyyanonvara (2016) [226]	87.00% 0.85
	Ragab, <i>et al.</i> (2017) [227]	93.00% 0.87
	Xiao, <i>et al.</i> (2019) [228]	90.50% 0.85
	Proposed HSG system (Classification-Case 3)	98.00% 0.99

It was observed from the tabular comparison that the proposed approach outperforms in terms of accuracy among the existing methods reported in the literature using the same dataset. A maximum improvement of 32.25% from Seoud, *et al.* [148] and minimum of 8.83% accuracy improvement from Xiao, *et al.* [228] is evident from the state-of-the-art methods. A cost-effective DR detection solution is obtained to classify the fundus images into Non-Diseased as well as different abnormality grades irrespective of FOV and resolution. The performance of our proposed framework of HSG is validated utilizing IDRiD dataset.

5.6 CONCLUSION

In this work, the HSG grading system for disease detection and DR severity classification utilizing SVM, KNN, and ANN classifiers was proposed. The level of severity is classified as grade 0, 1, 2 and 3 based on the number of anomalies as microaneurysms and haemorrhages. The exhaustive statistical analysis resulted in RIFV feature set consisting of twelve major features, which provides better classification results than the results obtained using original 14 featured IFV set. The classification results are obtained for image attribute set as well as reduced attribute sets to rationalize the importance of statistical analysis in severity grade classification problem. Case 1 resulted in 98.10% accuracy values for SVM classifier employing RIFV, alternatively, 100% specificity, sensitivity, accuracy, and positive predictive values after feature set reduction using KNN and ANN classifiers. The accuracy values of 95.68%, 97.90% and 97.85% are observed for SVM, kNN and ANN classifier respectively, utilizing RIFV for Case 2. Case 3 using RIFV with SVM classifier provides 92.60% accuracy value and with KNN classifier, RIFV set yields accuracy of 95.30%.

For DR severity grading, the proposed approach yields good classification results for the ANN classifier for performance indices of accuracy, 98.00%; Sensitivity, 98.21%; Specificity, 99.31% and positive predictive value, 97.92%. Utilization of RIFV yields performance improvement of 1.53% and 2% for SVM and kNN classifiers, consecutively providing a significant improvement of 6.70% using ANN classifier.

A noteworthy performance improvement is realized from the state-of-the-art comparison and a maximum improvement of 32.25% and minimum of 8.83% accuracy improvement is evident. The validation on IDRiD dataset suggests that the proposed system provides improved performance regardless of dataset being utilized. The proposed HSG framework provides an effective solution for DR prognosis and screening by providing substantially improved performance of DR abnormalities classification. This work is application-oriented and helpful in accurate DR classification for effective diagnosis and timely treatment of severe retinal diseases. This work can track the disease progression over time and is dedicated to the treatment of DR. However apart from diabetic retinopathy, this work can also be applicable for the diagnosis several retina related eye disorders. The next chapter focuses on the use of the deep learning-based approach for DR severity grade classification to combat the challenges faced for machine learning based classification.

CHAPTER 6

**ENSEMBLED TRANSFER
LEARNING MODEL FOR DR
SEVERITY GRADING**

CHAPTER 6

ENSEMBLED TRANSFER LEARNING MODEL FOR DR SEVERITY GRADING

6.1 INTRODUCTION

Fundus imaging-based DR screening techniques are implemented widely because of their simplicity, convenient acquisition, and improved lesion visibility. The gap between highly professional ophthalmologists and the diabetic population has widened which initiates the need for automated DR diagnosis systems. The obvious symptoms of DR are not visible by naked eye, hence automatic DR detection is required to analyze the pattern and characteristics of diabetic retinopathy [220]. High clinical relevance of DR classification for better interpretation motivates many researchers for designing automated diagnosis system.

In the recent years, machine learning provides various computer-based alternative solutions for automated DR classification and diagnosis. These DR detection approaches use various techniques of feature extraction for gathering useful information (handcrafted features) from fundus images. These handcrafted features are extracted manually with variations in the visual characteristics of different lesions and must be robust to variations in different lesions [31]. Automated DR screening systems may adopt the handcrafted feature extraction approach for lesion identification. It ensures that the lesions are detected in isolation as well as in combination with other lesions, making patient referral to the ophthalmologist for further assessment and accurate decision making. Machine learning algorithms separates the classes of a classification problem based on the decision boundary and activation functions. These algorithms cannot learn the decision boundaries for non-linear inputs and are not capable of learning all the functions limiting their capabilities for solving the complex tasks. Also, the feature engineering module is integrated for enhancing the performance of machine learning approaches is a time-consuming process requiring strong expert domain knowledge. The features being utilized by the machine learning algorithms are needed to be identified by the domain expert to reduce the data complexity and learn more output classification patterns.

Deep learning has evolved as a breakthrough in order to automate the process of feature engineering by involving feature learning in an incremental manner while increasing the number of layers.

6.1.1 Deep Neural Networks

Deep learning is an end to end problem-solving approach without breaking the problem into different parts and then combining at the final stage, as in machine learning. Deep Neural Network (DNN) based architectures have surpassed manual grading systems in many applications. For image classification tasks, Convolutional Neural Network (CNN) has performed revolutionary and thus is being exploited for DR diagnosis systems. This is due to the fact that CNN model depends on huge volume of data for ensuring proper convergence without overfitting. The basic functioning architecture of CNN model is depicted in Figure 6.1 comprising input layer, stack of convolution layer, pooling layer, and fully connected layer followed by the output layer.

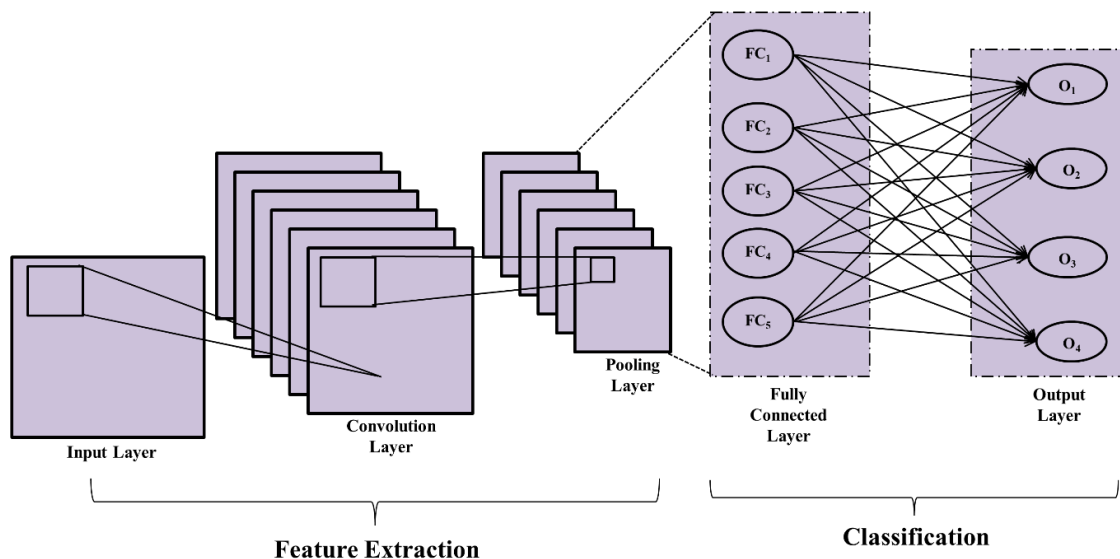


Figure 6.1: A basic CNN architecture as feature extractor and classifier

Feature extraction is done from the input layer using group of convolution and pooling layers. The convolution layers are implemented for making the CNN model to learn deeper features. The initial layers learn simple features such as edge, boundary and curve information whereas the inner deep layers learn other complex features. The last layer of CNN model learns features for the classification of fundus image into multiple DR grades. The feature vector obtained at the fully connected layer are

further subjected to classification and the classifier results are obtained at the output layer.

Unlike other machine learning approaches, CNN-based classification methods provide superior performance due to their property of scale, rotation, and field of view. This property makes it suitable for retinal fundus image based DR grading, since acquired fundus images are of different sizes and different fields of view. The automated prognosis for referred retinopathy is important to manage the workload on ophthalmologists by identifying patients who require significant eye care and specific treatment [229]. Despite the many advances made to use the convolutional neural networks for DR diagnosis, these systems still persist challenges for clinical applications. Some of these limitations are being addressed in this work using a transfer learning-based CNN approach.

6.1.2 Transfer Learning

A substantial amount of time and a large dataset is required for deep neural network training from scratch which is a complex task for medical domain, where typically a limited amount of annotated data is accessible. Therefore, in this particular domain, transfer learning plays a very significant role, allowing the use of pre-trained architectures which were previously used for addressing the problems of similar domain. Comparative to traditional task specific machine learning, transfer learning allows the learning of a new task based on the previously learned tasks making the learning process faster and more accurate without needing much of the training data [228-231]. The large datasets are used to train the pre-trained CNN networks on distinct object categories. The most popular dataset used in the pre-trained CNN models utilized for transfer learning is ImageNet dataset [232] that contains a huge number of images for training.

The algorithms based on deep learning approximates a function among input and output by random initialization of network parameters and gradual updation of these parameters while minimizing the loss function. The algorithms used to deal with this situation are variants of classical gradient descent algorithms, therefore, this type of approximation is referred to as gradient based learning. LeNet, one of the earliest gradient based learning methods which was given by Lecun *et al.* [34] in 1998 to promote the development of deep learning for handwritten and machine printed character recognition. This architecture emerges as initial CNN but was not popular

due to the lack of hardware resources, especially Graphics Processing Units (GPUs). With the advancement in technology, CNN became the finest choice for computer vision applications and various CNN architectures have been built since 2012 till date. There are various deep learning based state-of-the-art architectures which are openly shared for transfer learning across various domains. Figure 6.2 depicts the layered architecture of few pre-trained CNN networks.

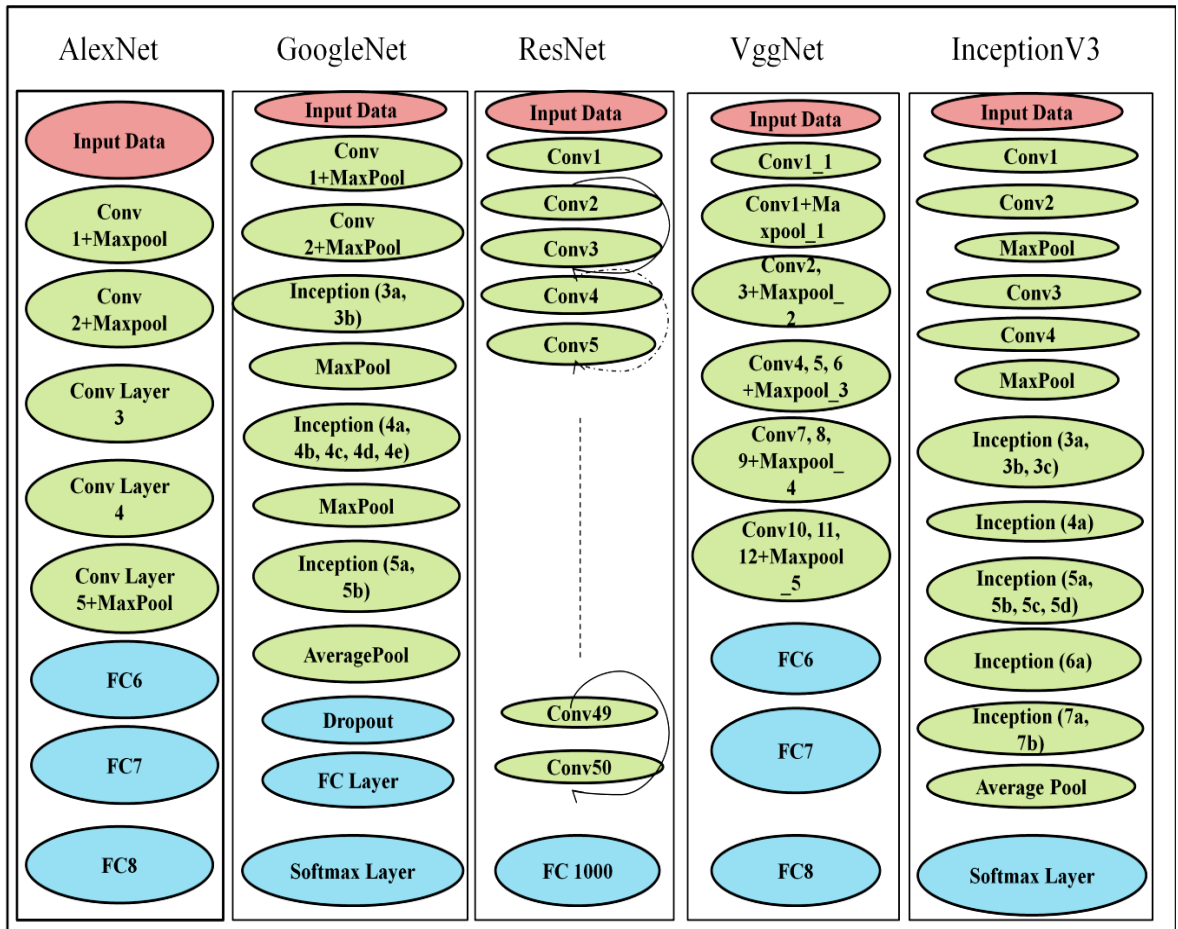


Figure 6.2: Network architecture of different pre-trained CNN models

AlexNet [35], GoogleNet [36], ResNet [37], VggNet [38], and Inception Networks [39] are different CNN architectures which have been proposed for various classification tasks. Transfer learning allows the training of different pre-trained CNN models using image data and the classification outcomes are directly obtained from the respective classification layers.

Transfer learning concept is basically inspired from the human capabilities of transferring the knowledge to perform a task more economically and accurately. This approach is particularly significant for dealing with the task specific application having limited amount of labelled data. Therefore, this approach has a wide applicability in image classification domain specifically in medical image processing. The transfer learning concept can be accomplished either by using the process of data mapping from various different domains to a common platform or by using the different domain samples while assigning individually different weights to them. The generic features are detected by the initial layers of the CNN architecture and dataset specific features are detected by the final layers.

The strategies involved in transfer learning involves:

- i.** Utilization of the complete futuristic architecture for target application that has been verified for its validity on various challenging datasets and training it from scratch.
- ii.** Elimination of actual fully connected layers out from pre-trained model, fine tuning the top network layers and while keeping the bottom layers frozen, adding new classification layer that suits the target task.
- iii.** Removal of original fully connected layers and freeze the entire network for using the CNN pre-trained layers as feature extractor and then adding a machine learning classifier like Support Vector Machine (SVM) at the network end.

This research work aims at examining the retinal fundus images to combat the challenge of early DR detection and provide a reliable solution to assist the ophthalmologists with DR severity grading. In Chapter 5, the machine learning methods were exploited for the DR detection and severity grade classification. These methods employ feature engineering module to extract clinically relevant features from the fundus images by investigating settings with prior expert knowledge. To remove the requirement of feature engineering module, deep learning function, subset of machine learning is exploited in this chapter to assess its suitability for DR classification due to its promising contribution towards medical image analysis.

The above-mentioned gradient based transfer learning strategies are used in this work to address DR classification problem and network performance validation. For

the detection of diseased and non-diseased DR classes, the state-of-the-art pre-trained CNN architectures have been utilized followed by the development of a new CNN architecture for binary classification. The most recent transfer learning based DR diagnostic approach reported by Saranya and Prabakaran [179] provides DR detection and grading by employing pre-processing and image resizing pipeline before providing them to the CNN network. This method provides better performance in terms of various performance metrics, thereby providing an efficient DR severity grading solution.

DR severity grading is addressed by adopting two approaches: first one utilizes the CNN pre-trained layers are considered as feature extractor and SVM classifier is implemented for DR severity classification. The second approach freezes the bottom layers of pre-trained CNN network while the fine tuning of initial network layers, followed by the addition of DR severity classification layer at the end of the network. The gradient based deep learning method identifies salient low-level features using its capability of extending the previously acquired knowledge to the DR training dataset. It reduces the generalization error by approximating and regularly updating the network parameters, thus utilized in this work.

6.2 GRADIENT BASED DEEP LEARNING METHODS

Deep learning models are the layered architectures which allows image feature learning at different hierarchical layers that are associated with fully connected layers to obtain the output. Gradient based deep learning has made considerable improvement in tackling complex problems but on the cost of larger amount of data and training time. However, the transfer of state of art deep learning networks provides easy implementation in various domains like computer vision, image recognition, etc. Transfer learning allow the utilization of a pre-trained network without its final layer, facilitating feature extraction for a new domain task. For DR classification problem, the main constraint is the availability of large amount of annotated training samples per DR class. To address this issue gradient based transfer learning approach is implemented. The standard MESSIDOR dataset [43] have been utilized to classify fundus images with high accuracy into various DR stages as annotated by the experts.

The detailed description of the dataset along with the different DR stages; non-diseased, mild, moderate and severe NPDR graded as grade 0,1,2 and 3 respectively, are provided in Chapter 1. In this work, pre-trained network for DR classification problem through transfer learning is employed. This section provides gradient based transfer learning implementation of different pre-trained models along with the computations involved solve the DR classification problem.

6.2.1 Conventional CNN models

CNNs have been designated to address several computer-vision challenges like image recognition and classification, audio classification and natural language processing tasks. The rise of CNN based deep learning approaches for image classification initiated in 2012 by the introduction of AlexNet [35]. Since then, the usage of CNN for image recognition and classification has increased and various other architectures like GoogleNet [36], ResNet [37], VGGNet [38] and Inception Networks [39] were introduced to provide improved accuracy and eliminate the need for feature engineering in image classification problem.

i. AlexNet

Alexnet [35] is an eight layered architecture in which first five layers are a stack of convolutional and max pooling layers, followed by the three subsequent fully connected layers. The complete description of filter size, stride and number of filters in each layer is provided in Table 6.1. AlexNet accepts the input image of size as expressed by Eq. (6.1).

$$H_1 \times W_1 \times C_1 = 227 \times 227 \times 3 \quad (6.1)$$

where H_l is the height, W_l is the width and C_l refers to channel number associated with the input image.

The first convolutional layer comprises of $k = 96$ filters of $F \times F = 11 \times 11$ size, stride (s) = 4 and padding (p) = 0. Therefore, output size of convolutional filter is calculated using Eq. (6.2).

$$\begin{aligned} & \text{For } \left(H_2 = \frac{H_1 - F + 2P}{s} + 1 \right), \left(W_2 = \frac{W_1 - F + 2P}{s} + 1 = 55 \right), (C_2 = k) \\ \xrightarrow{\text{yields}} & \left(H_2 = \frac{227 - 11 + 0}{4} + 1 = 55 \right), \left(W_2 = \frac{227 - 11 + 0}{4} + 1 = 55 \right), (C_2 = 96) \end{aligned}$$

$$\text{Output size} = H_2 \times W_2 \times C_2 = 55 \times 55 \times 96 \quad (6.2)$$

The number of trainable parameters calculated using the weight information (W_c) and the bias (B_c) is expressed by Eq. (6.3). For filter size $F = 11$, number of filters $k = 96$ and number of channels $C_1 = 3$.

$$W_c = F^2 \times C_1 \times k \text{ and } B_c = k$$

$$\text{Number of Trainable Parameters} = W_c + B_c \quad (6.3)$$

$$\xrightarrow{\text{yields}} (11^2 \times 3 \times 96) + 96 = 34944 \text{ parameters}$$

Max pooling layer is the second layer of architecture, whose output size depends upon the output of the preceding convolutional layer, $H_2 \times W_2 \times C_2 = 55 \times 55 \times 96$ with pooling filter size $F \times F = 3 \times 3$ and stride (s) = 3 given by Eq. (6.4).

$$\begin{aligned} & \text{For } H_p = \frac{H_2 - F}{s} + 1, W_p = \frac{W_2 - F}{s} + 1, D_p = C_2 \\ \xrightarrow{\text{yields}} & H_p = \left(\frac{55 - 3}{2} + 1 \right), W_p = \left(\frac{55 - 3}{2} + 1 \right), D_p = 96 \end{aligned}$$

$$\text{Output size of Pooling Layer} = H_p \times W_p \times D_p = 27 \times 27 \times 96 \quad (6.4)$$

Since the pooling layer computes a fixed function, no trainable parameters are present in this layer. The output size, trainable parameters of other convolutional and the output size of pooling layers are computed using the above-mentioned equations (Eq. (6.1) to Eq. (6.4)).

The output size of fully connected layers is a vector of length equal to the amount of neurons present in the corresponding layer. The amount of parameters are computed using Eq. (6.5).

For ($O = 6 \times 6$) output size of the previous layer, ($k = 256$) filters present in previous layer and ($N_{FC} = 4096$) neurons present in fully connected layer, weight (W_{FC}) and bias (B_{FC}) are computed as:

$$W_{FC} = O^2 \times k \times N_{FC} = 6^2 \times 256 \times 4096 \text{ and } B_{FC} = N_{FC} = 4096$$

$$\begin{aligned} \text{Number of Trainable Parameters in Fully Connected layer 6} &= W_c + B_c \quad (6.5) \\ &\xrightarrow{\text{yields}} 37,748,236 + 4096 = 37,752,832 \text{ paramters} \end{aligned}$$

Similarly, the output sizes and parameters of other layers of AlexNet pre-trained model are computed and are presented in Table 6.1.

Table 6.1: Layer wise description of network parameters in AlexNet architecture

Layer Index	Type	Learnables			Output Size	Parameters
		Filter Size	Stride	Number of Filters / Pooling type		
0	Input data	-----	-----	-----	(227×227×3)	-----
1	Convolution Layer 1	(11×11)	4	96	(55×55×96)	34,944
2	Pooling Layer 1	(3×3)	2	Max Pool	(27×27×96)	-----
3	Convolution Layer 2	(5×5)	1	256	(27×27×256)	6,14,656
4	Pooling Layer 2	(3×3)	2	Max Pool	(13×13×256)	-----
5	Convolution Layer 3	(3×3)	1	384	(13×13×384)	8,85,120
6	Convolution Layer 4	(3×3)	1	384	(13×13×384)	13,27,488
7	Convolution Layer 5	(3×3)	1	256	(13×13×256)	8,84,992
8	Pooling Layer 5	(3×3)	2	Max Pool	(6×6×256)	-----
9	Fully Connected Layer 6	-----	-----	4096	(1×1×4096)	37,752,832
10	Fully Connected Layer 7	-----	-----	4096	(1×1×4096)	16,781,312
11	Fully Connected Layer 8	-----	-----	1000	(1×1×1000)	4,097,000

For this particular transfer learning based application, the final fully connected layer is replaced with the 4 categories of DR severities: non-diseased, mild, moderate and severe DR, thereby reducing the parameters of the Fully Connected layer 8 (FC8) from 4,097,000 to 16,388.

The parameters evaluated for performance evaluation of the pre-trained models are training time-elapsed by convolution neural network, accuracy and cross-entropy loss. The percentage of correctly predicting the test data utilizing the trained model is observed from accuracy. The cross-entropy loss evaluates classification model performance ranging in between 0 to 1. Accuracy should be maximized and cross-entropy loss should be minimized for a perfect classification case.

A fixed epoch size of 20 and number of iterations are kept constant to 200 for the complete computation. The observed outcomes for accuracy, time-elapsed, and cross-entropy loss are represented in Table 6.2.

Table 6.2: Time-elapsed, accuracy and cross-entropy loss performance for AlexNet

Epoch	Iterations	Time Elapsed	Accuracy	Cross-Entropy Loss
1	1	00:00:02	50.11%	0.7912
2	20	00:00:19	52.34%	0.7852
3	30	00:00:47	50.11%	0.7791
4	40	00:01:31	61.47%	0.7696
5	50	00:02:43	52.34%	0.7581
6	60	00:03:47	65.59%	0.7558
7	70	00:04:59	65.59%	0.7489
8	80	00:05:09	51.47%	0.7378
9	90	00:06:38	55.58%	0.7231
10	100	00:07:56	58.93%	0.7152
11	110	00:08:48	61.47%	0.7112
12	120	00:09:52	61.47%	0.7052
13	130	00:10:16	65.59%	0.7001
14	140	00:11:26	68.95%	0.6996
15	150	00:12:06	68.95%	0.6981
16	160	00:13:22	71.24%	0.6858
17	170	00:14:56	71.24%	0.6805
18	180	00:15:05	73.33%	0.6782
19	190	00:16:19	73.33%	0.6768
20	200	00:17:04	73.33%	0.6763

Table 6.2 depicts performance statistics of Alexnet model providing the maximum accuracy of 73.33%. The total computation time of 17 minutes 04 seconds was taken for network training. The further increase of epoch size beyond this point does not show any significant improvement in the accuracy value. Cross-entropy loss value also reduces at every epoch and the minimum of 0.6763 at 20th epoch.

The reduced depth and learning rate of AlexNet architecture during the training process is a disadvantage of this network, which leads to the introduction of GoogleNet that builds a dense network roughly twice as deeper as AlexNet.

ii. GoogleNet

GoogleNet [36] is the manifestation of the Inception architecture that allows increasing number of units for every stage without affecting computational efficiency. The network is 22 layers deep and having the input size of $227 \times 227 \times 3$. The detailed description of filter size, stride and number of filters of each layer is provided in Table 6.3 along with the output size of each layer. The network parameters are computed for the entire architecture in the similar way as done for AlexNet using Eq. (6.1) - Eq. (6.4).

Table 6.3: Layer wise description of network parameters in GoogleNet Architecture

Layer Index	Type	Learnables			Output Size	Parameters
		Filter Size	Stride	Number of Filters / Pooling type		
0	Input data	-----	-----	-----	($227 \times 227 \times 3$)	-----
1	Convolution Layer 1	(7×7)	2	64	($112 \times 112 \times 64$)	27,000
2	Pooling Layer 1	(3×3)	2	Max Pool	($56 \times 56 \times 64$)	-----
3	Convolution Layer 2	(3×3)	1	192	($56 \times 56 \times 192$)	112,000
4	Pooling Layer 2	(3×3)	2	Max Pool	($28 \times 28 \times 192$)	-----
5	Inception (3a)	-----	-----	-----	($28 \times 28 \times 256$)	159,000
6	Inception (3b)	-----	-----	-----	($28 \times 28 \times 480$)	380,000
7	Pooling Layer 3	(3×3)	2	Max Pool	($14 \times 14 \times 480$)	-----
8	Inception Module (4a)	-----	-----	-----	($14 \times 14 \times 512$)	364,000
9	Inception Module (4b)	-----	-----	-----	($14 \times 14 \times 512$)	437,000
10	Inception Module (4c)	-----	-----	-----	($14 \times 14 \times 512$)	463,000
11	Inception Module (4d)	-----	-----	-----	($14 \times 14 \times 528$)	580,000
12	Inception Module (4e)	-----	-----	-----	($14 \times 14 \times 832$)	840,000
13	Pooling Layer 4	(3×3)	2	Max Pool	($7 \times 7 \times 832$)	-----
14	Inception Module (5a)	-----	-----	-----	($7 \times 7 \times 832$)	1,072,000
15	Inception Module (5b)	-----	-----	-----	($7 \times 7 \times 1024$)	1,388,000
16	Pooling Layer 5	(3×3)	2	Average Pool	($1 \times 1 \times 1024$)	-----
17	Dropout Layer	-----	-----	-----	($1 \times 1 \times 1024$)	-----
18	Fully Connected Layer	-----	-----	-----	($1 \times 1 \times 1000$)	1,000,000
19	Softmax Layer	-----	-----	-----	($1 \times 1 \times 1000$)	-----

For DR classification, the final softmax layer of the network is replaced with the 4 DR severity categories. The parameter evaluation of transfer learning utilizing GoogleNet pre-trained model, for measuring time elapsed, accuracy and cross-entropy loss by keeping the values of epoch size and iterations constant is shown in Table 6.4.

Table 6.4: Time-elapsed, accuracy and cross-entropy loss performance for GoogleNet

Epoch	Iterations	Time Elapsed	Accuracy	Cross-Entropy Loss
1	1	00:00:34	51.51%	0.7891
2	20	00:01:17	53.21%	0.7782
3	30	00:01:57	53.21%	0.7721
4	40	00:02:31	51.51%	0.7685
5	50	00:03:45	55.34%	0.7643
6	60	00:04:43	55.34%	0.7589
7	70	00:06:47	57.71%	0.7523
8	80	00:08:59	57.71%	0.7484
9	90	00:10:09	58.81%	0.7431
10	100	00:12:38	58.81%	0.7394
11	110	00:14:56	61.21%	0.7291
12	120	00:15:48	58.81%	0.7262
13	130	00:16:52	62.56%	0.7189
14	140	00:17:16	62.56%	0.7145
15	150	00:18:26	63.89%	0.7034
16	160	00:19:06	63.89%	0.7022
17	170	00:20:22	64.52%	0.6987
18	180	00:21:56	64.52%	0.6952
19	190	00:22:05	65.56%	0.6879
20	200	00:23:51	65.56%	0.6864

The tabular representation reveals that the total 23 minutes 51 seconds of time is elapsed for the network training and maximum accuracy of 65.56% is maintained by the GoogleNet model. The cross-entropy reduction is also observed 0.6864 at 20th epoch which is the minimum loss value for this architecture.

GoogleNet provides lower error rate as compared to other CNN derivatives but the accuracy value saturates while building a deeper network. ResNet is an alternative for this problem which uses the gated skip connection.

iii. ResNet

ResNet [37] takes the advantage of increasing network depth while using the gated skip connections and batch normalization for improving network's capability for generalization.

Table 6.5: Layer wise description of network parameters in ResNet architecture

Layer Index	Type	Learnables			Output Size	Parameters
		Filter Size	Stride	Number of Filters / Pooling type		
0	Input data	----	----	----	(227×227×3)	----
1	Convolution Layer 1	(7×7)	2	64	(112×112×64)	9,472
2	Pooling Layer 1	(3×3)	2	Max Pool	(56×56×64)	----
3	Convolution Layer 2	(3×3)	1	64	(56×56×64)	38,928
4	Convolution Layer 3	(3×3)	1	64	(56×56×64)	38,928
5	Convolution Layer 4	(3×3)	1	64	(56×56×64)	38,928
6	Convolution Layer 5	(3×3)	1	64	(56×56×64)	38,928
7	Convolution Layer 6	(3×3)	1	64	(56×56×64)	38,928
8	Convolution Layer 7	(3×3)	1	64	(56×56×64)	38,928
9	Pooling Layer 1	(3×3)	2	Max Pool	(56×56×64)	----
10	Convolution Layer 8	(3×3)	1	128	(28×28×128)	147,584
11	Convolution Layer 9	(3×3)	1	128	(28×28×128)	147,584
12	Convolution Layer 10	(3×3)	1	128	(28×28×128)	147,584
13	Convolution Layer 11	(3×3)	1	128	(28×28×128)	147,584
14	Convolution Layer 12	(3×3)	1	128	(28×28×128)	147,584
15	Convolution Layer 13	(3×3)	1	128	(28×28×128)	147,584
16	Convolution Layer 14	(3×3)	1	128	(28×28×128)	147,584
17	Convolution Layer 15	(3×3)	1	128	(28×28×128)	147,584
18	Pooling Layer 1	(3×3)	2	Max Pool	(28×28×128)	----
19	Convolution Layer 16	(3×3)	1	256	(14×14×256)	590,080
20	Convolution Layer 17	(3×3)	1	256	(14×14×256)	590,080
21	Convolution Layer 18	(3×3)	1	256	(14×14×256)	590,080
22	Convolution Layer 19	(3×3)	1	256	(14×14×256)	590,080
23	Convolution Layer 20	(3×3)	1	256	(14×14×256)	590,080
24	Convolution Layer 21	(3×3)	1	256	(14×14×256)	590,080
25	Convolution Layer 22	(3×3)	1	256	(14×14×256)	590,080
26	Convolution Layer 23	(3×3)	1	256	(14×14×256)	590,080
27	Convolution Layer 24	(3×3)	1	256	(14×14×256)	590,080
28	Convolution Layer 25	(3×3)	1	256	(14×14×256)	590,080
29	Convolution Layer 26	(3×3)	1	256	(14×14×256)	590,080
30	Convolution Layer 27	(3×3)	1	256	(14×14×256)	590,080
31	Pooling Layer 1	(3×3)	2	Max Pool	(14×14×256)	----
32	Convolution Layer 28	(3×3)	1	512	(7×7×512)	2,359,808
33	Convolution Layer 29	(3×3)	1	512	(7×7×512)	2,359,808
34	Convolution Layer 30	(3×3)	1	512	(7×7×512)	2,359,808
33	Convolution Layer 31	(3×3)	1	512	(7×7×512)	2,359,808
34	Convolution Layer 32	(3×3)	1	512	(7×7×512)	2,359,808
35	Convolution Layer 33	(3×3)	1	512	(7×7×512)	2,359,808
36	Pooling Layer 2	-----	-----	2048/Average Pooling	(1×1×2048)	----
37	Fully Connected Layer 1	-----	-----	1000	(1×1×1000)	513,000

The layer-wise depiction of the network is represented in Table 6.5 illustrating the layer indexing, type, size of filter and filter count, stride, output size and amount of parameters. The generalization capabilities and powerful representation of ResNet have boosted its applications in various image recognition and classification tasks. It comprises of 60 million trainable parameters with gated connections and the transfer learning is performed by replacing the last fully connected layers with DR classification categories. The various performance parameters evaluated for ResNet model are tabulated in Table 6.6.

Table 6.6: Time-elapsd, accuracy and cross-entropy loss performance for ResNet

Epoch	Iterations	Time Elapsed	Accuracy	Cross-Entropy Loss
1	1	00:00:56	50.08%	0.7832
2	20	00:02:43	52.78%	0.7753
3	30	00:03:38	53.25%	0.7732
4	40	00:04:55	50.08%	0.7623
5	50	00:06:44	52.78%	0.7604
6	60	00:07:38	55.44%	0.7596
7	70	00:09:47	57.42%	0.7558
8	80	00:11:29	57.42%	0.7498
9	90	00:13:56	58.11%	0.7475
10	100	00:15:46	58.11%	0.7442
11	110	00:16:49	61.45%	0.7237
12	120	00:17:53	61.45%	0.7221
13	130	00:18:42	62.69%	0.7157
14	140	00:19:36	62.69%	0.7138
15	150	00:21:08	63.93%	0.7098
16	160	00:23:42	63.93%	0.7041
17	170	00:24:36	64.87%	0.6982
18	180	00:25:51	64.87%	0.6976
19	190	00:26:06	65.78%	0.6862
20	200	00:27:46	65.83%	0.6841

From the observations it is found that maximum of 65.83% accuracy is achieved with reduction of 0.6841 in cross-entropy loss for 20th epoch and 200th iteration. The measured time of 27 minutes 26 seconds is elapsed for network training.

ResNet architecture is deeper but somewhat complex, therefore, VggNet came into existence due to its simpler implementation while maintaining the increased depth.

iv. VggNet

This network has simple implementation utilizing the same filter size of 3×3 throughout the architecture. The input size of $224 \times 224 \times 3$ is accepted by VggNet [38] and the detailing of filter size, stride and the count of filters for each layer is provided in Table 6.7. The number of parameters and output size are calculated in similar way as done for AlexNet which are tabulated in the following table.

Table 6.7: Layer wise description of network parameters in VggNet16 architecture

Layer Index	Type	Learnables			Output Size	Parameters
		Filter Size	Stride	No. of Filters / Pooling type		
0	Input data	----	----	----	$(224 \times 224 \times 3)$	----
1	Convolution Layer 1	(3×3)	1	64	$(224 \times 224 \times 64)$	1,792
3	Convolution Layer 2	(3×3)	1	64	$(112 \times 112 \times 64)$	36,928
4	Pooling Layer 1	(3×3)	2	Max Pool	$(112 \times 112 \times 64)$	----
5	Convolution Layer 3	(3×3)	1	128	$(112 \times 112 \times 128)$	73,856
6	Convolution Layer 4	(3×3)	1	128	$(112 \times 112 \times 128)$	147,584
4	Pooling Layer 2	(3×3)	2	Max Pool	$(112 \times 112 \times 128)$	----
7	Convolution Layer 5	(3×3)	1	256	$(56 \times 56 \times 256)$	295,168
8	Convolution Layer 6	(3×3)	1	256	$(56 \times 56 \times 256)$	590,080
9	Convolution Layer 7	(3×3)	1	256	$(56 \times 56 \times 256)$	590,080
10	Pooling Layer 3	(3×3)	2	Max Pool	$(56 \times 56 \times 256)$	----
11	Convolution Layer 8	(3×3)	1	512	$(28 \times 28 \times 512)$	1,180,160
12	Convolution Layer 9	(3×3)	1	512	$(28 \times 28 \times 512)$	2,359,808
13	Convolution Layer 10	(3×3)	1	512	$(28 \times 28 \times 512)$	2,359,808
14	Pooling Layer 4	(3×3)	2	Max Pool	$(28 \times 28 \times 512)$	----
15	Convolution Layer 11	(3×3)	1	512	$(14 \times 14 \times 512)$	2,359,808
16	Convolution Layer 12	(3×3)	1	512	$(14 \times 14 \times 512)$	2,359,808
17	Convolution Layer 13	(3×3)	1	512	$(14 \times 14 \times 512)$	2,359,808
18	Pooling Layer 5	(3×3)	2	Max Pool	$(7 \times 7 \times 512)$	----
19	Fully Connected Layer 6	----	----	4096	$(1 \times 1 \times 4096)$	102,764,544
20	Fully Connected Layer 7	----	----	4096	$(1 \times 1 \times 4096)$	16,781,312
21	Fully Connected Layer 8	----	----	1000	$(1 \times 1 \times 1000)$	4,097,000

VggNet16 consists of 138 million parameters providing improved performance with simpler implementation. The fundus images for DR classification are subjected to input layer of pre-trained network and the final layers determines the classification features. The network performance indices are observed as time elapsed, accuracy and the cross-entropy loss while maintaining constant epoch size and iterations. Table 6.8 provides the tabular representation of performance outcomes obtained for VggNet16 model.

Table 6.8: Time-elapsed, accuracy and cross-entropy loss VggNet16

Epoch	Iterations	Time Elapsed	Accuracy	Cross-Entropy Loss
1	1	00:00:55	55.56%	0.6928
2	20	00:02:19	55.56%	0.6914
3	30	00:03:57	56.67%	0.6895
4	40	00:05:31	56.67%	0.6921
5	50	00:06:05	57.78%	0.6846
6	60	00:06:43	58.89%	0.6874
7	70	00:05:17	60.00%	0.6887
8	80	00:05:59	66.67%	0.6882
9	90	00:06:09	66.67%	0.6901
10	100	00:07:18	73.33%	0.6838
11	110	00:07:56	73.33%	0.6818
12	120	00:08:48	81.90%	0.6830
13	130	00:09:52	82.50%	0.6912
14	140	00:10:04	82.50%	0.6853
15	150	00:10:56	83.67%	0.6794
16	160	00:11:06	84.14%	0.6859
17	170	00:12:22	85.87%	0.6786
18	180	00:13:53	85.87%	0.6594
19	190	00:14:85	87.50%	0.6495
20	200	00:15:16	87.50%	0.6394

The performance statistics of VggNet model provides the maximum accuracy of 87.50% consuming a total computation time of 15 minutes 16 seconds for network training. It was also observed that the cross-entropy loss value reduces at every epoch with minimum of 0.6394 cross-entropy loss at 20th epoch.

The exceptional performance is provided by VggNet but the drawback is its usage of higher storage space making this network to train slowly with tedious deployment. To address this shortcoming, Inception V-3 model is introduced.

v. Inception V-3

Another variant of Inception models that is popularly being used nowadays to address image classification and recognition task is Inception V-3 [39]. The input layer expects the images of size of $299 \times 299 \times 3$ and the output size and trainable parameter calculations are done using the equations mentioned in section 6.2.1 using the values of network learnables provided in Table 6.9.

Table 6.9: Layer wise description of network parameters in Inception V-3 architecture

Layer Index	Type	Learnables			Output Size	Parameters
		Filter Size	Stride	Number of Filters / Pooling type		
0	Input data	----			$(299 \times 299 \times 3)$	----
1	Convolution Layer	(3×3)	2	32	$(149 \times 149 \times 32)$	896
2	Convolution Layer	(3×3)	1	32	$(147 \times 147 \times 32)$	9,248
3	Convolution Layer	(3×3)	1	64	$(147 \times 147 \times 64)$	18,496
4	Pooling Layer	(3×3)	2	Max Pool	$(73 \times 73 \times 64)$	----
5	Convolution Layer	(1×1)	1	80	$(73 \times 73 \times 80)$	5,200
6	Convolution Layer	(3×3)	1	192	$(71 \times 71 \times 192)$	138,432
7	Pooling Layer	(3×3)	2	Max Pool	$(35 \times 35 \times 192)$	----
8	Inception Module A	----	----	256	$(35 \times 35 \times 256)$	----
9	Inception Module A	----	----	288	$(35 \times 35 \times 288)$	----
10	Inception Module A	----	----	288	$(35 \times 35 \times 288)$	----
11	Inception Module B	----	----	768	$(17 \times 17 \times 768)$	----
12	Inception Module C	----	----	768	$(17 \times 17 \times 768)$	----
13	Inception Module C	----	----	768	$(17 \times 17 \times 768)$	----
14	Inception Module C	----	----	768	$(17 \times 17 \times 768)$	----
15	Inception Module C	----	----	768	$(17 \times 17 \times 768)$	----
16	Inception Module D	----	----	2048	$(8 \times 8 \times 2048)$	----
17	Inception Module E	----	----	2048	$(8 \times 8 \times 2048)$	----
18	Inception Module E	----	----	2048	$(8 \times 8 \times 2048)$	----
19	Pooling Layer	(8×8)	8	2048/Avg Pool	$(1 \times 1 \times 2048)$	----
20	Softmax Output Layer	----	----	1000	$(1 \times 1 \times 1000)$	2,049,000

The final layers of Inception V-3 model are retrained maintaining the knowledge which the network has learned during its original training process. This learned knowledge is applied to the small DR classification dataset and the network performance is observed. Table 6.10 provides the tabular representation of performance parameters evaluated when the retinal images are provided to the Inception V-3 model.

Table 6.10: Time-elapsed, accuracy and cross-entropy loss for Inception V-3 model

Epoch	Iterations	Time Elapsed	Accuracy	Cross-Entropy Loss
1	1	00:00:52	60.00%	0.721
2	20	00:01:19	51.32%	0.793
3	30	00:02:47	53.21%	0.762
4	40	00:04:31	55.67%	0.771
5	50	00:06:15	62.17%	0.762
6	60	00:08:43	55.67%	0.732
7	70	00:11:47	62.17%	0.824
8	80	00:13:59	65.21%	0.765
9	90	00:15:09	62.17%	0.691
10	100	00:19:38	65.21%	0.682
11	110	00:21:56	55.67%	0.710
12	120	00:24:48	60.00%	0.652
13	130	00:25:52	62.17%	0.681
14	140	00:27:16	65.21%	0.684
15	150	00:30:26	71.57%	0.695
16	160	00:33:06	75.33%	0.672
17	170	00:35:22	75.33%	0.681
18	180	00:36:56	80.00%	0.672
19	190	00:37:05	82.14%	0.669
20	200	00:38:50	82.14%	0.665

The tabular comparison shown in Table 6.10 reveals that the accuracy of 82.14% is provided by the Inception V-3 model after completing 20 epoch and 200 iterations. The minimum of 0.665 of cross-entropy loss is achieved at the maximum epoch size of 20 consuming a total time of 38 minutes and 50 seconds in the entire execution. It has been observed that the network accuracy improves from 60% to 82.14% from 1st epoch to 20th epoch utilizing 200 iterations, however, the network accuracy does not improve beyond this value even after increasing the maximum epoch size or iterations.

There exist numerous CNN models that are utilized for performing different designated tasks. After evaluation of various pre-trained CNN models, a new architecture of CNN has been proposed for addressing the DR detection problem and provide better efficiency for the classification of retinal fundus images into two classes: non-diseased and DR affected.

6.2.2 Ensembled Deep Learning DR Detection Model for Binary Classification

A new Ensembled Deep Learning DR Detection (EDLDR) model is proposed in this work, which uses 1200 images initially for its pre-training until a substantial level is achieved for more accurate classification with better performance. The process of the proposed Deep Learning DR (DLDR) classification model is represented in Figure 6.3.

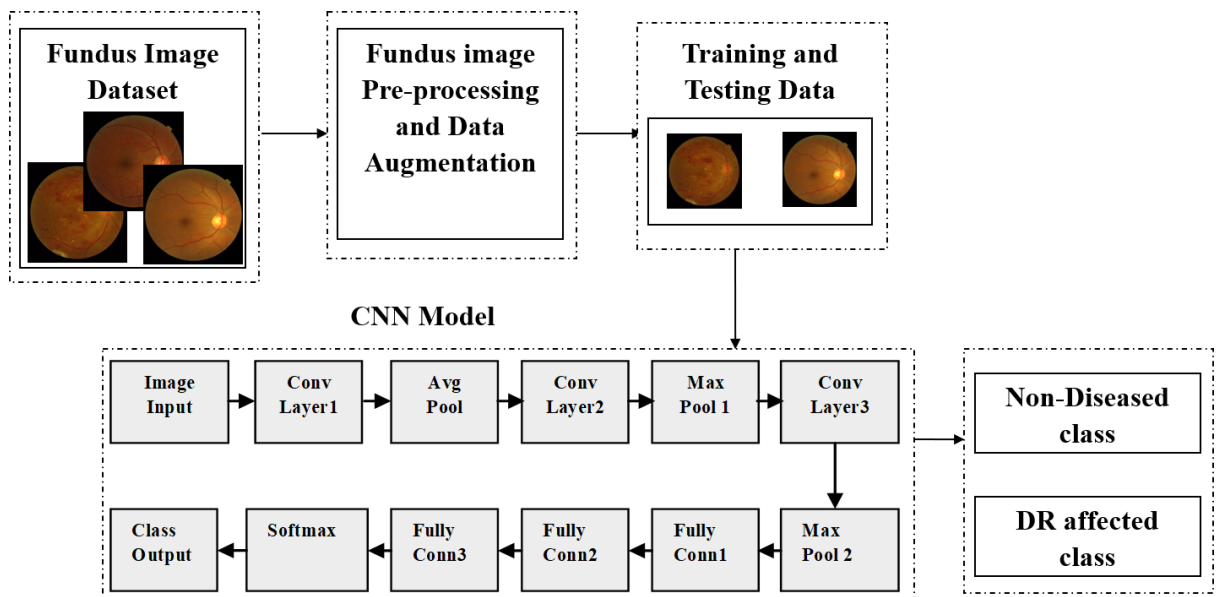


Figure 6.3: Flowchart of proposed DLDR classification model

The proposed DLDR model is provided with the iterative input of pre-processed and augmented training data. The different functioning layers determines efficient features which are required for classification and with the increase in number of layers the model becomes more efficient. Inter and intra pixel variability of fundus images is removed using pre-processing steps and all the images are resized to 128×128 before feeding them to the network. The step of data augmentation is implemented for improving the localization capability of network by applying 90 to 180 degree rotations, horizontal and vertical flips, shifts randomly. The class size is also increased

using the data augmentation step, because of limited training samples. Low learning rate of 0.0001 was tested for overall epoch size considering the 70% samples from the whole dataset and remaining data of 30% is kept for testing. In testing phase, the model discovers image features that are learnt during training and further classifies the image accordingly.

From literature, various models consisting stack of convolution layer, pooling layer and fully connected layer have been studied along with variation in filter number and size [161, 164]. In order to improve the learning capability of network, the output of convolution layer is routed through the non-linear function, thereby increasing its non-linear property. The layer wise description of proposed deep learning models in this research work detailed in Figure 6.4.

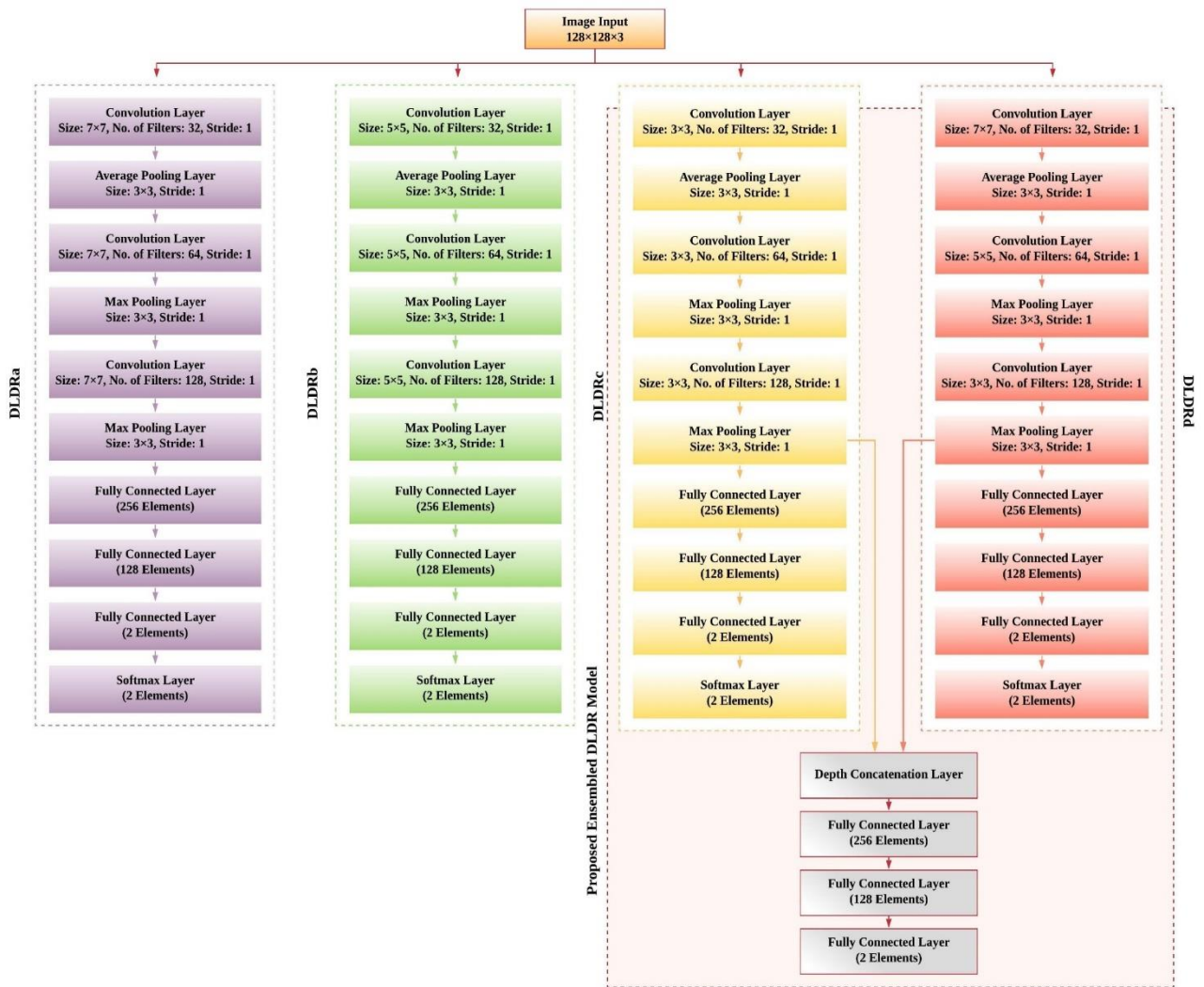


Figure 6.4: Layer wise depiction of the proposed DLDR models

The architecture of proposed DLDR models are comprised of 12 functioning layers with alteration in filter size of convolution. The considered filter size for all convolution layers for *DLDRa*, *DLDRb* and *DLDRc* models are 7×7 , 5×5 and 3×3 , respectively. The convolution filter size of *DLDRd* model is varied, where the filter size of initial layer is 7×7 , followed by 5×5 filter size for next layer and filter size of 3×3 for last convolution layer. This variation in filter size is done to evaluate the effect of varying filter size and number of filters for providing high learning capacity with improved classification performance. Average pooling and max pooling layers are considered as pooling layers in proposed model. In this research work both pooling options are considered with kernel size of 3×3 and stride of 1×1 . Three of fully connected layers are utilized for accomplishing CNN flattening, in order to reduce the immediate dropout for last classification layer. The softmax activation function is utilized for predicting the classification, whereas the chances of overfitting are reduced by performing dropout.

An ensemble CNN architecture is proposed with filter sizes of *DLDRc* and *DLDRd* which are concatenated before routing the features through fully connected layers to obtain better performance along with loss reduction.

The size of input fundus image provided to initial layer of network is represented by Eq. (6.6).

$$H_1 \times W_1 \times C_1 = 128 \times 128 \times 3 \quad (6.6)$$

where H_1 is the height, W_1 is the width and C_1 represents number of channel present in the input fundus image.

The first convolutional layer comprises of $k = 32$ filters of size $(F \times F) = 7 \times 7$, stride $(s) = 1$ and padding $(p) = 0$. Thus, the outsize of the first convolutional filter is calculated using Eq. (6.7).

$$\text{For } \left(H_2 = \frac{128 - 7 + 0}{1} + 1 = 122 \right), \left(W_2 = \frac{128 - 7 + 0}{4} + 1 = 122 \right), (C_2 = 32)$$

$$\text{Output size} = H_2 \times W_2 \times C_2 = 122 \times 122 \times 32 \quad (6.7)$$

The number of trainable parameters calculated using the weight information (W_c) and the bias (B_c) is expressed by Eq. (6.8). For filter size $F = 7$, number of filters $k = 32$ and number of channels $C_1 = 3$.

$$W_c = F^2 \times C_1 \times k = (7^2 \times 3 \times 32) \text{ and } B_c = k = 32$$

$$\text{Number of Trainable Parameters} = W_c + B_c \quad (6.8)$$

$$\xrightarrow{\text{yields}} 4,704 + 96 = 4,736 \text{ paramters}$$

The output size of max pooling layer is measured using the output of the preceding convolutional layer, $H_2 \times W_2 \times C_2 = 122 \times 122 \times 32$ with pooling filter size $F \times F = 3 \times 3$ and stride (s) = 1 given by Eq. (6.9).

$$\text{For } H_p = \frac{H_2 - F}{s} + 1, W_p = \frac{W_2 - F}{s} + 1, D_p = C_2$$

$$\xrightarrow{\text{yields}} H_p = \left(\frac{122 - 3}{1} + 1 \right), W_p = \left(\frac{122 - 3}{1} + 1 \right), D_p = 32$$

$$\text{Output size of Pooling Layer 1} = H_p \times W_p \times D_p = 120 \times 120 \times 32 \quad (6.9)$$

Similarly, the output size as well as trainable parameters for other convolutional layers and the output size of other pooling layers are computed and are tabulated in Table 6.11. The trainable parameter of fully connected layers is evaluated using Eq. (6.10) and its output size is given by a vector length which is equal to the total number of neurons present in layer. For ($O = 104 \times 104$) output size of the previous layer, ($k = 128$) number of filters present in previous layer and ($N_{FC} = 256$) number of neurons in fully connected layer, weight (W_{FC}) and bias (B_{FC}) are computed as:

$$W_{FC} = O^2 \times k \times N_{FC} = 104^2 \times 128 \times 256 \text{ and } B_{FC} = N_{FC} = 256$$

$$\text{Number of Trainable Parameters in Fully Connected layer 1} = W_c + B_c \quad (6.10)$$

$$\xrightarrow{\text{yields}} 354,418,688 + 256 = 354,418,944 \text{ paramters}$$

$$\text{Similarly, Number of Parameters in FC2} = (256 \times 128) + 128 = 32,896$$

$$\text{Number of Parameters in FC3} = (128 \times 2) + 2 = 258$$

Table 6.11: Layer-wise specifications of network parameters for the proposed DLDR models

Layer Name	No. of Filter	Stride	DLDR a			DLDR b			DLDR c			DLDR d		
			Filter Size	Output Size	Parameter									
Image Input Layer	-----	-----	128×128×3	-----	-----	128×128×3	-----	-----	128×128×3	-----	-----	128×128×3	-----	-----
Convolution Layer	32	1	7×7	122×122×32	4,736	5×5	124×124×32	2,432	3×3	126×126×32	896	7×7	122×122×32	4,736
Average Pooling Layer	-----	1	3×3	120×120×32	-----	3×3	122×122×32	-----	3×3	124×124×32	-----	3×3	120×120×32	-----
Convolution Layer	64	1	7×7	114×114×64	100,416	5×5	118×118×64	51,264	3×3	122×122×64	18,496	5×5	116×116×64	51,264
Max Pooling Layer	-----	1	3×3	112×112×64	-----	3×3	116×116×64	-----	3×3	120×120×64	-----	3×3	114×114×64	-----
Convolution Layer	128	1	7×7	106×106×128	401,536	5×5	112×112×128	204,928	3×3	118×118×128	73,856	3×3	112×112×128	73,856
Max Pooling Layer	-----	1	3×3	104×104×128	-----	3×3	110×110×128	-----	3×3	116×116×128	-----	3×3	110×110×128	-----
Fully Connected Layer	-----	1	256	1×1×256	354,418,944	256	1×1×256	396,493,056	256	1×1×256	440,926,464	256	1×1×256	396,493,056
Fully Connected Layer	-----	1	128	1×1×128	32,896	128	1×1×128	32,896	128	1×1×128	32,896	128	1×1×128	32,896
Fully Connected Layer	-----	1	2	1×1×2	258	2	1×1×2	258	2	1×1×2	258	2	1×1×2	258
Softmax Layer	-----	1	2	1×1×2	-----	2	1×1×2	-----	2	1×1×2	-----	2	1×1×2	-----
Classification Output Layer	-----	1	2	1×1×2	-----	2	1×1×2	-----	2	1×1×2	-----	2	1×1×2	-----

The computations of layer-wise specifications of the proposed DLDR model are illustrated in Table 6.11. The conventional classification methods studied in literature suffers from the issue of class imbalance class, thereby inclining towards the majority class. Further, the results as poor performance of classification for minority class. The EDLDR model proposed in this work presents high learning rate but the issue of class imbalance is still same. Therefore, for addressing the class imbalance issue, this proposed work focuses on utilizing same number of images for target classes. Further, the consequence of class imbalance is reduced by introducing data augmentation and thus better classification outcomes are achieved.

6.2.3 Results of EDLDR CNN model

The performance of EDLDR CNN model is observed by measuring the accuracy, time elapsed and cross-entropy loss [33, 161]. Accuracy is the percentage of correct test data prediction utilizing trained model, whereas time elapsed is measured as the time required to train CNN model. The performance of classification model is evaluated using cross-entropy loss and its value lies in a range from 0 to 1, with zero cross-entropy loss for accurate classification case. The observed results obtained from testing all proposed models on MESSIDOR dataset are tabulated in Table 6.12. The experimental results reveal that maximum accuracy for each model is achieved at 20th epoch with 200 iterations, after this the accuracy saturates.

For *DLDRa* model the observed value of accuracy at 20th epoch is 75% along with reduction of 0.675 in cross-entropy loss and the time elapsed in order to train this model is 1 minutes 51 seconds. The accuracy value for model *DLDRb* at 20th epoch is 53.33% with reduction of 0.689 in cross-entropy loss consuming 1 minutes 35 seconds time that is comparatively less than *DLDRc* model. The experimental percentage accuracy value for model *DLDRc* at 20th epoch is 60% along with the reduction of 0.738 in cross-entropy loss and consuming 1 minutes 25 seconds of elapsed time. The maximum accuracy is observed from *DLDRd* model with percentage accuracy value of 87.51% at 20th epoch with reduction of 0.637 in cross-entropy loss and consuming 1 minute and 23 seconds of time at 200th iteration. After comparing the results obtained for four DLDR models, it is observed that proposed *DLDRd* model outperforms and presents better outcomes at 0.0001 base learning rate. The value of cross-entropy loss is also observed less in comparison with other proposed deep learning models.

Table 6.12: Performance Metrics of the proposed DLDR models for MESSIDOR dataset

Models	Filter Size Variation	Epoch					
		1	2	5	10	15	20
<i>DLDRa</i>	32 Filters of size (7×7)	33.33%	40.00%	53.33%	60.00%	73.33%	75.00%
	64 Filter of size (7×7)	00:18	00:44	00:56	01:09	01:22	01:51
	128 Filter of size (7×7)	Cross-entropy Loss	0.715	0.703	0.709	0.677	0.667
<i>DLDRb</i>	32 Filters of size (5×5)	26.67%	33.33%	40.00%	46.67%	50.00%	53.33%
	64 Filter of size (5×5)	00:10	00:35	00:47	01:01	01:26	01:35
	128 Filter of size (5×5)	Cross-entropy Loss	0.689	0.707	0.705	0.698	0.693
<i>DLDRc</i>	32 Filters of size (3×3)	13.33%	33.33%	46.67%	50.00%	53.33%	60.00%
	64 Filter of size (3×3)	01:25	01:17	01:06	00:54	00:31	00:11
	128 Filter of size (3×3)	Cross-entropy Loss	0.699	0.698	0.695	0.691	0.693
<i>DLDRd</i>	32 Filters of size (7×7)	33.31%	46.76%	53.34%	66.67%	75.08%	87.51%
	64 Filter of size (5×5)	00:08	00:29	00:52	01:04	01:16	01:23
	128 Filter of size (3×3)	Cross-entropy Loss	0.708	0.697	0.700	0.691	0.679

The performance of proposed EDLDR model is analyzed by varying the epoch size from 1 to 20 and for iteration count ranges from 1 to 200 at constant base learning rate of 0.0001. The performance analysis of proposed EDLDR model for varying epoch size is represented in Figure 6.5.

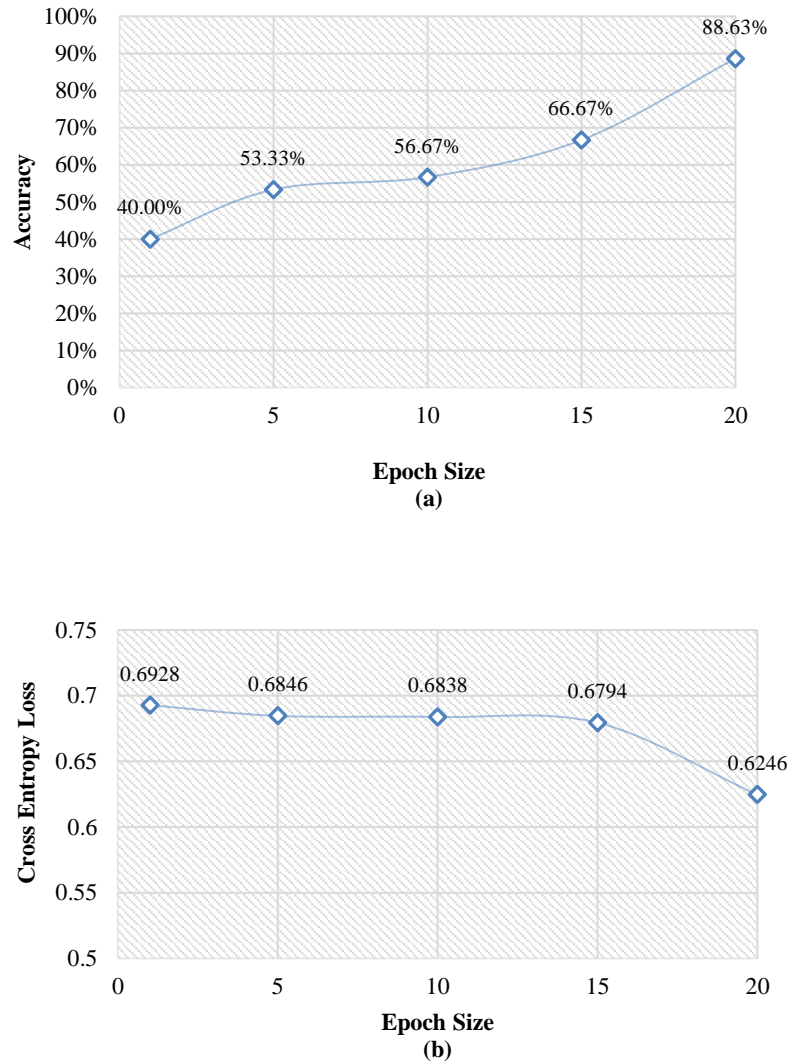


Figure 6.5: Results of the proposed EDLDR CNN model (a) Accuracy (b) Cross Entropy Loss

From Figure 6.5, it can be seen that with the increase in epoch size ranging from 1 to 20, percentage accuracy value increases from 40% to 88.63%. For EDLDR model, the cross-entropy value of 0.963 at epoch size 1 reduces to 0.625 at epoch size 20. The time consumed by proposed model is 3 minutes 41 seconds. The proposed network model efficiently identifies DR classification features from fundus images for the accurate distinction between normal and DR infected cases.

For the performance validation, same processed input fundus images are evaluated on various mainstream architectures for comparing the outcomes with proposed EDLDR model. The comparison of all models for 200 iterations, with epoch size 20 and batch size 15 along with constant base learning rate of 0.0001 is drawn in Figure 6.6.

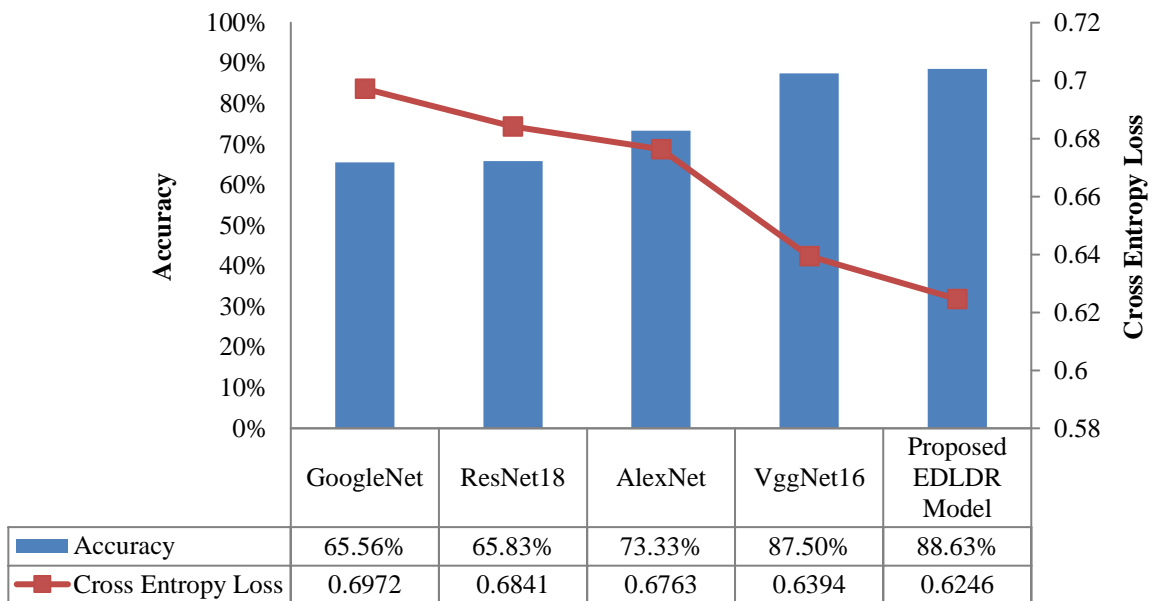


Figure 6.6: Comparison of different Pre-trained models with the proposed EDLDR model

It is observed from the comparative analysis that the proposed EDLDR model presents the accuracy of 88.63% and cross-entropy reduction of 0.6246. The proposed EDLDR model offers significantly improved performance with percentage accuracy improvement of 1.13% and 0.02% reduction in cross-entropy loss comparative to VggNet16 pre-trained model.

In the further part of this research, the pre-trained CNN networks are utilized to distinguish between the different DR severities. From the literature survey for DR severity grading using CNN, it is revealed that the use of transfer learning provides better outcomes compared to the introduction of completely new CNN architectures [230, 231]. Deep Neural Network training from scratch is somewhat challenging for medical domain where typically a limited number of annotated data is available. Thus, transfer learning based automated DR severity grading alternates are presented in this work for severity grade classification.

6.3 PROPOSED METHODOLOGY FOR DEEP LEARNING BASED DR GRADING

The Deep neural networks employing CNN model have proven superior in image classification problems and thus they are also introduced in DR diagnosis application. This research work focuses on developing a transfer learning-based CNN system that can automatically detect lesions and assess its severity grade at different DR stages. CNNs addresses DR classification problem by utilizing the hierarchical and discriminative feature learning approach that classifies the DR severity grades automatically without prior knowledge from experienced experts in this domain. In this work two different DR severity grading approaches are adopted, one employing the CNN pre-trained layers for feature extraction and thereby providing the extracted features to the SVM classifier and the other freezing the bottom layers of the CNN pre-trained network while fine tuning the initial network layers and then adding DR severity classification layer at network end. Both the deep learning based approaches are discussed in the following section in detail.

6.3.1 Transfer-Learning based Automated DR Severity Grading Detection System

The transfer learning based automated DR classification system aims at providing a competent solution for differentiating the fundus images and their severity levels. This approach employs CNN model architecture as a feature extractor followed by a separate feature selection module and a supervised SVM classification method for DR identification and prediction. DR severity grade classification is achieved in this transfer learning based model utilizing various sequential steps that are illustrated in Figure 6.7.

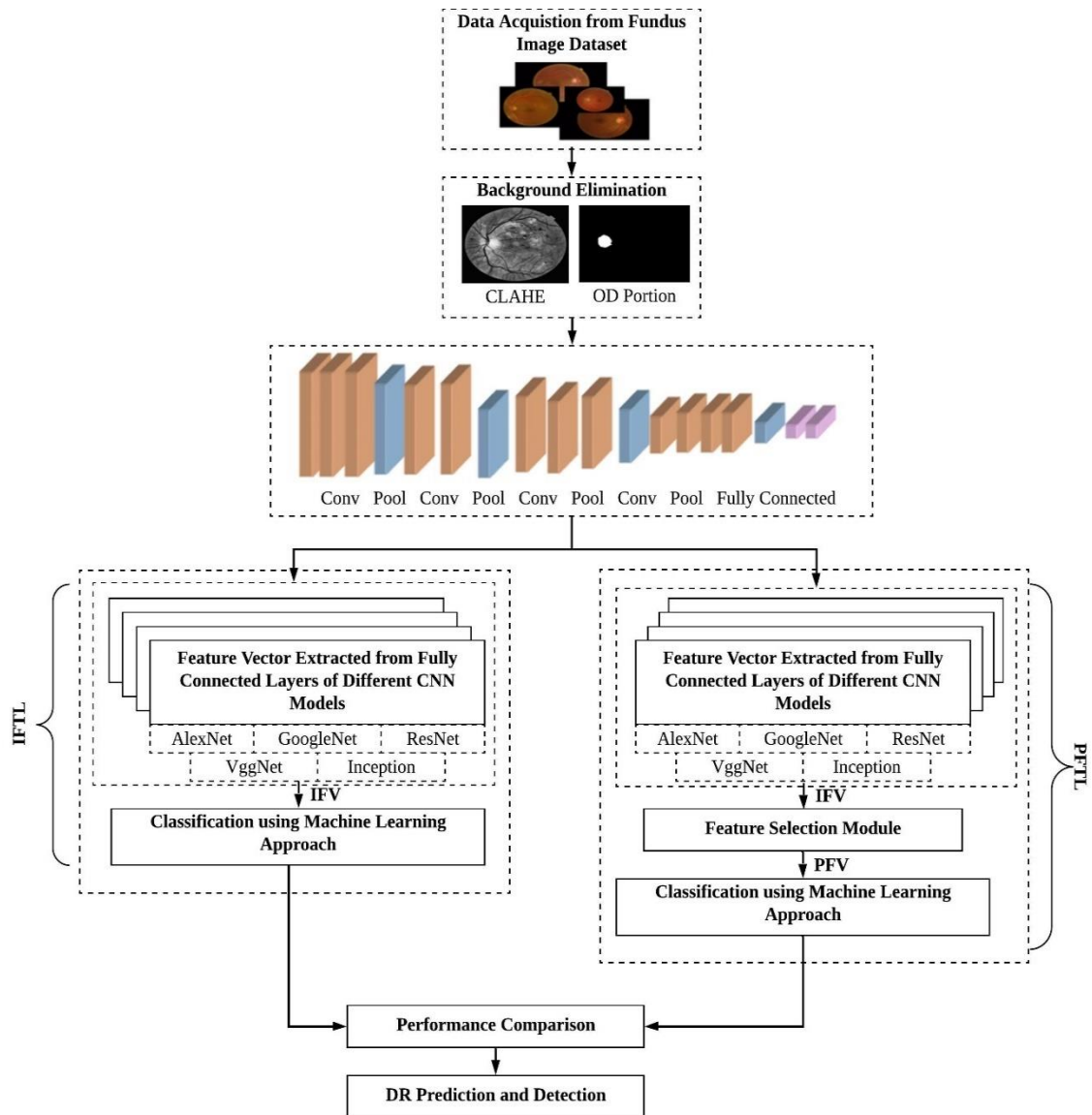


Figure 6.7: Transfer learning based automated DR detection system

*Note: CLAHE-Contrast Limited Adaptive Histogram Equalization, OD- Optical Disc, IFV- Image Feature Vector, PFV- Prominent Feature Vector, IFTL- Image Feature based Transfer Learning, PFTL- Prominent Feature based Transfer Learning

Transfer learning approach aims at building a good classifier by overcoming the limitation of lack of labelled data. Transfer learning extracts the source knowledge and applies that knowledge to the target application domain. This technique effectively replaces the traditional machine learning approaches that learns task without prior knowledge.

Two transfer-learning based models namely, Image Feature based Transfer Learning (IFTL) and Prominent Feature based Transfer Learning (PFTL) are proposed in this work for the detection of DR severities.

The linear combination of previous layer outputs from the preceding convolution and pooling layers acts as the input to the fully connected layers of these proposed models. The estimated probabilities are calculated depending upon the activation functions. The prediction task is performed for other testing samples utilizing automatically extracted CNN features of the trained model.

6.3.1.1 Image Feature based Transfer Learning Model

The steps involved in the proposed IFTL approach are data acquisition, background elimination, Image Feature Vector (IFV) Extraction and Retinal Fundus Image Classification using IFV. In the proposed approach, IFV is extracted from the fully connected layer of CNN architecture which is further provided to machine learning based SVM classification for the prediction DR severity grades. SVM based classification approach improves the generalization ability of CNN while minimizing the errors and enhancing the classification accuracy. Figure 6.8 depicts the flowchart of the proposed IFTL approach.

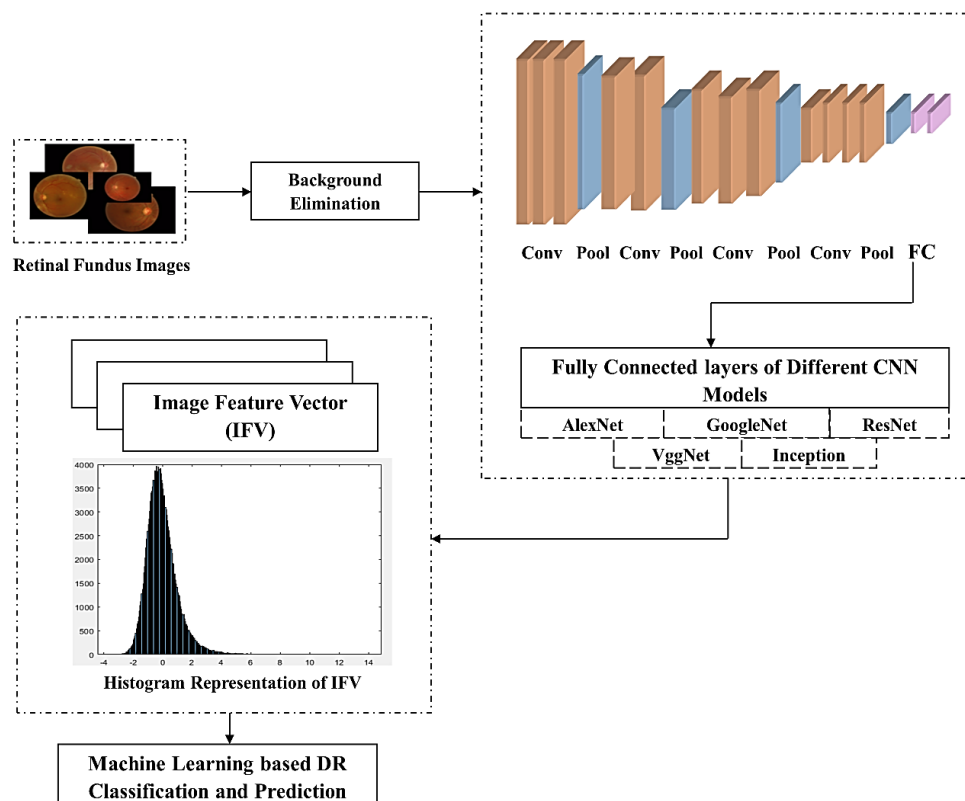


Figure 6.8: Flowchart of proposed IFTL approach

The artefacts in the raw fundus images due to capturing of fundus image at varying surrounding conditions, resolutions, different field of views, poor image contrast, inadequate illumination, patient's movement, bad positioning of lens, etc. [158, 208] are removed using background segmentation method discussed in Chapter 3. This step ensures the differentiation of actual lesion regions from the noisy background data [48, 195]. Another anatomical structure OD is localized due to its irrelevance in the anomaly detection stage. Boundary localization is accomplished using the combination of Circular Hough Transform and morphological closing operation detailed in Chapter 3, treating the largest circular region in the intensity plane as the OD portion [189, 233].

Data augmentation step is employed to mitigate the class imbalance and small dataset problem. Horizontal and vertical flips, random rotations of 90-180 degrees, random zooming of [0.85 to 1.15] steps are involved in data augmentation stage for increasing the number of training samples as well as balance the class size. Overfitting is avoided using this step improving the classification performance [229]. Image pre-processing phase and data augmentation step are introduced for making the proposed system resistant towards variation attenuation, insufficient illumination and different orientations.

In this work, implementation of AlexNet [35], GoogleNet [36], ResNet [37], VggNet [38] and Inception [39] pre-trained CNN networks for fundus image classification application. The fully connected layers of CNN pre-trained models are responsible for extraction of image features to obtain IFVs. Fully connected layers, FC8 layer, AlexNet; softmax layer, GoogleNet; FC1000, ResNet; FC8, VggNet; softmax layer, Inception V-3 respectively are used to extract IFVs in order to achieve significant performance improvement.

Improved accuracy outcomes for grading features of normal and abnormal fundus images into various grades are obtained using different classifier combination in the literature. The flexibility of future event prediction utilizing the past learning from the labelled dataset is the major advantage of machine learning based classification techniques. Machine learning functioning depends upon the prediction of intended output by error measurement between the obtained outcomes and the correct outcome, thereby ensuring modification in the learning algorithm.

The literature review reveals the suitability of SVM Classification method appropriate for DR prediction problem as it categorizes the testing data creating a hyperplane using labelled training data. This method is practically applicable for both binary as well as multi-class classification and the classifier details are provided in Chapter 1 [23, 24]. One-against-rest approach is utilized for dealing with the DR classification problem utilizing the tuning parameters; regularization parameter and gamma to obtain accurate classification results.

6.3.1.2 Prominent Feature based Transfer Learning Model

CNN model acting as feature extractor yields the extracted IFV having similar and complex representation increasing the system complexity. System complexity is reduced by removing the irrelevant features using feature selection process to yield only the prominent features for classification. Prominent Feature Vector (PFV) is selected for classification using machine learning based SVM classifier in the proposed PFTL approach depicted in Figure 6.9.

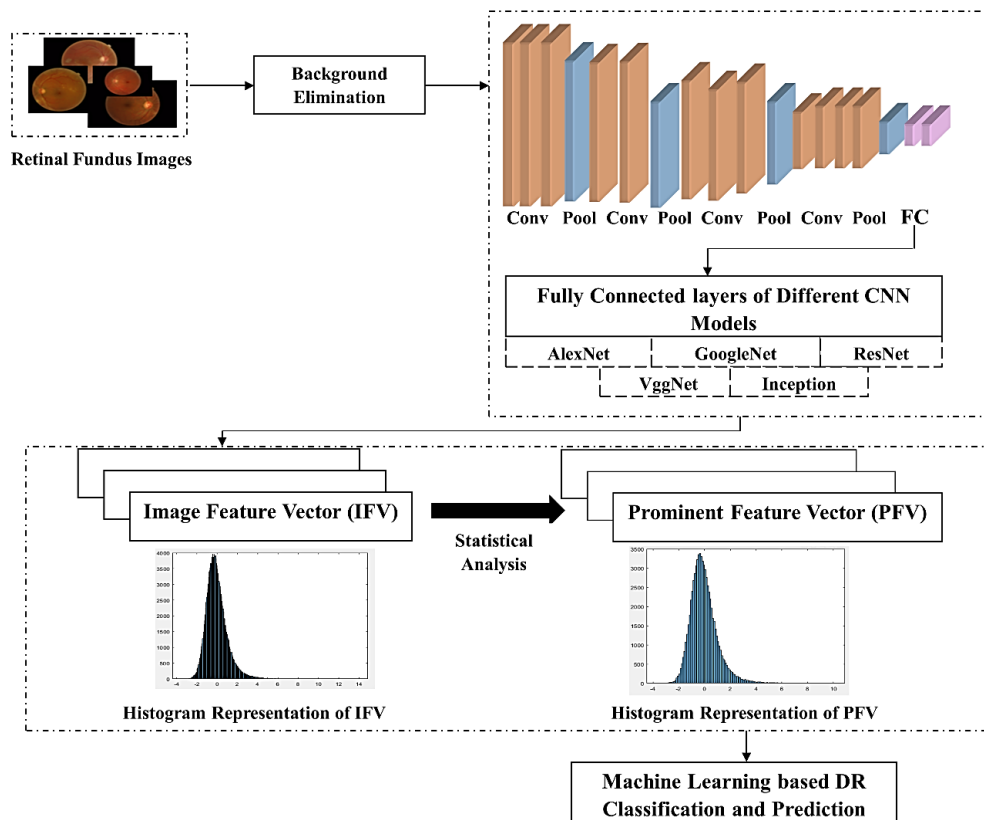


Figure 6.9: Flowchart of proposed PFTL model

Two different transfer learning based DR detection models have been proposed in this work using the CNN network for the extraction of feature vector which are further classified using machine learning approach. The extracted IFV through fully connected layer of different CNN models is directly utilized in IFTL transfer learning approach which is further utilized for training the supervised machine learning SVM classifier. However, the proposed PFTL approach utilizes a feature selection module pipeline in between feature extractor and the classifier to yield better performance outcome.

Statistical t -test and ANOVA tools are utilized in this work for reducing the dimensional complexity reduction thereby increasing the accuracy. Only the most prominent features are selected from the complete feature vector by performing the significant value (p -value) analysis. The significance p -value for a particular feature less than 0.05 indicating its prominence to be selected for classification. The features showing p -value $>$ 0.05 are discarded indicating their moderate or weak significance for the classification process [48, 208, 230].

It is seen from the histogram representation given in Figure 6.9 that PFV lies in the similar range as that of IFV even after discarding the irrelevant features thereby providing better classification outcomes. The highly peaked features in IFV are the outliers which are therefore removed employing statistical feature selection approach. Statistical feature reduction methods ensure the feature vector reduction from somewhat identical/ similar elements and transfers the most significant feature vectors to the classification stage.

This optimal feature selection step employing statistical approach is useful in shifting the feature space with higher dimensionality to the lower dimensionality comprising only the most PFV. The interrelated features are removed using this statistical feature selection process yielding PFV containing relevant features only.

These selected features are further provided for supervised SVM classification improving the effectiveness of severity classification in terms of various performance parameters. Dimensionality reduction introduced using optimal feature selection step improves the performance of network for its storage and computational time. The results of IFTL and PFTL approaches implemented in this work are provided in the following sub-section along with their comparative analysis with the state of art techniques.

The later part of this research is focused on model testing and generalization to obtain improved accuracy, thus we proposed a novel methodology on the basis of deep learning for improved feasibility and robustness of CNN based approach in the real-time DR classification scenario. To address DR severity grading and the challenges of previous methods, this research proposes an effective framework contributing a Quadrant Ensembled Inception V-3 (QEIV-3) CNN model for classification of NPDR severity. This quadrant ensembled approach makes the proposed system more suited for small lesions present in retinal fundus images that are not visible using the full retinal image for computer-aided diagnosis. The methodology for the proposed CNN-based approaches is provided in detail in the next section.

6.3.2 Quadrant Ensembled Inception V-3 Framework

The proposed CNN architecture is inspired from the transfer learning approach that allows the knowledge transfer from one domain to the other without the need for much extensive feature training [186]. An input size of 299×299 is expected by the model input layer. Directly using the fundus image as a whole and resizing it to such a small dimension may lead to misidentification of some small microaneurysms and exudates that were previously visible in the original sized fundus images. Therefore, to mitigate this limitation, the original fundus image is initially resized to 600×600 pixels and is further cropped into four quadrants of size 300×300 , preserving the lesion information. The process of division of pre-processed fundus image into four different quadrants is illustrated in Figure 6.10.

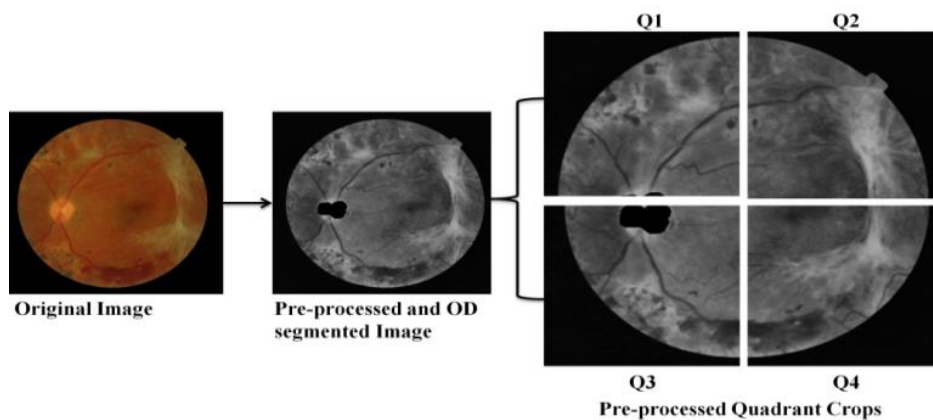


Figure 6.10: Fundus image cropping strategy

The retinal fundus image crops of four different quadrants are used as the input to four different Inception V-3 models. The four quadrant crops of fundus segments are provided to four different Inception-V3 models and their output at the fully connected layers are further concatenated and provided to a single softmax classification output layer. This adjustment in the experimental setup provides better output capacity increasing the number of free parameters.

The complete CNN model structure utilized in this work is provided in Figure 6.11. However, this should be noted that the 299×299 sized pre-processed and data augmented fundus quadrant crops are provided as the input to the initial network layer.

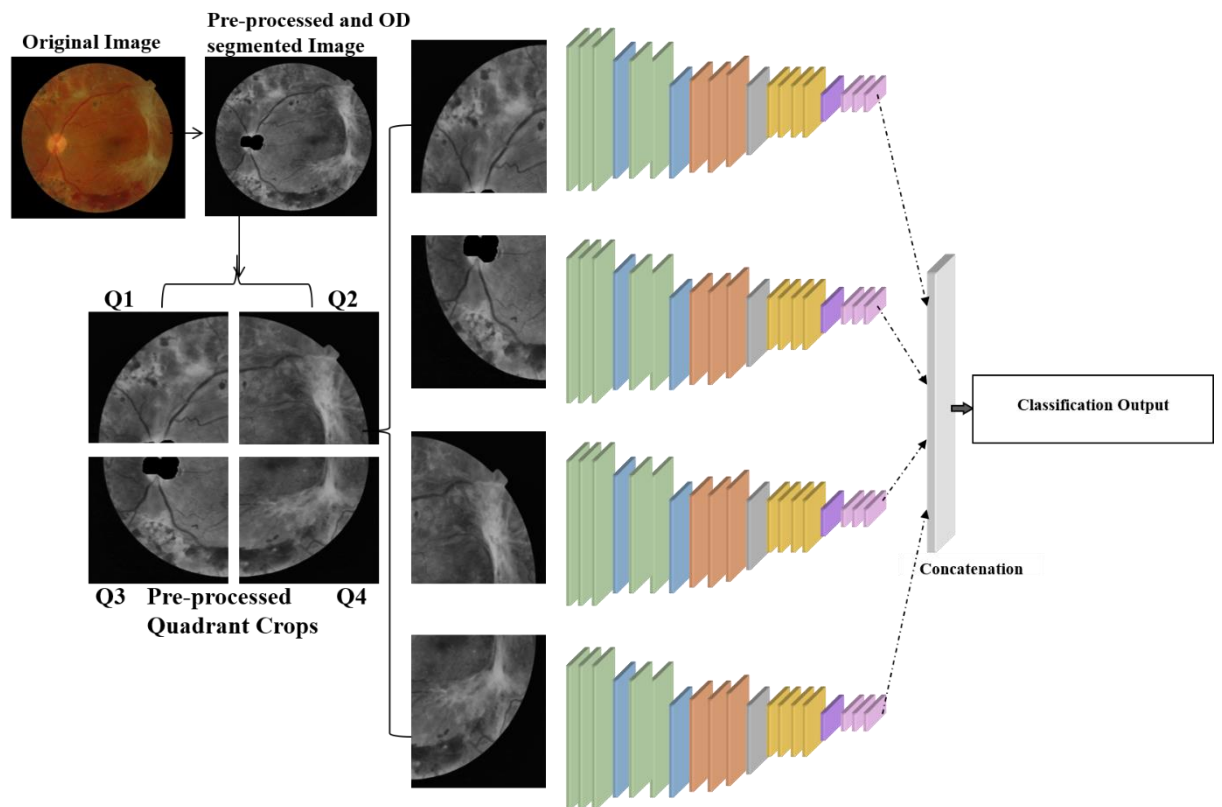


Figure 6.11: Structure of proposed Quadrant Ensembled Inception V-3 CNN model

Data augmentation phase is introduced in this proposed model for increasing the limited number of training samples, in order to improve the performance of network by utilizing an augmented dataset. Thus, the data shortage problem for neural network is overcome by dividing each fundus into four quadrant crops and using the augmentation process. Also, the sampling data is increased by utilizing the data augmentation strategy for more delicate learning of features from fundus images. As depicted from Figure 6.11, the retinal fundus image is subjected to quadrant cropping

after the stage of image pre-processing and OD segmentation steps. These quadrant crops are further provided to four Inception V-3 models for DR severity grading. Inception V-3 CNN architecture as revealed in the prior sections provides superior performance with lowest error rate as compared to the other contemporary CNN models. The model capacity is improved by identification of small lesion features at different fundus quadrants using QEIV-3 model. The methodology of the proposed model is partitioned into different sequential steps that are elaborated in Figure 6.12.

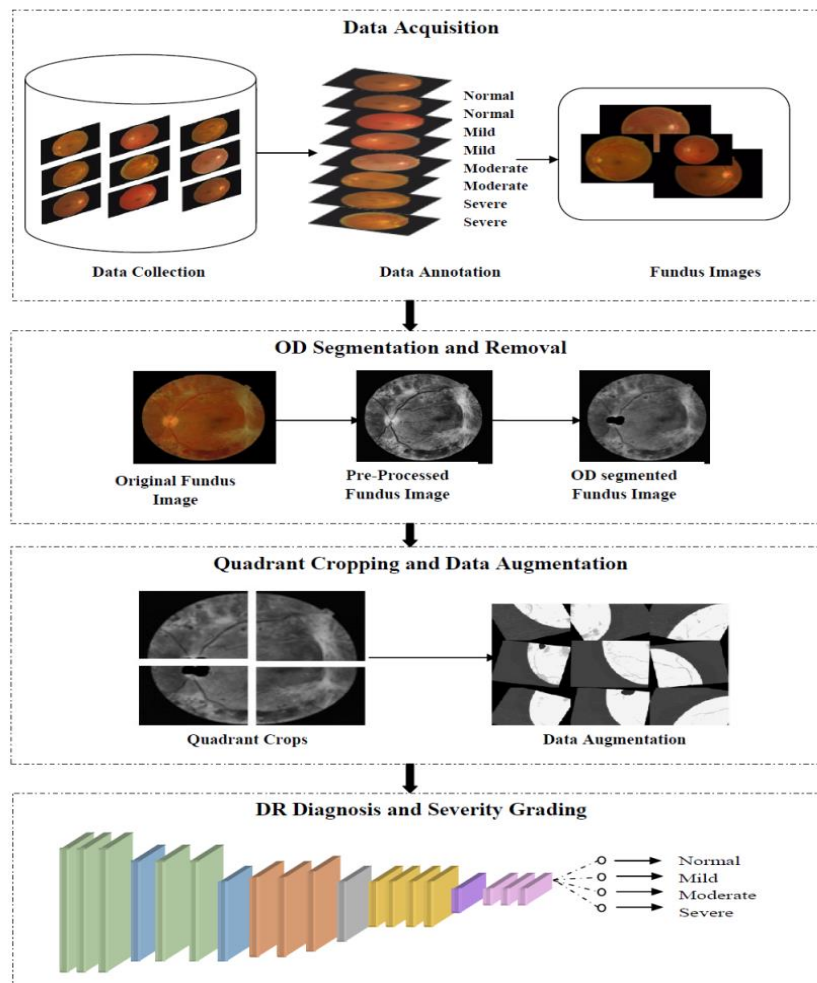


Figure 6.12: Proposed QEIV-3 framework for DR severity grading

The methodology adopted in this work follows the sequential framework involving data acquisition, pre-processing steps including OD segmentation and removal, quadrant cropping and data augmentation followed by DR diagnosis and severity grading. All these sequential steps are elaborated in detail in the previous chapters, however, a brief description is provided for better linkage and understanding.

Data Acquisition: The different fundus image datasets such as DRIVE [40], STARE [41], DIARETDB0 [42] and MESSIDOR [43] that are particularly designated for different DR related diagnosis tasks are employed in this work for the analysis of various abnormalities of DR affected eyes. All of these fundus image datasets varies in the availability of images, image size, field of view and DR related annotations. The MESSIDOR [43] dataset contains DR severity grading with proper annotations in integer terms indicating the degree of severity levels. Four degrees of severities ranging from 0 to 3 is indicated against every individual fundus image where, severity level 0 indicates no DR symptoms, severity levels 1, 2 and 3 are designated to mild, moderate and severe DR grades respectively as discussed in Chapter 5.

Optical Disc segmentation: Two steps are involved in OD segmentation stage, a pre-processing step (denoising and contrast enhancement) followed by boundary localization which are discussed in Chapter 3.

Fundus Image Pre-processing: Pre-processing step is used before providing the acquired fundus images to the network. This step is essential to achieve optimal classification outcomes for DR fundus image classification as it is beneficial in differentiating between the actual lesion and non-lesion features in a fundus image. Size and color normalization, fundus image denoising, CLAHE and OD localization steps are employed in this work which are elaborated in Chapter 3 [195, 208]. Black background border is removed from all the fundus images and image resizing is employed to resize these fundus images to 600×600 pixels dimension. Fundus images are captured using different cameras having different color temperatures and varying illumination, thus, color normalization is also an important step in pre-processing.

Another important step to suppress the isolated noise is image denoising. For this median filter [48] is used, which can better distinguish between the isolated noise and legitimate image features representing some kind of discontinuities [209].

OD Boundary Localization: Optical disc localization is another important step after image denoising as OD is an important anatomical feature that is needed to be extracted for effectual DR pathology diagnosis. OD boundaries are localized using morphological closing operation that determines the OD portion as the largest circular region in the intensity plane. This OD portion is subtracted from the pre-processed

fundus image to obtain segmented fundus image after OD removal as discussed in Chapter 3 [195, 208].

Data Augmentation: A successful neural network demands sufficient amount of training data to design a CNN model that fits to the target application. However, for medical domain, there is only a limited amount of annotated data and the collection of more annotations is expensive and laborious task indulging the experienced ophthalmologists. Another limitation lies in the practical implementation is class imbalance problem to differentiate between the images of different diseased classes. Data augmentation is used to mitigate such constraints of neural networks while improving the network localization ability. The steps involved in data augmentation involves: flipping at both horizontal and vertical axis, random rotation from 90 to 180 degrees and random zooming in the range of [0.85, 1.15] [235]. This process results as increment in number of training samples and also tackles the issue of imbalance by making the model resistant towards variation attenuation, inadequate illumination and different orientations [235-237]. The algorithm of the proposed QEIV-3 model is:

Algorithm: Proposed QEIV-3 Model

Input: Retinal Fundus Images.

Output: Diabetic Retinopathy grades distinguishing the fundus images.

START

Step 1: Read the images from the image datastore and resize all the images to size 600×600 pixels.

Step 2: Annotate the resized images into different DR grades; normal, mild, moderate and severe.

Step 3: Apply pre-processing and OD segmentation steps to obtain OD segmented image.

Step 3.1: Image pre-processing

- Apply color normalization by modelling the fundus image ($I(x,y)$) having $R_{x,y}$, $G_{x,y}$, $B_{x,y}$ pixel values in each of the corresponding channel.
- Apply median filtering on $I(i,j)$ to distinguish isolated noise from legitimate image features like some kind of discontinuities, edges or lines.

- Apply CLAHE on the denoised image to obtain final pre-processed output image ($I_{pre-processed}$).

Step 3.2: OD segmentation

- Convert the pre-processed image ($I_{pre-processed}$) into HSV plane to extract the intensity values.
- Apply Morphological closing operation and contour filling.
- Identify the largest circular region which is indicated as OD portion ($I_{ODportion}$).
- Obtain the OD segmented image ($I_{ODsegmented}$) after OD removal.

$$I_{ODsegmented} = I_{pre-processed} - I_{ODportion}$$

Step 4: Divide all the OD segmented images ($I_{ODsegmented}$) into four quadrants: $I_{Q1/4}$, $I_{Q2/4}$, $I_{Q3/4}$ and $I_{Q4/4}$.

Step 5: Apply data augmentation steps on all the quadrant crops:

- Horizontal and vertical flipping.
- Random rotation at an angle of 90-180 degrees.
- Random zooming in the range of [0.85, 1.15].

Step 6: Feed the data augmented fundus image crops to four different Inception-V3 CNN networks.

Step 7: Apply model concatenation at the final fully connected layers of all the four Inception-V3 networks.

Step 8: Obtain the classification output in the form of four DR classes; normal, mild, moderate, severe.

Step 9: Access the network performance in terms of classification accuracy and cross-entropy loss.

END

This innovation of proposed QEIV-3 model lies in providing superior accuracy by achieving a huge amount of free parameters. The proposed system has also been validated using other mainstream models, suggesting that the results obtained by our proposed system outperform current trending state of art systems. Standard MESSIDOR dataset is used to validate the feasibility and effectiveness in the context of various performance indices.

6.4 RESULTS AND DISCUSSION

This section presents the evaluation of proposed models considering various performance indices. The MESSIDOR dataset comprising of 1200 images in total which are separated into training and testing set using 70% - 30% criteria by partitioning 840 fundus images to be used for training whereas 360 of fundus images for testing purpose with 10-fold cross validation to prevent poor randomization. Primarily, the results for transfer learning based automated DR detection system are presented followed by the outcomes for proposed QEIV-3 approach.

6.4.1 Results of Transfer Learning based Automated DR Detection System

In this approach, statistical analysis methods are utilized to reduce IFV into PFV and the prominent features are provided to SVM classifier to achieve robust severity grade classification performance considering sensitivity, specificity, PPV, F-measure and accuracy. The proposed models are validated using different evaluation parameters presented in Table 6.13.

The tabular representation reveals that phenomenal classification performance is achieved using PFTL approach. PFTL approach reduces the feature disparities of IFTL using the statistical feature selection method to obtain optimal PFV for proficient DR classification. Finest performance for Inception V-3 is observed utilizing PFTL approach and comparably better performance is achieved for Vgg16 CNN model in terms of various performance parameters. The Inception V-3 model achieved maximum of 90.51% accuracy for PFTL approach whereas, remarkable performance is achieved using Vgg16, Vgg19 and AlexNet CNN models.

The sensitivity and specificity parameters observed in Table 6.13 provide the goodness of diagnostic test and its value should also be higher for disease identification. PFTL model provides sensitivity values of 89.89% and 89.32% for Vgg16 and Inception V-3 models respectively. Maximum of 91.75% specificity, 92% PPV and 90.64% F-measure is achieved using Inception V-3 network architecture for PFTL approach, indicating higher probability of DR classification system for correct grading of DR cases without giving false positive result.

Table 6.13: Evaluation parameters for the proposed IFTL and PFTL approaches

Classifier		AlexNet	GoogleNet	ResNet	Vgg16	Vgg19	InceptionV-3
Parameters							
Image Feature Transfer Learning Approach (IFTL)	Sensitivity	60.37%	64.00%	69.90%	61.70%	75.00%	75.49%
	Specificity	61.70%	64.00%	71.13%	60.38%	75.00%	69.44%
	PPV	64.00%	64.00%	72.00%	58.00%	75.00%	77.00%
	F-Measure	62.13%	64.00%	70.93%	59.79%	75.00%	76.24%
	Accuracy	61.01%	64.00%	70.50%	61.10%	75.00%	76.61%
Prominent Feature Transfer Learning Approach (PFTL)	Sensitivity	88.64%	75.00%	81.82%	89.89%	88.12%	89.32%
	Specificity	90.00%	75.00%	76.92%	89.12%	88.89%	91.75%
	PPV	88.64%	75.00%	75.00%	89.00%	89.00%	92.00%
	F-Measure	88.64%	75.00%	78.26%	89.44%	88.56%	90.64%
	Accuracy	89.36%	75.00%	79.17%	89.50%	88.50%	90.51%

6.4.1.1 Comparative Analysis of different transfer learning approaches

The conventional CNN based classification method, IFTL approach, and optimized PFTL approach are graphically compared in terms of their accuracy values in Figure 6.13.

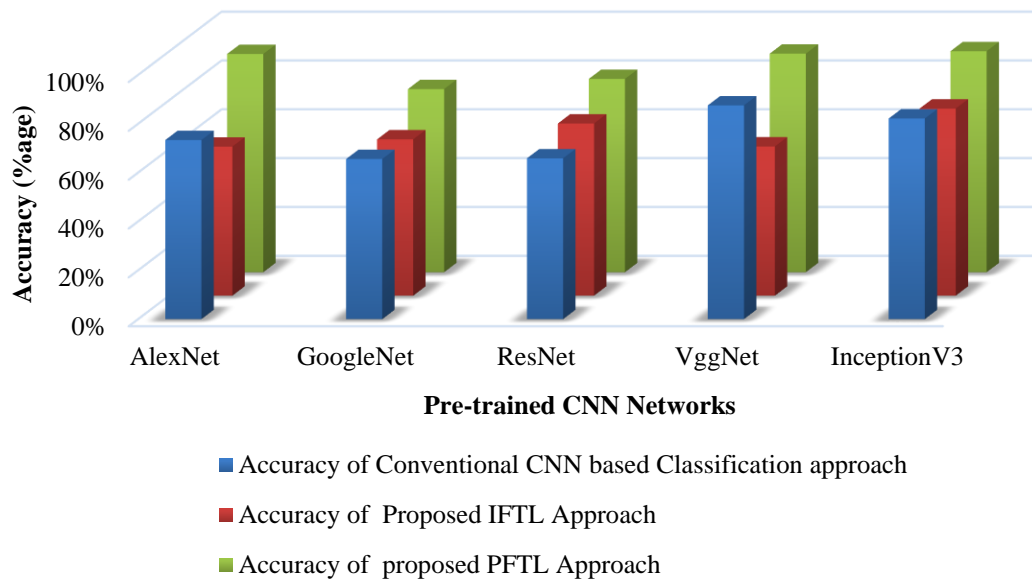


Figure 6.13: Comparative analysis of accuracies for Conventional, IFTL and PFTL approaches

Accuracy analysis provides the proportion of accurately predicted DR cases out of the entire population. Figure 6.13 reveals that the highest accuracy is obtained for optimal DR classification PFTL approach using statistically selected feature set. Maximum of 90.51% accuracy is observed for Inception V-3 pre-trained CNN model applying PFTL approach that is higher to both the other compared approaches. On the contrary, conventional CNN model yields 87.50% accuracy while 76.61% accuracy is observed for IFTL approach. The comparison points towards trade-off is involved with the computational time using Inception V-3 CNN model equipped with PFTL approach.

The VggNet and AlexNet CNN models provide better performance for DR classification problem, but large computational requirements (due to large convolutional layer width) of these architectures makes the model deployment inefficient in terms of memory and time.

On the contrary, the redundant CNN activations with a sparse dense construction of Inception module reduces the computation requirements of CNN model. Also, the Inception module reduces the total number of network parameters achieving better performance at faster rate. The fully connected layer is replaced with global average pooling at the end of network after the last convolutional layer to provide better performance while reducing the computational requirements. The robustness of our technique is validated after comparing the proposed PFTL approach with the other automated DR screening methods.

6.4.1.2 Comparative Analysis with existing state-of-the-art techniques

The DR classification techniques have come into existence with the technological advancement surpassing the machine learning techniques by developing new deep learning paradigms. Table 6.14 provides a comparative examination of proposed PFTL approach with other DR classification methods found in the literature.

Table 6.14: Comparative analysis of proposed PFTL with existing CNN models

Technique	Accuracy	Percentage Accuracy Improvement
Antal <i>et al.</i> [2012] [135]	82.01%	10.36%
Perdomo, <i>et al.</i> [2016] [238]	77.00%	17.54%
Vo, <i>et al.</i> [2016] [239]	87.00%	4.03%
Johari, <i>et al.</i> [2018] [240]	88.30%	2.50%
Lam, <i>et al.</i> [2018] [161]	74.50%	21.49%
Sarki, <i>et al.</i> [2019] [241]	85.87%	5.40%
Proposed PFTL	90.51%	Selected

Comparative analysis of the proposed PFTL model with other state of art approaches over a generalized MESSIDOR dataset providing the maximum percentage improvement of 21.49% over Lam, *et al.* (2018) [161] and 2.50% of minimum accuracy improvement is observed over the method proposed by Johari, *et al.* (2018) [240].

The other existing methods provides accuracy improvement of 10.36%, with Antal, *et al.* (2012) [135]; 17.54%, Perdomo, *et al.* (2016) [238]; 4.03%, Vo, *et al.* (2016) [239] and 5.40%, Sarki, *et al.* (2019) [241] respectively. This work uses the advantage of transfer learning, prominent features selection and machine learning approach for DR severity grade classification.

From the illustrations, it is found that the fundamental requirement for transfer learning is the choice of pre-trained models that can perform the source task suitably. Thus, QEIV-3 transfer learning strategy is employed for the instigation of DR classification to achieve high network performance. Further in this section, the results evaluated for proposed QEIV-3 model are discussed to get an oversight of its performance for DR severity grading.

6.4.2 Results of the proposed QEIV-3 model

The proposed QEIV-3 model is validated by evaluating the performance for time elapsed, accuracy and cross-entropy loss while maintaining constant 0.0001 of base learning rate, epoch size and number of iterations. The outcomes obtained are analyzed varying the epoch size from 1 to 20 while increasing the number of iterations from 1 to 200. Base learning rate of 0.0001 is considered while doing the experiments considering the batch size of 15 [234]. The proposed model involves data cropping and data augmentation for evaluation considering two different cases.

Case 1: QEIV-3 CNN network evaluation model without OD Localization and Contrast enhancement

Case 2: QEIV-3 CNN network evaluation model with OD Localization and Contrast enhancement

Case 1 considers original fundus images after data augmentation and data cropping are provided directly to QEIV-3 model and its performance is evaluated in terms of various parameters. However, case 2 considers original retinal fundus image after utilizing contrast enhancement followed by optical disc localization. OD segmented fundus images after contrast enhancement are subjected to data cropping and augmentation before feeding them to the network.

i. Experimental Evaluation of Case 1

QEIV-3 CNN network is utilized in this case and the network performance is assessed by measuring time elapsed, accuracy and cross-entropy loss.

Table 6.15 provides the performance evaluation of the proposed quadrant ensembled Inception V-3 model. The statistics depicted in Table 6.15 presents performance indices of CNN model involving image cropping and data augmentation stages while excluding pre-processing and OD localization steps. The proposed QEIV-3 model provides the accuracy of 86.67% for 20th epoch at 200th iteration. Number of fundus image samples determines the epoch size and iteration count. The performance outcome saturates for evaluation beyond the epoch size 20. Cross-entropy of 0.374 is observed at 20th epoch taking the total computation time of 48 minutes 41 seconds. The network accuracy improves from 50% at 1st epoch to 86.67% at the 20th epoch which is the maximum accuracy achieved for this particular CNN model.

Table 6.15: Results of proposed QEIV-3 model without OD localization and contrast enhancement

Epoch	Iterations	Accuracy	Cross-entropy Loss	Time Elapsed
1	1	50.00%	0.755	00:00:42
2	20	61.72%	0.658	00:02:17
3	30	55.47%	0.665	00:04:52
4	40	61.72%	0.660	00:06:34
5	50	53.91%	0.708	00:08:12
6	60	66.41%	0.618	00:10:40
7	70	60.94%	0.647	00:13:57
8	80	67.97%	0.604	00:15:39
9	90	62.50%	0.832	00:18:06
10	100	60.94%	0.815	00:20:35
11	110	71.09%	0.556	00:23:06
12	120	53.33%	0.695	00:25:43
13	130	86.67%	0.287	00:27:32
14	140	66.67%	0.565	00:29:16
15	150	60.00%	0.550	00:31:46
16	160	80.00%	0.481	00:35:06
17	170	73.33%	0.447	00:38:32
18	180	80.00%	0.300	00:41:57
19	190	86.67%	0.441	00:45:15
20	200	86.67%	0.374	00:48:41

This quadrant based approach yields better performance, however, the system efficiency and reliability is improved considering image pre-processing pipeline involving contrast limited adaptive histogram equalization and optical disc segmentation modules for the second case.

ii. Experimental Evaluation of Case 2

The processed fundus image input is provided to the proposed CNN architecture after applying image pre-processing and OD localization steps. Table 6.16 depicts the evaluation outcomes to check the effect of on CNN network performance of applying Image Pre-processing (CLAHE and OD Removal), Image cropping and Data Augmentation.

Table 6.16: Results proposed QEIV-3 model with OD localization and contrast enhancement

Epoch	Iterations	Accuracy	Cross-entropy Loss	Time Elapsed
1	1	53.33%	0.695	00:00:52
2	20	60.00%	0.694	00:03:29
3	30	61.11%	0.652	00:05:18
4	40	63.89%	0.632	00:07:09
5	50	73.33%	0.685	00:09:32
6	60	66.67%	0.619	00:10:42
7	70	80.00%	0.545	00:12:27
8	80	86.67%	0.522	00:13:37
9	90	100.00%	0.462	00:14:49
10	100	66.67%	0.691	00:15:59
11	110	75.00%	0.559	00:18:18
12	120	72.22%	0.569	00:20:41
13	130	80.00%	0.46	00:23:09
14	140	69.44%	0.573	00:26:09
15	150	73.33%	0.518	00:29:44
16	160	80.00%	0.454	00:32:09
17	170	93.33%	0.355	00:34:32
18	180	86.67%	0.335	00:37:28
19	190	93.33%	0.283	00:40:04
20	200	93.33%	0.291	00:43:57

Inception V-3 model implementation statistics after applying Image Pre-processing, Image cropping and Data Augmentation provides the much greater accuracy outcomes of 93.33% than that obtained for case 1 at 20th epoch and 200th.

A much reduced cross-entropy value of 0.291 is obtained for the proposed Inception V-3 derivative model taking 43 minutes 41 seconds training time. 53.33% network accuracy at 1st epoch is improved to 93.33% at the 20th epoch considering 200 iterations. Cross-entropy loss also reduces from 0.695 to 0.291 at every epoch size. From these experimental outcomes obtained for both the cases, it is revealed that the strategy used in the proposed Quadrant Ensembled Inception V-3 model provides improved accuracy outcomes and reduced cross-entropy loss as compared to the original Inception V-3 model without employing image pre-processing and OD removal.

6.4.2.1 Comparison of Inception V-3 and proposed QEIV-3 model

Inception V-3 model and proposed Quadrant Ensembled Inception V-3 (QEIV-3) models (Case 1 and Case 2) performances are compared in terms of different performance parameters in Figure 6.14.

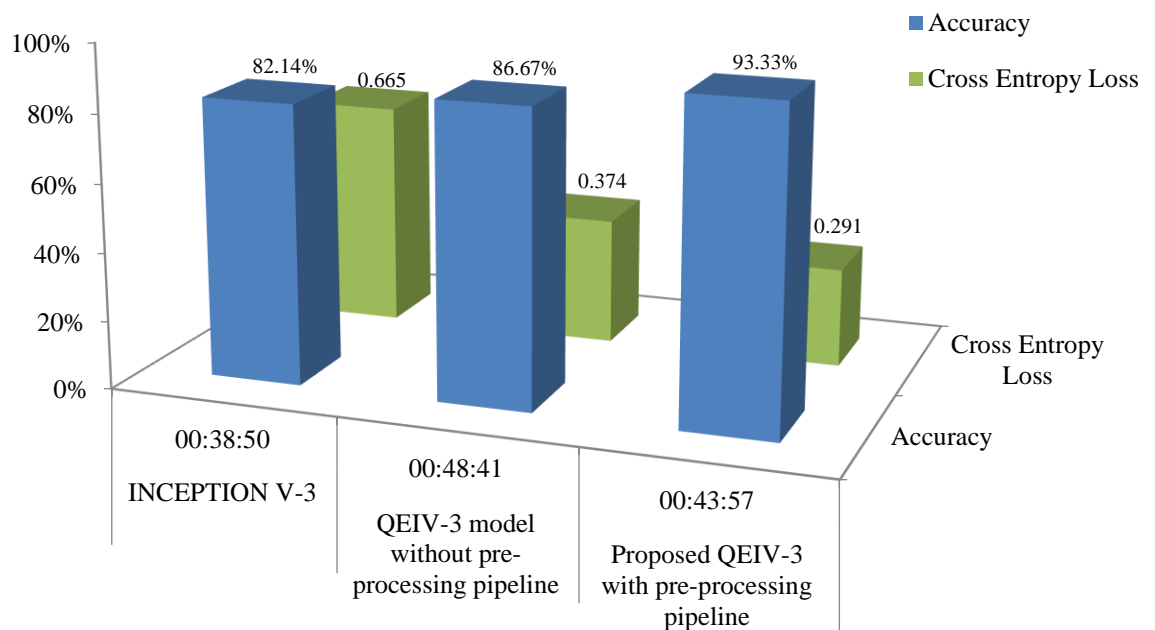


Figure 6.14: Performance comparison of Inception V-3 and proposed QEIV-3 models

The graphical comparison done in Figure 6.14 reveals that our proposed model provides remarkable improvement comparative to the basic Inception V-3 model.

An improved accuracy is observed ranging from 82.14% to 93.33% with significant cross-entropy drop from 0.665 to 0.291.

From the above comparison, it is observed that proposed method has made a significant accuracy improvement of 6.66% as compared to the QEIV-3 derivative without pre-processing pipeline and 11.19% comparative to the classical Inception V-3 approach. The time is a trade off in this case and time taken for Inception V-3 model is 38 minutes 50 seconds. However, QEIV-3 models take 48 minutes 42 seconds and 43 minutes 57 seconds for both case 1 and case 2, respectively. After comparative analysis of Inception V-3, QEIV-3 without and with pre-processing pipeline, the different pre-trained CNN models are compared.

6.4.2.2 Comparison of different Pre-trained models for MESSIDOR dataset

Mainstream AlexNet, ResNet and VggNet models are also evaluated using the same set of processed input images and the results are compared with the classical Inception V-3 as well as proposed QEIV-3 models. Figure 6.15 illustrates the comparison of all models with 20 epoch size, 200 iterations, batch size of 15 and considering base learning rate of 0.0001 as constant.

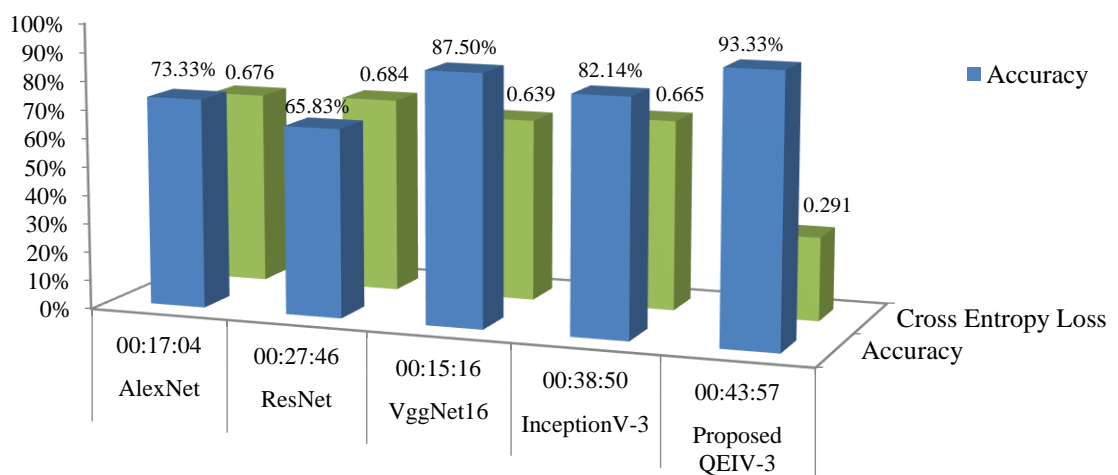


Figure 6.15: Comparison of different Pre-trained models for MESSIDOR dataset

AlexNet model comprising of less layers take the least computational time of 17 minutes 4 seconds while achieving the network accuracy of 73.33% that is

comparatively less when compared to other networks. The best accuracy outcomes are yielded by the proposed Inception V-3 derivative providing accuracy of 93.33% with cross-entropy loss of 0.291. Inception model and its derivatives provide better performance in terms of both the performance parameters while maintaining a tradeoff with the computational time.

6.4.2.3 Comparison of proposed QEIV-3 model with other automated DR screening methods

The DR related research work is primarily focused on utilizing the machine learning based methods and not much progress is encountered in convolutional neural network based DR classification methods. However, despite of this challenge, Table 6.17, provides a comparative examination of existing DR classification methods with proposed QEIV-3 model in terms of its accuracy value.

Table 6.17: Comparative analysis of proposed QEIV-3 model with existing CNN models

Techniques	Accuracy	Percentage Improvement
Vo and Verma (2016) [239]	89.7%	4.01%
Wang, <i>et al.</i> (2017) [156]	91.1%	2.41%
Li, <i>et al.</i> (2017) [160]	92.0%	1.41%
Johari, <i>et al.</i> (2018) [240]	88.3%	5.66%
Li, <i>et al.</i> (2019) [242]	92.6%	0.75%
Saranya & Prabakaran (2020) [179]	90.9%	2.64%
Proposed QEIV-3 Model	93.3%	Selected

The tabular comparison provides the accuracy outcomes for the generalized MESSIDOR dataset obtained from proposed approach without feature specific detection. Our proposed approach presents the accuracy improvement of 5.66% with other state of art techniques. The comparison of our research work is drawn with the recent deep learning based approach adopted by Saranya & Prabakaran [179] discussed in the literature review, utilizes MESSIDOR and IDRiD dataset for validation purpose. It is observed from the comparison that the proposed QEIV-3 model outperforms the existing multi-stage DR classification and grading without the requirement feature specific detection.

6.5 CONCLUSION

The demand for automated DR diagnosis systems has increased due to the large diabetes population and the prevalence of cases of retinopathy among them. The literature suggests that much achievement has been achieved in many DR-related domains such as vessel segmentation, lesion detection, etc. However, the results obtained differ from real-world applications for clinical practices; systems that provide DR severity grading are more reliable for practical applications. To improve the feasibility and robustness of CNN based approach for real-time DR classification scenario, four CNN based DLDR models were built leading to a proposed ensembled CNN architecture to address the DR classification into healthy and diseased fundus. The trained EDLDR model delivers 88.63% of accuracy rate with 0.637 of cross-entropy loss for providing immediate diagnosis for diseased or non-diseased fundus image utilizing one single image per eye. The proposed model offers improvement in accuracy of 1.13% with reduction in cross-entropy loss of 0.02% in comparison with the VggNet16 pre-trained CNN model. To address, DR severity grading, the work initially presents a PFTL approach employing CNN model architecture as a feature extractor followed by a separate feature selection module and a supervised SVM classification method achieving a maximum accuracy of 90.51% using the Inception V-3 model. The obtained experimentation reveals the capability of proposed transfer learning based system for faster and efficient DR diagnosis providing maximum improvement of 21.49% when compared with the state of the art techniques using the same dataset.

Further, to improve the classification accuracy and cross-entropy loss and provide a feasible DR severity grading solution, in this work, we proposed an automated DR grading system using deep neural network-based architecture. The proposed Quadrant Ensembled Inception V-3 architecture incorporates a pre-processing pipeline with optical disc removal stage to improve grading efficiency. The QEIV-3 model achieves 93.33% of accuracy with reduction of 0.291% in cross-entropy loss. Compared with other state of art techniques using the same dataset, there was an improvement of 5.66%. The comparison with state of art techniques justifies the diagnostic capability of our proposed approach validating its generalization capabilities and robustness.

CHAPTER 7

CONCLUSION AND FUTURE SCOPE

CHAPTER 7

CONCLUSION AND FUTURE SCOPE

The demand for automated DR diagnosis system have fostered due to large diabetic population and pervasiveness of retinopathy cases among them. Early stage diagnosis and intervention is critical in reducing the risk of acute retinal complications which may lead to complete blindness if left untreated for a long time. This thesis primarily focuses on the effectual DR lesion discrimination and provide a feasible DR severity grading framework. Different methods have been developed for providing a mass screening solution to the ophthalmologists by indicating the occurrence of a particular DR lesion, tracking the progression of the disease and reducing the risk of inevitable vision loss. The complete research work has been concluded by presenting the conclusion, contribution and future scope of this entire research.

7.1 CONCLUSION AND CONTRIBUTION

This research work encompasses the development of an efficient, reliable and computationally competent system for severity grading of DR vision abnormalities. The techniques and models developed are able to accurately distinguish the retinal physiological landmarks, detect the pathological symptoms and effectually categorize the DR severity grades.

Extensive literature survey reveals the importance of retinal landmark segmentation for effectual lesion detection. Physiological structure segmentation is essential to reduce the chances of false lesion detection having similar features as these anatomies. The alternatives present in the literature have certain limitations of poor contrast and uneven illumination in image acquisition. Optical disc localization methods are limited to identify exact boundaries as OD has blurred edges and blood vasculature segmentation is challenging due to the disparity in vessel width. These shortcoming in the existing work are addressed by developing an efficient OD localization and blood vessel segmentation approaches. A Circular Hough Transform based OD localization technique and Hybrid Blood Vessel Extraction Approach using Morphological

Reconstruction (HBV-MR) are developed for the automated OD localization and blood vessel segmentation in the first part of this research work. Improved diagnostic performance is achieved by involving the combination of image pre-processing and post processing steps to remove retinal fundus image discrepancies. An extensive feature set is derived and optimal feature selection is done based on descriptive and statistical analysis for pixel-based classification of retinal landmarks. An exhaustive investigation is done employing visual, statistical and performance-based analysis on the benchmark datasets that reveals the robustness of the proposed approaches. The results obtained for these approaches provides remarkable improvement and demonstrates their viability for retinal landmark segmentation.

There is a need to improve the distinction capability of the actual DR lesions from the background noise and retinal physiological structures. Automated lesion detection is tedious as a result of color, shape and intensity resemblance. Thus, after precise segmentation of retinal anatomies, pathology detection is addressed in this work by proposing a hybrid lesion detection technique. A Hybrid Lesion Detection (HLD) technique is proposed for the detection of DR abnormalities present in the retinal fundus images. Two different fundus image discrimination strategies are adopted; a fundus image discrimination approach distinguishing between the non-DR and DR affected fundus images, and DR lesion discrimination approach for differentiating between red and yellow lesions. The comprehensive feature set is derived and statistically analyzed for optimal feature selection. The main contribution lies in significant improvement of candidate classification scheme using multi-layer perceptron networks that provide 5.90% accuracy improvement and least run-time complexity. The quantitative and qualitative investigation of the proposed technique reveals its viability by providing successful discrimination ability between the non-DR and DR affected fundus images. A robust alternative solution is achieved using the proposed approach for advanced DR diagnosis by explicitly locating the abnormality with optimally improved categorization ability of red and yellow lesions.

Subsequent to lesion discrimination, a DR severity grading framework was proposed to track the appearance and progression of the disease. Retinal feature patterns are recognised which enable the monitoring of the appropriate severity levels. Hierarchal Severity Grading (HSG) system is proposed in this work to categorize the

different DR severities based on the rules devised by ophthalmic experts utilizing different classifier combinations. The inclusive feature set is reduced to prominent feature set employing statistical analysis leading to improved classification outcomes, which can aid the ophthalmologists in understanding the likelihood of vision loss. The feature reduction strategy adopted in this framework removes the feature disparities. A remarkable percentage improvement of 32.25% is seen when compared to the existing techniques maintaining a trade-off with the computational time. The performance validation of the proposed system on latest IDRiD (2018) dataset provides improved performance, thus determining its generalization capabilities independent of dataset being used.

Later in this work, a DR grading system is proposed for fundus image categorization on the basis of retinal pathological changes utilizing CNN to provide the mass screening solution. An ensemble deep learning based model have been proposed for two class classification. The Ensembled Deep Learning DR (EDLDR) model provides effective diagnostic proficiency while providing 1.13% accuracy improvement comparative to the VggNet16 pre-trained CNN model. DR severity grading is addressed by proposing two different transfer learning models; namely, Prominent Feature based Transfer Learning (PFTL) model and Quadrant Ensembled Inception V-3 (QEIV-3) model. PFTL model utilizes CNN architecture for feature extraction followed by a separate feature selection module and a supervised SVM classification method yielding the maximum accuracy of 90.51%. Inception V-3 model is utilized in the proposed QEIV-3 approach, integrating a pre-processing and data augmentation pipeline to improve the grading efficiency while replacing feature engineering. The novelty of the proposed models lies in optimal performance by obtaining large number of free parameters for computer aided diagnosis and its robustness is verified through 10-fold cross-validation. The comparative analysis shows the outperformance yielding accuracy improvement of 5.66% with the other state-of-the-art methods, establishing its generalization and viability for DR diagnosis. The proposed method provides superior performance employing data augmentation strategy that provides the flexibility of scale, rotation and field of view invariance.

The comparative validation of our models with the other mainstream models reveal that the results achieved by the proposed system outperforms the current state-of-the-art systems.

7.2 FUTURE SCOPE

Despite of all the attempts to contribute towards accurate DR diagnosis by developing various techniques and systems, the scope still prevails for future investigation. The aspects which can be explored in the future for this research work are presented as follows.

- i.** Extension of the research work on 3D retinal imaging platform to identify the disease progression over time for establishing its generalization competences.
- ii.** Addressing neovascularization and vitreous haemorrhage problems causing proliferative diabetic retinopathy, ultimately leading to retinal detachment.
- iii.** Deployment of deep learning based DR screening approach to provide diagnostic assistance to the ophthalmologists.

LIST OF PUBLICATIONS

LIST OF PUBLICATIONS

JOURNALS

1. Charu Bhardwaj, Shruti Jain, Meenakshi Sood, “Hierarchical Severity Grade Classification of Non-Proliferative Diabetic Retinopathy”, *Journal of Ambient Intelligence and Humanized Computing*, 2020.
<https://doi.org/10.1007/s12652-020-02426-9> (SCI Indexed, IF: 4.594)
2. Charu Bhardwaj, Shruti Jain, Meenakshi Sood, “Diabetic Retinopathy Severity Grading Employing Quadrant Based Inception-V3 Convolution Neural Network Architecture”, *International Journal of Imaging Systems and Technology*, 2020.
<https://doi.org/10.1002/ima.22510> (SCI Indexed, IF: 1.925)
3. Charu Bhardwaj, Shruti Jain, Meenakshi Sood, “Diabetic Retinopathy Lesion Discriminative Diagnostic System for Retinal Fundus Images”, *Advanced Biomedical Engineering*, vol. 9, pp. 71-82, 2020. (ESCI, Scopus Indexed)
4. Charu Bhardwaj, Shruti Jain, Meenakshi Sood, “Retinal Blood Vessel Localization to Expedite PDR Diagnosis”, *Periodicals of Engineering and Natural Sciences*, vol. 8, no. 3, pp.1233-1246, 2020. (Scopus Indexed)
5. Charu Bhardwaj, Shruti Jain, Meenakshi Sood, “Two-Tier Grading System for NPDR Severities of Diabetic Retinopathy in Retinal Fundus Images”, *Recent Patents on Engineering*, 2020.
<https://doi.org/10.2174/1872212114666200109103922> (Scopus Indexed)
6. Charu Bhardwaj, Shruti Jain, Meenakshi Sood, “Automatic Blood Vessel Extraction of Fundus Images Employing Fuzzy Approach”, *Indonesian Journal of Electrical Engineering and Informatics*, vol. 7, no. 4, pp.757-771, 2019.
(Scopus Indexed)
7. Charu Bhardwaj, Shruti Jain, Meenakshi Sood, “Computer Aided Hierarchal Lesion Classification for Diabetic Retinopathy Abnormalities”, *International Journal of Recent Technology and Engineering*, vol. 8, no. 1, pp.2880-2887, 2019.
(Scopus Indexed)

8. Charu Bhardwaj, Shruti Jain, Meenakshi Sood, “Automated Diagnostic Hybrid Lesion Detection System for Diabetic Retinopathy Abnormalities”, *International Journal of Sensors, Wireless Communications and Control*, 2019. <https://doi.org/10.2174/2210327909666191126092411> (Scopus Indexed)
9. Charu Bhardwaj, Shruti Jain, Meenakshi Sood, “Performance analysis of retinal features for diabetic retinopathy characterisation and diagnosis”, *International Journal of Business and Systems Research*, 2019.

In Press (Scopus Indexed)

UNDER REVIEW

1. Charu Bhardwaj, Shruti Jain, Meenakshi Sood, “Transfer Learning based Robust Automatic Detection System for Diabetic Retinopathy Grading”, *Neural Computing and Applications*. (SCI Indexed)

CONFERENCES

1. Charu Bhardwaj, Shruti Jain, Meenakshi Sood, “Diabetic Retinopathy Detection from Eye Fundus Images with Parameter Tuning for Convolutional Neural Networks”, *5th International Conference on Signal Processing, Computing and Control (ISPCC 2k19)*, 2019.
2. Charu Bhardwaj, Shruti Jain, Meenakshi Sood, “Appraisal of Pre-processing Techniques for Automated Detection of Diabetic Retinopathy”, *Fifth International Conference on Parallel, Distributed and Grid Computing (PDGC)*, pp. 734-739, 2018. IEEE.

BOOK CHAPTERS

1. Charu Bhardwaj, Shruti Jain, Meenakshi Sood, “Deep Learning Based Diabetic Retinopathy Prediction of Colored Fundus Images with Parameter Tuning”, *Advances in Computational Intelligence Techniques*, Springer, pp. 53-62, 2020. (Scopus Indexed)
2. Charu Bhardwaj, Shruti Jain, Meenakshi Sood, “Automated Optical Disc Segmentation and Blood Vessel Extraction for Fundus Images using Ophthalmic Image Processing”, *Communications in Computer and Information Science (CCIS) Springer*, vol. 955, pp. 1-13, 2018. (Scopus Indexed)

REFERENCES

REFERENCES

- [1] C. Garhart, and V. Lakshminarayanan, “Anatomy of the Eye,” in *Handbook of Visual Display Technology*, vol.1. Heidelberg: Springer, 2015, pp. 73-83.
- [2] “The Nervous System.” Available: <http://www.zo.utexas.edu/faculty/sjasper/bio301L/nervous.html>. [Accessed: 16-March-2019].
- [3] J. Broder, *Diagnostic Imaging for the Emergency Physician E-Book*. Elsevier Health Sciences, 2011. [Online] Available: books.google.com.
- [4] G. Dougherty, *Medical image processing: techniques and applications*. Springer Science & Business Media, 2011. [Online] Available: springer.com.
- [5] M. Can, “Boosted networks for the diagnosis of cardiovascular diseases,” *Periodicals of Engineering and Natural Sciences*, vol. 1, no. 2, pp. 5-16, 2013.
- [6] M. D. Abràmoff, J. M. Reinhardt, S. R. Russell, J. C. Folk, V. B. Mahajan, M. Niemeijer, and G. Quellec, “Automated early detection of diabetic retinopathy,” *Ophthalmology*, vol. 117, no. 6, pp. 1147-1154, 2010.
- [7] P. De Boever, T. Louwies, E. Provost, L. I. Panis, and T. S. Nawrot, “Fundus photography as a convenient tool to study microvascular responses to cardiovascular disease risk factors in epidemiological studies,” *Journal of Visualized Experiments (JoVE)*, vol. 92, no. e51904, 2014.
- [8] M. Bhende, S. Shetty, M. K. Parthasarathy, and S. Ramya, “Optical coherence tomography: A guide to interpretation of common macular diseases,” *Indian journal of ophthalmology*, vol. 66, no. 1, pp. 20, 2018.
- [9] J. G. Fujimoto, C. Pitris, S. A. Boppart, and M. E. Brezinski, “Optical Coherence Tomography: An Emerging Technology for Biomedical Imaging and Optical Biopsy,” *Neoplasia*, vol. 2, no. 1, pp. 9–25, 2000.
- [10] P. Saedi, P. Salpea, S. Karuranga, I. Petersohn, B. Malanda, E. W. Gregg, and R. Williams, “Mortality attributable to diabetes in 20–79 years old adults, 2019 estimates: Results from the International Diabetes Federation Diabetes Atlas,” *Diabetes research and clinical practice*, pp. 108086, 2020.
- [11] “IDF Diabetes Atlas 9th edition 2019”, *Diabetesatlas.org*, 2020. [Online]. Available: <https://diabetesatlas.org/en/>. [Accessed: 17- Aug- 2018].
- [12] N. Kourgialis, “Diabetic Retinopathy – silently blinding millions of people world-wide,” Available: <http://atlas.iapb.org/vision-trends/diabetic-retinopathy/>. [Accessed: 17-Aug-2018).
- [13] “Visual impairment and blindness, fact Sheet N28,” *World Health Organization report*, Available: <http://www.who.int/mediacentre/factsheets/fs282/en/> [Accessed: 15-Dec-2018).
- [14] S. S. Kar and S. P. Maity, “Automatic Detection of Retinal Lesions for Screening of Diabetic Retinopathy,” *IEEE Transactions on Biomedical Engineering*, vol. 65, no. 3, pp. 608–618, 2018.

- [15] C. Sinthanayothin, J. F. Boyce, H. L. Cook, and T. H. Williamson, "Automated localisation of the optic disc, fovea, and retinal blood vessels from digital colour fundus images," *British Journal of Ophthalmology*, vol. 83, no. 8, pp. 902–910, 1999.
- [16] J. Vaishnavi, S. Ravi, M. A. Devi, and S. Punitha. "Automatic diabetic assessment for diabetic retinopathy using support vector machines," *International Journal of Control Theory Applications*, vol. 9, no. 7, 2016.
- [17] M. M. Habib, R. A. Welikala, A. Hoppe, C. G. Owen, A. R. Rudnicka, and S. A. Barman, "Detection of microaneurysms in retinal images using an ensemble classifier," *Informatics in Medicine Unlocked*, vol. 9, pp. 44–57, 2017.
- [18] V. Handšková, J. Pavlovičová, M. Oravec, and R. Blaško. "Diabetic rethinopathy screening by bright lesions extraction from fundus images," *Journal of Electrical Engineering*, vol. 64, no. 5, 2013.
- [19] J. M. Shivaram, R. Patil, and H. S. Aravind, "Automated detection and quantification of haemorrhages in diabetic retinopathy images using image arithmetic and mathematical morphology methods," *International Journal of Recent Trends in Engineering*, vol. 2, no. 6, pp. 174, 2009.
- [20] S. Sharma, S. Jain, and S. Bhusri, "Two class classification of breast lesions using statistical and transform domain features," *Journal of Global Pharma Technology*, vol. 9, no. 7, pp. 18-24, 2017.
- [21] D. A. Clausi, "An analysis of co-occurrence texture statistics as a function of grey level quantization," *Canadian Journal of remote sensing*, vol. 28, no. 1, pp. 45-62, 2002.
- [22] S. Bhusri, S. Jain, and I. Virmani, "Classification of Breast Lesions using the Difference of Statistical Features," *Research Journal of Pharmaceutical, Biological and Chemical Sciences (RJPBCS)*, vol. 7, no. 4, pp. 1365-1372, 2016.
- [23] S. S. Lachure, J. S. Lachure and S. D. Gupta, "Computer based identification of diabetes retinopathy using texture parameters," *International Journal in IT & Engineering*, vol. 2, no. 12, pp. 1-14, 2014.
- [24] M. Sood, and S. V. Bhooshan, "Design and development of prediction model to detect seizure activity utilizing higher order statistical features of EEG signals," *Research Journal of Pharmaceutical, Biological and Chemical Sciences*, vol. 5, no. 3, pp. 1129-1145, 2014.
- [25] S. Roychowdhury, D. D. Koozekanani, and K. K. Parhi, "DREAM: Diabetic Retinopathy Analysis Using Machine Learning," *IEEE Journal of Biomedical and Health Informatics*, vol. 18, no. 5, pp. 1717-1728, 2014.
- [26] U. R. Acharya, C. M. Lim, E. Y. K. Ng, C. Chee, and T. Tamura, "Computer-based detection of diabetes retinopathy stages using digital fundus images," *Proceedings of the institution of mechanical engineers, part H: journal of engineering in medicine*, vol. 223, no. 5, 2009, pp. 545-553.
- [27] A. Khashman and K. Dimililer, "Neural Networks Arbitration for Optimum DCT Image Compression," in *EUROCON 2007 - The International Conference on Computer as a Tool*, 2007, pp. 151-156.

- [28] A. Khashman, "Application of an emotional neural network to facial recognition," *Neural Computing and Applications*, vol. 18, no. 4, pp. 309-320, 2009.
- [29] A. A. Adekunle, A. Khashman, E. O. Olaniyi, and O. K. Oyedotun, "Diabetic retinopathy diagnosis using neural network arbitration," *Bulletin of the Transilvania University of Brasov. Mathematics, Informatics, Physics. Series III*, vol. 10, no. 1, pp. 179, 2017.
- [30] M. Garcia, C. I. Sanchez, M. I. Lopez, A. Diez, and R. Hornero, "Automatic detection of red lesions in retinal images using a multilayer perceptron neural network," in *30th Annual International Conference of the IEEE Engineering in Medicine and Biology Society*, 2008, pp. 5425-5428.
- [31] I. Qureshi, J. Ma, and Q. Abbas, "Recent Development on Detection Methods for the Diagnosis of Diabetic Retinopathy," *Symmetry*, vol. 11, no. 6, 2019.
- [32] K. Xu, D. Feng, and H. Mi, "Deep Convolutional Neural Network-Based Early Automated Detection of Diabetic Retinopathy Using Fundus Image," *Molecules*, vol. 22, no. 12, 2017.
- [33] S. Mohammadian, A. Karsaz, and Y. M. Roshan, "Comparative Study of Fine-Tuning of Pre-Trained Convolutional Neural Networks for Diabetic Retinopathy Screening," in *24th National and 2nd International Iranian Conference on Biomedical Engineering (ICBME)*, 2017, pp. 1-6.
- [34] Y. LeCun, B. E. Boser, J. S. Denker, D. Henderson, R. E. Howard, W. Hubbard, and L. D. Jackel, "Handwritten digit recognition with a back-propagation network," in *Advances in Neural Information Processing Systems*, 1990, pp. 396-404.
- [35] A. Krizhevsky, I. Sutskever, and G. E. Hinton, "ImageNet Classification with Deep Convolutional Neural Networks," in *Advances in Neural Information Processing Systems*, 2012, pp. 1097-1105.
- [36] C. Szegedy, W. Liu, Y. Jia, P. Sermanet, S. Reed, D. Anguelov, and A. Rabinovich, "Going deeper with convolutions," in *Proceedings of the IEEE conference on computer vision and pattern recognition*, 2015, pp. 1-9.
- [37] K. He, X. Zhang, S. Ren, and J. Sun, "Deep residual learning for image recognition," in *Proceedings of the IEEE conference on computer vision and pattern recognition*, 2016, pp. 770-778.
- [38] K. Simonyan and A. Zisserman, "Very Deep Convolutional Networks for Large-Scale Image Recognition," *ArXiv14091556 Cs*, 2015.
- [39] C. Szegedy, V. Vanhoucke, S. Ioffe, J. Shlens, and Z. Wojna, "Rethinking the Inception Architecture for Computer Vision," in *Proceedings of the IEEE conference on computer vision and pattern recognition*, pp. 2818-2826, 2016.
- [40] J. Staal, M. D. Abramoff, M. Niemeijer, M. A. Viergever, and B. van Ginneken, "Ridge-based vessel segmentation in color images of the retina," *IEEE Transactions on Medical Imaging*, vol. 23, no. 4, pp. 501-509, 2004.

- [41] A. D. Hoover, V. Kouznetsova, and M. Goldbaum, "Locating blood vessels in retinal images by piecewise threshold probing of a matched filter response," *IEEE Transactions on Medical Imaging*, vol. 19, no. 3, pp. 203-210, 2000.
- [42] T. Kauppi, V. Kalesnykiene, J. K. Kamarainen, L. Lensu, I. Sorri, A. Raninen, J. Pietilä, "The diaretdb1 diabetic retinopathy database and evaluation protocol," *In British Machine Vision Conference (BMVC)*, vol. 1, 2007, pp. 1-10.
- [43] E. Decencière, X. Zhang, G. Cazuguel, B. Lay, B. Cochener, C. Trone, and B. Charton, "Feedback on a publicly distributed image database: the Messidor database," *Image Analysis & Stereology*, vol. 33, no. 3, pp. 231-234, 2014.
- [44] P. Porwal, S. Pachade, R. Kamble, M. Kokare, G. Deshmukh, V. Sahasrabudde, and F. Meriaudeau, "Indian diabetic retinopathy image dataset (IDRiD): a database for diabetic retinopathy screening research," *Data*, vol. 3, no. 3, pp. 25, 2018.
- [45] Q. Li and R. M. Nishikawa, *Computer-Aided Detection and Diagnosis in Medical Imaging*, Boca Raton: CRC Press, 2015. [Online] Available: Taylor & Francis.
- [46] B. Halalli, and A. Makandar, "Computer aided diagnosis-medical image analysis techniques," in *Breast Imaging*, vol. 85, IntechOpen, 2018.
- [47] M. Sood, "Performance analysis of classifiers for seizure diagnosis for single channel EEG data," *Biomedical and Pharmacology Journal*, vol. 10, no. 2, pp. 795-803, 2017.
- [48] C. Bhardwaj, S. Jain, and M. Sood, "Automatic Blood Vessel Extraction of Fundus Images Employing Fuzzy Approach," *Indonesian Journal of Electrical Engineering and Informatics (IJEI)*, vol. 7, no. 4, Nov. 2019.
- [49] K. G. M. M. Alberti, and P. Z. Zimmet, "Definition, diagnosis and classification of diabetes mellitus and its complications. Part 1: diagnosis and classification of diabetes mellitus," *Provisional report of a WHO consultation. Diabetic medicine*, vol. 15, no. 7, pp. 539-553, 1998.
- [50] C. Sinthanayothin, J. F. Boyce, H. L. Cook, and T. H. Williamson, "Automated localization of the optic disk, fovea, and retinal blood vessels from digital colour fundus images," *British Journal of Ophthalmology*, vol. 83, no. 8, pp. 902-910, 1999.
- [51] A. Dehghani, H. A. Moghaddam, and M. S. Moin, "Optic disc localization in retinal images using histogram matching," *EURASIP Journal on Image and Video Processing*, no. 1, pp. 19, 2012.
- [52] P. Manjiri, M. Ramesh, R. Yogesh, S. Manoj, D. Neha, "Automated localization of optic disk, detection of microaneurysms and extraction of blood vessels to bypass angiography," *In Proceedings of the 3rd International Conference on Frontiers of Intelligent Computing: Theory and Applications (FICTA)*, 2014, pp. 579-587.
- [53] N. Muangnak, P. Aimmanee, S. Makhanov, and B. Uyyanonvara, "Vessel transform for automatic optic disk detection in retinal images," *IET Image Processing*, vol. 9, no. 9, pp. 743-750, Sep. 2015.

- [54] D. D. Rathod, R. R. Manza, Y. M. Rajput, M. B. Patwari, M. Saswade, and N. Deshpande, "Localization of Optic Disc using HRF database," *In IEEE's International Conferences for Convergence Of Technology, Pune, India*, 2015.
- [55] O. Phyo, and A. Khaing, "Automatic detection of optic disc and blood vessels from retinal images using image processing techniques," *IJRET: International Journal of Research in Engineering and Technology*, vol. 3, no. 3, pp. 300-307, 2014.
- [56] R. S. Prakash, R. Aditya, Y. Sameer, S. Parameswari, and G. S. Kumar, "Retinal blood vessel extraction and optical disc removal," *Int. J. Res. Eng. Technol.*, vol. 4, no. 04, pp. 80-83, 2015.
- [57] N. Muangnak, P. Aimmanee, and S. Makhanov, "Automatic optic disk detection in retinal images using hybrid vessel phase portrait analysis," *Medical & biological engineering & computing*, vol. 56, no. 4, pp. 583-598, 2018.
- [58] A. Salazar-Gonzalez, D. Kaba, Y. Li, and X. Liu, "Segmentation of the Blood Vessels and Optic Disk in Retinal Images," *IEEE Journal of Biomedical and Health Informatics*, vol. 18, no. 6, pp. 1874-1886, Nov. 2014.
- [59] V. K. Jestin, and R. R. Nair, "Extraction of Retinal Blood Vessels and Optic Disk for Eye Disease Classification," *In Proceedings of Fifth International Conference on Soft Computing for Problem Solving*, 2016, pp. 573-584.
- [60] S. Roychowdhury, D. D. Koozekanani, S. N. Kuchinka, and K. K. Parhi, "Optic Disc Boundary and Vessel Origin Segmentation of Fundus Images," *IEEE J. Biomed. Health Inform.*, vol. 20, no. 6, pp. 1562-1574, Nov. 2016.
- [61] S. Roychowdhury, D. D. Koozekanani, and K. K. Parhi, "Screening fundus images for diabetic retinopathy," in *Conference Record of the Forty Sixth Asilomar Conference on Signals, Systems and Computers (ASILOMAR)*, Nov. 2012, pp. 1641-1645.
- [62] R. Perfetti, E. Ricci, D. Casali, and G. Costantini, "Cellular Neural Networks with Virtual Template Expansion for Retinal Vessel Segmentation," *IEEE Transactions on Circuits and Systems II Express Briefs*, vol. 54, no. 2, pp. 141-145, 2007.
- [63] A. Aquino, M. E. Gegúndez-Arias, and D. Marín, "Detecting the Optic Disc Boundary in Digital Fundus Images Using Morphological, Edge Detection, and Feature Extraction Techniques," *IEEE Transactions on Medical Imaging*, vol. 29, no. 11, pp. 1860-1869, 2010.
- [64] S. Sarangi, A. Mohapatra, and S. K. Sabut, "A comparative evaluation of diabetic retinal vascular structures using edge detection techniques," *International Journal of Telemedicine and Clinical Practices*, vol. 1, no. 1, pp. 111-120, 2015.
- [65] D. S. Sisodia, S. Nair, and P. Khobragade, "Diabetic Retinal Fundus Images: Preprocessing and Feature Extraction for Early Detection of Diabetic Retinopathy," *Biomedical and Pharmacology Journal*, vol. 10, no. 2, pp. 615-626, 2017.
- [66] J. Majumdar, D. Kundu, S. Tewary, S. Ghosh, S. Chakraborty, and S. Gupta, "An Automated Graphical User Interface based System for the Extraction of Retinal

- Blood Vessels using Kirsch's Template," *International Journal of Advanced Computer Science and Applications*, vol. 6, no. 6, pp. 86-93, 2015.
- [67] A. Al-Marghilnai, and R. F. Mansour, "Wavelet filter techniques for segmenting retinal blood vessels," *International Journal of Advanced and Applied Sciences*, vol. 4, no. 9, pp. 156-160, 2017.
- [68] S. Kaur, and K. S. Mann, "Optimized retinal blood vessel segmentation technique for detection of diabetic retinopathy," *International Journal of Advanced Research in Computer Science*, vol. 8, no. 9, 2017.
- [69] M. E. Gegundez-Arias, A. Aquino, J. M. Bravo, and D. Marin, "A Function for Quality Evaluation of Retinal Vessel Segmentations," *IEEE Transactions of Medical Imaging*, vol. 31, no. 2, pp. 231-239, 2012.
- [70] D. Marín, A. Aquino, M. E. Gegundez-Arias, and J. M. Bravo, "A New Supervised Method for Blood Vessel Segmentation in Retinal Images by Using Gray-Level and Moment Invariants-Based Features," *IEEE Transactions on Medical Imaging*, vol. 30, no. 1, pp. 146-158, 2011.
- [71] Z. Hu, M. Niemeijer, M. D. Abramoff, and M. K. Garvin, "Multimodal Retinal Vessel Segmentation from Spectral-Domain Optical Coherence Tomography and Fundus Photography," *IEEE Transactions of Medical Imaging*, vol. 31, no. 10, pp. 1900-1911, 2012.
- [72] S. Roychowdhury, D. D. Koozekanani, and K. K. Parhi, "Blood Vessel Segmentation of Fundus Images by Major Vessel Extraction and Subimage Classification," *IEEE Journal Biomedical Health and Informatics*, vol. 19, no. 3, pp. 1118-1128, May 2015.
- [73] D. Zhang and Y. Zhao, "Novel Accurate and Fast Optic Disc Detection in Retinal Images with Vessel Distribution and Directional Characteristics," *IEEE Journal Biomedical Health and Informatics*, vol. 20, no. 1, pp. 333-342, 2016.
- [74] J. I. Orlando, E. Prokofyeva, and M. B. Blaschko, "A Discriminatively Trained Fully Connected Conditional Random Field Model for Blood Vessel Segmentation in Fundus Images," *IEEE Transactions on Biomedical Engineering*, vol. 64, no. 1, pp. 16-27, 2017.
- [75] J. Almotiri, K. Elleithy, and A. Elleithy, "A Multi-Anatomical Retinal Structure Segmentation System for Automatic Eye Screening Using Morphological Adaptive Fuzzy Thresholding," *IEEE Journal of Translational Engineering in Health and Medicine*, vol. 6, pp. 1-23, 2018.
- [76] J. Almotiri, K. Elleithy, and A. Elleithy, "Retinal Vessels Segmentation Techniques and Algorithms: A Survey," *Applied Sciences*, vol. 8, no. 2, 2018.
- [77] R. F. Mansour, "Evolutionary Computing Enriched Computer-Aided Diagnosis System for Diabetic Retinopathy: A Survey," *IEEE Reviews in Biomedical Engineering*, vol. 10, pp. 334-349, 2017.
- [78] P. Costa, A. Galdran, M. I. Meyer, M. Niemeijer, M. Abramoff, A. M. Mendonça, and A. Campilho, "End-to-End Adversarial Retinal Image Synthesis," *IEEE Transactions on Medical Imaging*, vol. 37, no. 3, pp. 781-791, 2018.

- [79] B. Sumathy and S. Poornachandra, "Feature extraction in retinal fundus images," in *International Conference on Information Communication and Embedded Systems (ICICES)*, pp. 798-802, 2013.
- [80] S. Yu, D. Xiao, and Y. Kanagasigam, "Machine Learning Based Automatic Neovascularization Detection on Optic Disc Region," *IEEE Journal Biomedical Health and Informatics*, vol. 22, no. 3, pp. 886-894, 2018.
- [81] R. Geetharamani, and L. Balasubramanian, "Automatic segmentation of blood vessels from retinal fundus images through image processing and data mining techniques," *Sadhana*, vol. 40, no. 6, pp. 1715-1736, 2015.
- [82] T. A. Soomro, M. Paul, J. Gao, and L. Zheng, "Retinal blood vessel extraction method based on basic filtering schemes," in *IEEE International Conference on Image Processing (ICIP)*, 2017, pp. 4422-4426.
- [83] J. Dash and N. Bhoi, "A thresholding based technique to extract retinal blood vessels from fundus images," *Future Comput. Inform. J.*, vol. 2, no. 2, pp. 103–109, Dec. 2017.
- [84] Z. Yavuz and C. Köse, "Blood Vessel Extraction in Color Retinal Fundus Images with Enhancement Filtering and Unsupervised Classification," *Journal of Healthcare Engineering*, 2017.
- [85] T. A. Soomro, T. M. Khan, M. A. U. Khan, J. Gao, M. Paul, and L. Zheng, "Impact of ICA-Based Image Enhancement Technique on Retinal Blood Vessels Segmentation," *IEEE Access*, vol. 6, pp. 3524-3538, 2018.
- [86] Z. Fan, J. Lu, C. Wei, H. Huang, X. Cai, and X. Chen, "A Hierarchical Image Matting Model for Blood Vessel Segmentation in Fundus Images," *IEEE Transactions on Image Processing*, vol. 28, no. 5, pp. 2367-2377, May 2019.
- [87] F. M. Villalobos-Castaldi, E. M. Felipe-Riverón, and L. P. Sánchez-Fernández, "A fast, efficient and automated method to extract vessels from fundus images," *Journal of Visualization*, vol. 13, no. 3, pp. 263-270, 2010.
- [88] M. Ben Abdallah, J. Malek, K. Krissian, and R. Tourki, "An automated vessel segmentation of retinal images using multiscale vesselness," in *Eighth International Multi-Conference on Systems, Signals Devices*, 2011, pp. 1-6.
- [89] J. Kaur, and H. P. Sinha, "Automated detection of retinal blood vessels in diabetic retinopathy using Gabor filter," *International Journal of Computer Science and Network Security (IJCSNS)*, vol. 12, no. 4, pp. 109, 2012.
- [90] J. Odstreilik, R. Kolar, A. Budai, J. Hornegger, J. Jan, J. Gazarek, and E. Angelopoulou, "Retinal vessel segmentation by improved matched filtering: evaluation on a new high-resolution fundus image database," *IET Image Processing*, vol. 7, no. 4, pp. 373-383, 2013.
- [91] M. Frucci, D. Riccio, G. S. di Baja, and L. Serino, "Using Contrast and Directional Information for Retinal Vessels Segmentation," in *Tenth International Conference on Signal-Image Technology and Internet-Based Systems*, 2014, pp. 592-597.

- [92] N. P. Singh, R. Kumar, and R. Srivastava, "Local entropy thresholding based fast retinal vessels segmentation by modifying matched filter," in *Communication Automation International Conference on Computing*, 2015, pp. 1166-1170.
- [93] S. Sharma, and E. V. Wasson, "Retinal blood vessel segmentation using fuzzy logic," *Journal of Network Communications and Emerging Technologies*, vol. 4, no. 3, 2015.
- [94] Z. Jiang, J. Yopez, S. An, and S. Ko, "Fast, accurate and robust retinal vessel segmentation system," *Biocybernetics and Biomedical Engineering*, vol. 37, no. 3, pp. 412-421, 2017.
- [95] N. Muangnak, P. Aimmanee, and S. Makhanov, "Automatic optic disk detection in retinal images using hybrid vessel phase portrait analysis," *Medical & Biological Engineering & Computing*, vol. 56, no. 4, pp. 583-598, 2018.
- [96] S. S. Kar, and S. P. Maity, "Automatic detection of retinal lesions for screening of diabetic retinopathy," *IEEE Transactions on Biomedical Engineering*, vol. 65, no. 3, pp. 608-618, 2017.
- [97] K. Ram, G. D. Joshi, and J. Sivaswamy, "A Successive Clutter-Rejection-Based Approach for Early Detection of Diabetic Retinopathy," *IEEE Transactions on Biomedical Engineering*, vol. 58, no. 3, pp. 664-673, 2011.
- [98] L. Seoud, T. Hurtut, J. Chelbi, F. Cheriet, and J. M. P. Langlois, "Red Lesion Detection Using Dynamic Shape Features for Diabetic Retinopathy Screening," *IEEE Transactions on Medical Imaging*, vol. 35, no. 4, pp. 1116-1126, 2016.
- [99] I. Lazar and A. Hajdu, "Retinal Microaneurysm Detection Through Local Rotating Cross-Section Profile Analysis," *IEEE Transactions on Medical Imaging*, vol. 32, no. 2, pp. 400-407, 2013.
- [100] R. Inbarathi, and R. Karthikeyan, "Detection of retinal hemorrhage in fundus images by classifying the splat features using SVM," *International Journal of Innovative Research in Science, Engineering and Technology*, vol. 3, no. 3, pp. 1979-1985, 2014.
- [101] M. U. Akram, A. Tariq, S. A. Khan, and S. A. Bazar, "Microaneurysm detection for early diagnosis of diabetic retinopathy," in *International Conference on Electronics, Computer and Computation (ICECCO)*, 2013, pp. 21-24.
- [102] L. Dai, R. Fang, H. Li, X. Hou, B. Sheng, Q. Wu, and W. Jia, "Clinical Report Guided Retinal Microaneurysm Detection with Multi-Sieving Deep Learning," *IEEE Transactions on Medical Imaging*, vol. 37, no. 5, pp. 1149-1161, 2018.
- [103] M. Niemeijer, B. van Ginneken, J. Staal, M. S. A. Suttorp-Schulten, and M. D. Abramoff, "Automatic detection of red lesions in digital color fundus photographs," *IEEE Transactions on Medical Imaging*, vol. 24, no. 5, pp. 584-592, 2005.
- [104] G. Quellec, S. R. Russell, and M. D. Abramoff, "Optimal Filter Framework for Automated, Instantaneous Detection of Lesions in Retinal Images," *IEEE Transactions on Medical Imaging*, vol. 30, no. 2, pp. 523-533, 2011.

- [105] A. Rocha, T. Carvalho, H. F. Jelinek, S. Goldenstein, and J. Wainer, "Points of Interest and Visual Dictionaries for Automatic Retinal Lesion Detection," *IEEE Transactions on Biomedical Engineering*, vol. 59, no. 8, pp. 2244-2253, 2012.
- [106] M. Partovi, S. H. Rasta, and A. Javadzadeh, "Automatic detection of retinal exudates in fundus images of diabetic retinopathy patients," *Journal of Research Clinical Medicine*, vol. 4, no. 2, 2016.
- [107] V. Handšková, J. Pavlovičova, M. Oravec, and R. Blaško, "Diabetic Retinopathy Screening by Bright Lesions Extraction from Fundus Images," *Journal of Electrical Engineering*, vol. 64, no. 5, pp. 311-316, 2013.
- [108] I. Sadek, M. Elawady, and A. E. R. Shabayek, "Automatic Classification of Bright Retinal Lesions via Deep Network Features," *ArXiv170702022 Cs*, 2017.
- [109] R. Priya, and P. Aruna, "Diagnosis of diabetic retinopathy using machine learning techniques," *ICTACT Journal on Soft Computing*, vol. 3, no. 4, pp. 563-575, 2013.
- [110] M. P. Paing, S. Choomchuay, and M. D. Rapeeporn Yodprom, "Detection of lesions and classification of diabetic retinopathy using fundus images," in *9th Biomedical Engineering International Conference (BMEiCON)*, 2016, pp. 1-5.
- [111] N. Yalçın, S. Alver, and N. Uluhatun, "Classification of retinal images with deep learning for early detection of diabetic retinopathy disease," in *26th Signal Processing and Communications Applications Conference (SIU)*, 2018, pp. 1-4.
- [112] J. Lachure, A. V. Deorankar, S. Lachure, S. Gupta, and R. Jadhav, "Diabetic Retinopathy using morphological operations and machine learning," in *IEEE International Advance Computing Conference (IACC)*, 2015, pp. 617-622.
- [113] E. V. Carrera, A. González, and R. Carrera, "Automated detection of diabetic retinopathy using SVM," in *IEEE XXIV International Conference on Electronics, Electrical Engineering and Computing (INTERCON)*, 2017, pp. 1-4.
- [114] J. E. Koh, E. Y. Ng, S. V. Bhandary, A. Laude, and U. R. Acharya, "Automated detection of retinal health using PHOG and SURF features extracted from fundus images," *Applied Intelligence*, vol. 48, no. 5, pp. 1379-1393, 2018.
- [115] R. Karthikeyan, and P. Alli, "Feature selection and parameters optimization of support vector machines based on hybrid glowworm swarm optimization for classification of diabetic retinopathy," *Journal of Medical Systems*, vol. 42, no. 10, pp. 195, 2018.
- [116] A. W. Reza, and C. Eswaran, "A decision support system for automatic screening of non-proliferative diabetic retinopathy," *Journal of medical systems*, vol. 35, no. 1, pp. 17-24, 2011.
- [117] C. Agurto, V. Murray, E. Barriga, S. Murillo, M. Pattichis, H. Davis, and P. Soliz, "Multiscale AM-FM Methods for Diabetic Retinopathy Lesion Detection," *IEEE Transactions on Medical Imaging*, vol. 29, no. 2, pp. 502-512, 2010.
- [118] M. Usman Akram, S. Khalid, A. Tariq, S. A. Khan, and F. Azam, "Detection and classification of retinal lesions for grading of diabetic retinopathy," *Computers in Biology and Medicine*, vol. 45, pp. 161-171, 2014.

- [119] M. R. K. Mookiah, U. R. Acharya, V. Chandran, R. J. Martis, J. H. Tan, J. E. Koh, and A. Laude, "Application of higher-order spectra for automated grading of diabetic maculopathy," *Medical & Biological Engineering & Computing*, vol. 53, no. 12, pp. 1319-1331, 2015.
- [120] M. N. Zahoor and M. M. Fraz, "Fast Optic Disc Segmentation in Retina Using Polar Transform," *IEEE Access*, vol. 5, pp. 12293-12300, 2017.
- [121] L. Dai, B. Sheng, Q. Wu, H. Li, X. Hou, W. Jia, and R. Fang, "Retinal microaneurysm detection using clinical report guided multi-sieving CNN," In *International Conference on Medical Image Computing and Computer-Assisted Intervention*, 2017, pp. 525-532.
- [122] R. Srivastava, L. Duan, D. W. K. Wong, J. Liu, and T. Y. Wong, "Detecting retinal microaneurysms and hemorrhages with robustness to the presence of blood vessels," *Computer Methods and Programs in Biomedicine*, vol. 138, pp. 83-91, 2017.
- [123] J. I. Orlando, E. Prokofyeva, M. del Fresno, and M. B. Blaschko, "An ensemble deep learning based approach for red lesion detection in fundus images," *Computer Methods and Programs in Biomedicine*, vol. 153, pp. 115-127, 2018.
- [124] P. Ram, and T. R. Swapna, "A Study on Various Quantification Algorithms for Diabetic Retinopathy and Diabetic Maculopathy Grading," In *Computational Vision and Bio Inspired Computing*, pp. 412-421, 2018.
- [125] F. F. Wahid, K. Sugandhi, and G. Raju, "Two Stage Histogram Enhancement Schemes to Improve Visual Quality of Fundus Images," In *International Conference on Advances in Computing and Data Sciences*, 2018, pp. 1-11.
- [126] E. J. Carmona, J. M. Molina-Casado, "Simultaneous segmentation of the optic disc and fovea in retinal images using evolutionary algorithms," *Neural Computing and Applications*, pp. 1-19, 2020.
- [127] M. U. Akram, A. Tariq, M. A. Anjum, and M. Y. Javed, "Automated detection of exudates in colored retinal images for diagnosis of diabetic retinopathy," *Applied Optics*, vol. 51, no. 20, pp. 4858-4866, 2012.
- [128] H. Tjandrasa, R. E. Putra, A. Y. Wijaya, and I. Arieshanti, "Classification of non-proliferative diabetic retinopathy based on hard exudates using soft margin SVM," in *IEEE International Conference on Control System, Computing and Engineering*, 2013, pp. 376-380.
- [129] M. U. Akram, A. Tariq, S. A. Khan, and M. Y. Javed, "Automated detection of exudates and macula for grading of diabetic macular edema," *Computer Methods and Programs in Biomedicine*, vol. 114, no. 2, pp. 141-152, 2014.
- [130] K. A. Goatman, A. D. Fleming, S. Philip, G. J. Williams, J. A. Olson, and P. F. Sharp, "Detection of New Vessels on the Optic Disc Using Retinal Photographs," *IEEE Transactions on Medical Imaging*, vol. 30, no. 4, pp. 972-979, 2011.
- [131] S. Wang, H. L. Tang, L. I. Al Turk, Y. Hu, S. Sanej, G. M. Saleh, T. Peto, "Localizing Microaneurysms in Fundus Images through Singular Spectrum Analysis," *IEEE Trans. Biomed. Eng.*, vol. 64, no. 5, pp. 990-1002, 2017.

- [132] S. Morales, K. Engan, V. Naranjo, and A. Colomer, "Retinal Disease Screening Through Local Binary Patterns," *IEEE Journal of Biomedical and Health Informatics*, vol. 21, no. 1, pp. 184-192, 2017.
- [133] A. A. Adekunle, A. Khashman, E. O. Olaniyi, and O. K. Oyedotun, "Diabetic retinopathy diagnosis using neural network arbitration. Bulletin of the Transilvania University of Brasov," *Mathematics, Informatics, Physics. Series III*, vol. 10, no. 1, pp. 179, 2017.
- [134] J. Xu, X. Zhang, H. Chen, J. Li, J. Zhang, L. Shao and G. Wang, "Automatic Analysis of Microaneurysms Turnover to Diagnose the Progression of Diabetic Retinopathy," *IEEE Access*, vol. 6, pp. 9632-9642, 2018.
- [135] B. Antal and A. Hajdu, "An Ensemble-Based System for Microaneurysm Detection and Diabetic Retinopathy Grading," *IEEE Transactions on Biomedical Engineering*, vol. 59, no. 6, pp. 1720-1726, 2012.
- [136] P. Kahai, K. R. Namuduri, and H. Thompson, "A Decision Support Framework for Automated Screening of Diabetic Retinopathy," *International Journal of Biomedical Imaging*, vol. 2006, pp. e45806, 2006.
- [137] F. Aptel, P. Denis, F. Rouberol, and C. Thivolet, "Screening of diabetic retinopathy: Effect of field number and mydriasis on sensitivity and specificity of digital fundus photography," *Diabetes and Metabolism*, vol. 34, no. 3, pp. 290-293, 2008.
- [138] B. Dupas, T. Walter, A. Erginay, R. Ordonez, N. Deb-Joardar, P. Gain, J.-C Klein, P. Massin, "Evaluation of automated fundus photograph analysis algorithms for detecting microaneurysms, haemorrhages and exudates, and of a computer-assisted diagnostic system for grading diabetic retinopathy," *Diabetes Metab.*, vol. 36, no. 3, pp. 213-220, 2010.
- [139] M. N. Ashraf, Z. Habib, and M. Hussain, "Texture Feature Analysis of Digital Fundus Images for Early Detection of Diabetic Retinopathy," in *Imaging and Visualization 2014 11th International Conference on Computer Graphics*, 2014, pp. 57-62.
- [140] M. A. Al-Jarrah and H. Shatnawi, "Non-proliferative diabetic retinopathy symptoms detection and classification using neural network," *Journal of Medical Engineering and Technology*, vol. 41, no. 6, pp. 498-505, 2017.
- [141] B. Harangi, "Skin lesion classification with ensembles of deep convolutional neural networks," *Journal of Biomedical Informatics*, vol. 86, pp. 25-32, 2018.
- [142] C. D. R. Wulandari, S. A. Wibowo, and L. Novamizanti, "Classification of Diabetic Retinopathy using Statistical Region Merging and Convolutional Neural Network," in *IEEE Asia Pacific Conference on Wireless and Mobile (APWiMob)*, 2019, pp. 94-98.
- [143] A. ElTanboly, M. Ismail, A. Shalaby, A. Switala, A. El-Baz, S. Schaal, and M. El-Azab, "A computer-aided diagnostic system for detecting diabetic retinopathy in optical coherence tomography images," *Medical physics*, vol. 44, no. 3, pp. 914-923, 2017.

- [144] D. Kumar, G. W. Taylor, and A. Wong, "Discovery Radiomics with CLEAR-DR: Interpretable Computer Aided Diagnosis of Diabetic Retinopathy," *IEEE Access*, vol. 7, pp. 25891-25896, 2019.
- [145] A. Tariq, M. U. Akram, A. Shaukat, and S. A. Khan, "Automated detection and grading of diabetic maculopathy in digital retinal images," *Journal of Digital Imaging*, vol. 26, no. 4, pp. 803-812, 2013.
- [146] S. K. Somasundaram, and P. Alli, "A machine learning ensemble classifier for early prediction of diabetic retinopathy," *Journal of Medical Systems*, vol. 41, no. 12, pp. 201, 2017.
- [147] R. Srivastava, D. W. K. Wong, L. Duan, J. Liu, T. Y. Wong, "Red lesion detection in retinal fundus images using Frangi-based filters," In *37th Annual International Conference of the IEEE Engineering in Medicine and Biology Society (EMBC)*, 2015, pp. 5663-5666.
- [148] L. Seoud, J. Chelbi, and F. Cheriet, "Automatic Grading of Diabetic Retinopathy on a Public Database," in *Proceedings of Ophthalmic Medical Image Analysis International Workshop*, vol. 2, 2015, pp. 97-104.
- [149] M. Sankar, K. Batri, and R. Parvathi, "Earliest diabetic retinopathy classification using deep convolution neural networks," *International Journal of Advanced Engineering and Technology*, vol. 10, no. M9, 2016.
- [150] R. Pires, H. F. Jelinek, J. Wainer, S. Goldenstein, E. Valle, and A. Rocha, "Assessing the Need for Referral in Automatic Diabetic Retinopathy Detection," *IEEE Transactions on Biomedical Engineering*, vol. 60, no. 12, pp. 3391-3398, 2013.
- [151] B. Antal and A. Hajdu, "Evaluation of preprocessing methods for microaneurysm detection," in *8th International Symposium on Image and Signal Processing and Analysis (ISPA)*, 2013, pp. 723-726.
- [152] S. S. Rahim, C. Jayne, V. Palade, and J. Shuttleworth, "Automatic detection of microaneurysms in colour fundus images for diabetic retinopathy screening," *Neural computing and applications*, vol. 27, no. 5, pp. 1149-1164, 2016.
- [153] S. Poddar, B. Kumar Jha, and C. Chakraborty, "Quantitative clinical marker extraction from colour fundus images for non-proliferative Diabetic Retinopathy grading," in *International Conference on Image Information Processing*, 2011, pp. 1-6.
- [154] A. D. Fleming, S. Philip, K. A. Goatman, G. J. Williams, J. A. Olson, and P. F. Sharp, "Automated detection of exudates for diabetic retinopathy screening," *Physics in Medicine and Biology*, vol. 52, no. 24, pp. 7385-7396, 2007.
- [155] Q. Abbas, I. Fondon, A. Sarmiento, S. Jiménez, and P. Alemany, "Automatic recognition of severity level for diagnosis of diabetic retinopathy using deep visual features," *Medical & Biological Engineering & Computing*, vol. 55, no. 11, pp. 1959-1974, 2017.

- [156] Z. Wang and J. Yang, "Diabetic Retinopathy Detection via Deep Convolutional Networks for Discriminative Localization and Visual Explanation," *ArXiv170310757 Cs*, 2019.
- [157] F. Yu, J. Sun, A. Li, J. Cheng, C. Wan, and J. Liu, "Image quality classification for DR screening using deep learning," in *39th Annual International Conference of the IEEE Engineering in Medicine and Biology Society (EMBC)*, 2017, pp. 664-667.
- [158] Z. Gao, J. Li, J. Guo, Y. Chen, Z. Yi, and J. Zhong, "Diagnosis of diabetic retinopathy using deep neural networks," *IEEE Access*, vol. 7, pp. 3360-3370, 2018.
- [159] M. Mateen, J. Wen, Nasrullah, S. Song, and Z. Huang, "Fundus Image Classification Using VGG-19 Architecture with PCA and SVD," *Symmetry*, vol. 11, no. 1, 2019.
- [160] X. Li, T. Pang, B. Xiong, W. Liu, P. Liang, and T. Wang, "Convolutional neural networks based transfer learning for diabetic retinopathy fundus image classification," in *10th International Congress on Image and Signal Processing, Biomedical Engineering and Informatics (CISP-BMEI)*, 2017, pp. 1-11.
- [161] C. Lam, D. Yi, M. Guo, and T. Lindsey, "Automated Detection of Diabetic Retinopathy using Deep Learning," *AMIA Summits on Translational Science proceedings*, 2018, pp. 147–155.
- [162] Y. Yang, T. Li, W. Li, H. Wu, W. Fan, and W. Zhang, "Lesion detection and grading of diabetic retinopathy via two-stages deep convolutional neural networks," In *International Conference on Medical Image Computing and Computer-Assisted Intervention*, 2017, pp. 533-540.
- [163] V. Chandore, and S. Asati, "Automatic detection of diabetic retinopathy using deep convolutional neural network," *Int J Adv Res Ideas Innov Technol*, vol. 3, pp. 633-41, 2017.
- [164] V. Gulshan L. Peng, M. Coram, M. C. Stumpe, D. Wu, A. Narayanaswamy, and R. Kim, "Development and Validation of a Deep Learning Algorithm for Detection of Diabetic Retinopathy in Retinal Fundus Photographs," *Journal of the American Medical Association (JAMA)*, vol. 316, no. 22, pp. 2402–2410, Dec. 2016.
- [165] M. Melinščak, P. Prentašić, and S. Lončarić, "Retinal vessel segmentation using deep neural networks," In *10th International Conference on Computer Vision Theory and Applications (VISAPP 2015)*, 2015.
- [166] M. D. Abramoff, J. M. Reinhardt, S. R. Russell, J. C. Folk, V. B. Mahajan, M. Niemeijer, and G. Quellec, "Automated early detection of diabetic retinopathy," *Ophthalmology*, vol. 117, no. 6, pp. 1147-1154, 2010.
- [167] R. Gargeya and T. Leng, "Automated Identification of Diabetic Retinopathy Using Deep Learning," *Ophthalmology*, vol. 124, no. 7, pp. 962-969, 2017.
- [168] G. Quellec, K. Charrière, Y. Boudi, B. Cochener, and M. Lamard, "Deep image mining for diabetic retinopathy screening," *Medical Image Analysis*, vol. 39, pp. 178-193, 2017.

- [169] D. K. Prasad, L. Vibha, and K. R. Venugopal, "Early detection of diabetic retinopathy from digital retinal fundus images," in *IEEE Recent Advances in Intelligent Computational Systems (RAICS)*, 2015, pp. 240-245.
- [170] N. Du and Y. Li, "Automated identification of diabetic retinopathy stages using support vector machine," in *Proceedings of the 32nd Chinese Control Conference*, 2013, pp. 3882-3886.
- [171] N. Gurudath, M. Celenk, and H. B. Riley, "Machine learning identification of diabetic retinopathy from fundus images," in *IEEE Signal Processing in Medicine and Biology Symposium (SPMB)*, 2014, pp. 1-7.
- [172] W. Cao, J. Shan, N. Czarnek, and L. Li, "Microaneurysm detection in fundus images using small image patches and machine learning methods," in *IEEE International Conference on Bioinformatics and Biomedicine (BIBM)*, 2017, pp. 325-331.
- [173] L. Nanni, S. Ghidoni, and S. Brahmam, "Handcrafted vs. non-handcrafted features for computer vision classification," *Pattern Recognit.*, vol. 71, pp. 158-172, Nov. 2017.
- [174] G. Litjens, T. Kooi, B. E. Bejnordi, A. A. A. Setio, F. Ciompi, M. Ghafoorian, and C. I. Sánchez, C. I., "A survey on deep learning in medical image analysis," *Medical Image Analysis*, vol. 42, pp. 60-88, 2017.
- [175] M. Alban, T. Gilligan, "Automated detection of diabetic retinopathy using fluorescein angiography photographs," *Report of Stanford Education*, 2016.
- [176] H. Pratt, F. Coenen, D. M. Broadbent, S. P. Harding, and Y. Zheng, "Convolutional neural networks for diabetic retinopathy," *Procedia Computer Science*, vol. 90, pp. 200-205, 2016.
- [177] R. F. Mansour, "Deep-learning-based automatic computer-aided diagnosis system for diabetic retinopathy," *Biomedical engineering letters*, vol. 8, no. 1, pp. 41-57, 2018.
- [178] J. Goncalves, T. Conceicao, F. Soares, "Inter-observer Reliability in Computer-aided Diagnosis of Diabetic Retinopathy," In *HEALTHINF*, pp. 481-491, 2019.
- [179] P. Saranya, S. Prabakaran, "Automatic detection of non-proliferative diabetic retinopathy in retinal fundus images using convolution neural network," *Journal of Ambient Intelligence and Humanized Computing*, 2020.
- [180] S. Masood T. Luthra, H. Sundriyal, M. Ahmed, "Identification of diabetic retinopathy in eye images using transfer learning," In *International Conference on Computing, Communication and Automation (ICCCA)*, 2017, pp. 1183-1187.
- [181] H. Takahashi, H. Tampo, Y. Arai, Y. Inoue, H. Kawashima, "Applying artificial intelligence to disease staging: Deep learning for improved staging of diabetic retinopathy," *PloS one*, vol. 12, no. 6, pp. e0179790, 2017.
- [182] R. Ghosh, K. Ghosh, and S. Maitra, "Automatic detection and classification of diabetic retinopathy stages using CNN," in *4th International Conference on Signal Processing and Integrated Networks (SPIN)*, pp. 550-554, Feb. 2017.

- [183] J. I. Orlando, E. Prokofyeva, M. del Fresno, and M. B. Blaschko, "Learning to detect red lesions in fundus photographs: An ensemble approach based on deep learning," *arXiv preprint arXiv:1706.03008*, 2017.
- [184] W. Zhang, J. Zhong, S. Yang, Z. Gao, J. Hu, Y. Chen, and Z. Yi, "Automated identification and grading system of diabetic retinopathy using deep neural networks," *Knowledge-Based Systems*, vol. 175, pp. 12–25, 2019.
- [185] M. Y. T. Yip, Z. W. Lim, G. Lim, N. D. Quang, H. Hamzah, J. Ho, V. Bellemo, Y. Xie, X. Q. Lee, M. L. Lee, W. Hsu, T. Y. Wong, D. S. W. Ting, "Enhanced Detection of Referable Diabetic Retinopathy via DCNNs and Transfer Learning," *In Asian Conference on Computer Vision*, pp. 282-288. Springer, Cham, 2018.
- [186] Z. Gao, J. Li, J. Guo, Y. Chen, Z. Yi, and J. Zhong, "Diagnosis of Diabetic Retinopathy Using Deep Neural Networks," *IEEE Access*, vol. 7, pp. 3360–3370, 2019.
- [187] R. C. Gonzalez, R. E. Woods, and S. L. Eddins, *Digital Image Processing using MATLAB*. Pearson Education India, 2004.
- [188] B. Janney, G. Meera, G. U. Shankar, S. Divakaran, and S. Abraham, "Detection and classification of exudates in retinal image using image processing techniques," *Journal of Chemical and Pharmaceutical Sciences*, vol. 8, pp. 541-546, 2015.
- [189] M. Abdullah, M. M. Fraz, and S. A. Barman, "Localization and segmentation of optic disc in retinal images using circular Hough transform and grow-cut algorithm," *PeerJ*, 4, e2003, 2016.
- [190] Y. Alomari, S. N. H. S. Abdullah, and K. Omar, "Randomized Circle Detection Performance Based on Image Difficulty Levels and Edge Filters," *In FIRA RoboWorld Congress*, 2013, pp. 361-374.
- [191] S. Badsha, A. W. Reza, K. G. Tan, and K. Dimyati, "A new blood vessel extraction technique using edge enhancement and object classification," *Journal of Digital Imaging*, vol. 26, no. 6, pp. 1107-1115, 2013.
- [192] Y. Becerikli, and T. M. Karan, "A new fuzzy approach for edge detection," *In International Work-Conference on Artificial Neural Networks* (pp. 943-951). Springer, Berlin, Heidelberg, 2005.
- [193] F. Huang, B. Dashtbozorg, J. Zhang, E. Bekkers, S. Abbasi-Sureshjani, T. T. Berendschot, and B. M. ter Haar Romeny, "Reliability of Using Retinal Vascular Fractal Dimension as a Biomarker in the Diabetic Retinopathy Detection," *Journal of Ophthalmology*, Sep. 14, 2016.
- [194] IBM Corp. IBM SPSS Statistics for Windows. Armonk, NY: IBM Corp; 2017. Available: <https://hadoop.apache.org>.
- [195] C. Bhardwaj, S. Jain, and M. Sood, "Automated optical disc segmentation and blood vessel extraction for fundus images using ophthalmic image processing," *In International Conference on Advanced Informatics for Computing Research*, Singapore, 2018, pp. 182-194.
- [196] C. Bhardwaj, S. Jain, and M. Sood, "Retinal blood vessel localization to expedite PDR diagnosis," *Periodicals of Engineering Natural Science*, vol. 8, no. 3, 2020.

- [197] J. I. Orlando, K. van Keer, J. B. Breda, H. L. Manterola, M. B. Blaschko, and A. Clausse, "Proliferative diabetic retinopathy characterization based on fractal features: Evaluation on a publicly available dataset," *Medical Physics*, vol. 44, no. 12, pp. 6425-6434, 2017.
- [198] Xiaoyi Jiang and D. Mojon, "Adaptive local thresholding by verification-based multithreshold probing with application to vessel detection in retinal images," *IEEE Transactions on Pattern Analysis and Machine Intelligence*, vol. 25, no. 1, pp. 131-137, 2003.
- [199] M. E. Martinez-Perez, A. D. Highes, A. V. Stanton, S. A. Thorn, N. Chapman, A. A. Bharath, K. H. Parker, "Retinal vascular tree morphology: a semi-automatic quantification," *IEEE Transactions on Biomedical Engineering*, vol. 49, no. 8, pp. 912-917, 2002.
- [200] U. T. V. Nguyen, A. Bhuiyan, L. A. F. Park, and K. Ramamohanarao, "An effective retinal blood vessel segmentation method using multi-scale line detection," *Pattern Recognition*, vol. 46, no. 3, pp. 703-715, 2013.
- [201] A. G. Salazar-Gonzalez, Y. Li, and X. Liu, "Retinal blood vessel segmentation via graph cut," in *11th International Conference on Control Automation Robotics Vision*, 2010, pp. 225-230.
- [202] M. M. Fraz, P. Remagnino, A. Hoppe, B. Uyyanonvara, A. R. Rudnicka, C. G. Owen, and S. A. Barman, "Blood vessel segmentation methodologies in retinal images – A survey," *Computer Methods and Programs in Biomedicine*, vol. 108, no. 1, pp. 407-433, 2012.
- [203] A. M. R. R. Bandara and P. W. G. R. M. P. B. Giragama, "A retinal image enhancement technique for blood vessel segmentation algorithm," In *IEEE international conference on industrial and information systems (ICIIS)*, 2017, pp. 1-5.
- [204] M. Li, Q. Yin, and M. Lu, "Retinal blood vessel segmentation based on multi-scale deep learning," In *Federated Conference on Computer Science and Information Systems (FedCSIS)*, 2018, pp. 1-7.
- [205] S. Roy, A. Mitra, S. Roy, and S. K. Setua, "Blood vessel segmentation of retinal image using Clifford matched filter and Clifford convolution," *Multimedia Tools and Applications*, vol. 78, no. 24, pp. 34839-34865, 2019.
- [206] D. Adapa, A. N. Joseph Raj, S. N. Alisetti, Z. Zhuang, and G. Naik, "A supervised blood vessel segmentation technique for digital Fundus images using Zernike Moment based features," *Plos one*, vol. 15, no. 3, pp. e0229831, 2020.
- [207] M. Niemeijer, J. Staal, B. van Ginneken, M. Loog, and M. D. Abramoff, "Comparative study of retinal vessel segmentation methods on a new publicly available database," in *Medical Imaging 2004: Image Processing*, vol. 5370, pp. 648-656, 2004.
- [208] C. Bhardwaj, S. Jain, and M. Sood, "Hierarchical severity grade classification of non-proliferative diabetic retinopathy," *Journal of Ambient Intelligence and Humanized Computing*, pp. 1-22, 2020.

- [209] S. S. Rahim, V. Palade, J. Shuttleworth, and C. Jayne, "Automatic screening and classification of diabetic retinopathy and maculopathy using fuzzy image processing," *Brain informatics*, vol. 3, no. 4, pp. 249-267, 2016.
- [210] L. Giancardo, F. Meriaudeau, T. P. Karnowski, Y. Li, S. Garg, K. W. Tobin, E. Chaum, "Exudate-based diabetic macular edema detection in fundus images using publicly available datasets," *Medical Image Analysis*, vol. 16, no. 1, pp. 216-226, 2012.
- [211] S. D, N. B. Prakash, and N. Balagopal, "Automated Detection of Diabetic Retinopathy for Early Diagnosis using Feature Extraction and Support Vector Machine," *International Journal of Emerging Technology and Advanced Engineering*, vol. 2, no. 11, pp. 103-108, 2012.
- [212] K. Tripathi, H. Sohal, and S. Jain, "Comparative Analysis of Heart Rate Variability Parameters for Arrhythmia and Atrial Fibrillation using ANOVA," *Biomedical and Pharmacology Journal*, vol. 11, no. 4, pp. 1841-1849, 2018.
- [213] S. Solkar, and L. Das, "A New Approach for detection and classification of diabetic retinopathy using PNN and SVM classifiers," *IOSR Journal of Computer Engineering (IOSR-JCE)*, vol. 19, no. 9, pp. 62-68, 2017.
- [214] P. Costa, T. Araújo, G. Aresta, A. Galdran, A. M. Mendonça, A. Smailagic and A. Campilho, "EyeWeS: Weakly Supervised Pre-Trained Convolutional Neural Networks for Diabetic Retinopathy Detection," in *16th International Conference on Machine Vision Applications (MVA)*, 2019, pp. 1-6.
- [215] J. Nayak, P. S. Bhat, R. Acharya, C. M. Lim, and M. Kagathi, "Automated identification of diabetic retinopathy stages using digital fundus images," *Journal of Medical Systems*, vol. 32, no. 2, pp. 107-115, 2008.
- [216] M. P. Paing, S. Choomchuay, and M. R. Yodprom, "Detection of lesions and classification of diabetic retinopathy using fundus images," In *9th Biomedical engineering international conference (BMEiCON)*, 2016, pp. 1-5.
- [217] R. Saha, A. R. Chowdhury, S. Banerjee, and T. Chatterjee, "Detection of retinal abnormalities using machine learning methodologies," *Neural Network World*, vol. 28, no. 5, pp. 457-471, 2018.
- [218] Z. Fan, J. Lu, C. Wei, H. Huang, X. Cai, and X. Chen, "A hierarchical image matting model for blood vessel segmentation in fundus images," *IEEE Transactions on Image Processing*, vol. 28, no. 5, pp. 2367-2377, 2018.
- [219] X. Wang, X. Jiang, and J. Ren, "Blood vessel segmentation from fundus image by a cascade classification framework," *Pattern Recognition*, vol. 88, pp. 331-341, 2019.
- [220] G. G. Yen and W.-F. Leong, "A Sorting System for Hierarchical Grading of Diabetic Fundus Images: A Preliminary Study," *IEEE Transaction on Information Technology in Biomedicine*, vol. 12, no. 1, pp. 118-130, 2008.
- [221] J. Vaishnavi, S. Ravi, M. A. Devi, and S. Punitha, "Automatic diabetic assessment for diabetic retinopathy using support vector machines," *International Journal of Control Theory and Applications*, vol. 9, no. 7, pp. 3135-3145, 2016.

- [222] R. Lee, T. Y. Wong, and C. Sabanayagam, "Epidemiology of diabetic retinopathy, diabetic macular edema and related vision loss," *Eye and Vision*, vol. 2, no. 1, pp. 1-25, 2015.
- [223] C. P. Wilkinson, F. L. Ferris III, R. E. Klein, P. P. Lee, C. D. Agardh, M. Davis, and G. D. R. P. Group, "Proposed international clinical diabetic retinopathy and diabetic macular edema disease severity scales," *Ophthalmology*, vol. 110, no. 9, pp. 1677-1682, 2003.
- [224] R. Harini and N. Sheela, "Feature extraction and classification of retinal images for automated detection of Diabetic Retinopathy," in *Second International Conference on Cognitive Computing and Information Processing (CCIP)*, 2016, pp. 1-4.
- [225] P. J. Navarro, D. Alonso, and K. Stathis, "Automatic detection of microaneurysms in diabetic retinopathy fundus images using the L*a*b color space," *JOSA A*, vol. 33, no. 1, pp. 74-83, 2016.
- [226] A. Thammastitkul, and B. Uyyanonvara, "Diabetic Retinopathy Stages Identification Using Retinal Images," 2016.
- [227] S. Ragab, M. A. Nasser, D. Puig, "Improving the Performance of Diabetic Retinopathy Computer-Aided Diagnosis Systems Using an Ensemble of Texture Analysis Methods," in *Recent Advances in Artificial Intelligence Research and Development: Proceedings of the 20th International Conference of the Catalan Association for Artificial Intelligence*, vol. 300, 2017, pp. 16-25.
- [228] D. Xiao, A. Bhuiyan, S. Frost, J. Vignarajan, M. L. Tay-Kearney, Y. Kanagasingam, "Major automatic diabetic retinopathy screening systems and related core algorithms: a review," *Machine Vision and Applications*, vol. 30, no. 3, pp. 423-446, 2019.
- [229] D. S. Fong, L. Aiello, T. W. Gardner, G. L. King, G. Blankenship, J. D. Cavallerano, F. L. Ferris, R. Klein, "Retinopathy in Diabetes," *Diabetes Care*, vol. 27, no. 1, pp. s84-s87, 2004.
- [230] I. Kandel and M. Castelli, "Transfer Learning with Convolutional Neural Networks for Diabetic Retinopathy Image Classification. A Review," *Appl. Sci.*, vol. 10, no. 6, 2020.
- [231] W. L. Alyoubi, W. M. Shalash, and M. F. Abulkhair, "Diabetic retinopathy detection through deep learning techniques: A review," *Informatics in Medicine Unlocked*, vol. 20, p. 100377, Jan. 2020.
- [232] J. Deng, W. Dong, R. Socher, L.-J. Li, Kai Li, and Li Fei-Fei, "ImageNet: A large-scale hierarchical image database," in *IEEE Conference on Computer Vision and Pattern Recognition*, 2009, pp. 248-255.
- [233] B. Janney, G. Meera, G. U. Shankar, S. Divakaran, and S. Abraham, "Detection and classification of exudates in retinal image using image processing techniques," *Journal of Chemical and Pharmaceutical Sciences*, vol. 8, pp. 541-546, 2015.

- [234] K. Akyol, B. Şen, and S. Bayır, “Automatic Detection of Optic Disc in Retinal Image by Using Keypoint Detection, Texture Analysis, and Visual Dictionary Techniques,” *Computational and Mathematical Methods in Medicine*, 2016.
- [235] M. N. Bajwa, M. I. Malik, S. A. Siddiqui, A. Dengel, F. Shafait, W. Neumeier and S. Ahmed, “Two-stage framework for optic disc localization and glaucoma classification in retinal fundus images using deep learning,” *BMC Medical Informatics and Decision Making*, vol. 19, no. 1, 2019.
- [236] B. Durakovic, “Design of experiments application, concepts, examples: State of the art,” *Periodicals of Engineering and Natural Sciences*, vol. 5, no. 3, 2017.
- [237] C. Bhardwaj, S. Jain, and M. Sood, “Deep Learning Based Diabetic Retinopathy Prediction of Colored Fundus Images with Parameter Tuning,” In *Advances in Computational Intelligence Techniques*, pp. 53-62, 2020.
- [238] O. Perdomo, S. Ojalora, F. Rodríguez, J. Arevalo, and F. González, “A Novel Machine Learning Model Based on Exudate Localization to Detect Diabetic Macular Edema,” *Proceedings of Ophthalmic Medical Image Analysis International Workshop*, vol. 3, pp. 137-144, 2016.
- [239] H. H. Vo, and A. Verma, “New Deep Neural Nets for Fine-Grained Diabetic Retinopathy Recognition on Hybrid Color Space,” in *IEEE International Symposium on Multimedia (ISM)*, 2016, pp. 209-215.
- [240] M. Hazim Johari, H. Abu Hassan, A. Ihsan Mohd Yassin, N. Tahir, A. Zabidi, Z. Ismael Rizman, and N. Wahab, “Early Detection of Diabetic Retinopathy by Using Deep Learning Neural Network,” *International Journal of Engineering and Technology*, vol. 7, pp. 198-201, 2018.
- [241] R. Sarki, S. Michalska, K. Ahmed, H. Wang, and Y. Zhang, “Convolutional neural networks for mild diabetic retinopathy detection: an experimental study,” *bioRxiv*, p. 763136, 2019.
- [242] X. Li, X. Hu, L. Yu, L. Zhu, C.-W. Fu, and P.-A. Heng, “CANet: Cross-Disease Attention Network for Joint Diabetic Retinopathy and Diabetic Macular Edema Grading,” *IEEE Transactions on Medical Imaging*, vol. 39, no. 5, pp. 1483-1493, 2019.

APPENDICES

APPENDICES

APPENDIX-1: FEATURE ATTRIBUTES

This work utilizes diverse feature attributes for different DR diagnostic tasks. Four different feature sets exploited are fractal features, shape features, intensity features and textural features. The description of these feature sets is provided in this section.

1. Fractal Features

The first set of features utilized for extracted blood vessels analysis in Chapter 3 comprises of fractal dimensional features including fractal characteristics which consists of box-counting, information, and correlation dimensions. Fractal dimensions quantifies the self-similarity of branching patterns depending upon the box counting method. Blood vessels also have branch-like patterns and it is revealed from the literature that patients suffering from PDR have increased fractal dimensions due to increased bifurcated vascular patterns, thus this set of features is considered significant for DR screening [191, 195]. Three fractal dimensions are:

- i. **Box counting dimensions:** Box counting dimensions are defined as the total number of boxes having side length 'a' needed to cover vascular objects following the specified conditions.

$$\left(\frac{1}{a}\right)^{D_{BC}} \text{ as } a \text{ tends to } 0 \quad (1)$$

And Box-counting dimension is expressed by,

$$D_{Box_Count} = \lim_{a \rightarrow 0} \frac{\log N(a)}{\log \frac{1}{a}} \quad (2)$$

where $N(a)$ denotes the number of boxed covering vascular structure under analysis.

- ii. **Information dimensions:** Information dimensions are defined using Shannon entropy for each box count and it gives the exact information content of every box count. It can be expressed as,

$$D_{Inf_Dim} = \lim_{a \rightarrow 0} \frac{H(a)}{\log \frac{1}{a}} \quad (3)$$

here $H(a)$ denotes the sum of Shannon entropy for each of the cell in the box count of the vascular structure.

- iii. Correlation dimensions:** Correlation dimensions are approximated using probability density function denoted by,

$$C_a = \frac{1}{n^2} \sum_{i=1, j=1}^{n_a} \theta(a - \|p_i - p_j\|) \cong \sum_{i=1}^{n_r} p_{i^2}(a) \quad (4)$$

here $\theta(x)$ is the heaviside step function, p_i denotes the position of i^{th} pixel in the vascular structure and $p_i(r)$ signifies the probability of finding the vascular structure in i^{th} box.

Thus, the correlation dimensions of the vascular structure under analysis are denoted as,

$$D_{Corr_Dim} = \lim_{a \rightarrow 0} \frac{\log C(a)}{\log \frac{1}{a}} \quad (5)$$

Fractal dimensions (Box count, information and correlation) are calculated for vascular branching patterns to estimate self-similarity of extracted blood vessels with the ground truth vessels. Fractal feature based comparison relates the fractal dimensions for the extracted fundus images to ground truths provided by experts.

2. Shape Features

Shape features utilizes the geometrical region properties for each connected component in the retinal fundus image. Based on the elaborative literature survey, eleven shape features are exploited in this work including area, perimeter, major axis length, minor axis length, orientation, equivalent diameter, convex area, eccentricity, solidity, extent and compactness to determine the geometric properties of extracted retinal structures. All the shape features are detailed in Table 1.

Table 1: Shape feature set

Shape Features		
Features	Description	Formula
Area	Actual number of pixels in the selected region (Blood vessel or DR lesion in this work) i.e. the actual number of pixels in the region with intensity 1 in an image	$Area = \sum_{x,y=0}^{M,N} b(i,j)$ <p>where b (i,j) are boundary pixels with intensity 1 with each pixel element (i,j)</p>
Perimeter	Distance around the selected region boundary	$P = \sum_{i,j=0}^{M,N} E_d(i,j)$ <p>where $E_d(i,j) = 1$ if $b(i,j) == 2$</p>
Major Axis Length	Length of the major axis of ellipse (in pixels) that has same normalized second central moments as the selected region	Major axis length = $a + b$ where a, b are the distances from each focus to any point on the ellipse
Minor Axis Length	Length of the minor axis of ellipse (in pixels) that has same normalized second central moments as the selected region	Minor axis length = $(\sqrt{(a + b)^2 - f^2})$ where f is the distance between the foci and a, b are the distances from each focus to any point on the ellipse
Eccentricity	Eccentricity of the ellipse that has the same second-moments as the selected region	$E = \frac{f}{\text{major axis length}}$ where f is the distance between the foci
Convex Area	Number of pixels in the binary selected region	Convex Area = $\sum \text{binary}(i,j)$
Orientation	Angle between major axis of ellipse having same second moment as that of the pixels in the selected region and the x-axis	$O = \text{angle}(\text{horizontal and major axis})$
Equivalent diameter	Specifies the diameter of a circle with same area as the selected region	$d_e = \sqrt{\frac{4 \times Area}{\pi}}$
Solidity	Proportion of the pixels in the convex hull that are also in the selected region	$S = \frac{A_s}{\text{Convex Area}}$ where A_s = Area of selected shape
Extent	Ratio of pixels in the selected region to the pixels in the total bounding box	$Extent = \frac{A_s}{A_B}$ where A_s = Area of selected shape, A_B = Area of rectangular bounding box
Compactness	It is the measure of circularities in the selected region	$I_{Compactness} = \frac{\text{circumference}^2}{(4 \times \pi)Area}$

**Note: Selected region in our research work are the blood vessels or DR lesions whose features are to be extracted.*

3. Intensity Features

Intensity features exploits pixel properties to distinguish the selected region pixels from neighboring background pixels. Nine pixel based features including minimum, maximum, mean, median, mean absolute difference, standard deviation,

skewness and kurtosis are used to distinguish the useful pixels from neighboring background pixels.

Table 2: Intensity Feature Set

Intensity Features		
Features	Description	Formula
Minimum Intensity	Value of the pixel with the lowest intensity in the selected region	$I_{min} = \min (I(x, y))$
Maximum Intensity	Value of the pixel with the greatest intensity in the selected region	$I_{max} = \max (I(x, y))$
Mean Intensity	Mean of all the intensity values in the selected region	$I_{mean} = \text{mean} (I(x, y))$
Median Intensity	Median of all the intensity values in the selected region	$I_{median} = \{(n + 1) \div 2\}^{th}$
MAD Intensity	Mean absolute difference of all the intensity values in the selected region	$I_{MAD} = \frac{\sum x - I_{mean} }{N}$
SD Intensity	Standard deviation of all the intensity values in the selected region	$\sigma = \sqrt{\frac{\sum (x_i - I_{mean})^2}{N}}$
IQR	Inter-quartile range of all the intensity values in the selected region	$IQR = Q1 - Q3$
Skewness	Measure of the asymmetry of the probability distribution about the mean of selected region	$I_{Skewness} = \left(\frac{1}{m \times n}\right) \frac{\sum (I(x, y) - M)^3}{SD^3}$
Kurtosis	Measure of the tailedness of the probability distribution of selected region	$I_{Kurtosis} = \left(\frac{1}{m \times n}\right) \frac{\sum (I(x, y) - M)^4}{SD^4}$

where $I(x, y)$ is the grayscale image and $x \neq y$; $M = \left(\frac{1}{m \times n}\right) \sum_{x=0}^{m-1} \sum_{y=0}^{n-1} I(x, y)$, $SD = \sqrt{\left(\frac{1}{m \times n}\right) \sum_{x=0}^{m-1} \sum_{y=0}^{n-1} (I(x, y) - M)^2}$, Q1 is the first quartile and Q3 is the third quartile, N = all intensity values.

***Note:** Selected region in our research work are the blood vessels or DR lesions whose features are to be extracted.

4. Gray Level Co-occurrence Matrix (GLCM) Textural Features

Textural features exploit the textural properties of the detected selected region considering the spatial pixel relationships. Textural properties of identified anomalies are exploited using Gray-Level Co-occurrence Matrix (GLCM) textural features taking into consideration the spatial dependency of pixels in an image [21, 22, 23]. GLCM matrix is generated using different spatial orientations. Co-occurrence matrix of size $N \times N$ is denoted as $X_{i,j}$ where each element (i,j) are representative of frequency with which pixels of i^{th} gray level are spatially related to pixels with j^{th} gray level. Based on the literature review and relevance of features for this work, 14 GLCM features were extracted and are formulated in Table 3.

Table 3: Textural Feature set

Textural Features		
Feature	Description	Formula
Autocorrelation	Linear dependencies of gray level pixels at a specific point with respect to itself in the selected region	$\sum_{i,j=0}^{N-1} X_{i,j} \left[\frac{(i,j - \mu_{i,j})^2}{\sqrt{\sigma_{i=j}^2}} \right]$
Correlation	Linear dependencies of gray level pixels at a specific point with respect to each other in the selected region	$\sum_{i,j=0}^{N-1} X_{i,j} \left[\frac{(i - \mu_i)(j - \mu_j)}{\sqrt{\sigma_i^2 \sigma_j^2}} \right]$
Contrast	Measure of pixel intensities and its neighbour over the selected region	$\sum_{i,j=0}^{N-1} X_{i,j} (i - j)^2$
Cluster Shade	Measure of lack of symmetry or skewness in the selected region	$Sgn(A A ^{1/3})$ where $A = \sum_{i,j=0}^{N-1} \frac{(i+j-2\mu)^3 \times X_{i,j}}{\sigma^3 (\sqrt{2(1+Correlation)})^3}$
Cluster Prominence	Measure of grayscale variation in the selected region	$Sgn(B B ^{1/4})$ where $B = \sum_{i,j=0}^{N-1} \frac{(i+j-2\mu)^4 \times X_{i,j}}{4 \times \sigma^4 (1+Correlation)^2}$
Energy	Measure of pixel pair repetition or uniformity of selected region	$\sum_{i,j=0}^{N-1} X_{i,j}^2$
Entropy	Measure of randomness of selected region	$\sum_{i,j=0}^{N-1} X_{i,j} (-\ln(X_{i,j}))$
Homogeneity	Closeness of distribution of elements in the selected region	$\sum_{i,j=0}^{N-1} \frac{X_{i,j}}{1 + (i - j)^2}$
Inverse Difference Normalized	Difference between the neighbouring intensity values is normalized by total pixels in the selected region	$\sum_{i,j=0}^{N-1} \frac{C(i,j)}{1+ i-j }$ where $C(i,j) = \frac{X_{i,j}}{\sum_{i,j=1}^{N-1} X_{i,j}}$
Inverse Difference Moment Normalized	Difference of local homogeneity between the neighbouring intensity values normalized by total pixels in the selected region	$\sum_{i,j=0}^{N-1} \frac{C(i,j)}{1 + i - j ^2}$
Dissimilarity	Measures the mean gray level difference in distribution of pixels in the selected region	$\sum_{i,j=0}^{N-1} X_{i,j} i - j $
Maximum Probability	Max probability of distribution of pixels in the selected region	$\max(X_{i,j})$
InfoCorr1	Measure of information correlation in terms of its mutual information	$\frac{H_{XY} - H_{XY1}}{\max(H_X H_Y)}$
InfoCorr2	It is the measure of information correlation.	$(1 - \exp[-2(H_{XY2} - H_{XY})^{1/2}])$

where $H_{XY} = -\sum_i \sum_j p(i,j) \log(p(i,j))$, $H_{XY1} = -\sum_i \sum_j p(i,j) \log(p_x(i) p_y(j))$, $H_{XY2} = -\sum_i \sum_j p_x(i) p_y(j) \log(p_x(i) p_y(j))$, H_X and H_Y are the entropies of p_X and p_Y .

***Note:** Selected region in our research work are the DR lesions whose features are to be extracted.

These features are subjected to exhaustive statistical analysis for optimal feature selection which results in prominent features providing better performance for DR severity classification problem.

APPENDIX-2: FEATURE SELECTION TOOLS

Feature set normalization is an important step in statistical analysis. Graphical and exact methods are two ways to check the normality of data distribution. Box plot is a graphical analysis tool used to visualize the normality of feature set, however, Shapiro-Wilk test is used as an exact technique to compare the numerical values with standard normal distribution range. Statistical correlation analysis of the extracted feature set is performed utilizing Pearson and Spearman's correlation coefficients to quantify the relationship between feature variables considering the pair-wise linear correlation. In this research work, *t*-test and Analysis of Variance (ANOVA) statistical tool are used to decrease the dimensional complexity while increasing the performance. Feature selection resulting in dimensionality reduction is significant in improving the system performance in terms of computation time and storage. Statistical analysis methods adopted in this paper using SPSS package are based on box plots, Pearson correlation coefficient analysis, *t*-test and ANOVA.

1. Box plots: For the visual representation of the features, box plots are used as they are appropriate to represent the statistical data as a rectangular box of quartiles. Box plots are used to visually assess the features extracted for the proposed blood vessel segmentation approach. They suitably represent the statistical data in terms of quartiles demonstrating the 25 to 75% of the data distribution inside a rectangular box. Box plots indicate the five statistics; minimum value, first quartile, median value, third quartile, and maximum value.

The variability outside the bounds of upper and lower quartiles is indicated by the vertical lines extending from the box plot. Outliers are well indicated using box plot analysis outside the plot and the median is expressed by a vertical line inside the box. Box plots are well suited for the normality representation of more than one dataset graphically.

Feature selection is done on the basis of correlation analysis, Levene's *f*-test and *t*-test explained below. Equality of variance is determined using Levene's test

commonly known as f-test and equality of means is inferred from t -test. The f -test provides statistical evidence of whether the variances of the two samples are approximately equal or not.

- 2. Pearson Correlation Coefficient Analysis:** Pearson correlation measures the linear correlation between two sets of samples and its value ranges from -1 to 1. Pearson correlation coefficient value 1 shows total positive linear correlation between the samples and 0 shows no correlation. Total negative correlation is indicated by the value of Pearson correlation coefficient as -1.
- 3. Levene's test:** Based on the hypothesis assumption, Levene's inferential statistic test is used to assess the equality of variances for two or more than two groups. Its result depends upon the p -value and if the p -value significance level is less than 0.05 then it is considered significant otherwise not.
- 4. t -test and ANOVA:** t -test is a parametric test helpful in evaluating the sets of continuous data by comparing their means.

Analysis of Variance (ANOVA) inferential statistical tool analyses the difference or variation among the group means. This is basically the generalization of t -test for more than two groups as it provides the evidence of whether the means of several groups are equal or unequal. The significance of t -test and ANOVA are depicted by the p -value taken as less than 0.05 otherwise the test depicts insignificant value.

The statistical significance of Levene's test, t -test and ANOVA is given by the significance value (p -value) of the test which should be less than 0.05 to state any feature significant enough to reject the null hypothesis.

$$p = \begin{cases} p \leq 0.05 & \textit{indicates Strong Significance} \\ 0.01 < p \leq 0.05 & \textit{indicates Moderate Significance} \\ p > 0.05 & \textit{indicates Weak Significance} \end{cases}$$

The selected prominent features based on statistical analysis done using the above-mentioned tools are provided for the classification stage.